
Spatio-Spectrally Tailored Nonlinear Enhancement Cavities

Techniques for Attosecond Science at
Multi-10-MHz Repetition Rates

Maximilian Högner



München 2019

Spatio-Spectrally Tailored Nonlinear Enhancement Cavities

Techniques for Attosecond Science at
Multi-10-MHz Repetition Rates

Maximilian Högner

Dissertation
an der Fakultät für Physik
der Ludwig-Maximilians-Universität
München

vorgelegt von
Maximilian Högner
aus Regensburg

München, den 18.4.2019

Erstgutachter: Prof. Dr. Ferenc Krausz

Zweitgutachter: Prof. Dr. Thomas Udem

Tag der mündlichen Prüfung: 14. Juni 2019

Contents

Zusammenfassung	vii
Abstract	ix
List of Publications	xi
1 Introduction	1
1.1 Motivation	1
1.2 Research Goals	3
1.3 Outline	5
2 Theoretical Background and Numerical Models	11
2.1 High-Harmonic Generation as a Nonlinear Optical Conversion Process	11
2.1.1 Numerical Models	12
2.1.2 Validation	13
2.2 Interaction of a Cavity-Housed Nonlinearity and the Resonant Field	14
2.2.1 Intensity Clamping in Cavity-Enhanced HHG	14
2.2.2 Transverse Mode Deformations Caused by Cumulative Plasma	18
2.2.3 Temporal Dissipative Solitons in Free-Space Cavities	19
3 Optimization of Cavity-Enhanced High-Harmonic Generation	25
3.1  Cumulative Plasma Effects in Cavity-Enhanced HHG in Gases	27
3.2  Efficiency of Cavity-Enhanced HHG with Geometric Output Coupling	37
4 Toward a Cavity-Enhanced High-Harmonic Lighthouse	51
4.1  Generation of IAPs with Enhancement Cavities – a Theoretical Study	53
4.2  Tailoring the Transverse Mode of an Optical Resonator with Stepped Mirrors	73
4.3  Cavity-Enhanced Noncollinear High-Harmonic Generation	81
5 Outlook	101
5.1 Toward Cavity-Enhanced Generation of Isolated Attosecond Pulses	101
5.2 Future Directions for Free-Space Cavity Solitons	102
5.3 Multi-Color Enhancement Cavities	104
A Comparison of HHG Sources	109
References	115
Acknowledgments	131

Zusammenfassung

Breitbandige, passive optische Freistrahler-Resonatoren (Überhöhungsresonatoren, ÜR), die mit modengekoppelten Lasern betrieben werden, erlauben Weglängen- und Pulsenergie-Erhöhungen um mehrere Größenordnungen für ultrasensitive optische Messungen und das Treiben von nichtlinearen Konversionsprozessen mit niedriger Effizienz. Insbesondere ermöglichen sie kohärente Quellen extrem-ultravioletten (XUV) Lichts mit hoher Leistung durch die Erzeugung Hoher Harmonischer (HHG) in Gasen innerhalb des Resonators, mit Repetitionsraten von Dutzenden bis Hunderten von MHz. Während manche der im Rahmen dieser Dissertation entwickelten Techniken breitere Anwendbarkeit versprechen, liegt das Hauptaugenmerk dieser Arbeit auf der Weiterentwicklung und dem Verständnis von ÜR-basierten XUV-Strahlungsquellen, welche unter anderem für die Frequenzkamm-Metrologie und Photoelektronen-Emissions-Spektroskopie in diesem Photonenenergiebereich von Interesse sind. Die Hauptergebnisse dieser Dissertation können im Wesentlichen in zwei Themengebiete untergegliedert werden:

Erstens wurden, aufbauend auf der vorherigen Arbeit unserer Forschungsgruppe, zwei Aspekte der Gesamteffizienz der nichtlinearen Konversion untersucht: die nichtlineare Interaktion zwischen dem laserinduzierten Plasma im Generationsmedium und dem überhöhten Feld, und geometrische Auskoppelmethoden. Die resultierenden Einsichten haben zur Demonstration der ersten ÜR-basierten XUV-Quelle mit einer ähnlichen Konversionseffizienz wie in vergleichbaren Single-Pass-Experimenten geführt, mit einer Photonenergie, die diese Technologie für raumladungsfreie Photoelektronen-Emissions-Spektroskopie nützlich macht. Solche Studien waren bisher nur mit Single-Pass-HHG-Quellen bei wesentlich geringerer Repetitionsrate und dadurch stark beschränkten Datenerfassungsraten, oder durch Beschleunigeranlagen mit erheblich mehr Raumbedarf möglich, welche im Gegensatz zu HHG-basierten Quellen nicht ohne Weiteres sub-Nanosekunden-Auflösung bereitstellen können.

Zweitens untersucht diese Arbeit, in Anbetracht dieses neuen Anwendungsfelds, ob und wie diese technologische Plattform auch für die Erzeugung von isolierten Attosekundenpulsen benutzt werden kann, was raumladungsfreie Photoelektronen-Emissions-Mikroskopie mit räumlicher Auflösung im Nanometer- und zeitlicher Auflösung im Attosekundenbereich ermöglichen würde, und die Untersuchung von plasmonischen Feldern auf nanostrukturierten Oberflächen auf ihren intrinsischen Zeit- und Längenskalen erlauben würde. Dafür wurde ein Aufbau für die räumlich-zeitliche Manipulation von überhöhten Feldern entwickelt und dessen Praktikabilität theoretisch und experimentell gezeigt. Diese Methode fungiert als effizienter Leistungs- und Photonenenergie-skalierbarer Auskoppelmechanismus für XUV-Strahlung, die innerhalb von ÜR erzeugt wurde, und verspricht Resonator-überhöhte Erzeugung von isolierten Attosekundenpulsen und außerdem die monolithische Kombination mehrerer Resonatoren, die z.B. bei verschiedenen zentralen Wellenlängen betrieben werden, in einen einzigen Gesamtresonator.

Weiterhin wurden der theoretische Rahmen und die numerischen Modelle, die im Laufe dieser Dissertation entstanden sind, angewendet, um ein neuartiges Zeitbereichs-Solitonen-Regime in einem passiven Freistrahler-Resonator zu untersuchen, welches vor Kurzem in einem in unserer Gruppe durchgeführten Experiment gezeigt wurde.

Abstract

Broad-band, free-space passive optical resonators (enhancement cavities, EC) seeded by mode-locked lasers enable path length and pulse energy enhancements by several orders of magnitude for ultrasensitive optical measurements as well as for driving low-efficiency nonlinear conversion processes. In particular, they permit high-power coherent sources of extreme-ultraviolet (XUV) light via intracavity high-harmonic generation (HHG) in gases, with repetition rates in the tens to hundreds of MHz. While some of the techniques developed as part of this thesis promise broader applicability, this work puts its focus on the further development and understanding of EC-based sources of XUV radiation, which are, amongst others, of interest for frequency comb metrology and photo-electron emission studies in this photon energy range. The principal results of this thesis can be divided into two main topics:

First, building on previous work of our research group, two aspects of the overall efficiency of the nonlinear conversion were studied: the nonlinear interaction between the laser-induced plasma in the generation medium and the enhanced field, as well as geometric output coupling methods. The resulting insights led to the demonstration of the first EC-based XUV source with a similar conversion efficiency as achieved in comparable single-pass experiments, and with a photon rate which renders this technology useful for space-charge-free photoelectron emission studies. Such studies were previously only possible with single-pass HHG sources at significantly lower repetition rates and, therefore, severely limited data acquisition rates, or at accelerator facilities with a much larger footprint which, in contrast to HHG-based sources, cannot easily provide sub-nanosecond time resolution.

Second, considering this new field of application, this thesis investigates whether and how this technological platform can also be used for the generation of isolated attosecond pulses, which could enable space-charge-free photoelectron emission microscopy with nanometer spatial and attosecond temporal resolution and would allow the study of plasmonic fields on nanostructured surfaces on their intrinsic time and length scales. To this end, a scheme for the spatiotemporal manipulation of the enhanced field was developed, and its practicability was shown theoretically and experimentally. This method can serve as an efficient, power- and photon-energy-scalable output coupling mechanism for XUV radiation generated inside ECs, and promises to enable cavity-enhanced generation of isolated attosecond pulses and, besides, the monolithic combination of multiple resonators, operating, e.g., at different central wavelengths, in a single overall resonator.

Furthermore, the theoretical framework and numerical models accrued during this thesis were applied for the investigation of a novel temporal soliton regime in a passive free-space cavity, which was recently demonstrated in an experiment performed in our group.

List of Publications

1. S. Holzberger, N. Lilienfein, H. Carstens, T. Saule, **M. Högner**, F. Lücking, M. Trubetskov, V. Pervak, T. Eidam, J. Limpert, A. Tünnermann, E. Fill, F. Krausz, and I. Pupeza, “*Femtosecond enhancement cavities in the nonlinear regime*”, *Physical Review Letters* 115, 023902 (2015) [10.1103/physrevlett.115.023902](https://doi.org/10.1103/physrevlett.115.023902).
2. H. Carstens, **M. Högner**, T. Saule, S. Holzberger, N. Lilienfein, A. Guggenmos, C. Jocher, T. Eidam, D. Esser, V. Tosa, V. Pervak, J. Limpert, A. Tünnermann, U. Kleineberg, F. Krausz, and I. Pupeza, “*High-harmonic generation at 250 MHz with photon energies exceeding 100 eV*”, *Optica* 3, 366 (2016) [10.1364/optica.3.000366](https://doi.org/10.1364/optica.3.000366).
3. **M. Högner**, V. Tosa, and I. Pupeza, “*Generation of isolated attosecond pulses with enhancement cavities – a theoretical study*”, *New Journal of Physics* 19, 033040 (2017) [1367-2630/aa6315](https://doi.org/10.1088/1367-2630/aa6315). – included as Section 4.1
4. **M. Högner**, T. Saule, N. Lilienfein, V. Pervak, and I. Pupeza, “*Tailoring the transverse mode of a high-finesse optical resonator with stepped mirrors*”, *Journal of Optics* 20, 024003 (2018) [10.1088/2040-8986/aa9ece](https://doi.org/10.1088/2040-8986/aa9ece). – included as Section 4.2
5. T. Saule, **M. Högner**, N. Lilienfein, O. de Vries, M. Plötner, V. S. Yakovlev, N. Karpowicz, J. Limpert, and I. Pupeza, “*Cumulative plasma effects in cavity-enhanced high-order harmonic generation in gases*”, *APL Photonics* 3, 101301 (2018) [10.1063/1.5037196](https://doi.org/10.1063/1.5037196). – included as Section 3.1
6. T. Saule, S. Heinrich, J. Schötz, N. Lilienfein, **M. Högner**, O. deVries, M. Plötner, J. Weitenberg, D. Esser, J. Schulte, P. Russbuedt, J. Limpert, M. F. Kling, U. Kleineberg, and I. Pupeza, “*High-flux ultrafast extreme-ultraviolet photoemission spectroscopy at 18.4 MHz pulse repetition rate*”, *Nature Communications* 10, 458 (2019) [10.1038/s41467-019-08367-y](https://doi.org/10.1038/s41467-019-08367-y).
7. N. Lilienfein, C. Hofer, **M. Högner**, T. Saule, M. Trubetskov, V. Pervak, E. Fill, C. Riek, A. Leitenstorfer, J. Limpert, F. Krausz, and I. Pupeza, “*Temporal solitons in free-space femtosecond enhancement cavities*”, *Nature Photonics* 13, 214–218 (2019) [10.1038/s41566-018-0341-y](https://doi.org/10.1038/s41566-018-0341-y).
8. **M. Högner**, T. Saule, and I. Pupeza, “*Efficiency of cavity-enhanced high harmonic generation with geometric output coupling*”, *Journal of Physics B: Atomic, Molecular and Optical Physics* 52, 075401 (2019) [10.1088/1361-6455/ab06db](https://doi.org/10.1088/1361-6455/ab06db). – included as Section 3.2
9. **M. Högner**, T. Saule, S. Heinrich, N. Lilienfein, D. Esser, M. Trubetskov, V. Pervak, and I. Pupeza, “*Cavity-Enhanced Noncollinear High-Harmonic Generation*”, *Optics Express* 27, 19675–19691 (2019) [10.1364/OE.27.019675](https://doi.org/10.1364/OE.27.019675). – included as Section 4.3

Chapter 1

Introduction

1.1 Motivation

Lasers are sources of coherent electromagnetic radiation, consisting of three principal components: an energy supply (pump), a gain medium to which the energy is directed, and an electromagnetic resonator. The first such sources were realized in 1953 in the microwave spectral region by Gordon, Zeiger, and Townes [1, 2], and later in 1960 by Maiman in the optical region [3], and since then, lasers have found a multitude of applications in industry, medicine, communication, science, and many other fields.

Optical laser cavities, generally realized by a set of highly reflective mirrors, confine the contained electric field to discrete sinusoidal longitudinal eigenmodes, whose frequencies are, under ideal circumstances, equally spaced. A laser may operate at a single mode or at multiple modes simultaneously, depending on the bandwidth of the mirrors and contained elements like the gain medium. In general, multi-mode lasers have no fixed phase relation among the modes, which results in chaotic interference of the individual electric field oscillations. In the early 60s, methods were found to actively or passively phase-synchronize these modes [4]. This causes a qualitatively different behavior of these so-called *mode-locked lasers*: instead of operating at near-constant output power, they periodically emit intense pulses of light. The pulse duration is mainly determined by the lasing bandwidth, and can be as short as 5 fs [5, 6]. This development has led to a new field of research, ultrafast science, where physical and chemical processes at picosecond and femtosecond time scales are studied [7].

Because of their equal spacing, the frequencies of the eigenmodes are fully determined by two parameters: the spacing itself and the absolute frequency of one selected mode (see Fig. 1.1). In real lasers, these parameters are subject to statistic fluctuations, e.g., due to acoustic noise. If both parameters are stable over long periods of time, e.g., when stabilized by an electronic feedback system, this is referred to as *frequency comb* [8]. This technique has enabled frequency measurements of atomic transitions with relative precisions of up to 1×10^{-15} for the 1S-2S line in hydrogen [9], an improvement by two orders of magnitude compared to previous approaches [10], and the very accurate determination of physical constants and new frequency standards using optical clocks [11].

Beside taking advantage of the high temporal and frequency resolution of ultrafast laser

systems¹, the high peak intensity of the pulses of mode-locked lasers with subsequent compression and amplification schemes can be used to drive nonlinear processes. **High-harmonic generation** (HHG) allows the frequency upconversion to coherent vacuum and extreme ultraviolet (VUV/XUV, 6–124 eV) and soft X-ray (100 eV–5 keV) radiation, which can otherwise only be obtained with accelerator facilities with a much larger footprint, and is useful, e.g., for coherent imaging with nanometer-scale resolution [12], photoelectron emission spectroscopy (PES, [13–17]) and microscopy (PEEM [18–20]), coincidence spectroscopy [21–23], and XUV lithography [24]. In HHG, the photon emission is temporally confined to attosecond-time-scale bursts linked to the peaks of the driving field oscillations, which has enabled the transition from the typical time scales of the pulse envelope (several femtoseconds to picoseconds) to that of the field oscillations.

This has opened up a whole new field, dedicated to the investigation of processes on the attosecond time scale [25, 26]. Several methods have been demonstrated to obtain isolated attosecond pulses (IAP) instead of a train of attosecond bursts [14], e.g., using near-single-cycle driving pulses [27], taking advantage of the polarization-dependent efficiency of HHG [28], or introducing spatiotemporal couplings to angularly disperse the individual emissions [29–31]. The stabilization of the comb parameters, as described before, and a comb offset frequency of zero, is an important premise for achieving driving pulses with constant carrier-envelope phase and thus attosecond emissions with repeating shape and timing. The main workhorse of **attosecond physics** are pump-probe measurements, such as attosecond transient absorption spectroscopy [32, 33] or photoelectron emission spectroscopy (PES) in the presence of a strong longer-wavelength “dressing” pulse, whose delay relative to the XUV pulse is scanned. For the latter, the most important techniques are attosecond streaking [13, 15, 26, 34], which requires IAPs, and RABBITT [16, 35], which allows finer spectral resolution owing to the use of attosecond pulse trains [36]. From the resulting spectrograms, detailed information about the dressing pulse, the XUV pulse, and the timing of electronic dynamics inside the system under investigation can be extracted with attosecond resolution [15, 26, 34–41].

For lithography and coherent imaging, the main figure of interest is the number of XUV photons per time interval. However, in several important applications, other constraints play a major role: In studies involving the release and detection of charged particles, like PES, PEEM and coincidence spectroscopy, inter-particle Coulomb interactions affect the trajectories of the particles and, thus, hinder a reliable measurement of the quantities of interest. For PES, this results in a decrease of the spectral, and for PEEM also of the spatial resolution. This mechanism, known as space charge effect [42], can only be avoided by limiting the number of XUV photons, and thus the released particles, per pulse. The only possibility to scale the data acquisition rate is therefore to increase the repetition rate of the pulses. Especially for multi-dimensional photoelectron emission studies, e.g., with temporal and spatial resolution, such a scaling is compulsory for achieving viable measurement times.

Moreover, it is highly interesting to use HHG to convert a frequency comb at optical wave-

¹The simultaneously high resolution in both time and frequency domain may seem surprising at first, but is not a violation of the Gabor limit. For the Gabor limit, the relevant quantities are the length of the pulse train (infinity) and the spectral bandwidth, whereas the relevant quantities for the time and frequency resolution are given by the respective substructures in the time and frequency domain (the pulse duration and the linewidth of the comb modes).

lengths to the VUV/XUV spectral range [43–45]. Employing such sources, atomic, molecular, and low-lying nuclear transitions at these wavelengths can be measured with high precision, e.g., for use as a frequency standard, as an ultrasensitive benchmark for the theory of quantum electrodynamics, or to detect variations in fundamental physical constants [11, 46–48]. To this end, two conditions must be fulfilled: First, the frequency spacing of the comb modes (i.e., the repetition rate) must be larger than the linewidth of the transition. For some relevant transitions, this width can be in the tens of MHz [49]. And second, for single-photon transitions, the power per comb mode must be high enough to afford sufficient signal-to-noise ratio. For both requirements, it is advantageous to decrease the number of comb modes per frequency interval, i.e., increase the repetition rate.

Typically, laser systems employed for HHG operate at repetition rates well below 1 MHz. Scaling the repetition rate to the tens to hundreds of MHz, as desirable for the above-mentioned applications, while still providing sufficient pulse energy for efficient HHG at near-soft-X-ray photon energies is still an unmet challenge, even with present-day front ends relying on coherent combination of the output of several amplifiers [50].

Because HHG in gases is a process with a very low conversion efficiency (usually $\ll 1 \times 10^{-5}$), a promising approach for reaching the required peak intensities at high repetition rates is to recycle the energy of the driving pulse after it has passed the nonlinear medium. To this end, the beam is redirected into itself by a passive resonator geometry, referred to as **enhancement cavity** (EC, Fig. 1.2). The power is supplied by a seeding beam via a partially transmissive input coupling mirror, and destructive interference prevents that the power circulating in the EC leaks out of the cavity through the same mirror. Optimum destructive interference – which implies the transfer of the entire power to the EC – is only possible if the EC is impedance-matched, i.e., when the input coupler transmission equals the loss per round-trip. The power enhancement, which depends on the round-trip losses, the input coupler transmission and the total spectral phase of the mirror coatings and intracavity elements, can reach several orders of magnitude at pulse durations of just a few tens of femtoseconds [51–57].

1.2 Research Goals

At the time of the beginning of this doctoral project, a lot of research effort had already been invested into the development of ECs, in particular in scaling the driving peak power [54, 58, 59], XUV power and photon energy [48, 51, 53, 60–66], and in the development of efficient VUV/XUV output coupling mechanisms [53, 60, 67–74]. This had enabled the first application of this technology for the precision spectroscopy of transitions in xenon, argon and neon at wavelengths below 150 nm [48, 49].

However, one promise of cavity-enhanced HHG had still not been delivered: Because the XUV power can scale linearly with the driving power [75], it can be expected that the enhancement of the driving power is transferred to an enhancement of the overall conversion efficiency of the system, i.e., in principle such sources have the potential to provide higher XUV power than comparable single-pass sources. As can be seen in Fig. 1.3a (filled symbols), the performance of cavity-enhanced XUV sources had remained below that of single-pass systems. This indicates that the constraints set by the resonator entail inefficiencies in the XUV generation and output coupling processes, which counteract the significant enhancement of the driving power. One main objective of this thesis was to advance the understanding of these

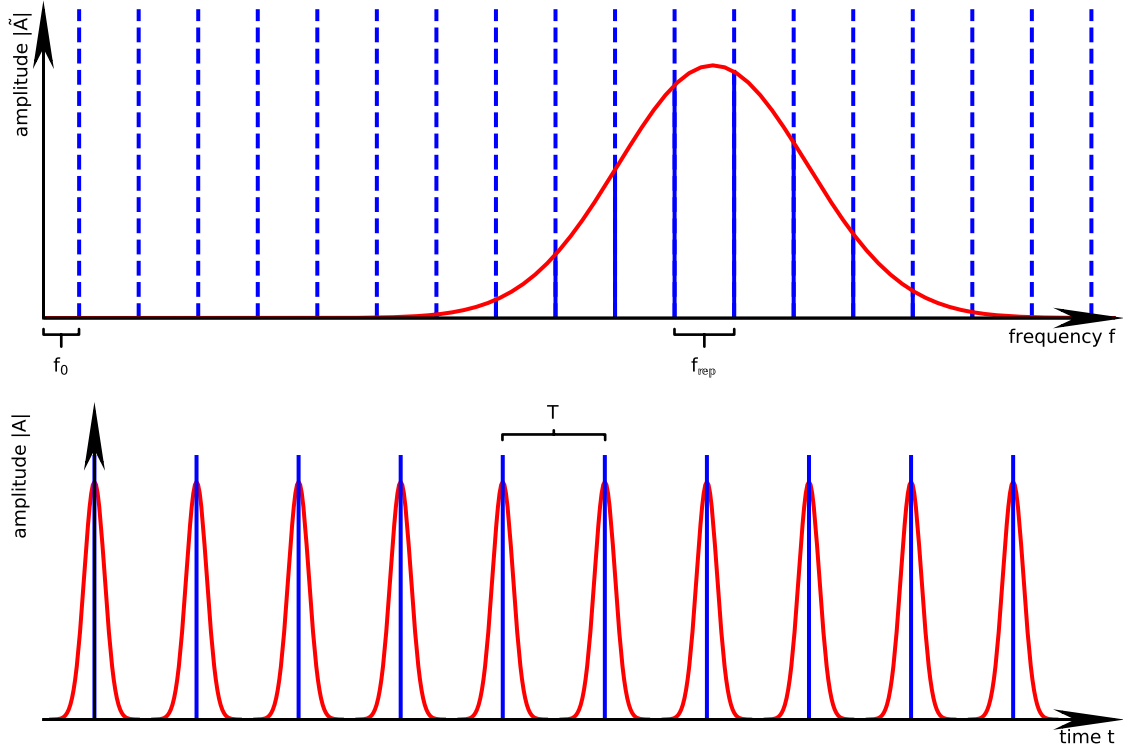


Figure 1.1: A frequency comb in the frequency (top) and time (bottom) domain. Its spectrum is given by $\tilde{A}(f) = [\sum_{f_j \in f_{\text{rep}}\mathbb{Z} + f_0} \delta(f - f_j)] \cdot \tilde{A}_e(f)$, where f is the frequency, f_{rep} the repetition rate, f_0 the comb offset frequency, \mathbb{Z} the set of integers, j the mode number, the sum term represents the comb structure (blue), $\tilde{A}_e(f)$ is the complex frequency-domain envelope (red), and δ is the Dirac delta function. The complex amplitude of the pulse train is given by the inverse Fourier transform $A(t) = \mathcal{F}^{-1}\{\tilde{A}(f)\} = [\sum_{t_k \in T\mathbb{Z}} \delta(t - t_k) \exp(i2\pi f_0 t_k)] * A_e(t)$, where t is the time, $T = 1/f_{\text{rep}}$ is the repetition period, the sum term represents the train structure (blue), the term $\exp(i2\pi f_0 t_k)$ is responsible for a constant slippage of the carrier-envelope phase between subsequent pulses, $A_e(t) = \mathcal{F}^{-1}\{\tilde{A}_e(f)\}$ is the complex envelope of one individual pulse (red), and $*$ denotes convolution.

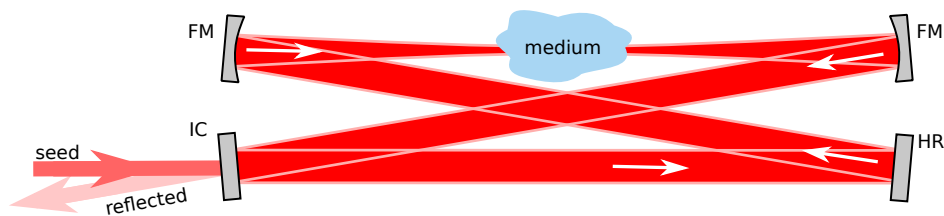


Figure 1.2: Schematic of an enhancement cavity housing a (nonlinear) medium. IC: partially transmissive input coupling mirror, HR: highly reflective plane mirror, FM: highly reflective focusing mirror.

inefficiencies and investigate ways of mitigating them. This could finally lead to very efficient XUV sources with high photon energy and repetition rate, and at the same time high photon rate, which would benefit not only frequency comb spectroscopy and ultrafast science, but all applications where coherent VUV/XUV radiation is needed.

Enabling photoemission studies at high repetition rates and photon energies would be particularly interesting when combined with spatial resolution and IAPs: then, plasmonic fields on nanostructured surfaces could be recorded on their intrinsic time and length scales (attoPEEM, [18–20]). To date, the shortest driving pulses demonstrated in ECs have durations of several cycles [57], owing to bandwidth limitations of the multilayer, highly reflective mirror coatings. Because mirrors supporting near-single-cycle pulses do not seem viable from today’s perspective, a gating method is desirable that allows to produce IAPs from multi-cycle driving pulses, without impeding the performance of the EC. The second main objective of this work was to develop such a method.

1.3 Outline

In this thesis, several advances toward reaching these goals are described. First of all, a quantitative model for the intracavity intensity clamping due to the plasma-induced refractive index modulation in the medium developed in our group [77]² has allowed better designs of cavity-based XUV sources by factoring in the tradeoff between high peak power enhancement and detrimental plasma effects. Even though, a high-repetition-rate experiment in our group [55] had failed to scale up the XUV power as expected from the relevant parameters when using easily ionizable atomic species as target gas. This raised the suspicion that the formation of a cumulative plasma in the gas target impairs the HHG process when the target atoms are not fully replenished between consecutive pulses. We studied cumulative effects in a systematic experiment [78]³ and confirmed them as a highly detrimental factor for the HHG conversion efficiency. By operating at a low enough repetition rate to avoid these effects, our group demonstrated the first cavity-enhanced XUV source with an overall conversion efficiency similar to that of comparable single-pass HHG sources [56], which is an order-of-magnitude improvement to the previous state of the art (see Fig. 1.3a). To elucidate how the conversion efficiency of the overall system (1.8×10^{-7}) unfolds from the power enhancement (35), the output coupling efficiency, and the intracavity conversion efficiency, we applied a numerical model⁴ to compute the output coupling efficiency (5%) at 37 eV and could thereby compute the conversion efficiency inside the EC ($0.05^{-1}/35 \cdot 1.8 \times 10^{-7} = 1.0 \times 10^{-7}$), which is only by a factor of 4.5 lower than the record in state-of-the-art single-pass systems [79]. This shows that the advanced understanding of plasma-related limitations has nowadays led to ECs where these effects have no major impact on the produced XUV power, and the main limitation is the efficiency of output coupling. To duly address this contribution to the overall efficiency, building on the data collected in the experiment for the investigation of cumulative effects, a quantitative analytical model for the efficiency of geometric output coupling using the fundamental mode (the only method which was shown to be scalable to high photon energies)

²I contributed a 3D validation of the employed 1D model.

³Publication included together with a statement of author contributions as Section 3.1.

⁴I developed the numerical model as a part of this thesis.

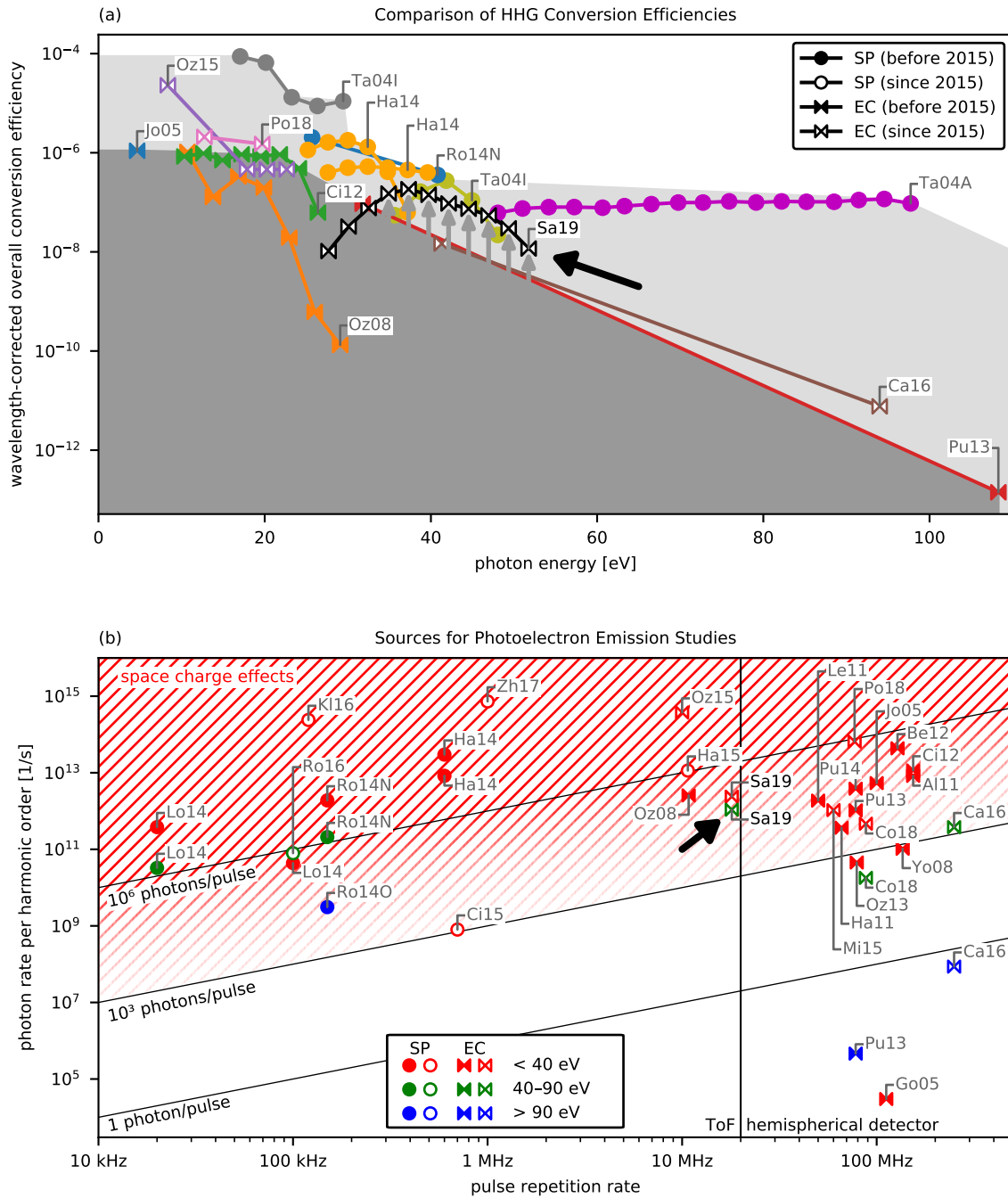


Figure 1.3: Comparison of HHG sources, based on the data in Table A.1. Filled/hollow symbols mark sources reported before/after the beginning of this doctoral project. The source developed in our group (Sa19, [56]) improved the conversion efficiency by an order of magnitude to the same level as record single-pass systems and operates in the optimum region for space-charge-free photoelectron emission studies with time-of-flight (ToF) spectrometers. a) Record conversion efficiencies of cavity-enhanced (EC, bow-tie-shaped symbols) and comparable single-pass (SP, circles) HHG sources, normalized to a wavelength of 1030 nm by correcting for the wavelength scaling by approximately a power of six [76]. The shaded areas identify regions reached by single-pass (light gray) and pre-2015 cavity-based (dark gray) sources. b) Comparison of photon rates of sources for photoelectron emission studies in different photon energy ranges. The red area marks the region prohibited by space-charge effects, and the vertical line at 20 MHz indicates where the use of ToF spectrometers becomes impracticable and hemispherical/retarding grid analyzers with lower data acquisition rates must be used.

was developed and verified as part of this thesis [80]⁵.

This investigation also led to the insight that, especially at lower harmonic orders, there is a clash between the optimum position of the gas target for output coupling and for optimum HHG efficiency. This trade-off can reduce the output coupled XUV power by orders of magnitude compared to single-pass HHG with the same driving pulse energy. Thus, it is desirable to investigate alternative geometric output coupling methods, e.g. with higher-order transverse modes [71, 73].

The greatly ameliorated XUV power at high repetition rates, enabled by higher seeding power and significantly better conversion efficiencies, has finally opened up a new field of application for cavity-based XUV sources, namely table-top photoemission spectroscopy experiments [56, 81, 82]. In particular, the source demonstrated in our group [56] is the first HHG-based source which provides the optimum number of photons per pulse to avoid space charge effects at typical focus sizes around 5–10 μm on the sample and a repetition rate compatible with time-of-flight spectrometers, and which reaches the necessary photon energies to simultaneously address core and valence band electronic states in metals (see Fig. 1.3b). In contrast to synchrotrons, which also reach this regime, it also provides time resolution in the femtosecond and, for RABBITT, attosecond regimes.

Further improvements of cavity-enhanced HHG over the last few years, namely ECs supporting wave-form stable seeding pulse trains [83], scaling up the photon rate around 100 eV to one photon per pulse at 250 MHz [55], and improving the bandwidth of ECs to allow for the enhancement of few-cycle pulses [57], have brought efficient sources of multi-10-MHz IAPs with photon energies around 100 eV into reach, which would enable attoPEEM. To find a suitable method for gating IAPs from few-cycle driving pulses, several potential methods that have been demonstrated in single-pass experiments were evaluated as part of this thesis. The most viable methods were simulated and their potential efficiency was compared. A new method, employing noncollinear optical gating [84, 85] via a tailored higher-order transverse cavity mode, was identified as the most promising scheme [86]⁶. As a next step, the necessary mode tailoring was demonstrated in a proof-of-principle experiment with a single-frequency laser [87]⁷. Then, using the experimental infrastructure of our group, the first noncollinear HHG in an enhancement cavity was demonstrated, and the resulting wave-front rotation in the focus was measured [88]⁸. These results provide a route toward isolated attosecond pulse generation with ECs.

In addition, this scheme can serve as a power- and photon-energy-scalable, highly efficient geometric output coupling method which promises to circumvent the aforementioned trade-off between HHG efficiency and output coupling efficiency. Together with spectral tailoring methods for mitigating intensity clamping and, thus, allowing for higher power enhancements [77], this could lead to high-repetition-rate, high-photon-energy HHG sources with orders of magnitude better overall conversion efficiencies than single-pass systems.

Finally, a recent experiment in our group demonstrated the first realization of a temporal dissipative soliton in a free-space EC [89]⁹. This novel regime for ECs promises applications

⁵Publication included together with a statement of author contributions as Section 3.2.

⁶Publication included together with a statement of author contributions as Section 4.1.

⁷Publication included together with a statement of author contributions as Section 4.2.

⁸Publication included together with a statement of author contributions as Section 4.3.

⁹The experiment was conducted by Nikolai Lilienfein and coworkers. I developed, together with Nikolai

for increasing the intensity stability, reducing the sensitivity on the mirror phase and scaling the bandwidth of ECs, and as a pulse compression scheme with excellent beam quality. The numerical model developed for this thesis was used to reproduce the experimental observations and to investigate the impact of key experimental parameters on the soliton dynamics.

This thesis is structured as follows: Chapter 2 is dedicated to a brief description of the numerical models developed in the course of this doctoral project. Three examples of interactions between cavity-housed nonlinearities and the enhanced field are presented, which were investigated employing these models, amongst others, the soliton EC.

Chapter 3 addresses the conversion efficiency of EC-based XUV sources. The contribution of cumulative plasma effects (Section 3.1) and the efficiency of geometric output coupling (Section 3.2) to the overall conversion efficiency are elucidated in two included peer-reviewed publications.

The second research goal, the generation of isolated attosecond pulses inside ECs, is covered in Chapter 4. In a first publication (Section 4.1), possible approaches were evaluated, and the most promising ones were simulated with the developed models. A new method, employing transverse mode tailoring, is suggested and identified as the preferred one in terms of stability and efficiency. The manipulation of a cavity mode with such mirrors was shown in an experiment (Section 4.2) and later applied to drive HHG in a femtosecond EC with a spatiotemporally coupled mode (Section 4.3).

In Chapter 5, we put these results in the context of future applications; specifically, the realization of photo-electron nanoscopy with attosecond resolution (attoPEEM), future directions with intracavity solitons, and possible further applications of the demonstrated spatiotemporal tailoring for the simultaneous enhancement of multiple beams with different central wavelengths.

Theoretical Background and Numerical Models

2.1 High-Harmonic Generation as a Nonlinear Optical Conversion Process

The key physical process that led to the development of attosecond science is frequency upconversion by HHG. An intuitive picture for HHG in monoatomic gases that can explain the main features observed in experiments was provided by Paul Corkum in 1993 [90] and later confirmed and complemented by a fully quantum-mechanical model by Maciej Lewenstein et al. [91]: First, the electric field of an intense laser pulse bends the Coulomb potential of the atom such that an electron is released (tunnel ionization, see Fig. 2.1). The electron is accelerated away from the atom by the same electric field that led to ionization. When the oscillating field changes its sign, the electron is driven back to the atom where it recombines. The potential energy and the kinetic energy acquired during propagation is then coherently emitted in the form of energetic photons.

In general, there are several possible electron trajectories leading to the same final photon energy. Because the electronic wave packet disperses during propagation, usually the most intense emissions stem from the two shortest trajectories, commonly referred to as “short trajectory” and “long trajectory”.

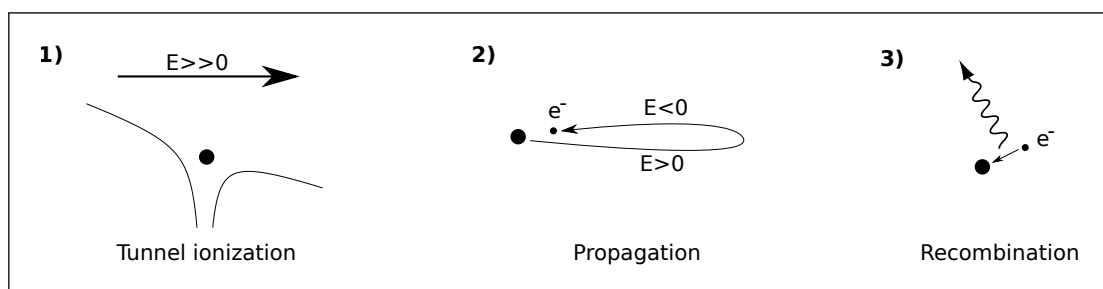


Figure 2.1: Three-step model for high-harmonic generation

Since HHG is a coherent process, the phase of the radiation emitted off an atom possesses a fixed relation to the phase of the driving pulse. Normally, high harmonics are produced in a macroscopic volume comprising many atoms of the same species. Then, the phase of all contributing emitters has to be matched for optimum generation efficiency. This leads to a coherent buildup of the radiation exiting the volume, whose intensity increases quadratically with the number of atoms.

2.1.1 Numerical Models

To accurately simulate HHG, a numerical model has to also account for macroscopic effects like reabsorption, field-induced plasma lenses, Kerr focusing, and all contributions relevant to phase matching (linear refractive index, intensity-dependent microscopic phase and amplitude, plasma and Kerr refractive index, geometric phase of the driving beam), all of which can significantly affect the overall conversion efficiency. For cavity-enhanced HHG, the interaction between the generation medium and the steady-state of the field excited in the EC must be considered. Therefore, in addition, a model for the propagation of the driving pulse in the resonator is needed. To model geometric output coupling methods, propagation through apertures and to the far field is important. In the following, the numerical models developed in the course of this thesis are briefly summarized.

Microscopic response for HHG The central component of the numerical model is a fast implementation of the Lewenstein formula for the single-atom dipole response, which is available as open-source software¹. The module supports elliptically polarized driving fields [94], ground state depletion due to ionization, and allows for computation with an additionally applied saddle-point analysis [95], which enables better separation between trajectories. To speed up the computation in the case of linear polarization, an optional envelope approximation² based on interpolation from precomputed dipole responses can be used [86].

Microscopic response for plasma and Kerr nonlinearities The microscopic response owing to the time-dependent plasma density during strong-field ionization can be computed with the model described in [96] as well as in an envelope approximation permitting a coarser discretization along the time axis [65]. Likewise, the microscopic response for a Kerr nonlinearity can be computed with and without envelope approximation. Further details can be found in Section 4.1.

Propagation through a nonlinear medium and high-harmonic buildup To compute the macroscopic response of a nonlinear medium, the forward wave equation [97] can be solved in 3+1 dimensions using an unconditionally stable integrator. This approach can be applied for pulse-induced phase modulation processes (Kerr nonlinearity, plasma-induced blueshift) as well as frequency upconversion processes (e.g., third-harmonic generation and

¹The HHGmax code [92] was developed in the course of my master's thesis [93] and extended throughout the doctoral project. Although it includes a very basic algorithm for the macroscopic propagation, only the single-atom part (pylewenstein module) was used in this thesis, and the macroscopic propagation was implemented independently.

²The envelope approximation is not part of HHGmax and was developed for this thesis.

HHG), and phase matching effects can be fully accounted for. For a faster computation and reduced memory consumption, the numerical model can take advantage of rotational and reflectional symmetries. A full description of the model can be found in Section 4.1.

Propagation through an optical free-space resonator The model also supports all ingredients needed to simulate the 3+1D propagation of a pulse through a resonator, accounting for the relevant spatial and spectral effects: broadband, interpolation-free free-space propagation between mirrors in paraxial approximation, arbitrary apertures, and optical elements with arbitrary spectral and transverse phases, e.g., multi-layer spherical mirrors under non-normal incidence or even tailored surface profiles. The same model can be applied for the propagation of the XUV radiation generated by HHG through output coupling apertures and into the far field. Details on the implementation can be found in Sections 4.1 and 4.2.

Transverse eigenmode determination for linear resonators A routine to determine the mode spectrum, i.e., the transverse eigenmodes along with their corresponding round-trip losses and phase shifts, of a given resonator geometry was implemented. Effects like astigmatism and spherical aberration can be accounted for, and it is possible to simulate mode tailoring methods using obstacles or special surface profiles. For details on the algorithm and an example of its application, see Section 4.2.

2.1.2 Validation

Single-Atom Dipole Response

To verify the correctness of the Lewenstein routine used in this thesis, its results were validated against the ones obtained in [98] using the Lewenstein model and the time-dependent Schrödinger equation, for the parameters used there (a xenon atom irradiated by a \cos^2 pulse centered at 1600 nm with a FWHM of 7.8 fs and a peak intensity of 5×10^{13} W/cm²). The dipole spectrum (Fig. 2.2) agrees well with the spectra shown in [98, Fig. 3b].

Propagation

To verify the implemented propagation algorithm for the driving field, it was applied to reproduce the results of [99], where a radial lighthouse effect under high ionization conditions was theoretically investigated with a numerical model with similar capabilities, but limited to cases with rotational symmetry. For this, the same ionization rates used there were assumed, the ionization loss term from [96] was neglected, and the linear and Kerr refractive indices of ionized atoms were assumed to be the same as for neutral atoms.

The model can reproduce the main features predicted there. The resulting plots shown in Fig. 2.3 can be directly compared to [99, Figs. 2,3].

As a second verification, the code was used to reproduce a cavity-enhanced HHG experiment conducted in our group where the XUV power per harmonic order was systematically recorded versus the two parameters backing pressure and gas target position³. The agreement between the simulations and the experiment shown in [80, Fig. 2]⁴ confirms the validity of the model in

³Publication included together with a statement of author contributions as Section 3.1.

⁴Publication included together with a statement of author contributions as Section 3.2.

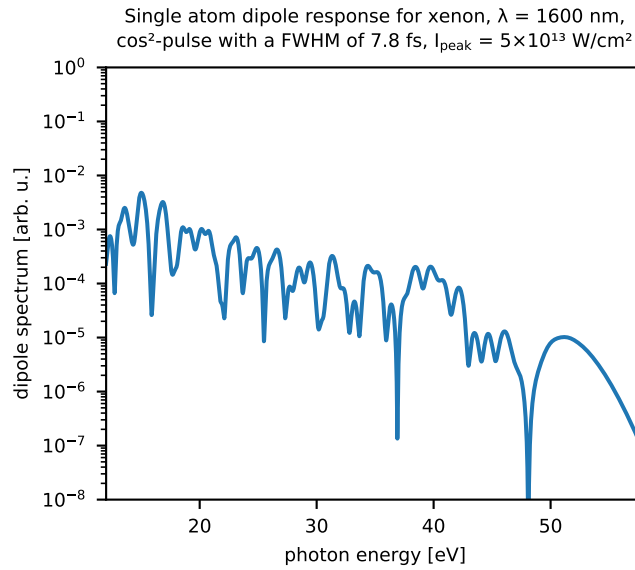


Figure 2.2: Validation of the implemented single-atom model against [98, Fig. 3b].

the parameter range relevant to cavity-enhanced HHG.

2.2 Interaction of a Cavity-Housed Nonlinearity and the Resonant Field

Compared to single-pass experiments, driving nonlinearities inside ECs comes with specific challenges and opportunities: To afford high enhancements, it is indispensable to efficiently reuse the energy of the pulse after it has passed through the nonlinear medium. In the simplest case, this means that the pulse should pass the nonlinearity largely unaffected, because even small changes accumulate over many round-trips, owing to the path-length-enhancing behavior of ECs. Such interactions between cavity-housed nonlinearities and the enhanced field can either be unwanted or they can be desired, e.g., when exploited for intracavity pulse compression. In this section, we give three examples of both types, which were investigated employing the models described in Section 2.1.

2.2.1 Intensity Clamping in Cavity-Enhanced HHG

In cavity-enhanced HHG, the target medium not only mediates the frequency upconversion to the XUV range, but also significantly interacts with the driving pulse. Beside the energy loss associated with the upconversion, which is generally negligible due to the low conversion efficiency of HHG, several effects have to be considered: First, the linear response of the medium (absorption, dielectric dispersion) can spectrally alter the driving pulse. Second, at high intensities, self-phase modulation due to the third-order susceptibility of the medium (Kerr effect) can cause spectral broadening and spatial effects (Kerr lensing). Third, HHG inherently requires ionization. Compared to the other two effects, strong-field-induced plasma formation is usually the most important limiting factor in the intensity regime of cavity-enhanced HHG

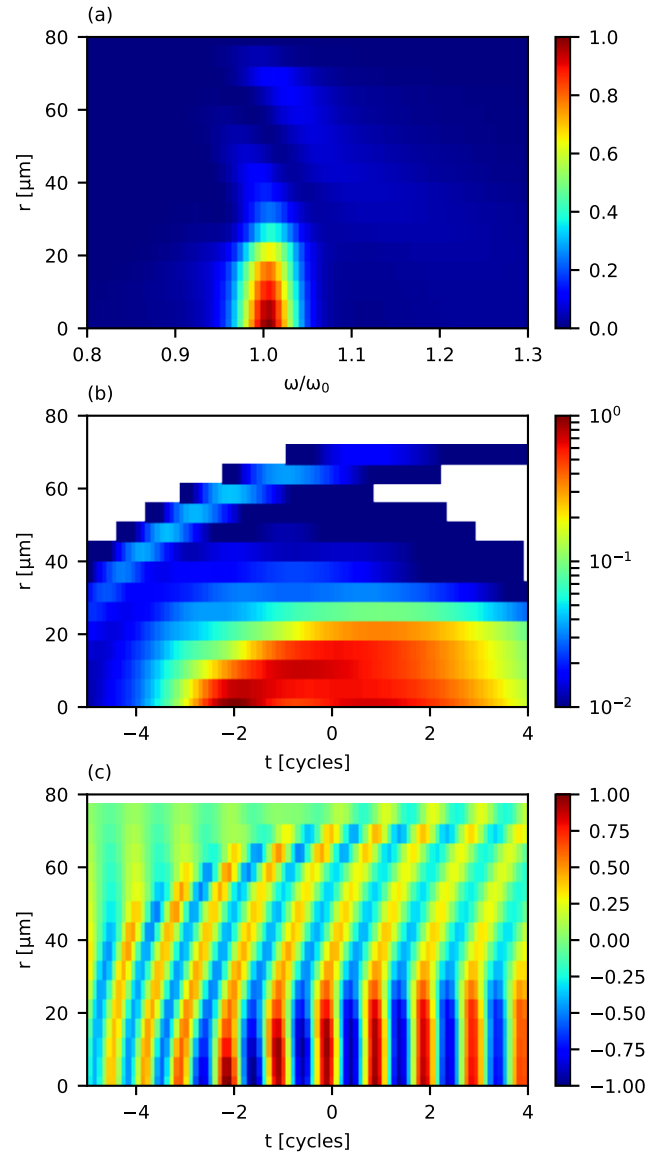


Figure 2.3: Validation of the implemented propagation model against [99, Figs. 2,3]. a) Spatio-spectral structure of the driving field at the exit plane of the medium, where ω is the angular frequency, ω_0 the central angular frequency of the field at the entrance plane, and r the radial coordinate. b) Spatiotemporal structure of the cycle-averaged driving field intensity at the exit plane, where t is the time coordinate. c) Normalized electric field at the exit plane, showing the wave-front rotation.

in inert gases and can affect the driving pulses in two ways [65, 66, 96, 100]: At high repetition rates, there is not enough time between subsequent pulses for the plasma embedded in the target gas stream to decay or to clear the interaction volume. This “cumulative” plasma has a spatially inhomogeneous, frequency-dependent linear refractive index that can spectrally and spatially distort the pulse. In addition, during strong-field ionization, the plasma density changes over the time scale of one pulse, leading to a time-dependent and spatially inhomogeneous refractive index. This pulse-induced phase modulation effect brings about spectral (blueshift and phase effects) and spatial alterations (plasma lensing).

These alterations impair the constructive interference of the recycled pulse with the seeding pulse and, therefore, lead to a drop in enhancement, which becomes more severe with increasing seeding power. As a consequence, at high seed power, the circulating power ceases to increase linearly with the seed power and exhibits a clamping behavior, as observed in various cavity-enhanced HHG experiments [51, 53, 63, 65, 66]. It has been recognized early that operating at lower finesse and, in exchange, increasing the seeding power allows to mitigate intensity clamping [51, 63, 65].

In our group, a systematic study on intensity clamping due to the ionization-induced phase modulation in standard-approach ECs was undertaken, resulting in a simple empirical clamping formula which allows selecting the optimum finesse \mathcal{F} given a desired intensity I_{Cl} [77]⁵:

$$I_{\text{Cl}}(\tau, \mathcal{F}, nl) = I_0 \times \left(\frac{\tau_0 - \alpha \mathcal{F}_0 - \beta n_0 l_0 - \gamma}{\tau - \alpha \mathcal{F} - \beta nl - \gamma} \right)^\delta \quad (2.1)$$

Here, τ is the pulse duration, n the gas density, l the gas target length, and I_0 , τ_0 , \mathcal{F}_0 , $n_0 l_0$, α , β , γ , and δ are constants tabulated in [77]. For the derivation this formula, the propagation of the driving pulse through the gas target was modeled with a simple 1D approach. To verify this approximation and determine its range of validity, 1D results were compared to 3D simulations conducted with the numerical model developed for this thesis.

To this end, the propagation of a 30-fs-long Gaussian driving pulse spectrally centered at 1040 nm through a xenon gas target with a length of 200 μm and a particle density of $4 \times 10^{18} \text{ cm}^{-3}$ was simulated for two cases: first, assuming a plane wave (1D case), and second, assuming a Gaussian mode with a beam waist of 20 μm and its focal plane at the gas target (3D case). For the 3D case, the resulting field was decomposed into Gauss-Hermite modes and higher-order modes were discarded to account for the spatial-mode-filtering behavior of ECs. The effective plasma-induced phase shift at the end of the pulse is compared in Fig. 2.4a. In Fig. 2.4b, the energy lost to higher-order modes and to ionization itself is shown, and the total loss is compared between the 1D and 3D model. It is evident that for xenon, the 1D model is a good approximation at intensities up to around $8 \times 10^{13} \text{ W/cm}^2$, but, at higher intensities, it overestimates the phase shift and underestimates the losses.

⁵The experiment and theoretical study was done by Simon Holzberger and coworkers. I contributed 3D simulations that validated the applied 1D model in a limited parameter range, computed the ionization-induced phase shift for different driving wavelengths and helped to find an advantageous tailored input coupler transmission curve.

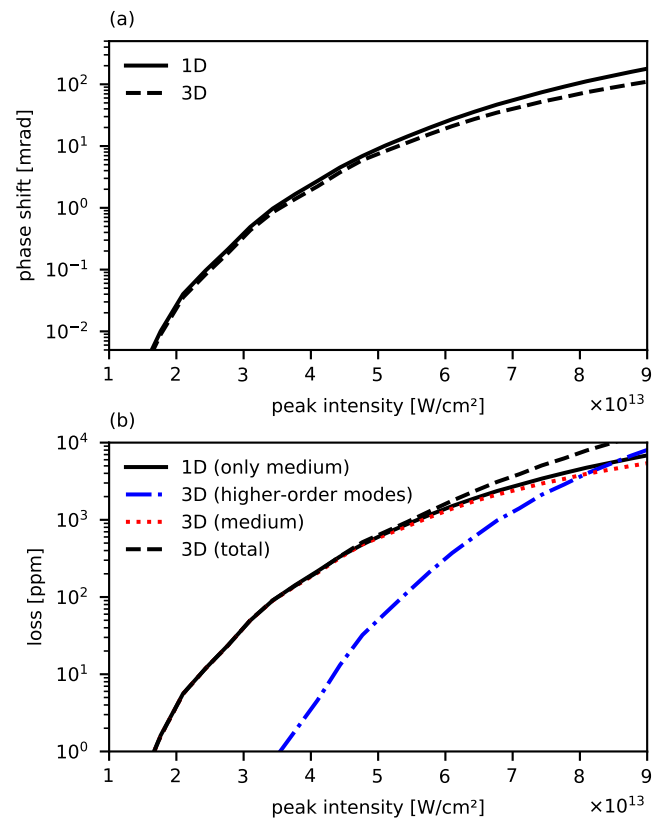


Figure 2.4: 3D validation of the 1D model for intensity clamping. (a) Total plasma-induced phase shift after the pulse. (b) Energy lost to higher-order modes and directly to ionization of the atoms in the medium.

2.2.2 Transverse Mode Deformations Caused by Cumulative Plasma

High repetition rates can lead to the formation of a cumulative plasma in the medium, with a linear but spatially inhomogeneous refractive index. In contrast to plasma lenses owing to the ionization-induced refractive index modulation, the cumulative plasma is assumed time-independent. Therefore, a resonator with this effect can still be treated as a linear resonator, in the sense that the operator which maps a mode (complex amplitude profile) to the resulting mode after one round-trip is a linear operator. The eigenmodes of an EC containing a homogeneous medium, i.e., the eigenstates of its round-trip operator, are the Gauss-Hermite modes, which form an orthogonal basis. The induced transverse phase of the cumulative plasma can alter the eigenmodes and respective complex eigenvalues (given by the round-trip phase and round-trip attenuation) of the resonator. In general, this can lead to an eigenspectrum that is not orthogonal, i.e., eigenmodes with a non-vanishing mutual overlap can exist.

In our group, cumulative effects were studied in a systematic experiment, showing a clear decline in the HHG conversion efficiency as soon as the plasma does not clear the interaction region between subsequent pulses [78]⁶. In this experiment, the deformations of the excited mode were also measured at three different repetition rates with otherwise identical parameters. Fig. 2.5g shows the mode profile on the output coupling mirror obtained while the EC was operated without gas jet, such that no cumulative effects are possible. When the argon gas was switched on (backing pressure 11 bar), the mode changed only slightly for the lowest employed repetition rate of 18 MHz, where the generated plasma still has enough time to leave the interaction volume, but more substantially at 36 MHz and 72 MHz (Figs. 2.5a, c, and e). Further analysis reveals that the distortions resemble higher-order Gauss-Hermite modes (Figs. 2.5d and f).

To reveal the underlying mechanisms, the numerical model described in Section 2.1 was applied to determine the eigenstates (modes) and eigenvalues (round-trip phase and attenuation) of a monochromatic round-trip operator of the EC, which comprises contributions from free-space propagation, reflection off spherical mirrors under oblique incidence, and the transverse phase caused by the cumulative plasma. For this, a wavelength of 1030 nm, a cavity length of 18.3 m, and incidence angles and a stability range position consistent with the mode size observed in Fig. 2.5g were assumed. The cumulative plasma was accounted for by a simple qualitative model, presuming a spatially dependent phase shift introduced in the focal plane.

The transverse dependency of this phase shift was chosen from the focal intensity profile (determined from the measured mode size) taken to the power of 2.5 and translated by $495 \text{ m/s} \cdot (72 \text{ MHz})^{-1} = 6.88 \text{ } \mu\text{m}$, where 495 m/s estimated velocity of the gas (see Figs. 2.6c). Simulations were conducted for three cases: without phase shift (Fig. 2.6a and below), a maximum phase shift of 0.15 rad (Fig. 2.6b and below), and a maximum phase shift of 0.19 rad (Fig. 2.6c and below). In each case, the eigenmodes of the model resonator, together with their respective round-trip phases ϕ_{rt} and attenuations $1 - L$, were determined numerically.

To excite an eigenmode in the resonator, its round-trip phase ϕ_{rt} must be matched to the phase change $\Delta\phi$ between consecutive pulses, as given by the frequency comb parameters of the seed (repetition rate and frequency offset). Then, the eigenmode is said to be resonant. In addition, the spatial profile of the seed must overlap with the eigenmode. To identify possibly resonant eigenmodes, a symmetric Gaussian seeding mode with optimum overlap for the case

⁶Publication included together with a statement of author contributions as Section 3.1.

without cumulative plasma was assumed, and the enhancement \mathcal{E} for each mode was computed versus $\Delta\phi$, according to the following formula (compare [101, eq. 3.32]):

$$\mathcal{E}(\Delta\phi) = \mathcal{O} \cdot \left| \frac{\sqrt{T}}{1 - \sqrt{1-L}\sqrt{1-T} \exp(i\Delta\phi - i\phi_{\text{rt}})} \right|^2 \quad (2.2)$$

Here, $T = 3\%$ is the input coupler transmission and \mathcal{O} the numerically determined spatial overlap with the seed. The resulting enhancement for all eigenmodes that are resonant near the fundamental mode of the empty EC is shown in Figs. 2.6d, e, and f. Eigenmodes with a maximum enhancement below 1 were omitted for clarity. It can be seen that the phase for which the fundamental mode is resonant shifts slightly when the density of the cumulative plasma increases. What is more, its enhancement drops, and the spatial profile becomes strongly distorted (Figs. 2.6h and i). Additionally, a higher-order eigenmode emerges, which resembles a distorted Gauss-Hermite mode.

Here, the calculated overlap between the two resonant eigenmodes remains below 10^{-4} , such that they can still be regarded as orthogonal. This allows to compute the excited mode of the cavity in good approximation by simply summing up the normalized resonant eigenmodes, weighted with their overlap with the seed. At the phase $\Delta\phi$ of the respective fundamental mode, this yields the spatial profiles shown in Figs. 2.6j, k, and l. It can be observed that newly emerged higher-order mode partially compensates for the distortions of the fundamental mode. Although the power enhancement for the fundamental mode drops significantly for the case with a phase shift of 0.19 rad (from 122 to 80), the superposition of all resonant modes still has a total enhancement of 117.

To show that this model qualitatively describes the experimentally observed data, the relative difference between the excited modes shown in Fig. 2.6j and Fig. 2.6l was computed (Fig. 2.5h). The observed distortion resembles the simulated distortion, even though the Gauss-Hermite modes corresponding to the distortions have a slightly higher order in the simulations, and is, in contrast to the experiment, of odd order in the y direction. These differences can be attributed to the very simple model for the transverse phase, and to deviations in the stability range position, incidence angle, and focusing mirror radius of curvature, all of which can alter the relative phase between different eigenmodes. The odd order in y direction indicates an asymmetry in this direction, e.g., the streaming direction of the gas jet could have been not perfectly parallel to the x axis.

2.2.3 Temporal Dissipative Solitons in Free-Space Cavities

Temporal cavity solitons are self-stabilizing optical pulses circulating in externally driven resonators enclosing a dispersive medium with Kerr nonlinearity and have been demonstrated in fiber resonators [102] and microresonators [103–108]. In our group, the first temporal cavity soliton in a free-space enhancement cavity was observed [89]⁷. One key innovation of the experiment was a tailored input coupler transmission curve, which has enabled unprecedented peak power enhancement and efficient intracavity pulse compression.

⁷The experiment was conducted by Nikolai Lilienfein. I developed, together with Nikolai Lilienfein, the numerical model and performed the simulations, and I contributed to the manuscript.

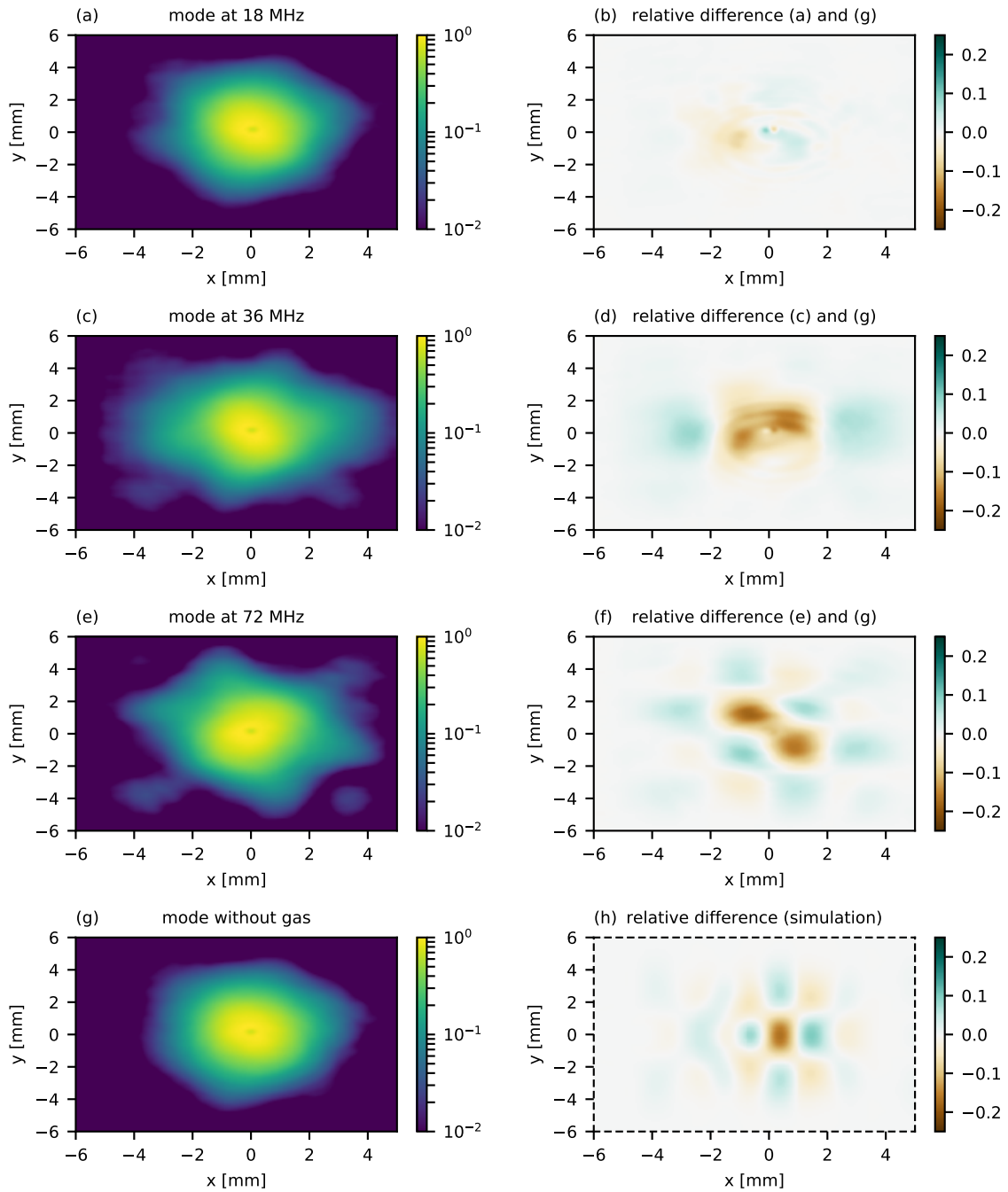


Figure 2.5: Observed mode deformations owing to cumulative plasma. (a), (c), (e): Transverse mode profile with gas, measured at different repetition rates with otherwise same parameters. (b), (d), (f): Relative difference between the mode profile measured with gas and without gas after normalization to the same power, for each repetition rate. (g) Mode profile measured in the empty cavity (no gas jet). (h) Simulated difference between the mode profile with gas and without gas at 72 MHz, see Figs. 2.6j and l.

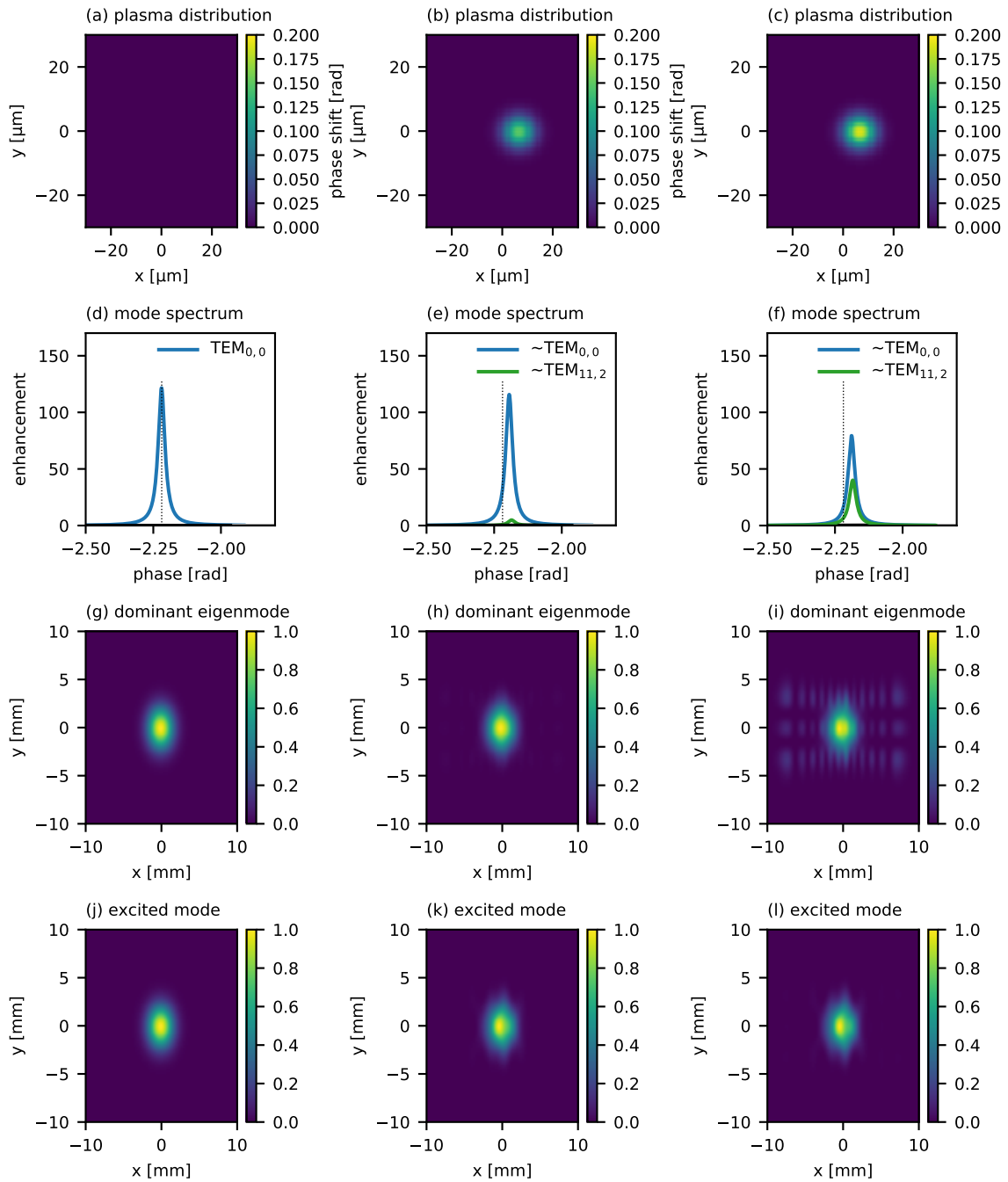


Figure 2.6: Simulated mode spectra with cumulative plasma. First row: assumed plasma distribution for the simulations, with different peak phase shifts. Second row: mode spectra of the simulated cavity assuming a spatially dependent phase shift in the focus plane, as shown above. Third row: profile of the dominant eigenmode. Fourth row: excited field, resulting from a superposition of the resonant eigenmodes.

The experimental setup comprises a 100-MHz standard bow-tie cavity with a thin Kerr medium placed in Brewster's angle near the focus and is described in detail in [89]. To quantitatively understand the experimental results, 1D simulations were performed. To this end, the cavity mirrors and the seed pulses were accurately characterized. With this data, the seeding repetition rate was scanned for different values of the comb offset frequency and the buildup of the pulse in the EC was simulated with and without nonlinearity, using a simple iterative approach:

$$\hat{A}_{n+1}(\omega) = \sqrt{1 - T_{\text{IC}}(\omega)}\sqrt{1 - L(\omega)} \hat{A}_n^{\text{nl}}(\omega) \exp [i\Phi_{\text{rt}}(\omega) + i(C_1\omega + C_0)] + \sqrt{T(\omega)} \hat{A}_{\text{laser}}(\omega) \quad (2.3)$$

$$A_n^{\text{nl}}(t) = A_n(t) \exp (-i\alpha|A_n(t)|^2) \quad (2.4)$$

$$\hat{A}_0(\omega) = 0 \quad (2.5)$$

Here, equation (2.3) describes the propagation of the pulse through the free-space resonator in the co-moving frame and the interference at the input coupler, and (2.4) accounts for the self-phase modulation inside the nonlinear medium. $A_n(t)$ is the complex envelope of the electric field inside the Kerr medium at round-trip number n , $\hat{A}_n(\omega)$ its Fourier transform, $T_{\text{IC}}(\omega)$ the spectral transmission of the input coupler, $L(\omega)$ the spectral loss per round-trip, $\Phi_{\text{rt}}(\omega)$ the total spectral round-trip phase of the cavity mirrors, α determines the strength of the nonlinearity, and $\hat{A}_{\text{laser}}(\omega)$ is the Fourier transform of the seeding pulse. The effective linear spectral phase arising from a detuning between the seeding comb parameters and the cavity resonances are accounted for by the phase term $C_1\omega + C_0$.

The resulting peak power enhancement is plotted in Figs. 2.7a and b. As can be seen, the nonlinearity causes a slight shift of the comb parameters for optimum enhancement. What is more, a step structure emerges in which substantially higher peak power enhancements are achieved compared to the case without nonlinearity. The average power enhancement, in contrast, is comparable, which already indicates that the circulating pulses are shorter than the seeding pulses (see line cuts in Figs. 2.7c and d). Because the seeding pulses are, in good approximation, bandwidth-limited, this can only happen via spectral broadening inside the Kerr medium, which is shown in Figs. 2.7e and f. The experimental spectrum (green) agrees well with the simulated spectrum (orange). In the time domain (Figs. 2.7g and h), the seeding pulses are compressed by a factor of 9.5.

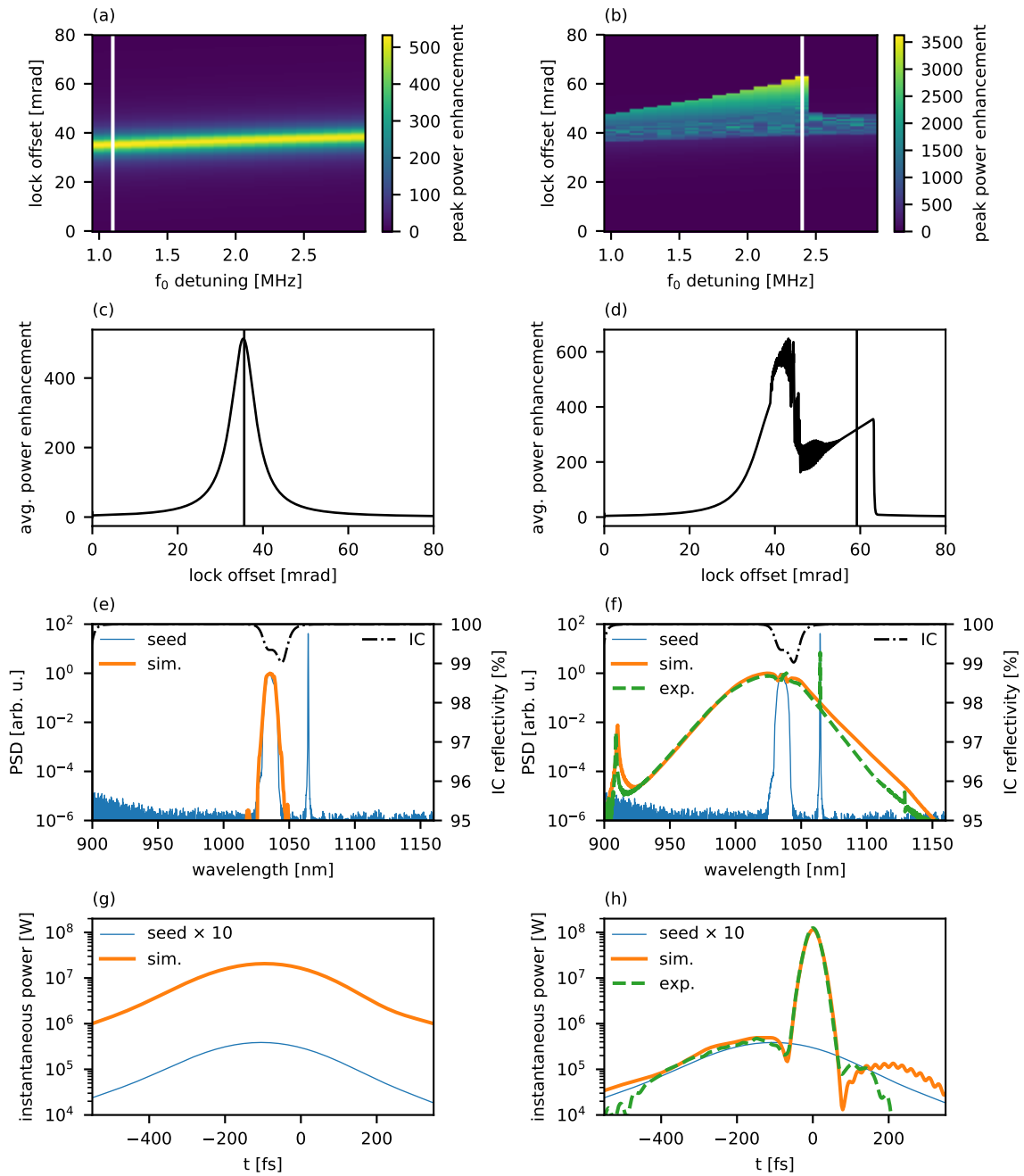


Figure 2.7: Simulated free-space cavity soliton in comparison to experimental data. Left: without nonlinearity. Right: with nonlinearity. (a,b) Simulated peak power enhancement for scanned comb parameters. (c,d) Average power enhancement versus lock offset, for the detunings marked with white lines in the plots above. (e,f) Simulated intracavity spectrum for comb parameters marked by vertical lines in plots above, along with the measured seed and intracavity spectra and the input coupler (IC) reflectivity. (g,h) Simulated temporal pulse shape for identical comb parameters, illustrating the intracavity pulse compression.

Chapter **3**

Optimization of Cavity-Enhanced
High-Harmonic Generation

3.1 Cumulative Plasma Effects in Cavity-Enhanced High-Order Harmonic Generation in Gases

as published in

APL Photonics (2018)

[78]

by

Tobias Saule, Maximilian Högner, Nikolai Lilienfein, Oliver de Vries, Marco Plötner, Vladislav S. Yakovlev, Nicholas Karpowicz, Jens Limpert, and Ioachim Pupeza

Contributions I participated in the planning, execution, evaluation and interpretation of the experiment, and in preparing the manuscript.

APL PHOTONICS 3, 101301 (2018)



Cumulative plasma effects in cavity-enhanced high-order harmonic generation in gases

Tobias Saule,^{1,2} Maximilian Högner,^{1,2} Nikolai Lilienfein,^{1,2} Oliver de Vries,³ Marco Plötner,³ Vladislav S. Yakovlev,^{1,2} Nicholas Karpowicz,¹ Jens Limpert,^{4,5,6} and Joachim Pupeza^{1,a}

¹Max-Planck-Institute of Quantum Optics, Hans-Kopfermann-Str. 1, 85748 Garching, Germany

²Ludwig-Maximilians-University Munich, Am Coulombwall 1, 85748 Garching, Germany

³Fraunhofer Institute for Applied Optics and Precision Engineering, Albert-Einstein-Str. 7, 07745 Jena, Germany

⁴Friedrich-Schiller-University Jena, Institute for Applied Physics, Albert-Einstein-Str. 15, 07745 Jena, Germany

⁵Helmholtz-Institute Jena, Fröbelstieg 3, 07743 Jena, Germany

⁶Active Fiber Systems GmbH, Wildenbruchstr. 15, 07745 Jena, Germany

(Received 22 April 2018; accepted 2 July 2018; published online 2 August 2018)

Modern ultrafast laser architectures enable high-order harmonic generation (HHG) in gases at (multi-) MHz repetition rates, where each atom interacts with multiple pulses before leaving the HHG volume. This raises the question of cumulative plasma effects on the nonlinear conversion. Utilizing a femtosecond enhancement cavity with HHG in argon and on-axis geometric extreme-ultraviolet (XUV) output coupling, we experimentally compare the single-pulse case with a double-pulse HHG regime in which each gas atom is hit by two pulses while traversing the interaction volume. By varying the pulse repetition rate (18.4 and 36.8 MHz) in an 18.4-MHz roundtrip-frequency cavity with a finesse of 187, and leaving all other pulse parameters identical (35-fs, 0.6- μ J input pulses), we observe a dramatic decrease in the overall conversion efficiency (output-coupled power divided by the input power) in the double-pulse regime. The plateau harmonics (25–50 eV) exhibit very similar flux despite the twofold difference in repetition rate and average power. We attribute this to a spatially inhomogeneous plasma distribution that reduces the HHG volume, decreasing the generated XUV flux and/or affecting the spatial XUV beam profile, which reduces the efficiency of output coupling through the pierced mirror. These findings demonstrate the importance of cumulative plasma effects for power scaling of high-repetition-rate HHG in general and for applications in XUV frequency comb spectroscopy and in attosecond metrology in particular. © 2018 Author(s). All article content, except where otherwise noted, is licensed under a Creative Commons Attribution (CC BY) license (<http://creativecommons.org/licenses/by/4.0/>). <https://doi.org/10.1063/1.5037196>

INTRODUCTION

Frequency upconversion of ultrashort, intense visible/near-infrared (VIS/NIR) laser pulses to the extreme-ultraviolet (XUV) spectral region via high-order harmonic generation (HHG) in noble gases lies at the core of table-top sources of broadband, coherent XUV radiation.¹ Customarily, the master-oscillator-power-amplifier (MOPA) systems driving HHG operate at pulse repetition rates in the range of several kHz, as a result of the trade-off between the high peak powers necessary for HHG and constraints on the average power in amplifiers. At these pulse repetition rates, the atoms interacting with the HHG-driving pulses usually leave the interaction volume long before the arrival of the subsequent pulse. In this highly relevant and widespread single-pass regime, the process of HHG has

^aioachim.pupeza@mpq.mpg.de



101301-2 Saule *et al.*

APL Photonics 3, 101301 (2018)

been extensively studied.¹ The recent advent of ultrafast laser technologies affording pulses suitable for HHG at repetition rates in the multi-MHz range^{2–16} has opened the door to applications barely fathomable with the well-established kHz technologies. Among those, precision spectroscopy with XUV frequency combs^{5,6,17} and high-speed multi-dimensional laser-dressed XUV photoemission spectroscopy^{18,19} are particularly prominent examples. However, for these repetition rates, the period between two pulses becomes comparable to—or shorter than—the time atoms take to travel through the volume where they can interact with the laser pulses. Consequently, the quantitative study of the cumulative plasma effects arising from the interaction of each atom with multiple pulses is necessary for designing and optimizing applications in this high-repetition-rate regime of HHG.

In this paper, we present an experimental comparison of HHG in the single-pulse (SP) regime (each atom is hit only once) with the case in which each atom interacts with two pulses of the driving laser (double-pulse, DP). To this end, we set up an 18.4-MHz-repetition-rate femtosecond enhancement cavity with either one circulating pulse or two circulating pulses and systematically evaluated the spectra and flux of the XUV radiation coupled out through a pierced mirror following the HHG focus. To investigate the cumulative plasma effects on the HHG process, the only parameter varied between these two cases was the pulse repetition frequency (18.4 MHz or 36.8 MHz), while the pulse parameters in the cavity (pulse energy, duration, and spatial profile) were kept constant within the accuracy of the diagnostics. To ensure that optimum generation conditions for each harmonic order and repetition rate are covered by the experiment, we performed complete scans of the target gas density and nozzle position along the optical axis. We observed a dramatic dependence of the conversion efficiency on the repetition rate, which can be attributed to cumulative plasma effects in the HHG target.

EXPERIMENTAL SETUP

In femtosecond enhancement cavities (EC), the pulses of a mode locked laser are coherently stacked and their energy is enhanced by up to several orders of magnitude. Peak intensities of several 10^{13} W/cm² at a cavity focus can be achieved, permitting HHG at repetition rates of several tens of MHz.^{5–12,18–22} ECs have been successfully used for a number of seminal HHG experiments at high repetition frequencies like direct XUV frequency comb spectroscopy,⁶ the determination of the coherence time of XUV frequency combs⁵ at 154 MHz repetition rate, and the generation of 100-eV frequency combs.^{10,11} However, despite affording circulating pulses shorter than 10 optical cycles with average powers on the 10-kW level,^{10–12} the number of XUV photons per pulse obtained with cavity-enhanced HHG cannot compete with direct, single-pass HHG.³ These results indicate that the presence of gas ionized by the preceding driving pulses reduces the HHG efficiency (per pulse), and the scaling of XUV power with the laser repetition rate deviates strongly from a linear dependence in this regime. For a direct and quantitative investigation of this effect, we designed an EC such that its repetition period equals the traversing time of the gas atoms through the interaction volume. Thus, when seeded with twice its fundamental repetition rate, each atom interacts with two pulses.

The experimental setup is shown in Fig. 1(a). The frontend seeding the enhancement cavity is described in Ref. 25. In brief, a titanium-sapphire (Ti:Sa) seed oscillator emits a 73.6-MHz pulse train, whose repetition frequency can be picked by an integer factor.²³ Chirped-pulse amplification employing Yb-doped fibers delivers 250-fs pulses with an energy of more than 1 μ J for repetition rates down to a few MHz. Spectral broadening in a large-mode-area (LMA) fiber with a 25- μ m core and subsequent temporal compression with chirped mirrors (CM) deliver 0.6- μ J, 35-fs pulses spectrally centered at 1030 nm, with repetition-rate-independent characteristics.²⁵ These pulses impinge on a 16.3-m (corresponding to the single round-trip distance for a repetition rate of 18.4-MHz) EC with an input coupler transmission of 3%. The EC has a finesse of 187 (considering the losses of 0.32% at the 150- μ m pierced output-coupling mirror). Compared to other output-coupling methods, this geometric method allows for broadband XUV output coupling of photon energies of 100 eV and higher and provides phase-locked collinear NIR pulses.¹⁸

In the experiments reported here, the EC was seeded with pulse trains of either 18.4 MHz or 36.8 MHz, resulting in comparable intra-cavity pulse parameters [Figs. 1(b)–1(d)]. An argon gas

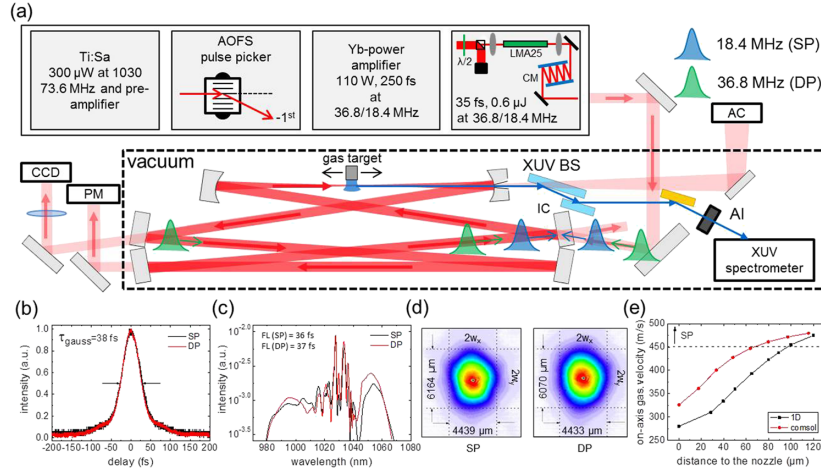


FIG. 1. (a) Experimental setup consisting of a Ti:Sa seed, an acousto-optic frequency shifter (AOFS) pulse picker,²³ an Yb-power-amplifier,²⁴ spectral broadening, chirped-mirror (CM) compression, and a 16.3-m enhancement cavity with either one (18.4 MHz, SP) circulating pulse or two (36.8 MHz, DP) circulating pulses. The spectral broadening is achieved in a solid-core large-mode-area (LMA) fiber with a 25- μm core diameter providing identical pulses at 36.8 MHz and 18.4 MHz, with 0.6 μJ and 35 fs.²⁵ The XUV radiation is coupled out through a pierced mirror¹¹ and guided to an XUV spectrometer by two multi-layer beam splitters (BS). Intracavity pulse parameters in the presence of the nonlinear gas target, for the two repetition rates: (b) autocorrelation (AC, $\tau_{\text{gauss}} = 38$ fs), (c) spectrum with Fourier-limits (FL) of 36 fs and 37 fs, respectively, (d) beam profile on the pierced mirror, imaged to the CCD camera. (e) Gas velocity along the flow direction of a 100- μm nozzle, derived by a 1D model²⁶ and confirmed via Comsol MultiPhysics. Complete replenishment of the gas target within 54 ns (repetition period of the SP regime) is achieved for velocities >450 m/s, at a beam waist of 12.3 μm .

target delivered by a 100- μm fused-silica end-fire nozzle was positioned at the focal region. The gas flow velocity at a distance of ~ 100 μm from the nozzle orifice was estimated to be 450 m/s [Fig. 1(e)] by a 1D model²⁶ as well as flow simulations using Comsol MultiPhysics. The curved mirrors of the EC ($f = 100$ mm) and the position in the stability range were chosen such that the beam waist was 12.3 μm . This results in peak intensities of several 10^{13} W/cm² and ensured SP configuration for the 18.4-MHz pulse train, meaning that an atom traverses the $1/e^2$ -intensity beam diameter within one repetition period. At 36.8 MHz, the atoms traverse this distance within 2 shots and, thus, we refer to this regime as the double-pulse (DP) configuration. The generated harmonics were coupled out of the cavity through a 150- μm opening in the mirror following the focus¹¹ and split from the fundamental beam by two multi-layer Nb₂O₅ beam splitters. To prevent hydrocarbon contaminations of the optics, we flushed the two cavity mirrors and two beam splitters subsequent to the XUV generation with ozone. The XUV beam was then directed to a grating spectrometer whose linearity with respect to the XUV flux was confirmed in a previous experiment. To exclude thermal effects in the system, all experiments reported here were performed at a maximum repetition rate of 36.8 MHz, corresponding to average powers of 11 W and 0.6 kW impinging on and circulating in the EC, respectively. For both repetition rates, stable operation of the system under constant conditions was possible for measurement times longer than 10 h.

RESULTS

To study the cumulative effects in a controlled way and to ensure comparable pulse parameters for the two repetition rates, for each data point, we recorded the intracavity average power, the pulse duration, and the beam profile on one mirror, in an actively locked¹⁰ steady state. This measurement also allows for the precise determination of the position of the nozzle with respect to the focus by evaluating the plasma-induced power clamping²⁰ for different target positions along the cavity beam. This delivers 2D maps for all the intra-cavity parameters regarding the backing pressure and

101301-4

Saule *et al.*

APL Photonics 3, 101301 (2018)

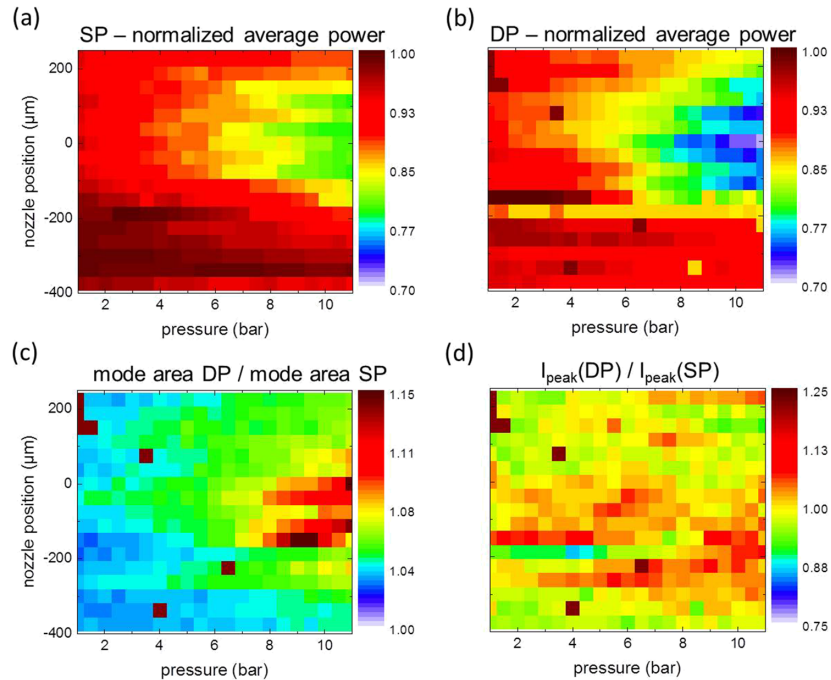


FIG. 2. [(a) and (b)] Normalized intra-cavity average power clamping maps for the SP and the DP, respectively. They demonstrate how the intra-cavity power level clamps as a function of the nozzle position and backing pressure. The experimentally determined focus position (see the text) is set to 0 μm . One immediate observation is that the DP configuration experiences stronger clamping in the focus region. (c) Ratio of the mode area of the DP versus the SP on the pierced mirror. The larger ratios in the focus region stem from changes in the DP mode area, while the relative changes in the SP mode area stay below 2.7%. (d) Ratio of the peak intensities (calculating from the mode size, average power, pulse duration, and target position) for the two repetition rates.

target position; they are depicted in Figs. 2(a)–2(d). Figures 2(a) and 2(b) show the average power in the cavity with the gas target being present, normalized to the average power in the empty cavity for the same input pulse parameters for the SP and the DP, respectively. They demonstrate that cumulative effects affect the cavity operation as the DP configuration clamps to 70% of the linear cavity, whereas the SP only clamps to 80% in the focus. Figure 2(c) illustrates the evolution of the DP cavity eigenmode on the pierced mirror with respect to the SP configuration by showing the ratio of the mode area of the DP to SP case for different experimental parameters. Here, the change in the mode area in the DP dominates the ratio, whereas the changes in the SP contribute little (<2.7%). The map reveals an opposing behavior compared to the average power [see (a) and (b)]. Taking these mode distortions into account, we can calculate the intra-cavity peak intensity by utilizing the mode size, average power, pulse duration, and target position. The data reveal similar values for both repetition rates [see Fig. 2(d)], which fits to the identical XUV cutoff in the following experiments.

With the focus as a reference point for the optical axis and well-characterized experimental conditions, we examined the output coupled XUV flux. Figure 3(a) shows the relative XUV flux per harmonic (integrated counts within one harmonic) for the SP (1st row) and the DP (2nd row) configuration, as a function of the nozzle position and backing pressure, for six different harmonics. The color scales are the same for each harmonic to facilitate the comparison between the two repetition rates. Figure 3(b) shows the XUV spectrum at the gas target pressure and position marked in (a), circles, for both repetition rates, where the flux of the 33rd harmonic is optimal for the SP configuration. In Fig. 3(c), each harmonic is plotted at its optimum values within the maps in

101301-5

Saule *et al.*

APL Photonics 3, 101301 (2018)

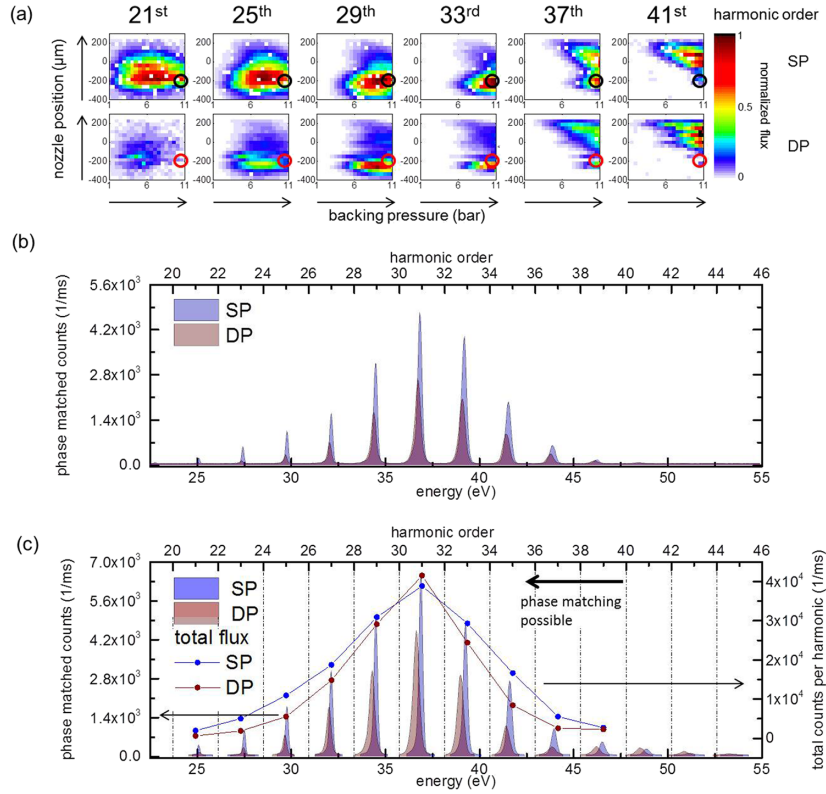


FIG. 3. (a) XUV flux measured as a function of the gas target position and backing pressure, for six different harmonics, for SP (1st row) and DP (2nd row). For each harmonic, the color scales are common to the SP and DP maps; they are normalized to the highest flux. The nozzle position of $0 \mu\text{m}$ marks the cavity focus determined as explained in the text. (b) XUV spectra for both repetition rates measured for the parameters indicated in (a) by the circles. (c) Stitched XUV spectrum for individually optimized conditions for SP and DP, taken from the positions on the maps with the highest flux. The dots represent the integrated flux within these harmonics.

Fig. 3(a). The data points connected with solid lines depict the counts spectrally integrated over each harmonic order.

DISCUSSION

Figure 3(a) shows that further increasing the pressure does not improve the flux for harmonic orders up to 39, which indicates that we achieved optimized phase matching conditions (under the boundary conditions of the EC) for these harmonics at both repetition rates. The target position was scanned over a large enough range to include the optimum positions.

Evidently, the SP configuration is preferable in terms of the total output coupled flux [Fig. 3(c)] and conversion efficiency. Figure 4(a) depicts the ratio of the XUV flux of the DP configuration and the SP one for each harmonic order. While a ratio of two would correspond to a linear scaling of the XUV flux with the repetition rate (keeping the pulse parameters constant), most harmonics manifest a ratio below unity, i.e., the DP yields even less flux than the SP configuration, despite twice the driving average power. This corresponds to a dramatic decrease in the overall conversion efficiency (output-coupled power divided by seed power) by up to a factor of 4 due to cumulative plasma effects.

At the same time, for all harmonics, the optimum generation conditions (target gas density and position) are very similar for the two repetition rates. This indicates that the ionization fraction in the

101301-6

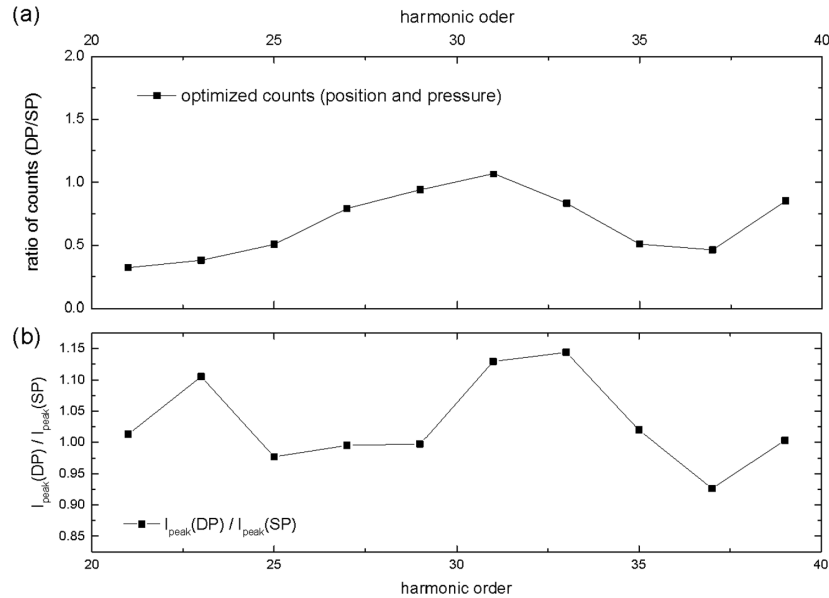
Saule *et al.*APL Photonics **3**, 101301 (2018)

FIG. 4. (a) Ratio of the output coupled flux for the DP versus the SP configuration. A value of 2 corresponds to the same conversion efficiency (output-coupled power divided by the input power) as double the average seed power is available for the DP configuration. (b) Ratio of the calculated peak intensity for the DP versus the SP case. The peak intensity was calculated from the mode size, focusing geometry, intra-cavity pulse duration, and calibrated intra-cavity power.

contributing part of the target gas is similar for both the SP and the DP, and the substantial decrease in flux can rather be attributed to a decrease in the generation volume: in the DP regime, the gas target is spatially partitioned into a part that was already hit by the previous pulse and propagated off-axis, contributing little to the flux (e.g., due to preionization), and a part with “fresh” ground-state gas atoms. This would affect the output coupled flux in two ways: first, fewer atoms contribute to HHG and second, the reduced generation volume results in a larger divergence of the harmonic beam and, thus, a lower output coupling efficiency. To confirm and disentangle these effects, a similar experiment with a Brewster plate^{8,12} or a diffraction-based output coupling method^{6,7} can be performed. This way the decrease in output coupling efficiency due to changes in the XUV beam profile can be scrutinized and possibly more profound conclusions about the physical processes can be extracted. Another meaningful single-pass experiment could be the generation of high harmonics with two slightly delayed pulses, analyzing the HHG yield and XUV mode profile with respect to the delay.

To exclude that the decrease in the flux in the DP configuration is due to a stronger intensity clamping of the driving field [Fig. 2(a)], we computed the peak intensity in the target for each point of the parameter scan, accounting for the measured pulse duration, cavity mode size, and target position. Figure 2(d) shows the peak intensity ratio between the DP and SP cases. It can be seen that the peak intensity is very similar in the two configurations, even though the average power clamping suggests otherwise. This can be attributed to small changes in the cavity mode size [see Fig. 2(c)]. At optimum parameters for each harmonic, the DP configuration even exhibits a slightly higher peak intensity [see Fig. 4(b)].

In conclusion, these findings elucidate the importance of cumulative plasma effects in multi-pass HHG, whose effects are already significant at the onset of the cumulative regime (two passes). The phase-matched plateau harmonics clamp to the same flux independently of the repetition rate. Our data show that this reduction of XUV flux is not a result of distortions of the circulating IR field. By contrast, we attribute these findings to a spatially inhomogeneous plasma distribution that hinders the output coupling efficiency of the pierced mirror and/or of the HHG generation itself.

101301-7 Saule *et al.*

APL Photonics 3, 101301 (2018)

For applications requiring multi-MHz, high-photon-energy, high-flux XUV pulses, these findings elucidate the benefit of a single-pulse regime achievable by adapting the repetition rate of the system and/or by speeding up the gas.^{7,10} With the same experimental setup, the repetition rate scalability of HHG in solids^{27–29} can in principle be examined by replacing the gas target with a thin Brewster plate.

ACKNOWLEDGMENTS

This work was supported by the project MEGAS in the frame of the Fraunhofer-Max-Planck Cooperation and by the German Research Foundation (DFG) via the Munich Centre for Advanced Photonics (MAP).

- ¹ M. Wegener, *Extreme Nonlinear Optics* (Springer, 2005).
- ² S. Hädrich, J. Rothhardt, M. Krebs, S. Demmler, A. Klenke, A. Tünnermann, and J. Limpert, "Single-pass high harmonic generation at high repetition rate and photon flux," *J. Phys. B: At., Mol. Opt. Phys.* **49**, 172002 (2016).
- ³ S. Hädrich, A. Klenke, J. Rothhardt, M. Krebs, A. Hoffmann, O. Pronin, V. Pervak, J. Limpert, and A. Tünnermann, "High photon flux table-top coherent extreme-ultraviolet source," *Nat. Photonics* **8**, 779–783 (2014).
- ⁴ S. Hädrich, M. Krebs, A. Hoffmann, A. Klenke, J. Rothhardt, J. Limpert, and A. Tünnermann, "Exploring new avenues in high repetition rate table-top coherent extreme ultraviolet sources," *Light: Sci. Appl.* **4**, e320 (2015).
- ⁵ C. Benko, T. K. Allison, A. Cingöz, L. Hua, F. Labaye, D. C. Yost, and J. Ye, "Extreme ultraviolet radiation with coherence time greater than 1 s," *Nat. Photonics* **8**, 530–536 (2014).
- ⁶ A. Cingöz, D. C. Yost, T. K. Allison, A. Ruehl, M. E. Fermann, I. Hartl, and J. Ye, "Direct frequency comb spectroscopy in the extreme ultraviolet," *Nature* **482**, 68–71 (2012).
- ⁷ A. K. Mills, T. J. Hammond, M. H. C. Lam, and D. J. Jones, "XUV frequency combs via femtosecond enhancement cavities," *J. Phys. B: At., Mol. Opt. Phys.* **45**, 142001 (2012).
- ⁸ C. Gohle, T. Udem, M. Herrmann, J. Rauschenberger, R. Holzwarth, H. A. Schüssler, F. Krausz, and T. W. Hänsch, "A frequency comb in the extreme ultraviolet," *Nature* **436**, 234–237 (2005).
- ⁹ R. J. Jones, K. D. Moll, M. J. Thorpe, and J. Ye, "Phase-coherent frequency combs in the vacuum ultraviolet via high-harmonic generation inside a femtosecond enhancement cavity," *Phys. Rev. Lett.* **94**, 193201 (2005).
- ¹⁰ H. Carstens, M. Högner, T. Saule, S. Holzberger, N. Lilienfein, A. Guggenmos, C. Jocher, T. Eidam, D. Esser, V. Tosa, V. Pervak, J. Limpert, A. Tünnermann, U. Kleineberg, F. Krausz, and I. Pupeza, "High-harmonic generation at 250 MHz with photon energies exceeding 100 eV," *Optica* **3**(4), 366–369 (2016).
- ¹¹ I. Pupeza, S. Holzberger, T. Eidam, H. Carstens, D. Esser, J. Weitenberg, P. Rußbüldt, J. Rauschenberger, J. Limpert, Th. Udem, A. Tünnermann, T. W. Hänsch, A. Apolonski, F. Krausz, and E. Fill, "Compact high-repetition-rate source of coherent 100 eV radiation," *Nat. Photonics* **7**, 608–612 (2013).
- ¹² J. Lee, D. R. Carlson, and R. J. Jones, "Optimizing intracavity high harmonic generation for XUV fs frequency combs," *Opt. Express* **19**(23), 23315–23326 (2011).
- ¹³ D. C. Yost, A. Cingöz, T. K. Allison, A. Ruehl, M. E. Fermann, I. Hartl, and J. Ye, "Power optimization of XUV frequency combs for spectroscopy applications," *Opt. Express* **19**, 23483 (2011).
- ¹⁴ P. Rußbüldt, D. Hoffmann, M. Höfer, J. Löhning, J. Luttmann, A. Meissner, J. Weitenberg, M. Traub, T. Sartorius, D. Esser, R. Wester, P. Loosen, and R. Poprawe, "Innoslab amplifiers," *IEEE J. Sel. Top. Quantum Electron.* **21**, 447 (2015).
- ¹⁵ O. Pronin, M. Seidel, F. Lücking, J. Brons, E. Fedulova, M. Trubetskov, V. Pervak, A. Apolonski, Th. Udem, and F. Krausz, "High-power multi-megahertz source of waveform-stabilized few-cycle light," *Nat. Commun.* **6**, 6988 (2015).
- ¹⁶ C. J. Saraceno, F. Emaury, C. Schriber, A. Diebold, M. Hoffmann, M. Golling, T. Südmeyer, and U. Keller, "Toward millijoule-level high-power ultrafast thin-disk oscillators," *IEEE J. Sel. Top. Quantum Electron.* **21**, 106 (2015).
- ¹⁷ A. Ozawa and Y. Kobayash, "VUV frequency-comb spectroscopy of atomic xenon," *Phys. Rev. A* **87**, 022507 (2013).
- ¹⁸ T. Saule, S. Heinrich, J. Schötz, N. Lilienfein, M. Högner, O. de Vries, M. Plötner, J. Weitenberg, D. Esser, J. Schulte, P. Rußbüldt, J. Limpert, M. F. Kling, U. Kleineberg, and I. Pupeza, "High-flux, high-photon-energy ultrafast extreme-ultraviolet photoemission spectroscopy at 18.4 MHz pulse repetition rate" (submitted).
- ¹⁹ C. Corder, P. Zhao, X. Li, M. D. Kershish, A. R. Muraca, M. G. White, and T. K. Allison, "An instrument for time-resolved photoelectron spectroscopy at 87 MHz," in *Frontiers in Optics, LM4F.6*, 2017.
- ²⁰ S. Holzberger, N. Lilienfein, H. Carstens, T. Saule, M. Högner, F. Lücking, M. Trubetskov, V. Pervak, T. Eidam, J. Limpert, A. Tünnermann, E. Fill, F. Krausz, and I. Pupeza, "Femtosecond enhancement cavities in the nonlinear regime," *Phys. Rev. Lett.* **115**, 023902 (2015).
- ²¹ T. K. Allison, A. Cingöz, D. C. Yost, and J. Ye, "Extreme nonlinear optics in a femtosecond enhancement cavity," *Phys. Rev. Lett.* **107**, 183903 (2011).
- ²² D. R. Carlson, J. Lee, J. Mongelli, E. M. Wright, and R. J. Jones, "Intracavity ionization and pulse formation in femtosecond enhancement cavities," *Opt. Lett.* **36**(15), 2991–2993 (2011).
- ²³ O. de Vries, T. Saule, M. Plötner, F. Lücking, T. Eidam, A. Hoffmann, A. Klenke, S. Hädrich, J. Limpert, S. Holzberger, T. Schreiber, R. Eberhardt, I. Pupeza, and A. Tünnermann, "Acousto-optic pulse picking scheme with carrier-frequency-to-pulse-repetition-rate synchronization," *Opt. Express* **23**(15), 19586–19595 (2015).
- ²⁴ J. Limpert, F. Stutzki, F. Jansen, H.-J. Otto, T. Eidam, C. Jauregui, and A. Tünnermann, "Yb-doped large-pitch fibres: Effective single-mode operation based on higher-order mode delocalization," *Light: Sci. Appl.* **1**, e8 (2012).
- ²⁵ T. Saule, S. Holzberger, O. De Vries, M. Plötner, J. Limpert, A. Tünnermann, and I. Pupeza, "Phase-stable, multi- μ J femtosecond pulses from a repetition-rate tunable Ti:Sa-oscillator-seeded Yb-fiber amplifier," *Appl. Phys. B* **123**, 17 (2017).
- ²⁶ G. Scoles, *Atomic and Molecular Beam Methods* (Oxford University Press, 1998), Vol. I, p. 17ff.

101301-8 Saule *et al.*

APL Photonics **3**, 101301 (2018)

- ²⁷ O. Schubert, M. Hohenleutner, F. Langer, B. Urbanek, C. Lange, U. Huttner, D. Golde, T. Meier, M. Kira, S. W. Koch, and R. Huber, "Sub-cycle control of terahertz high-harmonic generation by dynamical Bloch oscillations," *Nat. Photonics* **8**, 119–123 (2014).
- ²⁸ T. Luu, M. Garg, S. Kruchinin, A. Moulet, M. Hassan, and E. Goulielmakis, "Extreme ultraviolet high-harmonic spectroscopy of solids," *Nature* **521**, 498 (2015).
- ²⁹ K. F. Lee, X. Ding, T. J. Hammond, M. E. Fermann, G. Vampa, and P. B. Corkum, "Harmonic generation in solids with direct fiber laser pumping," *Opt. Lett.* **42**, 1113 (2017).

3.2 Efficiency of Cavity-Enhanced High Harmonic Generation with Geometric Output Coupling

as published in

Journal of Physics B (2019)

[80]

by

Maximilian Högner, Tobias Saule and Ioachim Pupeza

Contributions I performed the simulations, developed the theoretical model and wrote most of the manuscript.

OPEN ACCESS

IOP Publishing

Journal of Physics B: Atomic, Molecular and Optical Physics

J. Phys. B: At. Mol. Opt. Phys. 52 (2019) 075401 (12pp)

<https://doi.org/10.1088/1361-6455/ab06db>

Efficiency of cavity-enhanced high harmonic generation with geometric output coupling

M Högner^{1,2} , T Saule^{1,2} and I Pupeza^{1,2,3} ¹Max-Planck-Institut für Quantenoptik, Hans-Kopfermann-Straße 1, D-85748 Garching, Germany²Ludwig-Maximilians-Universität München, Am Coulombwall 1, D-85748 Garching, GermanyE-mail: mhoegner@mpq.mpg.de and ioachim.pupeza@mpq.mpg.de

Received 29 January 2019

Accepted for publication 13 February 2019

Published 12 March 2019



CrossMark

Abstract

Cavity-enhanced high-order harmonic generation (HHG) affords broadband, coherent extreme-ultraviolet (XUV) pulse trains with repetition rates of several tens of MHz. Geometrically coupling out the intracavity generated XUV beam through a small on-axis hole in the cavity mirror following the HHG focus has enabled scaling the photon energies attainable with this technology to 100 eV and more, promising new applications of XUV frequency-comb spectroscopy and attosecond-temporal-resolution, multidimensional photoelectron spectroscopy and nanoscopy. So far, in this approach the features of the macroscopic response of the gas target are neither accessible directly nor indirectly via the out-coupled XUV beam due to the loss of spatial information caused by the truncation at the hole. Here, we derive a simple analytical model for the divergence of the intracavity harmonic beam as a function of experimental design parameters such as gas target position, cavity geometry and driving pulse intensity, thereby establishing a connection between the measured XUV spectra and the macroscopic response of the intracavity nonlinear medium. We verify this model by comparison to numerical simulations as well as to systematic measurements, and apply it to elucidate a trade-off between the efficiency of geometric output coupling and that of the HHG process, and the underlying physical mechanisms. These findings illuminate the share of the output coupling efficiency to the overall HHG conversion efficiency and provide—together with previously studied plasma-related enhancement limitations—a holistic means of optimizing the overall efficiency with this architecture that uniquely combines high repetition rates with high photon energies. Furthermore, quantitatively connecting the output coupled, observable XUV radiation to the nonlinear conversion at the cavity focus allows for a better insight into the dynamics of intracavity HHG and might benefit other applications of femtosecond enhancement cavities, such as high-repetition-rate HHG spectroscopy.

Keywords: high harmonic generation, enhancement cavity, conversion efficiency, geometric output coupling

(Some figures may appear in colour only in the online journal)

1. Introduction

Since its discovery in the late 80s [1, 2], laser-driven high-order harmonic generation (HHG) in gases has become an

indispensable source of coherent, table-top extreme-ultraviolet (XUV) radiation for the study of femtosecond and attosecond time-scale electron dynamics in atoms, solids and molecules [3, 4]. In modern HHG systems, the nonlinear conversion is driven by amplified femtosecond pulses, reaching energies of several 100 μJ [5–9]. Typically, this results in repetition rates significantly lower than 1 MHz. However, some applications require operation in the multi-10 MHz repetition-rate regime. Examples include experiments involving the detection of charged particles such as photoelectron spectroscopy and microscopy [10–12] and coincidence measurements [7],

³ Author to whom any correspondence should be addressed.

 Original content from this work may be used under the terms of the [Creative Commons Attribution 3.0 licence](https://creativecommons.org/licenses/by/3.0/). Any further distribution of this work must maintain attribution to the author(s) and the title of the work, journal citation and DOI.

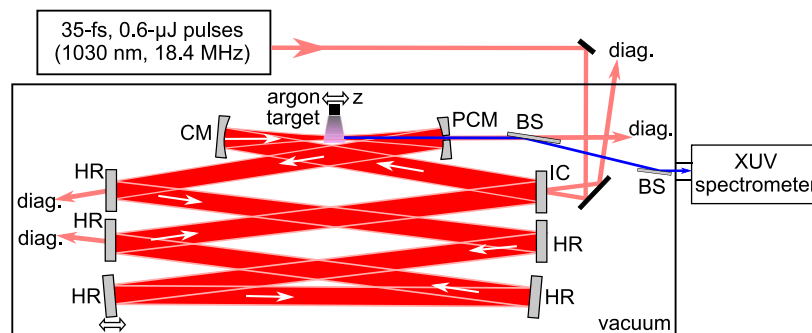


Figure 1. Setup for acquiring systematic p - z -maps of circulating power and XUV photon counts per harmonic order [19]. p : pressure, z : longitudinal target position relative to the focal plane, HR: highly reflective mirror, CM: curved HR mirror, PCM: pierced curved HR mirror, IC: input coupler, BS: XUV/IR beam splitter, diag.: diagnostics.

where space-charge effects limit the useful number of particles per pulse, and frequency-comb spectroscopy [13, 14] at high photon energies, where the power per comb line scales with the repetition rate and the comb spacing should be larger than the line width of the studied transition.

To date, femtosecond enhancement cavities (EC) constitute the most successful HHG approach combining high repetition rates with high XUV powers and high photon energies [15–17]. In cavity-enhanced HHG, the pulses passing the gas target are recycled with the help of a passive resonator housing the gas target (see figure 1). In doing so, inside of the EC a circulating pulse with an energy comparable to that of kHz HHG systems is obtained, without the necessity of reducing the repetition frequency of the original multi-MHz femtosecond front-end. Typically, in cavity-enhanced HHG, the pulse energy of the impinging laser is enhanced by around two orders of magnitude [15–19]. Coupling out the generated XUV radiation through a small on-axis opening in the mirror following the HHG focus [15, 20–22] has rendered the photon energies attainable with this technology scalable to 100 eV and more [15, 16].

While in state-of-the-art ECs circulating pulses of just a few tens of femtoseconds with multi-kW average powers have been demonstrated [16, 17], the overall conversion efficiencies (impinging power to out-coupled XUV power) of these systems have so far remained below the ones achieved with single-pass systems (see appendix A). This indicates that the constraints set by the resonator entail inefficiencies in the XUV generation and output coupling processes that counteract the significant enhancement of the impinging power. To reach the full potential of EC-based XUV sources, it is crucial to understand the individual contributions to these inefficiencies and investigate ways of mitigating them. Indeed, during the last years, considerable progress has been made in this direction. One such limitation is the phenomenon of intracavity intensity clamping, where plasma formation in the gas target on the time scale of a single pulse shifts the spectrum to shorter wavelengths and gives rise to a spectral phase, reducing the spectral overlap with the impinging pulse train and severely limiting the achievable XUV power [23, 24]. Furthermore, for high repetition rates, the generated

plasma embedded in the target gas stream can neither clear the interaction region nor decay before the arrival of the subsequent pulse, leading to the formation of a cumulative plasma. Recently, this has been shown to strongly impair the conversion efficiency [18, 19]. Decreasing the finesse of the resonator and increasing the gas velocity [18] or choosing a sufficiently low repetition rate [17, 19] constitute strategies of mitigating these effects, so that overall conversion efficiencies approaching that of single-pass systems were achieved [17].

In this work, we study the trade-off between intracavity XUV generation efficiency and geometric output coupling efficiency, which is governed by the position of the gas target relative to the focal plane. To this end, we developed a numerical model permitting to break down the overall conversion efficiency into its individual contributions, in particular the output coupling efficiency. We validate this model by finding excellent agreement with systematic measurements in a state-of-the-art cavity-enhanced HHG experiment, where the relevant parameters for output coupling and phase matching (backing pressure and gas target position) were scanned. Finally, we provide a physical explanation for the observed dependence of the output coupling efficiency on the target position and derive a simple approximation formula for the intracavity harmonic beam divergence.

These findings allow for relating the out-coupled XUV spectrum to the spatial and spectral shape of the XUV generated in the EC and, therefore, are crucial to understanding the intracavity HHG dynamics. In particular, alongside the mentioned insights concerning the plasma-related effects, they provide the missing piece for a complete picture of conversion efficiency contributions in photon-energy-scalable cavity-enhanced HHG.

2. Methods

2.1. Experimental data

The experimental setup for the acquisition of the parameter scans of XUV photon counts and driving average power is

described in detail in [19]. In short, a high-finesse 8-mirror resonator (see figure 1) with symmetric focusing (focal length 100 mm), operated near the inner stability edge and with an input coupler transmission of 3% was used to enhance 18.4 MHz, 35 fs, 0.6 μ J pulses spectrally centered at 1030 nm. XUV was generated in an argon gas target ejected from a 100 μ m diameter-opening-nozzle placed near the 12.3 μ m focus ($1/e^2$ -intensity radius, measured by imaging the mode on the output coupling mirror). XUV radiation was geometrically output-coupled through a 150 μ m diameter circular opening in the cavity mirror following the HHG focus. The driving intracavity pulses were characterized with an optical spectrum analyzer and an autocorrelator, yielding pulse durations of 38 fs. A full scan of the gas target position z relative to the focal plane ($z > 0$ signifies that the gas target is placed behind the laser focus) and the backing pressure p applied to the nozzle was performed and the circulating infrared (IR) power and, using an XUV spectrometer, the output-coupled XUV photon counts per harmonic order were recorded at each point, resulting in the p - z -maps shown in figure 2(a).

2.2. Computational model

Assuming a 35 fs Gaussian pulse spectrally centered at 1030 nm and a Gaussian beam with a beam waist of 12.3 μ m as the driving field, for each value of p and z we compute the harmonic field in a transverse plane following the gas target. For this, we numerically solve the first-order propagation equation for the IR and XUV with the 3D HHG model described in [25], without employing envelope approximations. We assume rotational symmetry to speed up the computation, and use the ionization-induced current derived in [26] and the strong-field approximation [27] as source terms. The computational model accounts for plasma-induced lensing, absorption and spectral blue-shift, as well as for Kerr focusing and self-phase modulation. The peak power was chosen proportional to the measured intracavity power (figure 2(a) of [19]), with a maximum of 0.36 GW for best agreement between simulations and experiment. The gas velocities and densities at the nozzle exit and at the interaction site were computed with the analytical model described in [28, p 17ff], presuming a reservoir temperature of 300 K and a 100 μ m nozzle placed at a distance of 120 μ m from the beam axis for best agreement with the experimental data. We assume flat-top density profiles at both positions and choose its diameter at the interaction site (176 μ m) so that the resulting gas flux agrees with the one at the nozzle exit. Propagation from the plane after the gas target to the pierced mirror was done with a Fresnel two-step propagator [29]. The out-coupled XUV power was then computed by spatially integrating over a circular aperture, and spectrally integrating over each harmonic order.

3. Results

The simulated out-coupled XUV power per harmonic order, in dependence of p and z , is depicted in figure 2(b). The

simulations reproduce well the main features observed in the experimental data (figure 2(a)).

To separate the XUV generation efficiency from the output coupling efficiency, we computed the XUV power before the output coupling mirror (figure 2(c)). Thus, the output coupling efficiency can be obtained by dividing the out-coupled power by the generated power (figure 2(d)).

To examine the impact of XUV reabsorption in the gas target, we repeated the simulation with a purely real XUV refractive index, effectively disabling reabsorption (figure 2(e)). Figure 2(f) shows the ratio of the generated XUV power with and without reabsorption. By comparing figures 2(c) and (e), one can see that reabsorption does not affect the qualitative shape of the p - z -maps for harmonic orders > 21 . We repeated the same simulation, but this time discarding the spectral phase of the XUV dipole response and neglecting refractive index in the XUV (figure 2(g)). This leads to perfectly constructive macroscopic interference, i.e. phase matching is enforced, so that the macroscopic response essentially only depends on the number of emitters and the microscopic efficiency. This allows us to isolate the effect of phase matching by dividing the generated XUV power (without reabsorption) by the one with enforced phase matching (figure 2(h)).

The p - z -maps depicted in figures 2(a)-(c), (e) and (g) were normalized to the maximum XUV power per harmonic order for better visibility. For a comparison of the maximum power per harmonic order in simulation and experiment, see figure 3(a).

4. Discussion

4.1. Agreement with the experiment

The experimental maps of the XUV photon counts (figure 2(a)) exhibit some distinctive features:

- (i) harmonic orders around the 33rd reach optimum power for target positions well before the focus, while the optimum position for higher and lower harmonic orders is close to the focus;
- (ii) the optimum pressure increases with increasing harmonic order;
- (iii) for higher harmonic orders, the maps exhibit a V-shaped structure, consisting of two regions with high power, one before the focus and one around the focus;
- (iv) figure 3(a) reveals that the highest power is achieved around the 31st harmonic, and the power drops to zero towards the harmonic orders 21st and 43rd.

All these features are clearly reproduced in the simulated maps (figure 2(b)), thus verifying the model and allowing us to use it to investigate the origins of these features and disentangle the contributing factors.

4.2. Explanation of the observed features

Feature (i) can be attributed partly to the output coupling efficiency (figure 2(d)) and partly to the microscopic

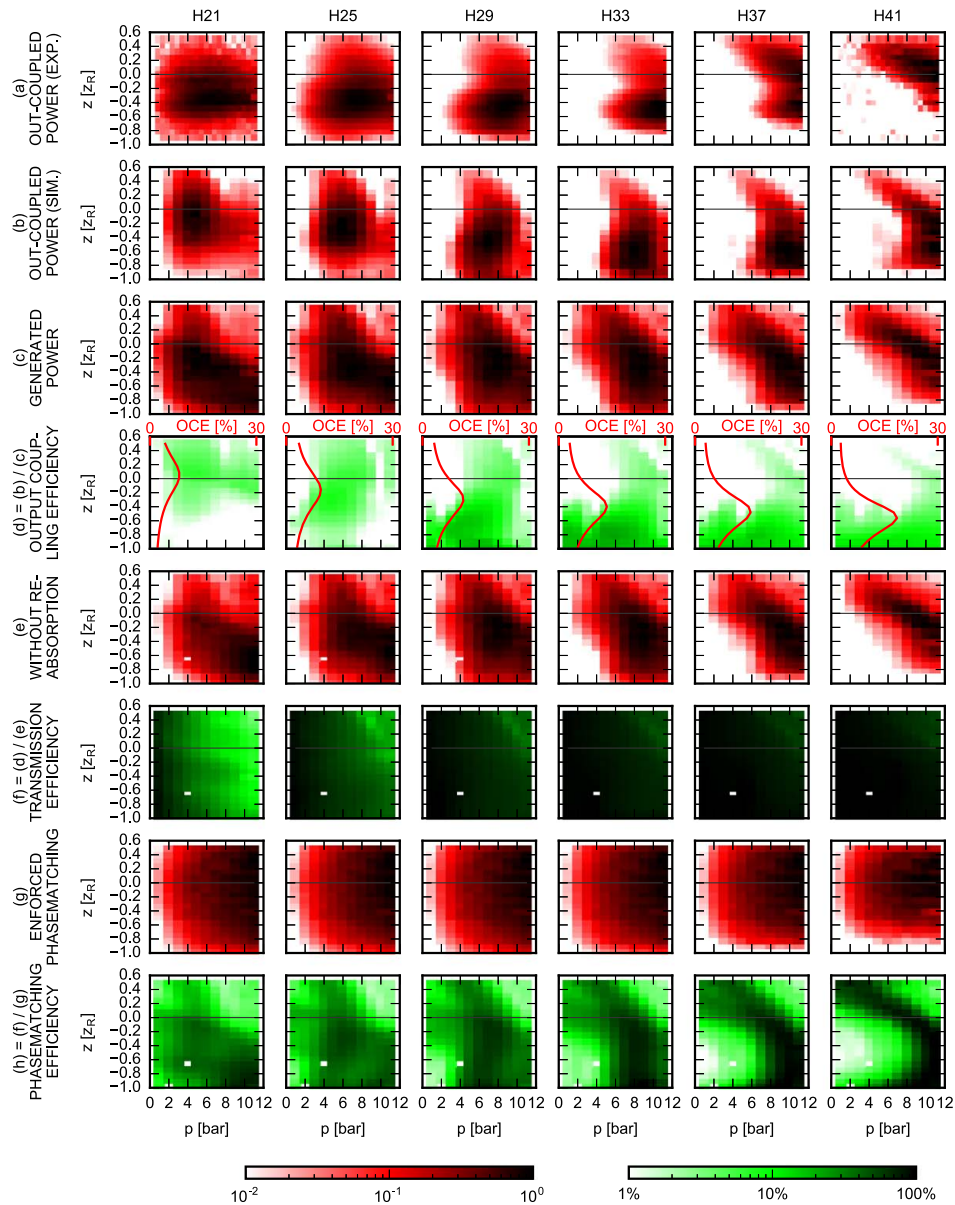


Figure 2. (a) Measured out-coupled XUV power for selected harmonic orders, taken from [19]. (b)–(h) Simulations. (b) Out-coupled XUV power. (c) Generated XUV power. (d) Output coupling efficiency, computed as the ratio between out-coupled and generated XUV power (color scale) and using the analytical formula (red line). (e) Generated XUV power without reabsorption. (f) Transmission efficiency, computed as the ratio between generated XUV power with and without reabsorption. (g) Generated XUV power with enforced phase matching and without reabsorption. (h) Phase matching efficiency, computed as the ratio of generated XUV power without and with enforced phase matching, both without reabsorption. (a), (b), (c), (e) and (g) are normalized for each harmonic order.

efficiency: for lower to intermediate harmonic orders, the optimum target position is dominated by the optimum output coupling efficiency, which is located close to the focal plane for lower orders, but significantly before the focal plane for

intermediate and higher harmonic orders (see section 4.4). For higher harmonic orders, however, the microscopic efficiency declines rapidly with increasing distance from the focus due to the high-harmonic cutoff (compare figure 2(g)).

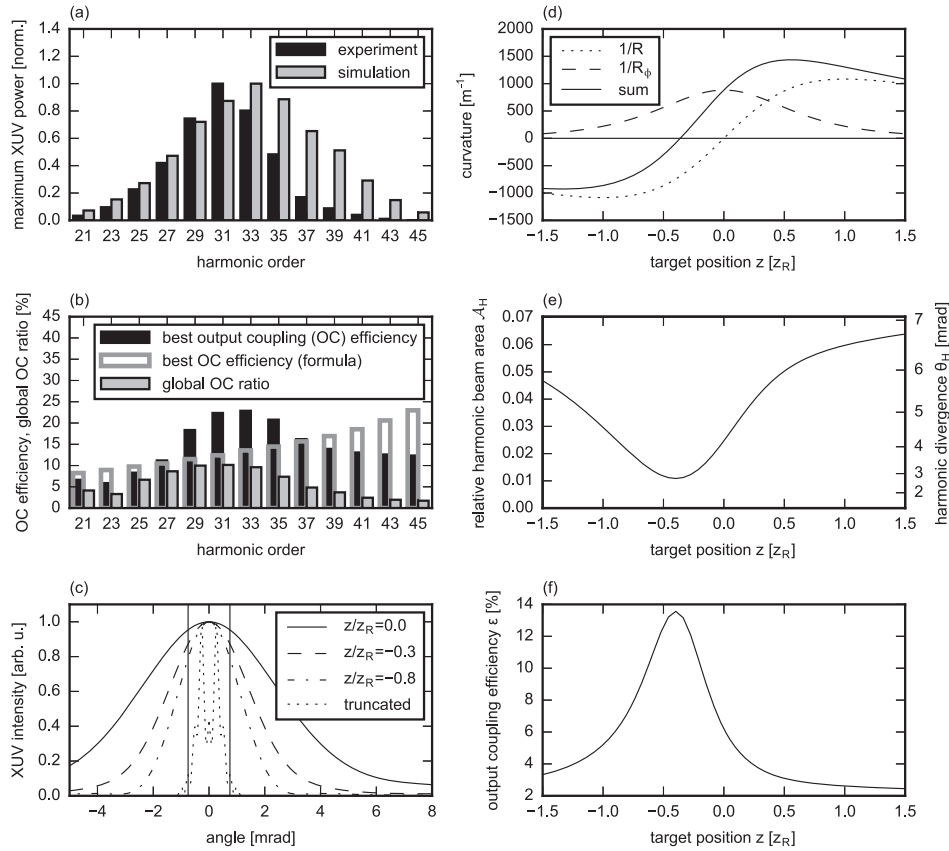


Figure 3. (a) XUV photon counts for each harmonic order at optimum target position and backing pressure, for experiment [19] and simulation, both normalized. (b) Optimum output coupling efficiencies for each harmonic as predicted by the numerical model (black) and the analytical model (gray edge), in comparison with the global output coupling ratio (optimum generated power to optimum out-coupled power from the numerical model, gray). (c) Simulated XUV beam profiles on the output coupling mirror for the 33rd harmonic generated at different gas target positions with a backing pressure of 8 bar. The vertical lines mark the hole diameter for a $150 \mu\text{m}$ hole placed 100 mm after the gas target, and the dotted line shows the beam profile far behind the truncating hole mirror for a gas target positioned $0.56z_R$ before the focus, where z_R is the Rayleigh range of the driving beam. (d) Composition of the harmonic beam wave-front curvature $1/R_H = 1/R + 1/R_\phi$ (solid line) according to the analytical model for the 33rd harmonic, where $1/R$ (dotted) is the curvature of the driving beam and $1/R_\phi$ (dashed) is the additional curvature caused by the transverse dependence of the intensity-dependent harmonic dipole phase. (e) The resulting relative harmonic beam area $\mathcal{A}_H = \theta_H^2/\theta^2$, where θ_H is the divergence of the harmonic beam and θ the divergence of the driving beam. (f) The computed output coupling efficiency for a $150 \mu\text{m}$ hole placed 100 mm after the gas target.

The connection between harmonic order and optimum pressure (ii) can be explained by phase-matching (figure 2(h)): The contribution to the phase mismatch from the intensity-dependent dipole phase increases with harmonic order [30] and must be compensated for by increasing the contribution from the linear refractive index of neutral argon atoms, i.e. by increasing the density.

The V-shaped structure at high harmonic orders (iii) can be attributed to a combination of phase matching and output coupling efficiency: while the phase-matching maps exhibit the same structure (figure 2(h)), the lower wing is barely present in the maps of the generated XUV power and emerges

due to the high output coupling efficiency before the focus (figures 2(c), (d)).

The trend in figure 3(b) (feature (iv)) can be explained by considering the intertwining of output-coupling efficiency, the phase-matching efficiency and the number of emitters: For lower harmonic orders, the regions of high generation efficiency and high output coupling efficiency coincide (figures 2(c), (d)). The phase-matching pressure increases with harmonic order (ii), leading to a higher number of emitters and therefore higher XUV power (figure 2(g)). Additionally, the output coupling efficiency increases slightly with harmonic order. This explains the increase of the out-

coupled signal from lower orders towards the 31st harmonic. The decline for higher harmonic orders can be attributed to the fact that the regions of good generation efficiency and good output coupling do not coincide (see section 4.3), and that the phase-matching pressure was outside of the scanned pressure interval for harmonic orders >41 .

4.3. Trade-off between output coupling efficiency and generation efficiency

To determine how strongly the output coupling affects the achievable power, we compute the ratio between maximum out-coupled power and maximum produced power within the scanned p/z range for each harmonic, i.e. the ratio of the per-harmonic maxima of figures 2(b) and (c). It can be seen that for harmonic orders >35 only 2%–5% of the achievable XUV power in the cavity are accessible after output-coupling (figure 3(b), gray). In contrast, the optimum OCE, i.e. the highest OCE reached within the scanned p/z range, reaches up to 7 times higher values (figure 3(b), black). Consequently, optimum OCE is not reached at the same p/z values as optimum generated power.

As noted above, optimum output coupling efficiency is reached far before the focus (figure 2(d)). On the other hand, for higher harmonic orders, the optimum generation efficiency is reached for target positions around the focus (figure 2(c)). Hence, the optimum out-coupled XUV power is a result of a trade-off between generation efficiency and output-coupling efficiency, determined by the position of the gas target. For the parameters used here, geometric output coupling reduces the XUV power attainable outside the cavity by one to two orders of magnitude compared to the optimum power generated inside the cavity and therefore constitutes an important contribution to the overall conversion efficiency.

4.4. Physical background

4.4.1. Output coupling efficiency. As observed above, the output coupling efficiency depends on the gas target position, and target positions before the focus are beneficial for harmonic orders ≥ 29 . This can be attributed to a decrease of the harmonic beam divergence at these positions, as can be seen in figure 3(c), where the beam profiles on the output coupling mirror for different target positions are compared for the 33rd harmonic at a backing pressure of 8 bar.

To understand the physical reason for this behavior, we derive a simple analytical formula for the divergence of the harmonic beam. To this end, we assume a simple power law for the intensity dependence of the single-atom dipole response and a linear intensity-dependent phase, and approximate the harmonic beam as a Gaussian beam (see appendix C):

$$\mathcal{A}_H = \frac{1}{N_H} \frac{(\hat{z}^3 + \hat{z} + 2\gamma)^2 + (1 + \hat{z}^2)^2 \delta}{(1 + \hat{z}^2)^3}. \quad (1)$$

Here, \mathcal{A}_H is the harmonic beam area relative to the driving beam area on the output coupling mirror, $\hat{z} = z/z_R$ is

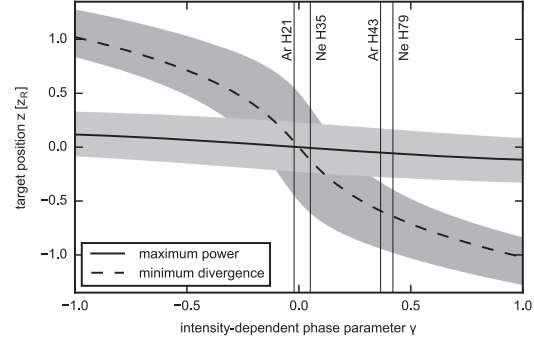


Figure 4. Optimum target position for generated XUV power (solid line) and output coupling (dashed line) versus the intensity-dependent phase parameter γ . The corridors mark the regions over which the power and the harmonic beam area deviate by less than a factor of 2 from the optimum values.

the scaled gas target position with the Rayleigh range z_R , and N_H , δ and γ are parameters describing the driving-intensity dependence of the single-atom dipole amplitude (N_H , $\delta = N_H^2/H^2$) and phase (γ) for a harmonic order H (see appendix B). The parameter $\gamma = \alpha_H I_f/H$ is referred to as *intensity-dependent phase parameter* in the following and depends on the intensity-dependent dipole phase gradient α_H and the intensity I_f in the focus.

Then, the output coupling efficiency can be written as

$$\epsilon = 1 - \exp(-2\mathcal{A}_o/\mathcal{A}_H), \quad (2)$$

where \mathcal{A}_o is the hole area relative to the driving beam area on the output coupling mirror. Figure 3(b) shows the agreement between the output coupling efficiency computed with this analytical formula and the values obtained from the simulations.

In good approximation, the relative harmonic beam area \mathcal{A}_H reaches its minimum (and thus, the output coupling efficiency ϵ its optimum) for gas target positions \hat{z}_{OC} where wave-front curvature $1/R_H$ of the harmonic beam in the plane of the gas target vanishes. This curvature comprises a contribution from the driving beam curvature $1/R$ and a contribution $1/R_\phi$ from the transverse harmonic phase that arises from the radially dependent driving field intensity (for details, see appendix C). In an intuitive picture, optimum output coupling efficiency is thus reached when the intensity-dependent harmonic phase balances out the wave-front curvature of the driving beam.

In figure 4, we show both contributions for the 33rd harmonic. As can be seen, the curvature $1/R_\phi$ due to the intensity-dependent harmonic phase is always positive for this harmonic order. Therefore, a vanishing total curvature $1/R_H$ is only possible at target positions before the focus, where the curvature $1/R$ of the driving beam is negative. Figures 3(e) and (f) show the resulting relative harmonic beam area and output coupling efficiency, respectively. This explains the decrease of the harmonic divergence for target positions before the focus, as observed in the simulated data (figure 3(c)).

4.4.2. Generated XUV power. With the same assumptions on the intensity-dependence of the single-atom dipole response and neglecting reabsorption as well as the Kerr and plasma contributions, we can also derive an analytical formula for the dependence of the generated XUV power on the gas target position. To this end, the phase matching pressure is calculated from the linear phase mismatch, the Gouy phase and the intensity-dependent dipole phase. Then, the harmonic power is estimated by considering the number of emitters and the dependence on the driving field intensity (see appendix D). For the parameters of the experiment, this formula predicts that optimum XUV power is generated for target positions very close to the focus ($|z/z_R| < 0.2$). For comparison, the numerical simulations predict optimum XUV power around $z/z_R = -0.25$ for all harmonics (see figure 2(c)).

4.4.3. Trade-off. The target position \hat{z}_{OC} for optimum output coupling as well as the position \hat{z}_{gen} for the optimum generated XUV power are functions of the parameters N_H , δ and γ . However, their dependence on N_H and δ is weak and can be neglected (see appendices C and D). Both optimum positions versus the intensity-dependent phase parameter γ are depicted in figure 4, alongside with corridors showing the \hat{z} ranges where the relative harmonic beam area doubles and the generated XUV power drops two half of the maximum, respectively. It becomes apparent that a trade-off detrimental for the accessible XUV power must be expected when the value of the intensity-dependent phase parameter deviates too much from zero.

Vertical lines in figure 4 mark the γ parameters for generation of harmonics in argon at a peak intensity of $1.5 \times 10^{14} \text{ W cm}^{-2}$ in the focus and in neon at $3 \times 10^{14} \text{ W cm}^{-2}$, for a driving wavelength of 1030 nm. As observed in the simulations for argon, the trade-off manifests itself mainly for higher harmonic orders. Figure 4 confirms that this finding can be generalized to HHG in neon.

4.4.4. Optimum output coupling efficiency. To compute the minimum harmonic beam area from the parameters N_H , δ and γ , one can use the fact that $\hat{z}_{OC}^3 + \hat{z}_{OC} + 2\gamma = 0$ (see appendix C). Then, equation (1) reads

$$\mathcal{A}_H(\hat{z}_{OC}) = \frac{\delta}{N_H} (1 + \hat{z}_{OC}^2)^{-1}, \quad (3)$$

where \hat{z}_{OC} only depends on γ (see figure 4). We can use this formula to predict the optimum output coupling efficiency for HHG in neon at a peak intensity of $3 \times 10^{14} \text{ W cm}^{-2}$. While γ and thus \hat{z}_{OC} are similar for neon and argon (figure 4), the prefactor $\frac{\delta}{N_H}$ tends to be much smaller in neon, e.g. by a factor of 4 for near-cutoff harmonics (see table B1). Formula (2) predicts output coupling efficiencies around 20% for near-cutoff harmonics in argon. Using the same geometry, optimum output coupling efficiencies up to 50% are expected in neon.

5. Conclusions

In conclusion, we employed a numerical model to reproduce and explain the main features observed in a cavity-enhanced

HHG experiment where the parameters relevant for output coupling and phase matching (backing pressure and gas target position) were systematically scanned. We disentangled the output coupling efficiency from reabsorption, phase matching and the microscopic efficiency with this model, unveiling a trade-off between XUV generation efficiency and output coupling, where the former reaches its optimum values when the gas target is positioned near the focus of the driving beam and the latter favors positions before the focus for the near-cutoff harmonic orders. Reducing the accessible XUV power by up to two orders of magnitude compared to the XUV power produced inside the cavity for the parameters of the studied experiment, we identified this trade-off as an important contribution to the overall conversion efficiency of cavity-based XUV sources with geometric output coupling. We derived an approximate formula for the divergence of the intracavity harmonic beam as a function of gas target position, driving intensity, harmonic order and focusing geometry and explained the physical mechanism behind the observed trade-off. This allowed us to generalize our findings towards HHG with higher photon energies, where a higher optimum output coupling efficiency, but a similar trade-off is expected.

The insights gained in this study provide a quantitative connection between the observable, out-coupled XUV spectrum and the spatial and spectral features of the intracavity macroscopic nonlinear response. On the one hand, together with a thorough understanding of plasma-related limitations, this provides a holistic picture of the different contributions to the overall conversion efficiency and can offer a route towards tapping the full potential of cavity-based XUV sources.

The presented numerical model can be used to investigate alternative geometric output coupling methods, e.g. using quasi-imaging [21, 22] or tailored TEM₀₁ modes [20, 31] which promise significantly higher output coupling efficiencies because they permit larger diameters for the output coupling openings thanks to on-axis minima on the mirrors. This may lead to highly efficient cavity-enhanced HHG sources, which will benefit the fields of coincidence spectroscopy, photo-electron spectroscopy/nanoscopy and frequency-comb spectroscopy. On the other hand, the link between the intracavity and the out-coupled XUV can also open up new fields of application, such as HHG spectroscopy at multi-10 MHz repetition rates [32].

Acknowledgments

This research was supported by the Fraunhofer Society/Max-Planck Society cooperation ‘MEGAS’. We are grateful to Nikolai Lilienfein and Johannes Weitenberg for helpful discussions.

Appendix A. Comparison of conversion efficiencies

To compare the record overall conversion efficiencies (driving power P_{in} before enhancement to accessible XUV power

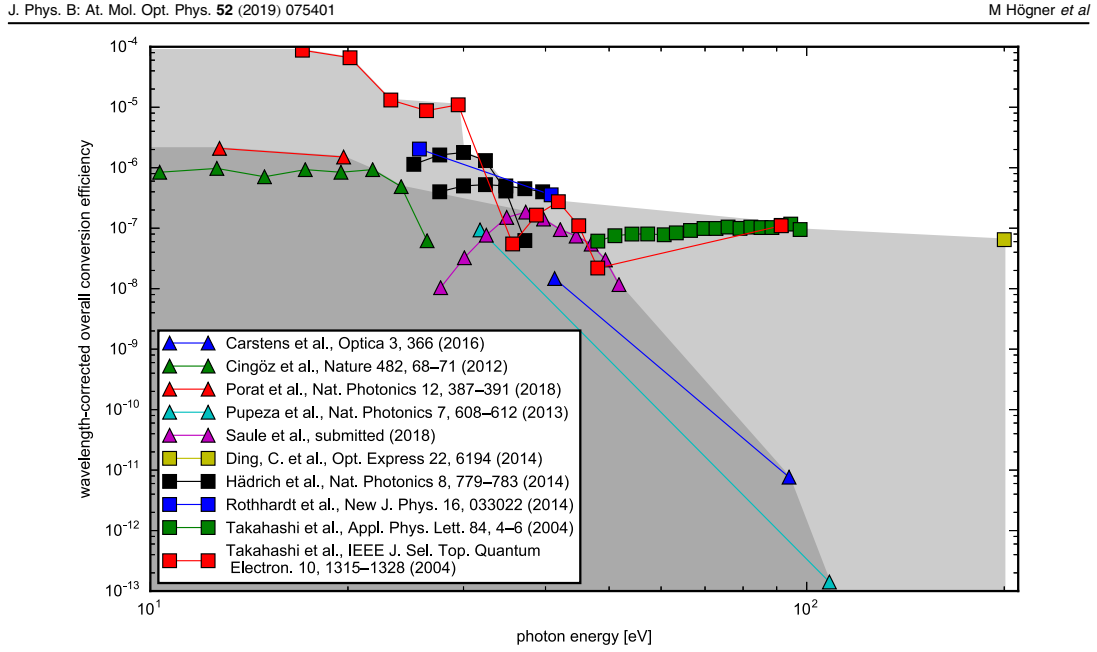


Figure A1. Wavelength-corrected overall conversion efficiencies (driving power before enhancement to accessible XUV power) of cavity-enhanced HHG systems (triangles) and single-pass HHG systems driven by freely propagating Gaussian beams (squares). The shaded areas mark the record conversion efficiencies reached with cavity-based (dark-gray) and single-pass (light-gray) sources.

P_{XUV}) achieved with cavity-based versus single-pass HHG systems, we considered the state-of-the-art sources summarized in [33, figure 3], considering only systems using a freely propagating Gaussian driving beam, and incorporated the results of [16, 17, 34, 35]. To allow for a comparison between systems with different driving wavelengths, we factored out the wavelength scaling of the HHG efficiency with roughly a power of six [36], resulting in a wavelength-corrected conversion efficiency $P_{\text{XUV}}/P_{\text{in}}(\lambda/1030 \text{ nm})^6$.

Figure A1 shows the obtained conversion efficiencies versus the generated photon energies. So far, the overall conversion efficiencies of EC-based sources (dark-gray area) have remained below that of single-pass systems (light-gray area). Keeping in mind that the XUV power generated by HHG in gas targets can scale linearly with the driving power [37], this indicates that inefficiencies in the intracavity XUV generation or the output coupling counteract the typical enhancements of the driving power by several orders of magnitude achieved in ECs.

Appendix B. Analytical model for the single-atom dipole response

For the derivation of the harmonic divergence formula (1) and the generation efficiency formula (D.5), we approximate

the intensity-dependence of the single-atom dipole response $d_H(I)$ for a harmonic order H by a power-law for the absolute value and a linear dependence for the phase (compare e.g. [30]):

$$d_H(I) \propto |I|^{N_H/2} \exp(i\alpha_H I + iH \arg E), \quad (\text{B.1})$$

where $I = \epsilon_0 c/2|E|^2$ is the intensity of the driving field E and N_H and α_H are fitting parameters depending on atomic species, harmonic order, driving field wavelength and on the driving field intensity. We determine α_H for the short trajectory with a Gabor-type analysis as described in [38], providing the intensity-dependent single-atom dipole response computed numerically using a saddle-point approximation [39], which has the advantage of clear separation between trajectories. The exponents N_H were determined by a power-law fit to the intensity-dependent single-atom dipole response in the cutoff region, computed numerically with the Lewenstein formula [27]. The excursion time was limited to 0.66 periods of the driving field to consider only the short trajectory. The resulting parameters for argon and neon are tabulated in table B1, together with the derived quantities $\delta = N_H^2/H^2$ and $\gamma = I\alpha_H/H$, and agree reasonably with the measured values of [30].

Table B1. Parameters used for the analytical model of the single-atom dipole response.

Atom	I (W cm ⁻²)	H	α_H (cm ² W ⁻¹)	N_H	γ	δ	δ/N_H
Ar	1.5×10^{14}	21	-0.3×10^{14}	8.06	-0.02	0.15	0.018
Ar	1.5×10^{14}	23	0.3×10^{14}	8.91	0.02	0.15	0.017
Ar	1.5×10^{14}	25	1.2×10^{14}	9.85	0.07	0.16	0.016
Ar	1.5×10^{14}	27	1.8×10^{14}	10.85	0.10	0.16	0.015
Ar	1.5×10^{14}	29	2.7×10^{14}	11.67	0.14	0.16	0.014
Ar	1.5×10^{14}	31	3.6×10^{14}	12.66	0.17	0.17	0.013
Ar	1.5×10^{14}	33	4.5×10^{14}	13.53	0.20	0.17	0.012
Ar	1.5×10^{14}	35	5.4×10^{14}	14.41	0.23	0.17	0.012
Ar	1.5×10^{14}	37	6.3×10^{14}	15.24	0.25	0.17	0.011
Ar	1.5×10^{14}	39	7.8×10^{14}	16.01	0.30	0.17	0.011
Ar	1.5×10^{14}	41	9.0×10^{14}	16.68	0.33	0.17	0.010
Ar	1.5×10^{14}	43	10.5×10^{14}	16.71	0.36	0.15	0.009
Ne	3.0×10^{14}	35	0.6×10^{14}	13.47	0.05	0.15	0.011
Ne	3.0×10^{14}	37	0.9×10^{14}	14.26	0.07	0.15	0.010
Ne	3.0×10^{14}	39	1.2×10^{14}	15.29	0.09	0.15	0.010
Ne	3.0×10^{14}	41	1.5×10^{14}	16.23	0.11	0.16	0.010
Ne	3.0×10^{14}	43	1.8×10^{14}	17.11	0.13	0.16	0.009
Ne	3.0×10^{14}	45	2.1×10^{14}	18.16	0.14	0.16	0.009
Ne	3.0×10^{14}	47	2.4×10^{14}	19.02	0.15	0.16	0.009
Ne	3.0×10^{14}	49	3.0×10^{14}	19.68	0.18	0.16	0.008
Ne	3.0×10^{14}	51	3.3×10^{14}	20.76	0.19	0.17	0.008
Ne	3.0×10^{14}	53	3.6×10^{14}	20.54	0.20	0.15	0.007
Ne	3.0×10^{14}	55	4.2×10^{14}	20.79	0.23	0.14	0.007
Ne	3.0×10^{14}	57	4.5×10^{14}	20.25	0.24	0.13	0.006
Ne	3.0×10^{14}	59	5.1×10^{14}	19.93	0.26	0.11	0.006
Ne	3.0×10^{14}	61	5.7×10^{14}	20.18	0.28	0.11	0.005
Ne	3.0×10^{14}	63	6.0×10^{14}	19.25	0.28	0.09	0.005
Ne	3.0×10^{14}	65	6.6×10^{14}	19.77	0.30	0.09	0.005
Ne	3.0×10^{14}	67	7.2×10^{14}	19.13	0.32	0.08	0.004
Ne	3.0×10^{14}	69	7.8×10^{14}	18.63	0.34	0.07	0.004
Ne	3.0×10^{14}	71	8.4×10^{14}	18.41	0.35	0.07	0.004
Ne	3.0×10^{14}	73	9.0×10^{14}	18.22	0.37	0.06	0.003
Ne	3.0×10^{14}	75	9.6×10^{14}	16.75	0.38	0.05	0.003
Ne	3.0×10^{14}	77	10.2×10^{14}	17.38	0.40	0.05	0.003
Ne	3.0×10^{14}	79	11.1×10^{14}	16.25	0.42	0.04	0.003

Appendix C. Formula for the XUV divergence

In a similar approach to [30], we approximate the harmonic field as a Gaussian beam by using a Taylor expansion of the radial intensity-dependent phase. In contrast to [30], we do not assume that the gas target is located in the focal plane.

The driving field $E(r)$ at the longitudinal position z of the gas target is given by

$$E(r) \propto \exp\left(-\frac{r^2}{w^2} - ik\frac{r^2}{2R}\right), \quad (\text{C.1})$$

where r is the radial coordinate, $k = 2\pi/\lambda$ the wave number, $w = w_0\sqrt{1 + z^2/z_R^2}$ the beam radius, R the wave-front radius of curvature, w_0 is the beam waist and $z_R = \pi w_0^2/\lambda$ is the Rayleigh range.

In the limit of a small gas target diameter, the harmonic field E_H in the exit plane of the gas target is proportional to the dipole response d_H , which, using (B.1) and (C.1), can be written as

$$\begin{aligned} E_H(r) &\propto d_H(r) \propto |I|^{N_H/2} \exp(i\alpha_H I(r) + iH \arg E(r)) \\ &\propto |E(r)|^{N_H} \cdot \exp\left(-ikH\frac{r^2}{2R} + i\alpha_H I(r)\right) \\ &= \exp(-r^2/w^2)^{N_H} \cdot \exp\left(-ikH\frac{r^2}{2R} \right. \\ &\quad \left. + i\alpha_H I_0 \exp(-2r^2/w^2)\right) \\ &\approx \exp(-N_H r^2/w^2) \cdot \exp\left(-ikH\frac{r^2}{2R} \right. \\ &\quad \left. + i\alpha_H I_0(1 - 2r^2/w^2)\right) \\ &\propto \exp(-N_H r^2/w^2) \cdot \exp\left(-ikH\frac{r^2}{2R} - i\alpha_H I_0 2r^2/w^2\right) \\ &= \exp(-N_H r^2/w^2) \cdot \exp\left(-ikH\frac{r^2}{2} \left(\frac{1}{R} + \frac{4\alpha_H I_0}{kHw^2}\right)\right) \\ &= \exp(-r^2/w_H^2) \cdot \exp\left(-\frac{ik_H r^2}{2R_H}\right), \end{aligned} \quad (\text{C.2})$$

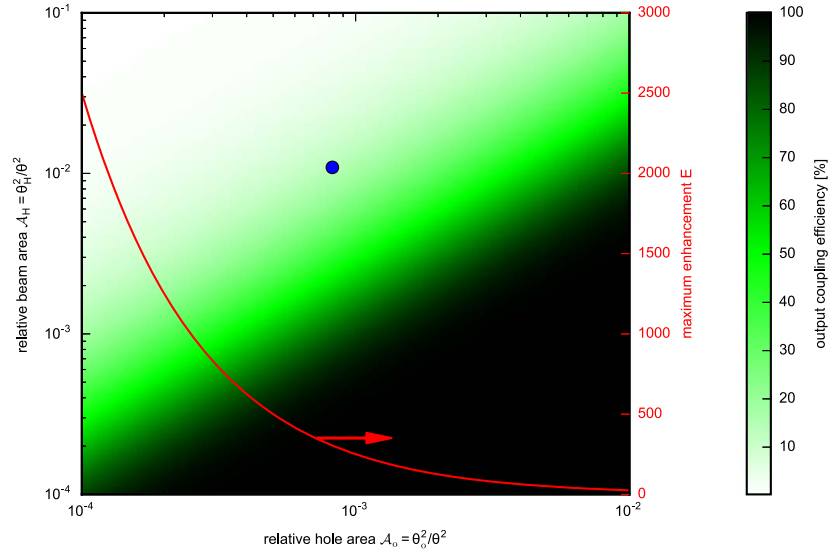


Figure C1. Dependence of the output coupling efficiency (color scale) on the relative hole area \mathcal{A}_o and relative harmonic beam area \mathcal{A}_H . The red line shows the theoretical maximum power enhancements possible for a given relative hole area. The dot marks the parameters of the 33rd harmonic in the simulated experiment.

where we defined the harmonic beam radius

$$w_H := w / \sqrt{N_H}, \quad (\text{C.3})$$

the harmonic radius of curvature

$$R_H := \frac{1}{1/R + 1/R_\phi}, \quad (\text{C.4})$$

the radius of curvature due to the intensity-dependent harmonic phase

$$R_\phi := \frac{k_H w^2}{4\alpha_H I_0}, \quad (\text{C.5})$$

the on-axis intensity

$$I_0 := I(0) = I_f (1 + z^2/z_R^2)^{-1}, \quad (\text{C.6})$$

where I_f is the intensity in the focus and the harmonic wave number

$$k_H := Hk. \quad (\text{C.7})$$

To determine the Rayleigh length $z_{R,H}$ of this Gaussian beam, we use the complex beam parameter q_H :

$$\begin{aligned} z_{R,H} &= \Im(q_H) = \Im\left(\frac{1}{q_H^{-1}}\right) = \Im\left(\frac{1}{R_H^{-1} - i2k_H^{-1}w_H^{-2}}\right) \\ &= \Im\left(\frac{R_H^{-1} + i2k_H^{-1}w_H^{-2}}{R_H^{-2} + 4k_H^{-2}w_H^{-4}}\right) = \frac{2R_H^2 k_H w_H^2}{k_H^2 w_H^4 + 4R_H^2}. \end{aligned} \quad (\text{C.8})$$

The divergence of a harmonic beam can be computed from its Rayleigh length like

$$\theta_H = \sqrt{\frac{2}{k_H z_{R,H}}} = \sqrt{\frac{k_H^2 w_H^4 + 4R_H^2}{R_H^2 k_H^2 w_H^2}} = \sqrt{\frac{w_H^2}{R_H^2} + \frac{4}{k_H^2 w_H^2}}. \quad (\text{C.9})$$

For a given hole radius r_o and distance Δz between output coupling mirror and focus, one can then compute the fraction of harmonic power transmitted through the hole, i.e. the output coupling efficiency ϵ . Introducing the relative hole area $\mathcal{A}_o := \theta_o^2/\theta^2$, the relative harmonic beam size $\mathcal{A}_H := \theta_H^2/\theta^2$ and the harmonic beam diameter $w_{M,H} := \Delta z \theta_H$ on the output coupling mirror, where $\theta = \sqrt{\frac{2}{k_R}}$ is the driving beam divergence and $\theta_o := r_o/\Delta z$ is the angle occupied by one hole radius, we can use the well-known formula for the fraction of power of a Gaussian beam transmitted through an aperture:

$$\begin{aligned} \epsilon &= 1 - \exp(-2r_o^2/w_{M,H}^2) = 1 - \exp\left(-2\frac{\theta_o^2 \Delta z^2}{\Delta z^2 \theta_H^2}\right) \\ &= 1 - \exp\left(-2\frac{\theta_o^2}{\theta^2} \frac{\theta^2}{\theta_H^2}\right) = 1 - \exp(-2\mathcal{A}_o/\mathcal{A}_H). \end{aligned} \quad (\text{C.10})$$

Figure C1 shows the dependence of the output coupling efficiency ϵ on \mathcal{A}_o and \mathcal{A}_H . Using a computer algebra system

to substitute the expressions defined above, it can be verified that

$$\mathcal{A}_H = \frac{1}{N_H} \frac{(\hat{z}^3 + \hat{z} + 2\gamma)^2 + (1 + \hat{z}^2)^2 \delta}{(1 + \hat{z}^2)^3}, \quad (\text{C.11})$$

where $\hat{z} = z/z_R$ is the scaled gas target position and $\gamma := \alpha_H I_f / H$ and $\delta := N_H^2 / H^2$. The term $\hat{z}^3 + \hat{z} + 2\gamma$ has exactly one real root \hat{z}_{OC} because its derivative is positive everywhere, and this root corresponds to the target positions for which $1/R_H$ vanishes (this is also easily verified by using a computer algebra system).

We numerically determined the minima of $\mathcal{A}_H(\hat{z})$ for values of γ from -1 to 1 and values of δ in the range tabulated in table B1 and found that the minima deviate by less than 0.04 from \hat{z}_{OC} . Consequently, the position of the minimum has no strong dependence on δ and \hat{z}_{OC} can be regarded as an excellent approximation for the optimum gas target position for output coupling.

Figure 4 shows the dependence of \hat{z}_{OC} on γ . The corridor marks the region over which \mathcal{A}_H deviates by less than a factor of 2 from the optimum value, assuming $\delta = 0.17$ (value for 33rd harmonic in argon). The diameter of the corridor increases with δ and remains between 0.20 and 1.0 for the tabulated values of δ .

Appendix D. Formula for the XUV power

Neglecting the plasma and Kerr phase, the on-axis phase of the driving Gaussian beam is

$$\phi_1(z) = -nkz + \underbrace{\arctan(z/z_R)}_{\text{Gouy phase}}, \quad (\text{D.1})$$

where n is the refractive index at the driving wavelength. Approximating the intensity-dependent harmonic dipole phase $\phi(I)$ by a linear dependence (see appendix B), the total harmonic dipole phase is then

$$\phi_H(z) = H\phi_1(z) + \underbrace{\alpha_H I(z)}_{\text{intensity-dependent phase}} + C. \quad (\text{D.2})$$

This yields an effective wave number of

$$\begin{aligned} k_{\text{eff}} &= -\partial_z \phi_H(z) = -H\partial_z \phi_1(z) - \alpha_H \partial_z I(z) \\ &= -H(-nk + \partial_z \arctan(z/z_R)) \\ &\quad - \alpha_H I_f \partial_z (1 + z^2/z_R^2)^{-1} \\ &= nkH - H \frac{1/z_R}{1 + z^2/z_R^2} + \alpha_H I_f (1 + z^2/z_R^2)^{-2} 2z/z_R^2, \end{aligned} \quad (\text{D.3})$$

where I_f is the peak intensity in the focus. Good phase matching is reached for $k_{\text{eff}} \approx n_H k H$, where H is the harmonic order and n_H is the refractive index at the

corresponding wavelength. $\Delta k_H = k_{\text{eff}} - n_H k H$ quantifies the phase mismatch and should vanish:

$$\begin{aligned} \Delta k_H &= Hk(n - n_H) - H \frac{1/z_R}{1 + z^2/z_R^2} \\ &\quad + \alpha_H I_f (1 + z^2/z_R^2)^{-2} 2z/z_R^2 \stackrel{!}{=} 0 \\ \Leftrightarrow Hk \Delta n_{\text{std}} \frac{\rho}{\rho_{\text{std}}} &= H \frac{1/z_R}{1 + z^2/z_R^2} \\ &\quad - \alpha_H I_f (1 + z^2/z_R^2)^{-2} 2z/z_R^2 \\ \Rightarrow \rho &\propto \frac{1}{1 + \hat{z}^2} - 2\gamma \frac{\hat{z}}{(1 + \hat{z}^2)^2}. \end{aligned} \quad (\text{D.4})$$

Here, we defined $\hat{z} := z/z_R$ and $\gamma := \frac{\alpha_H I_f}{H}$ (compare appendix C) and used $n - n_H = \frac{\rho}{\rho_{\text{std}}} \Delta n_{\text{std}}$, where ρ is the density in the gas target, ρ_{std} is the density at standard conditions and Δn_{std} the refractive index difference at standard conditions.

To estimate the harmonic power P_H generated in a harmonic order H at a certain position of the nozzle, we assume generation at the phase-matching density as given by (D.4) and that the amplitude E_H of the emitted harmonic field is proportional to the number of emitters (density \times mode size). The intensity-dependence of the single-atom dipole response is approximated by a power law (see appendix B), yielding

$$\begin{aligned} P_H &\propto E_H^2 \propto (\rho w^2 I^{N_H/2})^2 \propto (\rho(1 + \hat{z}^2)(1 + \hat{z}^2)^{-N_H/2})^2 \\ &= \rho^2 (1 + \hat{z}^2)^{2 - N_H}. \end{aligned} \quad (\text{D.5})$$

Using (D.5) and (D.4), we can estimate the generated harmonic power for a given gas target position \hat{z} and parameters γ and N_H . This allows us to numerically compute the target position for optimum power and the corridor over which P_H deviates by less than a factor of 2 from the optimum value (figure 4, for $N_H = 13.53$).

The optimum value \hat{z}_{gen} remains close to zero, deviating by less than 0.18 for values of γ from -1 to 1 and values of N_H in the range tabulated in table B1. The diameter of the corridor decreases slightly with N_H and remains between 0.34 and 0.60 .

ORCID iDs

M Högner  <https://orcid.org/0000-0002-6243-802X>
I Pupeza  <https://orcid.org/0000-0001-8422-667X>

References

- [1] McPherson A, Gibson G, Jara H, Johann U, Luk T S, McIntyre I A, Boyer K and Rhodes C K 1987 Studies of multiphoton production of vacuum-ultraviolet radiation in the rare gases *J. Opt. Soc. Am. B* **4** 595–601
- [2] Ferray M, L'Huillier A, Li X F, Lompre L A, Mainfray G and Manus C 1988 Multiple-harmonic conversion of 1064 nm

- radiation in rare gases *J. Phys. B: At. Mol. Opt. Phys.* **21** L31–5
- [3] Krausz F and Ivanov M 2009 Attosecond physics *Rev. Mod. Phys.* **81** 163–234
- [4] Krausz F and Stockman M I 2014 Attosecond metrology: from electron capture to future signal processing *Nat. Photon.* **8** 205–13
- [5] Constant E, Garzella D, Breger P, Mével E, Dorrer C, Le Blanc C, Salin F and Agostini P 1999 Optimizing high harmonic generation in absorbing gases: model and experiment *Phys. Rev. Lett.* **82** 1668–71
- [6] Rothhardt J *et al* 2014 53W average power few-cycle fiber laser system generating soft x rays up to the water window *Opt. Lett.* **39** 5224
- [7] Rothhardt J *et al* 2016 High-repetition-rate and high-photon-flux 70 eV high-harmonic source for coincidence ion imaging of gas-phase molecules *Opt. Express* **24** 18133
- [8] Lorek E, Larsen E W, Heyl C M, Carlström S, Paleček D, Zigmantas D and Mauritsson J 2014 High-order harmonic generation using a high-repetition-rate turnkey laser *Rev. Sci. Instrum.* **85** 123106
- [9] Hädrich S, Klenke A, Rothhardt J, Krebs M, Hoffmann A, Pronin O, Pervak V, Limpert J and Tünnermann A 2014 High photon flux table-top coherent extreme-ultraviolet source *Nat. Photon.* **8** 779–83
- [10] Chiang C-T, Huth M, Trützscher A, Kiel M, Schumann F O, Kirschner J and Widdra W 2015 Boosting laboratory photoelectron spectroscopy by megahertz high-order harmonics *New J. Phys.* **17** 013035
- [11] Mills A K, Zhdanovich S, Sheyerman A, Levy G, Damascelli A and Jones D J 2015 An XUV source using a femtosecond enhancement cavity for photoemission spectroscopy *Advances in X-ray Free-Electron Lasers Instrumentation III* 95121 *SPIE Optics + Optoelectronics (Proc. SPIE)* 9512
- [12] Corder C, Zhao P, Bakalis J, Li X, Kershner M D, Muraca A R, White M G and Allison T K 2018 Ultrafast extreme ultraviolet photoemission without space charge *Struct. Dyn.* **5** 054301
- [13] Ozawa A and Kobayashi Y 2013 Vuv frequency-comb spectroscopy of atomic xenon *Phys. Rev. A* **87** 022507
- [14] Cingöz A, Yost D C, Allison T K, Ruehl A, Fermann M E, Hartl I and Ye J 2012 Direct frequency comb spectroscopy in the extreme ultraviolet *Nature* **482** 68–71
- [15] Pupeza I *et al* 2013 Compact high-repetition-rate source of coherent 100 eV radiation *Nat. Photon.* **7** 608–12
- [16] Carstens H *et al* 2016 High-harmonic generation at 250 MHz with photon energies exceeding 100 eV *Optica* **3** 366
- [17] Saule T *et al* 2019 High-flux ultrafast extreme-ultraviolet photoemission spectroscopy at 18.4 MHz pulse repetition rate *Nat. Commun.* **10** 458
- [18] Porat G, Heyl C M, Schoun S B, Benko C, Dörre N, Corwin K L and Ye J 2018 Phase-matched extreme-ultraviolet frequency-comb generation *Nat. Photon.* **12** 387–91
- [19] Saule T, Högner M, Lilienfein N, de Vries O, Plötner M, Yakovlev V S, Karpowicz N, Limpert J and Pupeza I 2018 Cumulative plasma effects in cavity-enhanced high-order harmonic generation in gases *APL Photonics* **3** 101301
- [20] Moll K D, Jones R J and Ye J 2006 Output coupling methods for cavity-based high-harmonic generation *Opt. Express* **14** 8189
- [21] Pupeza I *et al* 2014 Cavity-enhanced high-harmonic generation with spatially tailored driving fields *Phys. Rev. Lett.* **112** 103902
- [22] Weitenberg J, Rußbüldt P, Pupeza I, Udem T, Hoffmann H-D and Poprawe R 2015 Geometrical on-axis access to high-finesse resonators by quasi-imaging: a theoretical description *J. Opt.* **17** 025609
- [23] Allison T K, Cingöz A, Yost D C and Ye J 2011 Extreme nonlinear optics in a femtosecond enhancement cavity *Phys. Rev. Lett.* **107** 183903
- [24] Holzberger S *et al* 2015 Femtosecond enhancement cavities in the nonlinear regime *Phys. Rev. Lett.* **115** 023902
- [25] Högner M, Tosa V and Pupeza I 2017 Generation of isolated attosecond pulses with enhancement cavities—a theoretical study *New J. Phys.* **19** 033040
- [26] Geissler M, Tempea G, Scrinzi A, Schnürer M, Krausz F and Brabec T 1999 Light propagation in field-ionizing media: extreme nonlinear optics *Phys. Rev. Lett.* **83** 2930
- [27] Lewenstein M, Balcou P, Ivanov M Y, L’huillier A and Corkum P B 1994 Theory of high-harmonic generation by low-frequency laser fields *Phys. Rev. A* **49** 2117
- [28] Scoles G 1988 *Atomic and Molecular Beam Methods* vol 1 (Oxford: Oxford University Press)
- [29] Voelz D G 2011 *Computational Fourier Optics—A MATLAB® Tutorial (Tutorial Texts in Optical Engineering vol 89)* (Bellingham, WA: SPIE) (<https://doi.org/10.1117/3.858456>)
- [30] Carlström S *et al* 2016 Spatially and spectrally resolved quantum path interference with chirped driving pulses *New J. Phys.* **18** 123032
- [31] Högner M, Saule T, Lilienfein N, Pervak V and Pupeza I 2018 Tailoring the transverse mode of a high-finesse optical resonator with stepped mirrors *J. Opt.* **20** 024003
- [32] Marangos J P 2016 Development of high harmonic generation spectroscopy of organic molecules and biomolecules *J. Phys. B: At. Mol. Opt. Phys.* **49** 132001
- [33] Rothhardt J, Tadesse G K, Eschen W and Limpert J 2018 Table-top nanoscale coherent imaging with XUV light *J. Opt.* **20** 113001
- [34] Rothhardt J, Krebs M, Hädrich S, Demmler S, Limpert J and Tünnermann A 2014 Absorption-limited and phase-matched high harmonic generation in the tight focusing regime *New J. Phys.* **16** 033022
- [35] Takahashi E J, Nabekawa Y and Midorikawa K 2004 Low-divergence coherent soft x-ray source at 13 nm by high-order harmonics *Appl. Phys. Lett.* **84** 4–6
- [36] Shiner A D *et al* 2009 Wavelength scaling of high harmonic generation efficiency *Phys. Rev. Lett.* **103** 073902
- [37] Heyl C M *et al* 2016 Scale-invariant nonlinear optics in gases *Optica* **3** 75
- [38] Balcou P, Dederichs A S, Gaarde M B and L’huillier A 1999 Quantum-path analysis and phase matching of high-order harmonic generation and high-order frequency mixing processes in strong laser fields *J. Phys. B: At. Mol. Opt. Phys.* **32** 2973
- [39] Ivanov M Y, Brabec T and Burnett N 1996 Coulomb corrections and polarization effects in high-intensity high-harmonic emission *Phys. Rev. A* **54** 742–5

Chapter **4**

Toward a Cavity-Enhanced High-Harmonic
Lighthouse

4.1 Generation of Isolated Attosecond Pulses with Enhancement Cavities – a Theoretical Study

as published in

New Journal of Physics (2017)

[86]

by

Maximilian Högnér, Valer Tosa, and Ioachim Pupeza

Contributions I developed the 3D model, carried out the simulations and theoretical considerations, and wrote most of the manuscript.



CrossMark

PAPER

Generation of isolated attosecond pulses with enhancement cavities
—a theoretical study

OPEN ACCESS

RECEIVED

25 December 2016

REVISED

15 February 2017

ACCEPTED FOR PUBLICATION

27 February 2017

PUBLISHED

29 March 2017

Original content from this work may be used under the terms of the [Creative Commons Attribution 3.0 licence](https://creativecommons.org/licenses/by/4.0/).

Any further distribution of this work must maintain attribution to the author(s) and the title of the work, journal citation and DOI.

M Högner^{1,2,4}, V Tosa³ and I Pupeza^{1,2}¹ Max-Planck-Institut für Quantenoptik, Hans-Kopfermann-Straße 1, D-85748 Garching, Germany² Ludwig-Maximilians-Universität München, Am Coulombwall 1, D-85748 Garching, Germany³ National Institute for R&D of Isotopic and Molecular Technologies, Donath 67-103, 400293 Cluj Napoca, Romania⁴ Author to whom any correspondence should be addressed.E-mail: mhoegner@mpq.mpg.de and ioachim.pupeza@mpq.mpg.de**Keywords:** enhancement cavity, high harmonic generation, isolated attosecond pulses, gating methods, output coupling**Abstract**

The generation of extreme-ultraviolet (XUV) isolated attosecond pulses (IAPs) has enabled experimental access to the fastest phenomena in nature observed so far, namely the dynamics of electrons in atoms, molecules and solids. However, nowadays the highest repetition rates at which IAPs can be generated lies in the kHz range. This represents a rather severe restriction for numerous experiments involving the detection of charged particles, where the desired number of generated particles per shot is limited by space charge effects to ideally one. Here, we present a theoretical study on the possibility of efficiently producing IAPs at multi-MHz repetition rates via cavity-enhanced high-harmonic generation (HHG). To this end, we assume parameters of state-of-the-art Yb-based femtosecond laser technology to evaluate several time-gating methods which could generate IAPs in enhancement cavities. We identify polarization gating and a new method, employing non-collinear optical gating in a tailored transverse cavity mode, as suitable candidates and analyze these via extensive numerical modeling. The latter, which we dub transverse mode gating (TMG) promises the highest efficiency and robustness. Assuming $0.7 \mu\text{J}$, 5-cycle pulses from the seeding laser and a state-of-the-art enhancement cavity, we show that TMG bares the potential to generate IAPs with photon energies around 100 eV and a photon flux of at least $10^8 \text{ photons s}^{-1}$ at repetition rates of 10 MHz and higher. This result reveals a roadmap towards a dramatic decrease in measurement time (and, equivalently, an increase in the signal-to-noise ratio) in photoelectron spectroscopy and microscopy. In particular, it paves the way to combining attosecond streaking with photoelectron emission microscopy, affording, for the first time, the spatially and temporally resolved observation of plasmonic fields in nanostructures. Furthermore, it promises the generation of frequency combs with an unprecedented bandwidth for XUV precision spectroscopy.

1. Introduction

Towards the end of the last century, the duration of pulses produced with modelocked lasers had approached the limits imposed by increasing material dispersion towards the ultraviolet, corresponding to just a few cycles of the carrier wave [1]. The ability to stabilize the carrier-to-envelope phase (CEP) of such pulses and to amplify them to intensities at which their electric fields rival the atomic Coulomb field allowed for the generation of extreme-ultraviolet (XUV) isolated attosecond pulses (IAPs) via the highly nonlinear process of high-harmonic generation (HHG). The first XUV-IAPs were shown in 2001 [2] and enabled experimental access to the hitherto fastest phenomena observable in real time, namely electron dynamics in atoms, molecules, solids and plasmas [1, 3].

Currently, titanium-sapphire-based (Ti:Sa) ultrashort-pulsed lasers represent the workhorse technology for experiments in attosecond physics. However, strong absorption and thermal lensing in the Ti:Sa gain medium

[4] limits the generation of high-energy ultrashort pulses to repetition rates significantly lower than 1 MHz. In particular experiments which involve the detection of charged particles would tremendously profit from IAPs at higher repetition rates: in this class of experiments, space charge effects limit the detection to ideally a single particle per shot, so that the data acquisition rate scales with the repetition rate rather than with the total photon flux. Examples include coincidence spectroscopy [5], time-resolved spectroscopy/microscopy of nano-plasmonic fields [6–8], and of ultrafast electron dynamics in nano-structured topological insulators [9], just to name a few.

Coherently stacking the pulses of a high-repetition-rate modelocked laser inside of a passive optical resonator, or enhancement cavity (EC), provides a convenient way to combine peak intensities on the order of 10^{14} W cm⁻² necessary for HHG in a gas target with pulse repetition rates of several (tens of) MHz [10, 11]. With the advent of Yb-based lasers, ECs have enabled reaching these intensities at the highest repetition rates so far, providing ultrashort pulses with the highest average powers ever demonstrated [12], and allowing for HHG with photon energies exceeding 100 eV at repetition rates as high as 250 MHz [13]. Just a few years ago, femtosecond ECs have been used for the first frequency comb spectroscopy experiments in the vacuum ultraviolet spectral region [14, 15]. Owing to recent progress concerning advanced cavity designs [12, 16], the quantitative understanding of the intracavity gas target nonlinearity [17–19], and thanks to scaling the bandwidth of ECs [20] and of phase-stable, high-power seeding laser systems [21–23], it seems feasible as from today's point of view to extend this technology to application in attosecond physics. However, state-of-the-art dielectric multilayer optics cannot cover the bandwidth necessary for single-cycle near-infrared pulses [20], which would enable the direct generation of IAPs in ECs.

In this paper we theoretically study the possibility of efficiently generating IAPs using ECs supporting pulses comprising several cycles. We identify and, employing thorough modeling, compare suitable time-gating methods and reach the conclusion that the generation of IAPs with sufficient photon flux for multi-MHz-repetition-rate experiments is within reach with current laser technology.

In section 2, we first review the state of the art of ultrashort-pulse ECs, deriving the parameter range for our study, and describe the computational model used for the simulations. In section 3, established gating methods are assessed for compatibility with the geometry, bandwidth and loss restrictions of ECs, allowing us to identify the most promising candidates. For a fair comparison of these candidates, all relevant parameters are optimized for IAPs with highest photon flux in a defined spectral range, within the technical constraints set by state-of-the-art experiments. Finally, in section 4 we compare the results of the optimized gating schemes, identify a preferred one and estimate the achievable photon flux. Section 5 concludes the paper and addresses the implications for time-resolved spectroscopy applications at high repetition rate.

2. Methods

2.1. State of the art of HHG in femtosecond ECs

HHG in ECs has been an active research topic in the last years, and many prerequisites to generate high-repetition-rate IAPs have already been established. First, XUV radiation is emitted collinearly with the strong driving beam, it needs to be separated without introducing too much loss to the driving field. Several approaches have been demonstrated, offering output coupling efficiencies between 5 and around 20% [24]. Most suitable for the generation of IAPs seem geometrical output coupling techniques [25, 26], which are power-scalable and do neither angularly disperse nor spectrally alter the XUV beam because it leaves the resonator without reflection or diffraction at an optical element.

Further, formation of plasma on the time scale of one pulse leads to a blueshift limiting the overlap of input and intracavity spectrum and thus the power enhancement. For high intensities, plasma lensing can be expected to affect the spatial overlap. This effect is quantitatively understood [17–19], and approaches to alleviate the limitations arising from the blueshift have been suggested [19].

The problems of thermal lensing, mirror damage and resonator stability were addressed in [12, 16, 27], identifying ways of progressively scaling the intracavity power. Thanks to these results, a state-of-the-art experiment demonstrated an enhancement-cavity-based 250 MHz HHG source reaching photon energies in excess of 100 eV and a photon flux of 9×10^7 photons s⁻¹ in a 2% bandwidth around 94 eV [13], which indicates that intracavity HHG has come to a point where it is potentially useful for ultrafast photoelectron spectroscopy and microscopy experiments. For this, 30 fs pulses at 1040 nm with a pulse energy of 0.7 μ J were power-enhanced a factor of 60 and focused down to $w_{0,x} \cdot w_{0,y} = (13.4 \mu\text{m})^2$, reaching peak intensities around 3×10^{14} W cm⁻² in a 200 μ m long neon gas target with an atomic density of $5n_{\text{std}}$ placed 0.5 Rayleigh ranges before the focus, where n_{std} is the atomic density of an ideal gas at IUPAC standard temperature and pressure and $w_{0,x}$ and $w_{0,y}$ are the beam waists in x and y direction. The XUV radiation was coupled out through a

120 μm -inner-diameter hole in the cavity mirror right after the focus, leaking and scattering approximately 1% of the intracavity power and coupling out 5% of the XUV radiation.

For waveform-stable IAPs, first of all it is a requirement that the enhanced comb has an offset frequency of zero. This can be accomplished by phase-stabilizing the seeding comb [22, 28, 29] and using tailored cavity mirrors [30]. Then, the XUV emission must be confined to only one attosecond burst per pulse. The bandwidth of currently available highly reflective (HR) mirrors does not allow to enhance pulses short enough to reach the single-cycle limit. However, recent work in our group [20] shows that a power enhancement of 75 is still possible with mirrors supporting pulses shorter than 20 fs at a central wavelength of 1050 nm, corresponding to 5.4 cycles.

2.2. Constraints for the theoretical study

Considering the aforementioned state-of-the-art HHG experiment [13] and the new results regarding the mirror bandwidth, for our study we assume the ability to enhance 17.5 fs pulses at 1040 nm in an empty cavity with zero offset frequency and $\leq 0.8\%$ round trip losses (corresponding to a power enhancement of 125 in the impedance-matched case). We presume that it is possible to generate phase-stable 17.5 fs pulses with a pulse energy of 0.7 μJ as seed for the EC. High-repetition-rate pulses with 17 fs and similar pulse energy have already been reported in [22].

Apart from the seeding pulse parameters and the round-trip losses, there are several other technical restrictions for intracavity HHG: the gas flowing through the nozzle deteriorates the vacuum causing XUV reabsorption amongst other effects, so there is a technical limit on the gas flux, which is proportional to $n \cdot L^2$, where n is the atomic density and L the target diameter. There is also a lower limit on the beam waist due to EC alignment sensitivity and astigmatism, and on beam diameter on the curved mirrors due to truncation. Finally, the peak intensity on the curved mirrors is limited by mirror damage. In our study, we restrict ourselves to parameters similar to the ones demonstrated in the reference experiment [13]:

- gas flux $n \cdot L^2 \leq 5 n_{\text{std}} \cdot (150 \mu\text{m})^2$,
- beam waist $w_0 \geq 14 \mu\text{m}$,
- beam diameter $w < 0.2D$ on curved mirrors, where $D = 25.4 \text{ mm}$,
- peak intensity on the curved mirrors $\leq 3.6 \times 10^9 \text{ W cm}^{-2}$.

2.3. Computational model

For an accurate theoretical description of HHG in gas targets, our model considers all relevant effects affecting the propagation of the driving field and the generation/propagation of the XUV field in the target: both fields experience linear refraction in transverse and in longitudinal direction, as well as absorption. Nonlinear effects on the driving field, most importantly plasma effects resulting in a spectral blue shift, defocusing and loss, as well as the Kerr effect causing focusing and self-phase modulation, are accounted for. For the XUV emission, the dipole response of an individual atom to the strong driving field is modeled, including polarization-dependent effects and depletion of the ground state.

A standard approach for HHG simulations is to employ a semiclassical model: the Maxwell equations are solved classically, whereas the dipole response is modeled quantum-mechanically. This approach is described in detail in [31]. Our model follows the standard approach, but in contrast to many computational models for HHG, our implementation is not limited to configurations with rotational symmetry. The model is also valid for polarized fields if vector quantities are used for the electric field and the polarization.

2.3.1. HHG model

For the description of XUV and driving field propagation through the gas target, we employ the forward wave equation [31], a first-order propagation equation obtained by applying the slowly evolving wave approximation [32] to the scalar wave equation in Fourier domain, using coordinates co-moving at vacuum speed of light (z is the propagation direction):

$$\partial_z E_{\text{IR}/\text{XUV}} = -\frac{ic}{2\omega} \Delta_{\perp} E_{\text{IR}/\text{XUV}} - \frac{i\omega}{2c\epsilon_0} P_{\text{IR}/\text{XUV}}. \quad (1)$$

Here, E_{IR} is the driving field and E_{XUV} the generated high harmonic radiation, and $P_{\text{IR}} = P_{\text{IR,lin}} + P_{\text{Kerr}} + P_{\text{plasma}}$ is the source term for the driving field and composed of the linear response $P_{\text{IR,lin}}(t) = \epsilon_0 \chi_c(t) E_{\text{IR}}(t)$, the Kerr contribution [33]

$$P_{\text{Kerr}}(t) = \epsilon_0 \chi^{(3)}(t) |E_{\text{IR}}(t)|^2 E_{\text{IR}}(t) \quad (2)$$

and the plasma contribution [34]

$$\partial_t P_{\text{Plasma}}(t) = I_p n_0 \frac{\partial_t \eta(t)}{|E_{\text{IR}}(t)|^2} E_{\text{IR}}(t) + \frac{e^2 n_0}{m_e} \int_{-\infty}^t \eta(t') E_{\text{IR}}(t') dt'. \quad (3)$$

The XUV source term $P_{\text{XUV}} = P_{\text{XUV,lin}} + P_{\text{dipole}}$ consists of the linear response $P_{\text{XUV,lin}}(\omega) = \epsilon_0 \chi(\omega) E_{\text{XUV}}(\omega)$ and the HHG term $P_{\text{dipole}}(t) = n_0 d(t)$ computed with the strong-field approximation (SFA), accounting for elliptic polarization [35, 36] and ground state depletion [37]. Here, I_p is the ionization potential of the atom, e , m_e denote the electronic charge and mass, respectively, $\chi_c(t) = n(t) \alpha_c$ the susceptibility at the driving field's carrier frequency, $\chi(\omega) = n_0 \alpha(\omega)$ the complex XUV susceptibility, $\chi^{(3)}(t) = n(t) \alpha^{(3)}$ the third-order susceptibility. Furthermore, $n(t) = n_0(1 - \eta(t))$ denotes the time-dependent atomic density of neutrals with n_0 being the total atomic density, $\eta(t) = 1 - \exp\left[-\int_{-\infty}^t w(E_{\text{IR}}(t')) dt'\right]$ the ionization fraction, α_c , $\alpha(\omega)$ and $\alpha^{(3)}$ the first- and third-order polarizabilities, and $w(E)$ the static ionization rate. The values for α_c , $\alpha(\omega)$ and $\alpha^{(3)}$ are taken from [38–40], respectively. We use static ionization rates $w(E)$ [41], obtained with the approach described in [42, 43]. We interpolate $\log(w(E))$ for lower intensities and obtain reasonable agreement with recently published rates [44] in the relevant intensity regime.

2.3.2. Computational implementation and optimizations

The first-order propagation equation is solved numerically in (k_x, k_y, z, ω) coordinates using a predictor–corrector Crank–Nicolson scheme, where spatial Fourier transforms are necessary in each z step to compute source terms. Large-distance propagation in vacuum, needed for modeling propagation to the EC mirrors, is done with a Fresnel two-step propagator [45], which allows us to use the same transverse discretization for each frequency component and thus avoid interpolation steps. In cases with rotational or reflectional symmetry, the spatial discrete Fourier transform is replaced by a quasi-discrete Hankel [46] transform/discrete cosine transforms and appropriate transverse discretization is used. The lack of rotational symmetry in some cases makes 3 + 1D simulations necessary. Without approximations, these would consume too much computational and memory resources for broad parameter scans. In these cases, we employed optional envelope approximations for the linear, Kerr, plasma and XUV source terms that permit a coarser t discretization in case of linear polarization (see appendix). The high-harmonic dipole response is computed by a fast, parallel C++ implementation of the SFA model [47]. The overall implementation was verified by reproducing the results of [48], amongst others.

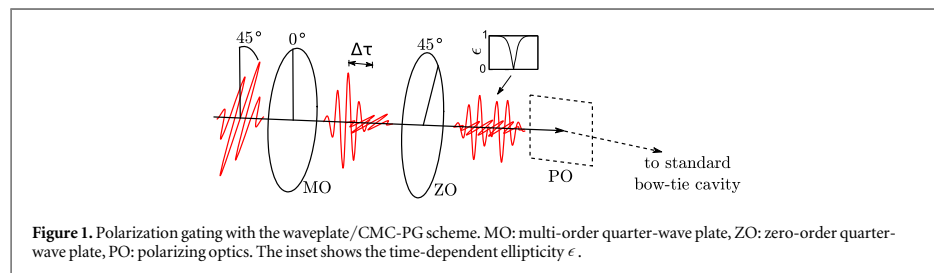
3. Results

3.1. Identification of promising gating methods for cavity-enhanced HHG

The intracavity field in an EC must be an eigenmode of the resonator geometry. Therefore, compared to single-pass HHG, cavity-enhanced HHG permits less freedom in choosing the driving field incident on the gas target, narrowing down the number of viable gating methods. Apart from that, efficiently driving HHG in a passive resonator comes with a few more particularities: first, low round-trip losses are necessary to maintain the main advantage of an EC, i.e., a high enhancement. This is not only hindered by absorbing elements in the cavity, but also by energy coupling to non-resonant eigenmodes through perturbation of temporal/spectral or spatial features of the circulating pulse, e.g., while passing the gas target. Second, to enable such low losses, HR multilayer dielectric mirrors are used as cavity mirrors which can provide well-behaved reflectivity and phase only over a limited bandwidth, imposing a lower limit on the duration of the circulating pulse. Furthermore, at high peak intensities, intracavity optics can manifest undesired nonlinear and thermal effects and, ultimately, damage. In the following, we shortly explain each considered gating method, examine their compatibility with the EC geometry and analyze each scheme with respect to round-trip losses, necessary pulse duration and power scalability.

Amplitude gating [49] relies on the fact that the driving field intensity determines the high harmonic cutoff, so by spectrally filtering the XUV, the emission can be confined to a short time window around the peak of the driving pulse's field, which allows for the production of IAPs. This scheme does not impose further conditions on the spectral or the temporal shape of the pulse incident on the target and is therefore compatible with the standard EC geometry. However, efficient amplitude gating has only been shown with sub-two-cycle pulses [49], while the bandwidth of HR mirrors currently limits the intracavity pulse duration to > 18 fs at a wavelength of 1050 nm [20], rendering this scheme unviable for intracavity IAP generation.

For *ionization gating*, there are two approaches: one is to fully ionize the gas within the first few cycles and therefore inhibit XUV emission from subsequent cycles [50]. Another possibility is to use phase matching in a high-density gas target: in the first few cycles, sufficient plasma is generated so that the critical free-electron



density is reached at which phase matching becomes impossible [51]. Like amplitude gating, these approaches would be compatible with the standard EC geometry. Commonly, cavity-enhanced HHG is performed in a tight-focusing regime with a high gas density to achieve good phase matching, and a low enough peak intensity to limit ionization-related clamping effects due to blue-shifting and plasma lensing [19]. On the contrary, ionization gating implies higher ionization levels than typically achieved in intracavity HHG—even the phase matching variant of ionization gating requires an ionization of 5%, using three-cycle pulses [51]. Although the use of input couplers with a tailored transmission curve and of mirrors correcting for the nonlinear phase have been suggested as a countermeasure against blueshift-induced clamping [19], this cannot reduce spatial effects due to plasma lensing, which are to be expected at such high ionization fractions. Moreover, the necessary pulse duration is out of reach with state-of-the-art mirrors. Therefore, efficient production of IAPs in ECs with ionization gating does not seem a viable route.

Polarization gating takes advantage of the fact that the HHG efficiency drops considerably with increasing ellipticity of the polarization [36]. By shaping the ellipticity of a pulse in a time-dependent manner, the harmonic emission can be confined to a time window with a duration on the order of a single half-cycle. As a standard EC with small incidence angles and geometric output coupling is basically insensitive to polarization, it is possible to apply such a scheme to the seed without modifications to the geometry of the EC. A straightforward way to shape the ellipticity is to produce two delayed, perpendicularly polarized copies of an initial pulse by passing a linearly polarized pulse through a multi-order quarter-wave plate with its optical axis rotated by 45° with respect to the polarization direction (see figure 1). The polarization of the resulting pulse then changes from linear to circular to linear. Then, circular and linear polarization are swapped by a zero-order quarter-wave plate with its optical axis parallel to the original pulse's polarization direction [52]. Interferometric polarization gating [53] produces a similarly shaped pulse by introducing the delays interferometrically, and offers the additional degree of freedom to choose the relative amplitudes of both polarization directions in the resulting pulse, permitting production of IAPs from multi-cycle driving pulses, at the expense of at least 50% loss to the driving pulse energy. In [54] a scheme called collinear many-cycle polarization gating (CMC-PG) based on the waveplate scheme is introduced, which adds the same degree of freedom using reflection off a silicon plate as a polarizer and achieves similar performance as interferometric gating, while it is easier to align and more stable. This scheme has been shown to produce IAPs from pulses as long as 33 fs at a wavelength of 800 nm, corresponding to 12.4 optical cycles [54]. Efficient intracavity HHG with 30 fs-pulses was already shown [13], approaching the optimum photon flux for time-resolved photoelectron emission experiments, and mirrors supporting even shorter pulses have been demonstrated [20], so CMC-PG is a viable candidate. To avoid damage at high intensities, the silicon plate can also be replaced by a broadband thin-film polarizer.

Several methods have been suggested using *multi-color collinear superpositions*: in [55], an XUV continuum around 100 eV is generated by mixing the 6.7-cycles-long driving pulse with its detuned second harmonic. (Generalized) double optical gating [56] is a combination of two-color gating with polarization gating. In both cases, the second harmonic allows to suppress harmonic emission from every other half-cycle, allowing for the production of IAPs with multi-cycle driving pulses. These schemes could in principle also work with a standard EC geometry—however, both colors would need to be enhanced with the same mirror set, which imposes a serious technological challenge. Another possibility is to produce the second component inside the cavity. However, the portion η of energy that can be converted to a second radiation component limits the power enhancement to maximally $1/\eta$, limiting the practicability of this approach. Non-collinear combination would also be an option, but an angle large enough to afford spatial separation would angularly disperse the harmonic radiation strongly when combining two different wavelengths [57], which is disadvantageous for time-domain applications.

The *angular streaking* method uses a driving pulse with a wave front rotating over the time scale of a single driving pulse. The XUV bursts take over the instantaneous wavefront orientation and are therefore emitted in different directions, allowing to separate IAPs by spatial filtering in the far field. One way of achieving such a

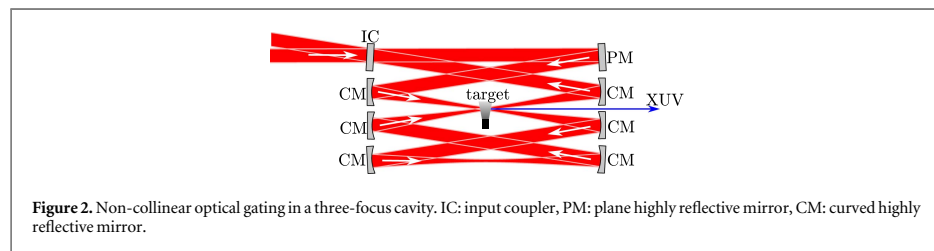


Figure 2. Non-collinear optical gating in a three-focus cavity. IC: input coupler, PM: plane highly reflective mirror, CM: curved highly reflective mirror.

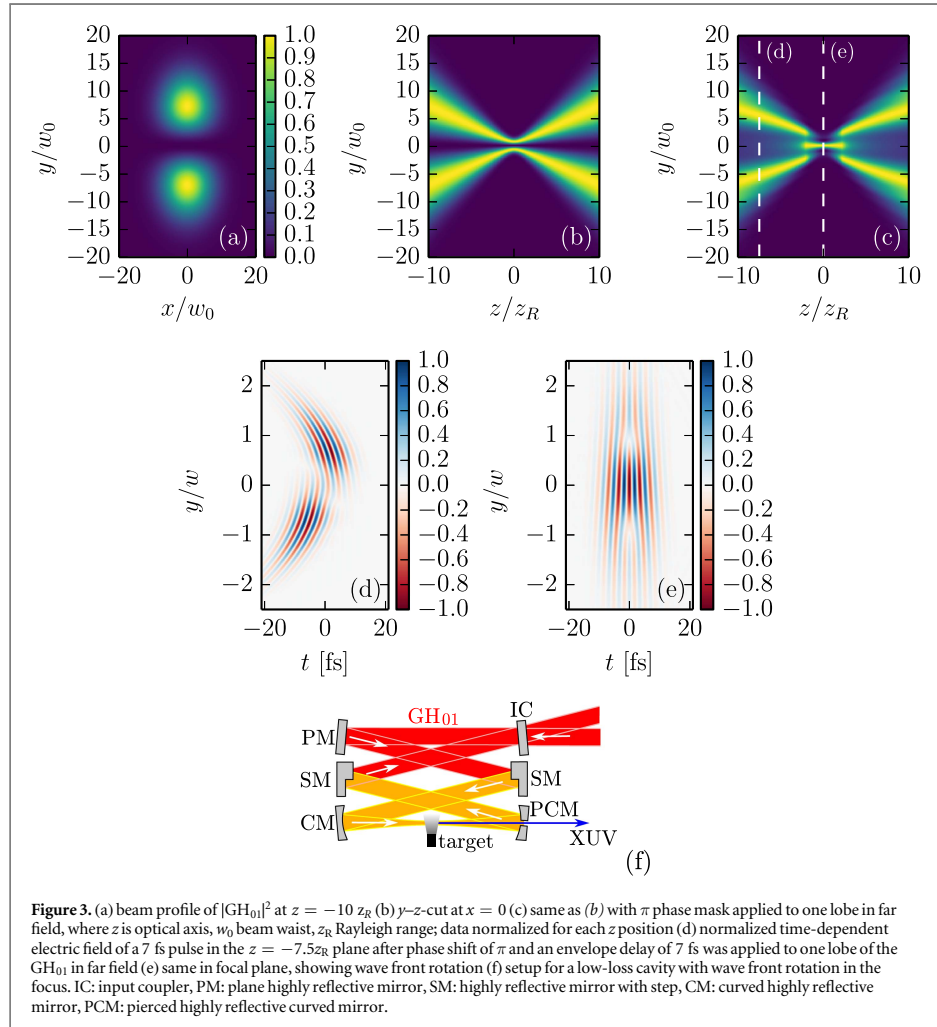
wave front rotation (WFR) is to impose a spatial chirp in one transverse direction on the pulse [58–60]. Such a spatially chirped pulse cannot propagate as an eigenmode of a standard resonator, because each frequency component has a different optical axis. Consequently, intracavity elements (e.g. wedges or gratings) would be necessary to introduce a WFR in the resonator, which, similar to the case of multi-color gating, come with significant technological challenges.

Another possibility to achieve WFR is *non-collinear optical gating* (NOG). Here, the idea is to cross two equally strong delayed pulses [61, 62]. Then, the wave front orientation will change continuously from the direction of the first pulse to the one of the second pulse, leading to an attosecond lighthouse effect as in the case of the spatially chirped driving pulse. For generating such a driving field using cavities, there exist several possibilities. The most obvious is to use two separate cavities for both pulses and cross their foci [26] (see figure 2). It is preferable to have three focused arms instead of two for alignment sensitivity reasons [16]. A third approach to realize a continuous WFR in an EC is to exploit the similarity of two crossed beams to some higher-order transverse eigenmodes. For instance, the Gauss–Hermite mode GH_{01} (figures 3(a) and (b)) consists of two well-separated lobes. If a π phase mask is applied to one of the lobes far before the focus [26], a single lobe emerges in the focal plane (figure 3(c)). Then, by also delaying the pulse envelopes of the lobes with respect to each other (figure 3(d)), it is possible to achieve WFR in the focus (figure 3(e)). Such a delay can be introduced by depositing material onto one half of a cavity mirror before applying the coating. The π phase mask can be achieved by choosing the step height as $(n + 0.5)/2$ times the wavelength, with an integer n , or by using different coatings for the two halves [30]. However, the resulting field distribution is not a resonator eigenmode. Thus, it is required to place the step mirror inside the cavity and compensate for the mode alteration after passing the focus (see figure 3(f)), which is possible with very low losses using a second step mirror (see appendix). In the following, we refer to this scheme as transverse mode gating (TMG). Alternatively, as suggested in [63], one can cross the driving pulse with a weaker but shorter pulse, which introduces a slight wave front tilt for the duration of the short pulse, resulting in temporally confined emission of harmonics in off-axis direction. This is possible without adaptation of the EC geometry.

Production of IAPs by NOG was only experimentally demonstrated with sub-two-cycle pulses [62]. However, [61] predicts that separation of an IAP is still possible with 10 fs pulses at 800 nm, which corresponds to 3.75 cycles, assuming a harmonic beamlet divergence angle of $0.1\Theta_0$, with Θ_0 denoting the divergence angle of the driving beam. As we show later, it is possible to obtain a significantly smaller beamlet divergence by placing the target before the focus, so non-collinear generation of IAPs at pulse durations realistic in cavities may come into reach.

The maximum crossing angle for efficient NOG is only $\pi \cdot \Theta_0$ [61]. This means that in the two-cavity and the three-focus approach, the curved mirrors next to the target have to be placed as close as possible to each other to avoid losses due to truncation of the mode. Reflection on a mirror cropped by a straight line in a distance of $\pi/2 \cdot \Theta_0$ from the center ideally leads to a round-trip loss of 0.64%. The same holds for gating by an external pulse, but in that case one can choose to truncate the intracavity beam less and the external beam more to allow for a better power enhancement. TMG does not suffer from truncation losses, however care must be taken that the distortion introduced by the first delay mirror is compensated well by the second one without introducing too much loss. As it will be shown later, these losses can be kept small if the delay mirrors are placed appropriately.

Commonly, the resonator length and the seed repetition rate must be actively stabilized with respect to each other to maintain constructive interference of the carrier of the seed pulse with the carrier of the circulating pulse. Likewise, for NOG, sub-wavelength precision and stability of alignment are necessary for constructive interference of the two beams in the intersection point. From all presented NOG variants, TMG appears to be the most stable, because the delay between the beams is implemented monolithically. So, from the point of view of truncation losses and experimental effort, TMG can be considered the most promising variant for intracavity NOG.

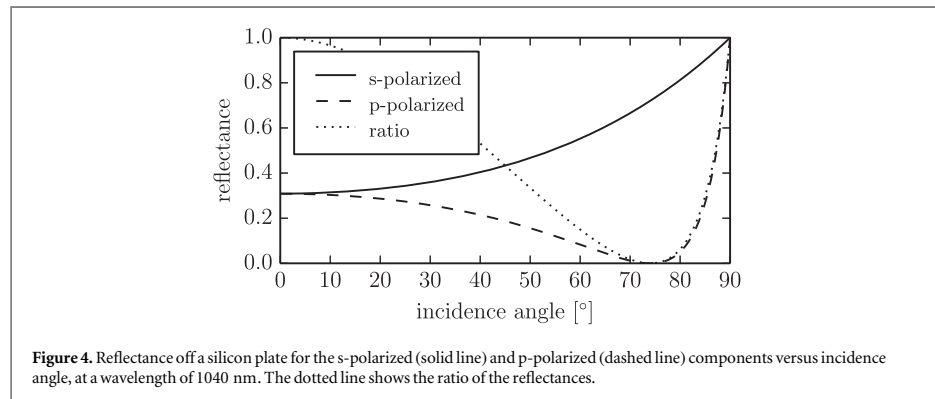


In conclusion, we reviewed possible schemes for intracavity production of IAPs and identified two promising approaches (CMC-PG and TMG) and we found significant reasons to prefer them over the remaining schemes. In the remainder of the paper, we aim at performing a fair comparison of polarization gating with TMG. For this, we optimize both gating methods for optimum photon flux using the same target parameters and considering the same technical restrictions.

3.2. Criteria for a fair comparison of viable gating schemes

For a fair comparison of the two considered gating schemes for cavity-enhanced HHG, we need to optimize the parameters of both methods for optimum photon flux, demanding the same minimum intensity contrast ratio of the IAPs and taking into account the same technical restrictions, as discussed in section 2, i.e., limited seed pulse energy, cavity losses, gas flux, beam waist, beam diameter on the curved mirrors and damage intensity. We optimize for output coupling through a hole (for CMC-PG) and a slit (for TMG) in the mirror following the focus, because geometrical output coupling does not angularly disperse the harmonic radiation, works over a broad bandwidth and it is suitable for high photon energies.

For each scheme, we identify parameters affecting the contrast ratio and perform a broad scan on them, which is enabled by the approximations and optimizations of the implemented computational model. Based on these parameters, we optimize the phase matching conditions and the output coupling. Accounting for losses to the circulating pulse by nonlinear effects in the gas target, we obtain a complete set of optimum parameters, allowing us to simulate the optimum case with a minimum number of approximations.



To be consistent, we need to impose the same contrast ratio for both schemes. Having in mind time-resolved photoelectron emission spectroscopy (PES) and microscopy (PEEM) applications, in the broad parameter scan we optimize for IAPs with an intensity contrast ratio better than 10 after spectral filtering for harmonic orders between 74 and 84 (88.2–100.1 eV), which is about the minimum required photon energy for time-resolved PEEM experiments. In the following step of optimizing the phase matching, we only require a contrast ratio of 6.66 to make sure that promising results are not excluded due to numerical deviations, e.g., due to neglecting propagation effects in the broad parameter scan.

We restrict the study to HHG in neon, which was already shown experimentally in ECs and is a suitable choice for the targeted photon energy range due to its high ionization potential.

3.3. Polarization gating

In the CMC-PG scheme, the contrast ratio is affected by the delay $\Delta\tau$ of the multi-order quarter-wave plate, the CEP φ_{CE} of driving pulse and the incidence angle φ_{p} on the polarizing optic. Parameters affecting the photon flux are the target position z_0 , the target length L , the atomic density n of the target gas, the driving pulse energy E_{IR} and the focusing w_0 , which affect the phase matching, and the hole diameter d for the output coupling.

In a first step, we optimize the parameters affecting the contrast ratio. For this, we compute the single-atom dipole response, scanning the delay $\Delta\tau$ from 0 to 25 fs in 1 fs steps, the carrier-envelope phase φ_{CE} from 0° to 180° in 5° steps and the incidence angle φ_{p} from 73.5° to 90° in 1.1° steps. This interval of incidence angles already covers all reflectance ratios and smaller angles would only result in higher losses to the p-polarized component (see figure 4). The long trajectory is suppressed by restricting the electron excursion time to values below 0.66 driving field periods, and the peak intensity is chosen to be $3 \times 10^{14} \text{ W cm}^{-2}$ in each case. For each parameter set, we compute the conversion efficiency $|d(t)|_{\text{max}}^2 / \int I_{\text{IR}}(t) dt$, where $d(t)$ is the single-atom dipole response envelope after a bandpass from harmonic order 74–84 and I_{IR} is the driving field intensity. The contrast ratio, i.e. the ratio between the global and the secondary maximum of $|d(t)|^2$, is also computed. Figure 5(a) shows that there is a tradeoff between the conversion efficiency and the contrast ratio. Choosing the parameter set with best efficiency and a contrast ratio ≥ 10 , we obtain an incidence angle $\varphi_{\text{p}} = 85.6^\circ$, a delay $\Delta\tau = 12$ fs and a CEP of $\varphi_{\text{CE}} = 115^\circ$, resulting in a contrast ratio of 10.5 (see figure 5(b)). The energy loss at the polarizing optic is 60.1%, i.e. 39.9% of the seed energy is available to the cavity.

After having determined the parameters for the optimum contrast ratio of the single-atom dipole response, the next step is to optimize the parameters affecting the phase matching ($z_0, L, E_{\text{IR}}, w_0, n$). The scaling law introduced in [64] states that a parameter set $z_0, L, E_{\text{IR}}, w_0, n$ is equivalent to a parameter set $z_0\eta^2, L\eta^2, E_{\text{IR}}\eta^2, w_0\eta, n/\eta^2$, where η is an arbitrary number and the XUV photon flux also scales with η^2 . This allows us to eliminate one parameter by using the following scale-invariant parameters: relative target position z_0/z_{R} , driving field peak intensity I , relative gas density $n \cdot z_{\text{R}}$ and relative target length L/z_{R} , where $z_{\text{R}} = \pi w_0^2 / \lambda$ is the Rayleigh range. The scale-invariant quantities corresponding to the pulse energy E and the XUV photon flux Φ_q are the relative pulse energy E_{IR}/η^2 and the relative XUV photon flux Φ_q/η^2 .

To enable a parameter scan on such a broad parameter range, which requires computing the single-atom dipole response on a spatial grid for each parameter set, we resort to several approximations and optimizations: first of all, we exploit rotational symmetry. The relative target length L/z_{R} is successively increased and the far-field on-axis harmonic peak intensity is calculated. This intensity will typically first increase with increasing target length and then decrease when the phase matching length is exceeded. The calculations stop when the intensity drops to 75% of the maximum or when L/z_{R} exceeds 1. We only save the harmonic spectra from H74

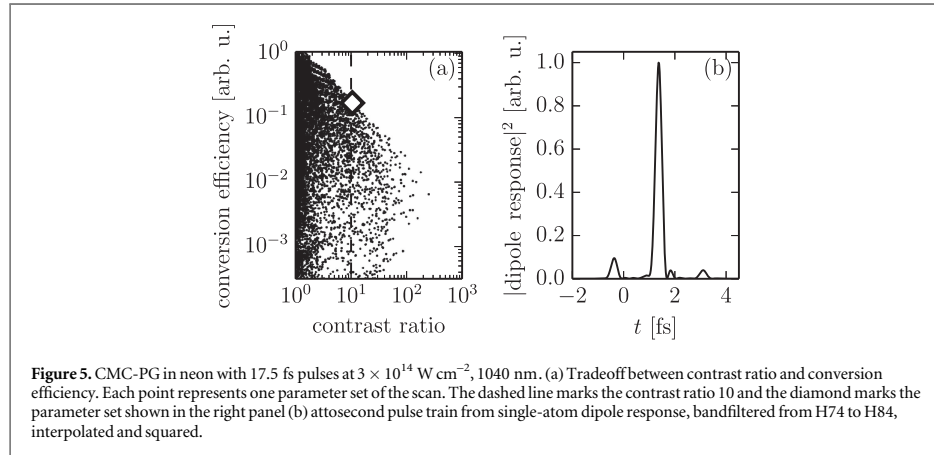


Figure 5. CMC-PG in neon with 17.5 fs pulses at $3 \times 10^{14} \text{ W cm}^{-2}$, 1040 nm. (a) Tradeoff between contrast ratio and conversion efficiency. Each point represents one parameter set of the scan. The dashed line marks the contrast ratio 10 and the diamond marks the parameter set shown in the right panel (b) attosecond pulse train from single-atom dipole response, bandfiltered from H74 to H84, interpolated and squared.

to H84 and discard the rest of the spectrum. We vary z_0/z_R from -1 to 1 in steps of 0.1 , the peak intensity from 2.0×10^{14} to $4.0 \times 10^{14} \text{ W cm}^{-2}$ in $0.2 \times 10^{14} \text{ W cm}^{-2}$ steps, and $n \cdot z_R$ from 0.5×10^{-3} to $0.5 \times 10^{-3} n_{\text{std}}$, using $0.5 \times 10^{-3} n_{\text{std}}$ steps. The step size in the direction of the optical axis is chosen as $z_R/400$.

For each set of scale-invariant parameters, we compute the driving field and the XUV radiation incident on the output coupling mirror. Then we also scan the relative output coupling hole diameter d/w from 0.1 to 0.6 in steps of 0.05 , where w is the driving beam radius at the output coupling mirror. This determines the output coupling efficiency as well as the losses of the circulating pulse at the pierced mirror (0.36% for $d/w = 0.6$).

Using the driving field on the output coupling mirror and the losses at the pierced mirror, we compute the achievable pulse-energy enhancement (see appendix). Together with the relative circulating pulse energy, this yields the relative seed pulse energy necessary to drive the cavity to reach the required peak intensity. The relative output coupled photon flux is determined from relative photon flux and output coupling efficiency.

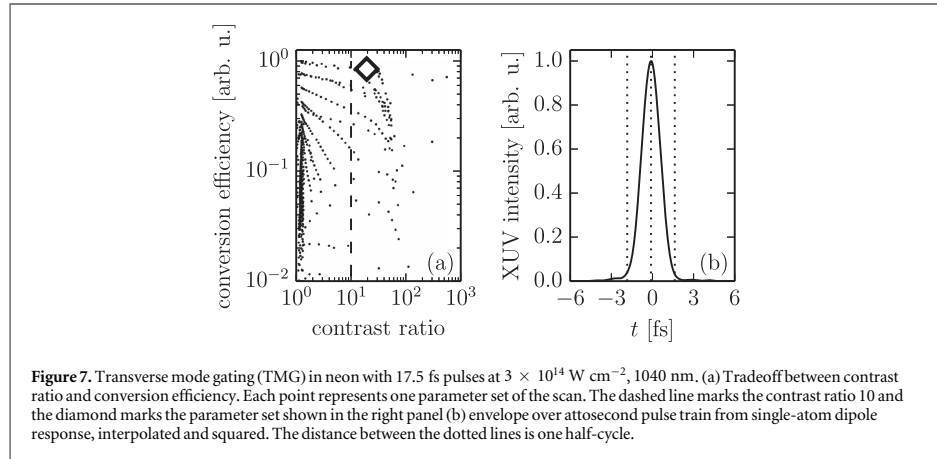
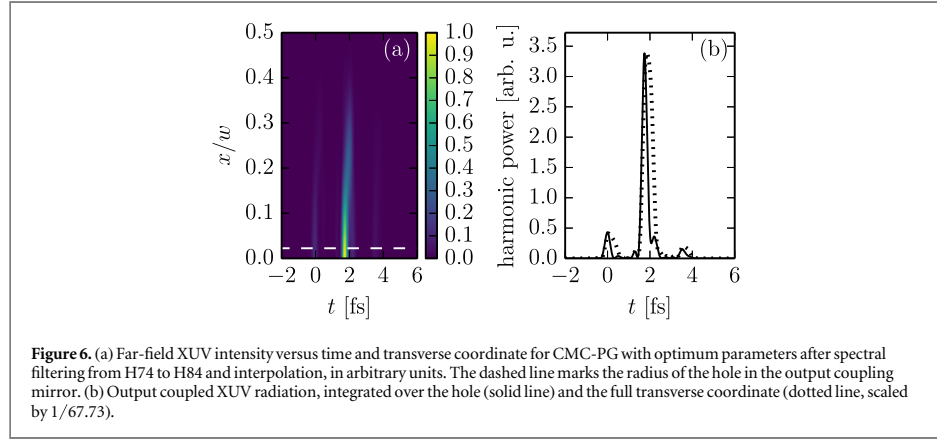
As we are interested in the parameters with optimum photon flux, we apply the scaling law to each parameter set, increasing the focus size to the maximum without violating any of the technical restrictions (gas flux, beam waist, beam diameter, peak intensity), and without requiring more than the available seed pulse energy. Of the assumed input pulse energy of $0.7 \mu\text{J}$, a fraction of 60.1% is lost at the polarizing optics of the gating scheme, leaving a pulse energy of $0.28 \mu\text{J}$ to seed the cavity. We only allow target lengths with a resulting contrast ratio better than 6.66 . The obtained optimum parameters are a peak intensity of $2.2 \times 10^{14} \text{ W cm}^{-2}$, an atomic density of $3.86n_0$, a beam waist of $14.64 \mu\text{m}$, a target length of $137.5 \mu\text{m}$, a target position at $-0.4z_R$ and a hole diameter of $0.045w$, leading to an estimated pulse-energy enhancement of 97.2 (considering nonlinearities). The curved mirrors must be placed at a distance of at least 70.6 mm from the focus in order to not exceed the assumed damage threshold.

With the optimum parameters, we repeat the simulation without suppressing the long trajectory. The resulting time-domain XUV intensity on output coupling mirror is shown in figure 6. The contrast ratio of the output coupled, spectrally filtered XUV radiation is 7.82 .

3.4. Transverse mode gating

Like with polarization gating, the achievable contrast ratio is affected by the delay $\Delta\tau$ and CEP φ_{CE} . Moreover, the relative target position z_0/z_R affects the XUV beamlet divergence angle [65] and thus the separation of harmonic bursts in the far field, so it is also an important parameter for the contrast ratio. As before, the parameters affecting the photon flux are L , E_{IR} , w_0 and n , as well as the width d of the slit in the output coupling mirror.

As a first step, we again determine the optimum parameters for the contrast ratio. Here, it is not sufficient to only compute single atom dipole responses, because transverse effects (beamlet divergence) must be accounted for. Therefore we compute the XUV far field in the limit on an infinitesimally thin gas target, scanning $\Delta\tau$ from 0 to 25 fs in 1 fs steps and the relative target position from -1.3 to 1.3 in steps of 0.1 , again at a fixed peak intensity of $3 \times 10^{14} \text{ W cm}^{-2}$. To reduce computation time, we use the short-trajectory envelope approximation for the dipole response around H79, and only consider one transverse direction: the one along which the harmonic bursts are angularly separated. For each parameter set, we compute the time-dependent on-axis XUV far field. Because the envelope approximation only yields spectral components in a narrow bandwidth around the targeted H79, this time-dependent field does not exhibit the individual bursts of an attosecond pulse



train, but rather represents an envelope over the pulse train. From this envelope $E(t)$, we can compute the contrast ratio of the attosecond pulse train, i.e. the ratio between global maximum and secondary maximum, which is expected at least one half-cycle before or after the global maximum, as

$$c = \frac{|E(t_0)|^2}{\max_{|t-t_0| > T/2} |E(t)|^2}, \quad (4)$$

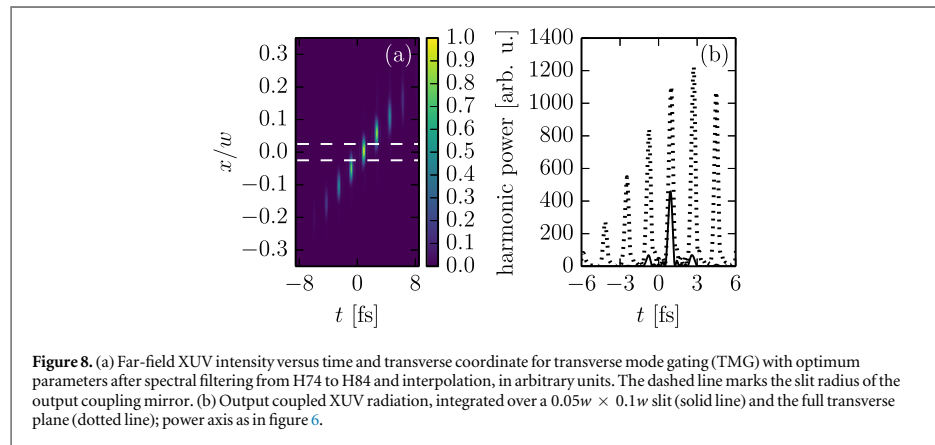
where t_0 is chosen so that $|E(t_0)|^2$ is maximal and $T/2$ the duration of a half-cycle. We also compute a conversion efficiency measure by relating the peak intensity of the XUV field with the necessary IR pulse energy:

$$\epsilon = \frac{|E(t_0)|^2}{\iint |E_{\text{IR}}(x, t)|^2 dx dt}. \quad (5)$$

Figure 7(a) shows the tradeoff between these two quantities. Choosing the parameter set with best efficiency and contrast ratio ≥ 10 as before, we get a target position of $-0.9z_R$ and a delay of 7 fs, resulting in a contrast ratio of 19.3 (figure 7(b)).

For the parameters of optimum contrast ratio, we optimize the phase matching parameters L , E_{IR} , w_0 and n by scanning the scale-invariant parameters L/z_R , I and $n \cdot z_R$. We compute in $3 + 1\text{D}$, exploiting reflectional symmetry in one spatial direction, and use envelope approximations for the driving field source terms as well as the short-trajectory envelope approximation for the XUV. As in the case of polarization gating, we only consider relative target lengths $L/z_R \leq 1$ and only compute until the photon flux (peak of the time-dependent on-axis far field) decreases to 75%. We vary the peak intensity and the relative gas density in the same parameter range.

For each set of scale-invariant parameters, we compute the driving field and the generated XUV radiation in the output coupling mirror plane. Then we scan the relative slit width d/w from 0.01 to 0.10 in steps of 0.01,



where w is the radius of the driving beam on the mirror. For $d/w = 0.10$, the round-trip loss is still below 0.07%. Figure 3(c) shows that the on-axis minimum of the GH_{01} mode in the far field is conserved if a phase shift is introduced to one lobe far from the focus, i.e. the circulating mode has an intensity minimum at the position of the slit, which explains the low losses. Thus, for these slit widths the loss is still not a limiting factor. However, the slit also serves to spatially separate one of the angularly dispersed harmonic beamlets. Increasing the slit size further would make it impossible to reach a good contrast ratio, as the results of the parameter scan will show later.

As for polarization gating, for each resulting parameter set we compute the necessary relative seed pulse energy and relative output-coupled photon flux, accounting for cavity round-trip losses, phase shift and output coupling efficiency. After that, we apply the scaling law to maximize the photon flux in each case without violating the same technical restrictions as in polarization gating, requiring a contrast ratio better than 6.66 and permitting 82.7% of $0.7 \mu\text{J}$ as seed pulse energy, where 82.7% is the maximum achievable overlap of a GH_{00} seed with the GH_{01} resonator eigenmode using a phase mask [66]. The resulting optimum parameters are a peak intensity of $2.6 \times 10^{14} \text{ W cm}^{-2}$, an atomic density of $4.6n_0$, a beam waist of $14.68 \mu\text{m}$, a target length of $156.3 \mu\text{m}$ and a slit width of $0.05w$, leading to an estimated pulse-energy enhancement of $108.3 \times 82.7\% = 89.6$. The distance between focus and curved mirror must be larger than 220.9 mm to avoid damage.

For the optimum parameters, we repeat the simulation without envelope approximations and considering both trajectories. The resulting time-domain XUV intensity evolution on the output coupling mirror is shown in figure 8, where a clear lighthouse effect can be seen which allows the separation of an IAP by spatial filtering at the slit. We observe that the contrast ratio can be improved if not only the slit width but also the slit length is limited; when choosing a $0.05w \times 0.1w$ slit the contrast ratio of the output coupled, spectrally filtered XUV radiation is 7.0. This can most likely be attributed to the larger divergence angle of the long-trajectory contribution to the harmonic far field. It can be seen that the harmonic beamlet divergence is on the order of $0.025\Theta_0$ —this explains the good angular separation of harmonic bursts even with 17.5 fs pulses.

4. Discussion

4.1. Comparison of TMG and polarization gating

Comparing figure 5(a) with figure 7(a), it can be seen that the trade-off between contrast ratio and conversion efficiency is much more critical in the CMC-PG scheme than in the TMG scheme. Also, the resulting XUV peak intensity is 135.7 times higher for TMG after optimizing under the previously specified constraints.

There are several reasons for this: in the CMC-PG scheme, only 39.9% of the seed energy is available, because one polarization direction must be suppressed, whereas in TMG up to 82.7% of the seed energy can be coupled into the cavity assuming optimum mode matching. Further, the resonator mode excited in TMG has an on-axis minimum in the middle of the output coupling mirror, leading to lower round-trip losses of the circulating pulse. Then, to reach the required contrast ratio, the delay for polarization gating must be chosen >12 fs while it is only 7 fs for TMG. Due to the larger delay, more pulse energy or a tighter focusing is needed to reach the same peak intensity in the focus, which results in a lower efficiency. Finally, the output coupling efficiency (fraction of the XUV power transmitted through the orifice to the whole XUV power incident on

output coupling mirror, computed at the peak of the IAP) is $1/67.73 = 1.5\%$ for CMC-PG, but 37.5% for TMG —for optimum beamlet divergence and thus optimum output coupling efficiency, the target has to be placed approximately one Rayleigh length before the focus, which is not possible in the case of CMC-PG because the necessary peak intensity can not be reached there due to the longer delay.

For these reasons, TMG can be regarded as the preferred method for implementation.

4.2. Photon flux estimation for TMG

To estimate the photon flux that can be obtained with the TMG scheme, assuming the determined optimum parameters, we also simulate HHG with the parameters of the reference experiment [13], using the same approach applied to obtain figures 6 and 8, and compare. The number of XUV photons produced per pulse (in the spectral range from H74 to H84) can be obtained by integrating the harmonic power over time and is 1.8 times higher for the simulated TMG case than in the simulated reference experiment. From this we can conclude that a similar photon flux as in the reference experiment (9×10^7 photons s^{-1}) can be obtained with TMG. However, it is important to note that the photon flux in the reference experiment was strongly limited by cumulative effects in the gas target due to the high repetition rate of 250 MHz [13] and that these cumulative effects were not included in the model. Therefore, the predicted photon flux should be regarded as a rather strong underestimation of the flux attainable with implementing this scheme at a repetition rate at which each gas atom is hit by a single pulse only. With state-of-the-art lasers operating at the highest repetition rates in this regime [29] and a pulse-energy-scalable compression scheme (e.g. [67]), the seed pulse energy can be increased accordingly. The scaling law of [64] allows to change the geometry of the EC setup such that the same total photon flux can be obtained at a significantly lower repetition rate, without violating the constraints of beam waist and peak intensity as given in section 2. The beam diameter on the curved mirrors and therefore the size of the substrates may have to be increased, however. The maximum allowed gas flux is not exceeded because the flux is scale-invariant if the nozzle size is only scaled in transverse direction. Therefore, scaling to lower repetition rates is possible without reducing the XUV photon flux.

Decreasing the repetition rate to a value where cumulative effects do not play a role anymore promises considerably better photon flux than demonstrated in [13]. For instance, gas flow simulations predict that at ~ 10 MHz and for typical beam waists, each atom is only hit by a single pulse.

5. Conclusions

In conclusion, we theoretically investigated possible time gating methods for the enhancement-cavity-assisted generation of isolated XUV attosecond pulses within the constraints of state-of-the-art laser technology. In particular, we identified polarization gating and TMG, a new method combining the ideas of NOG with higher-order mode output coupling, as viable gating methods for intracavity generation of IAPs. We presented an algorithm optimizing all relevant parameters for intracavity HHG in order to obtain optimum photon flux, considering the various trade-offs among finesse, focusing and the position, density and size of the gas target, and output coupling orifice size in the case of geometric output coupling, and applied it for a fair comparison between TMG and polarization gating. TMG is identified as the preferred method in terms of the photon flux and trade-off between efficiency and IAP contrast ratio. In contrast to other supposable intracavity non-collinear gating schemes, the delay in TMG is alignment-free and intrinsically stable because it is introduced by a monolithical step mirror.

We showed that using this scheme and taking advantage of state-of-the-art technical advances, IAPs at a photon energy and flux sufficient for time-resolved PES and PEEM experiments can be expected. Scaling laws predict that this photon flux can be achieved at repetition rates compatible with time-of-flight spectrometers when using non-circular gas nozzle orifices and sufficiently large mirror substrates. Given the recent advances of power scaling in resonators [12], broadband cavity mirrors [20], high-power phase-stable Yb-based seed lasers [29], and zero-offset-frequency resonators [30], the implementation of efficient, cavity-enhanced generation of IAPs comes into reach. Compared to state-of-the-art kHz sources of IAPs, the dramatic increase in repetition rate will have a corresponding impact on the signal-to-noise ratio in experiments in attosecond physics, promising to reveal nanoscopic information so far hidden under the measurement noise floor [8]. Equivalently, with such a source, the measurement time can be dramatically reduced, rendering applications which so far have been prohibited by long acquisition times, feasible. Just to name an example, the time-resolved investigation of the spatial dynamics of plasmonic fields in nanostructures, combining attosecond streaking with PEEM, comes into reach with such a source [6, 7].

In addition, such a source would constitute an XUV frequency comb with unique properties for precision spectroscopy [14, 15]: the high repetition rate corresponds to a high spacing between the comb lines, increasing the power per line. Furthermore, while common cavity-based XUV frequency combs are only available in small

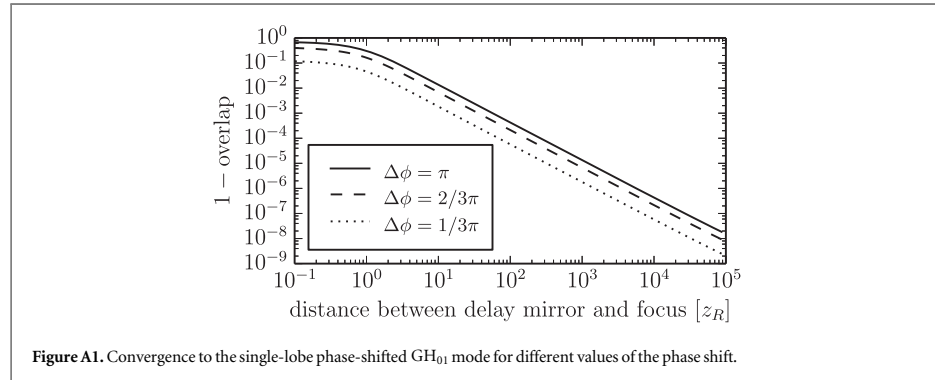


Figure A1. Convergence to the single-lobe phase-shifted GH_{01} mode for different values of the phase shift.

spectral ranges around the odd harmonic orders, such a source would allow precision spectroscopy over a broad spectral continuum.

Acknowledgments

This research was supported by the Fraunhofer Society/Max-Planck Society cooperation ‘MEGAS’. Valer Tosa acknowledges partial support from UEFISCDI projects 03ELI-RO/2016 and RU-TE-2014-4-0425. We thank Simon Holzberger, Henning Carstens, Nikolai Lilienfein and Vladislav Yakovlev for fruitful discussions.

Appendix A. Placement of delay mirrors in the TMG scheme

We show that WFR as discussed in section 3.1 and depicted in figure 3(e) can be achieved using a setup as shown in figure 3(f) without introducing significant round-trip losses. Our reasoning consists of three steps: first, we show that the same electric field distribution is obtained from a GH_{01} mode irrespective of the position along the optical axis at which the phase mask is placed, as long as it is placed sufficiently far from the focus. Then, we show that this field distribution exhibits point symmetry around the focus. Finally, we show that in a setup like in figure 3(f), the phase masks are imaged into planes far enough from the focus. We begin with only considering the π phase mask and then generalize the result for an additional delay.

To examine the sensitivity of the desired field distribution with respect to the distance Δz between phase mask and focus, we first compute the GH_{01} mode numerically at the delay mirror position. We then add a constant phase to one lobe and propagate to a position z_{ff} far behind the focus. Now we can analyze how strongly the field at z_{ff} depends on Δz . For this, we vary Δz and compute the overlap of the field at z_{ff} with a reference field at the same position obtained with $\Delta z = 10^{10}z_{\text{R}}$. Figure A1 shows that a good approximation to this reference field is already obtained if the delay mirror is placed at a distance $\Delta z > 100z_{\text{R}}$ before the focus, reaching overlap values better than 0.999 irrespective of the phase shift, which shows that losses are not significant for a targeted pulse-energy enhancement of ~ 100 .

For the second step of showing the symmetry of the field distribution, we assume that the phase mask is placed at $\Delta z = 10^{10}z_{\text{R}}$ and numerically compute the complex electric field amplitude $E(x, y, z)$ for different z positions behind the phase mask. We then compute the overlap of $E(x, y, z)$ with $E^*(-x, -y, -z)$. The overlap is 1 within numerical precision both for z positions far from the focus as well as near the focus.

As last step, we apply the mirror equation $d_i = \frac{d_o f}{d_o - f}$ to find out to which planes the step mirrors in figure 3(f) are imaged. Assuming $f > 100z_{\text{R}}$, which is the case for the determined optimum parameters of TMG, and assuming that the step mirrors are placed at a distance $d_o \in (f, 2f)$ from the curved mirrors, we obtain $d_i > 2f > f + 100z_{\text{R}}$, i.e., the first step mirror is imaged to a plane far behind the focus. Given the symmetry shown in the last step, we can conclude that we indeed obtain a mode that is a very good approximation to the desired field distribution, with an overlap of 0.999. A similar argument can be applied to the compensating step mirror.

In conclusion, we have shown that a single-lobe phase shift can be introduced and compensated without significant round-trip losses. Now we look at the case when we also add a single-lobe delay. In the spectral domain, introducing a delay Δt corresponds to multiplication with a factor of $\exp(i\Delta\varphi(\omega))$, where $\Delta\varphi(\omega) = \omega\Delta t$, i.e., delaying one lobe is equivalent to applying a phase mask on each spectral component, with

a frequency-dependent phase shift. Figure A1 shows that the overlap is even better for phase shifts $\Delta\varphi \neq \pi$, therefore the previous result can be generalized from phase-shifting to delaying one lobe.

Appendix B. Approximation of the pulse energy enhancement

When traversing the gas target, the driving pulse is altered in its spectral (magnitude as well as phase) and spatial features due to the linear refractive index of the gas, the Kerr effect and plasma formation. This limits the overlap between the input and the intracavity beam and, therefore, the achievable pulse-energy enhancement. After performing the parameter scan to optimize phase matching for the CMC-PG and TMG schemes, we need to estimate the enhancement to compute the necessary seed pulse energy.

To arrive at a suitable approximation, we follow a similar approach as [19] and decompose the field that has passed the gas target into Gauss–Hermite modes, which are the eigenmodes of an empty resonator. We denote the driving field that has passed the gas target by $A(x, y, \omega)$ (e.g. in the plane of the output coupling mirror). In the case of TMG, we have to compensate the one-sided phase shift π and delay $\Delta\tau$ to arrive at a field $A'(x, y, \omega)$ that can be compared to the resonator eigenmode, and which, in the case of an empty cavity, is just equal to the eigenmode:

$$A'(x, y, \omega) = \begin{cases} \exp[i(\omega - \omega_0)\Delta\tau] \exp(i\pi) A(x, y, \omega) & \text{for } y > 0, \\ A(x, y, \omega) & \text{for } y \leq 0. \end{cases} \quad (\text{B.1})$$

For CMC-PG, we just set $A'(x, y, \omega) = A(x, y, \omega)$. Then, we decompose A' into the resonator eigenmodes:

$$A'(x, y, \omega) = \sum_{n,m} c_{nm}(\omega) \text{GH}_{nm}(x, y, \omega), \quad (\text{B.2})$$

where

$$c_{nm}(\omega) = \iint \text{GH}_{nm}^*(x, y, \omega) A'(x, y, \omega) dx dy \quad (\text{B.3})$$

and GH_{nm} are the normalized Gauss–Hermite modes. We can compare the coefficients $c_{nm}(\omega)$ with coefficients $c_{nm}^0(\omega)$ obtained with the same approach but for a driving field that is not altered by a gas target. Denoting the resonant mode with GH_{NM} , with $(N, M) = (0, 0)$ for CMC-PG and $(N, M) = (0, 1)$ for TMG, we get $c_{nm}^0(\omega) = 0$ for $(n, m) \neq (N, M)$. We compute the energy loss L_m to non-resonant modes by comparing the energy in the resonant mode after passing the gas target with the energy of an unaltered mode:

$$\begin{aligned} L_m &= 1 - \frac{c\epsilon_0/2 \iiint |c_{NM}(\omega) \text{GH}_{NM}(x, y, \omega)|^2 dx dy d\omega}{c\epsilon_0/2 \iiint |c_{NM}^0(\omega) \text{GH}_{NM}(x, y, \omega)|^2 dx dy d\omega} \\ &= 1 - \frac{\int |c_{NM}(\omega)|^2 d\omega}{\int |c_{NM}^0(\omega)|^2 d\omega}. \end{aligned} \quad (\text{B.4})$$

The total round-trip loss L is the sum of losses L_m to non-resonant modes, losses due to the hole in the output coupling mirror (twice the loss that is caused by transmission through the orifice, also due to coupling to non-resonant modes [68]) and the assumed 0.8% losses of the empty cavity.

The spectral phase shift $\varphi(\omega)$ the pulse experiences while traversing the target can be computed by comparing the phases of the altered and the unaltered mode:

$$\varphi(\omega) = \arg \frac{c_{NM}(\omega)}{c_{NM}^0(\omega)}. \quad (\text{B.5})$$

The choice of the cavity length and the position in the stability range (and of the EC mirrors [30]) allows to compensate for the spectral phase shift by a polynomial of first order. Therefore, we fit a first-order polynomial $p(\omega)$ to $\varphi(\omega)$ (weighted by the spectral intensity) and subtract it to obtain the round-trip spectral phase shift

$$\varphi_{\text{rt}}(\omega) = \varphi(\omega) - p(\omega). \quad (\text{B.6})$$

The round-trip phase shift and loss together allow us to choose the optimum input coupler reflectance r^2 for maximum pulse-energy enhancement. Assuming a steady state in the cavity, the enhancement of a cavity seeded by CW light is [69]

$$E = \frac{1 - r^2}{(1 - rr_1)^2 + 4rr_1 \sin(\varphi_{\text{rt}}/2)} \quad \text{with } r_1 = \sqrt{1 - L}. \quad (\text{B.7})$$

To find a local maximum for $r \in [0, 1]$, we compute the roots of $\partial_r E$, which are

$$r_{\pm} = C \pm \operatorname{sgn} \cos \delta \sqrt{C^2 - 1} \quad \text{with } C = \frac{r_l^2 + 1}{2r_l \cos \delta}. \quad (\text{B.8})$$

Computing the enhancement E for r_+ and r_- and choosing the higher one, requiring $r \in [0, 1]$, yields the optimum pulse-energy enhancement and input coupler reflectance. To generalize to broad-band pulses, we apply this procedure for each wavelength and average over the results, again weighted by the spectral intensity.

Appendix C. Envelope approximation for the Kerr source term

Given complex envelope $\tilde{E}_{\text{IR}}(t)$, the electric field is $E_{\text{IR}}(t) = \Re\{\tilde{E}_{\text{IR}}(t) \exp i\omega_c t\}$. Neglecting terms oscillating at $3\omega_c$, which describe harmonic generation, (2) can be written as

$$P_{\text{Kerr}} \approx \Re\{\epsilon_0 \chi^{(3)} / 4 |\tilde{E}_{\text{IR}}|^2 \tilde{E}_{\text{IR}} \exp i\omega_c t\} = \Re\{\tilde{P}_{\text{Kerr}}(t) \exp i\omega_c t\} \quad (\text{C.1})$$

with the source term envelope

$$\tilde{P}_{\text{Kerr}}(t) = \epsilon_0 \chi^{(3)} / 4 |\tilde{E}_{\text{IR}}|^2 \tilde{E}_{\text{IR}}. \quad (\text{C.2})$$

Appendix D. Envelope approximation for the plasma source term

For the plasma source term $J = \partial_t P_{\text{plasma}}$, we employ the envelope approximation to (3) as suggested in [18]:

$$\tilde{J}(t) = \left[i\tilde{r}_0 \lambda n_0 \tilde{\eta} - I_p n_0 \frac{(1 - \tilde{\eta}) w_{\text{peak}}}{4I} \right] \tilde{E}_{\text{IR}} / \frac{-\mu_0 c}{2}. \quad (\text{D.1})$$

The source term envelope $\tilde{P}(t) = \mathcal{F}^{-1}\{P(\omega + \omega_c)\}(t)$ can be computed from $P(\omega) = -i/\omega \cdot J(\omega) = -i/\omega \cdot \mathcal{F}\{\tilde{J}(t)\}(\omega - \omega_c)$ without resorting to finer time discretization.

Here, \mathcal{F} denotes temporal Fourier transform, r_0 is the classical electron radius, $\tilde{\eta}(t)$ is the ionization fraction computed from cycle-averaged ionization rates, w_{peak} is the ionization rate at the electric field maximum of the cycle and I is the intensity.

Appendix E. Envelope approximation for the XUV source term

We obtain an envelope approximation for the XUV source term by approximating the linearly polarized driving electric field locally by a CW field and then using precomputed dipole responses. This leads to a significant speedup in the calculation of the dipole response, because the envelope approximation allows coarser time discretization and the lookup of precomputed responses is fast.

We denote the harmonic dipole response obtained from the SFA with neglected ground state depletion for a cosine driving field $A \cos(\omega_c t)$ by $d_{\text{cos}}(A, t)$. Delaying the driving field by $-\Delta t$ just delays the harmonic response correspondingly, therefore the dipole response for a delayed cosine driving field $A \cos(\omega_c(t + \Delta t))$ is $d_{\text{cos}}(A, t + \Delta t)$.

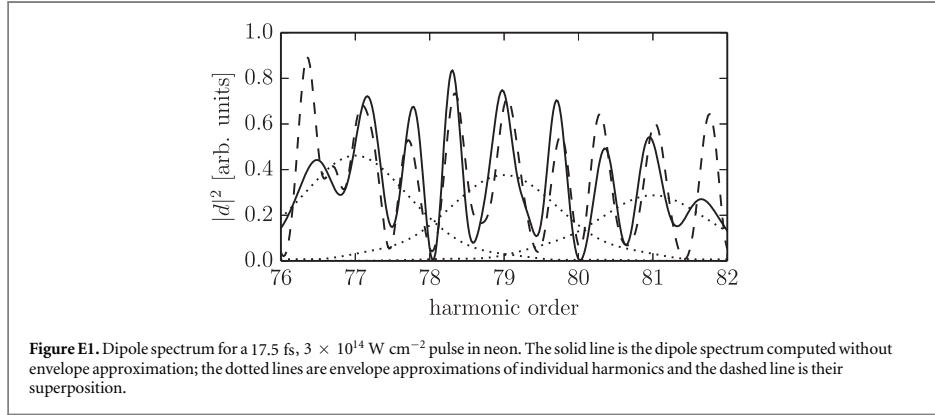
Now, provided that the complex driving field envelope $\tilde{E}_{\text{IR}}(t)$ varies slowly compared to one cycle, we can approximate the driving field $E_{\text{IR}}(t)$ in the vicinity of t' by

$$\begin{aligned} E_{\text{IR}}(t) &= \Re\{\tilde{E}_{\text{IR}}(t) \exp i\omega_c t\} \approx \Re\{\tilde{E}_{\text{IR}}(t') \exp i\omega_c t\} \\ &= |\tilde{E}_{\text{IR}}(t')| \cdot \cos[\omega_c t + \arg E_{\text{IR}}(t')] \\ &= |\tilde{E}_{\text{IR}}(t')| \cdot \cos[\omega_c(t + \arg E_{\text{IR}}(t')/\omega_c)], \end{aligned} \quad (\text{E.1})$$

which is a cosine field with the amplitude $A = |\tilde{E}_{\text{IR}}(t')|$, delayed by $\Delta t = \arg E_{\text{IR}}(t')/\omega_c$. The dipole response to such a CW driving field would be

$$\begin{aligned} d_{\text{CW}}(t) &= d_{\text{cos}}(|A|, t + \Delta t) \\ &= d_{\text{cos}}(|\tilde{E}_{\text{IR}}(t')|, t + \arg E_{\text{IR}}(t')/\omega_c). \end{aligned} \quad (\text{E.2})$$

Neglecting long-timescale effects like ground state depletion and considering that the time scale on which HHG happens, which is given by the electron excursion time, is typically below one cycle, we can use $d_{\text{CW}}(t)$ as an approximation of the real dipole response $d(t)$ in the vicinity of t' . Applying this approximation for all t' and selecting the contribution of a single harmonic order will lead us to an envelope approximation for the dipole response.



For convenience, we express the cosine dipole response for each amplitude as a Fourier series

$$d_{\cos}(A, t) = \Re \left[\sum_q c_q(A) \exp(iq\omega_c t) \right], \quad (\text{E.3})$$

where q is the harmonic order. The harmonic spectra $c_q(A)$ can then be precomputed for each amplitude A . Substituting yields

$$\begin{aligned} d(t) &\approx d_{\text{CW}}(t) \\ &= d_{\cos}(|E_{\text{IR}}(t)|, t + \arg E_{\text{IR}}(t)/\omega_c) \\ &= \Re \left[\sum_q c_q(|E_{\text{IR}}(t)|) \exp[iq\omega_c(t + \arg E_{\text{IR}}(t)/\omega_c)] \right]. \end{aligned} \quad (\text{E.4})$$

This formula allows to only consider the contribution $d_q(t)$ from a single harmonic order q by choosing only one term of the series:

$$d_q(t) \approx \Re \{ c_q(|E_{\text{IR}}(t)|) \exp[iq\omega_c(t + \arg E_{\text{IR}}(t)/\omega_c)] \}. \quad (\text{E.5})$$

Until now, we inherently assumed that HHG happens instantaneously. In reality, this is not the case—in the three-step model, the emitted electron travels some time before recombination happens. Further, the ground state of the atom gets depleted due to partial ionization. We can account for both effects in a limited manner by multiplying the dipole response by the squared absolute value of the ground state amplitude $|a(t)|^2 = 1 - \eta(t)$, where $\eta(t)$ is the ionization fraction, and introducing an artificial lag Δt , which will in general depend on the harmonic order q and on the considered trajectory:

$$\begin{aligned} d_q(t) &\approx \Re \{ |a(t - \Delta t)|^2 c_q(|E_{\text{IR}}(t - \Delta t)|) \\ &\quad \cdot \exp[iq\omega_c(t - \Delta t + \arg E_{\text{IR}}(t - \Delta t)/\omega_c)] \}. \end{aligned} \quad (\text{E.6})$$

We can decompose $d_q(t)$ into an envelope and a rapidly oscillating term, $d_q(t) = \Re \{ \tilde{d}_q(t) \exp iq\omega_c t \}$, with

$$\begin{aligned} \tilde{d}_q(t) &\approx |a(t - \Delta t)|^2 c_q(|E_{\text{IR}}(t - \Delta t)|) \\ &\quad \cdot \exp[-iq\omega_c \Delta t] \cdot \exp[iq \arg E_{\text{IR}}(t - \Delta t)]. \end{aligned} \quad (\text{E.7})$$

This envelope can be computed without the requirement of sub-cycle time resolution.

We verify the approximation by computing the dipole spectrum around H79 in neon for a 17.5 fs gaussian pulse with a peak intensity of 3×10^{14} W cm⁻². The CW spectra $c_q(A)$ are precomputed with the SFA model with limited excursion time to suppress the long trajectory. We compute the dipole spectrum without envelope approximation, and the envelope approximation for H77, H79 and H81, which overlap due to the short pulse duration. As can be seen in figure E1, their superposition is a good approximation around H79, while the agreement gets worse further away because neighboring harmonics were not considered. The lag was chosen equally for the three neighboring harmonics to be $0.12T$, where T is the duration of one cycle, to get optimum overlap.

In the limit of long pulses, the envelope $\tilde{d}_q(t)$ can be regarded as the scaled envelope of an attosecond pulse train obtained by spectral filtering around the harmonic order q : for long pulses, the individual harmonics do not overlap. Then, the spectrum of $\tilde{d}_q(t)$ is a good approximation to the spectrum of the SFA dipole response $d(t)$ in the spectral range from harmonic order $q - 1$ to $q + 1$. This also means that we can obtain $d_q(t)$ by applying a

bandfilter to $d(t)$ around the harmonic order q with a bandwidth of two harmonic orders. In the time domain, after eliminating the oscillation with frequency $q\omega_c$, this bandfilter corresponds to a convolution with a half-cycle-long time window, therefore smoothing out the individual bursts of the attosecond pulse train $d(t)$. We can conclude that $\tilde{d}_q(t)$ is the smoothed-out version of the attosecond pulse train $d(t)$, which is approximately proportional to the envelope of the pulse train if the individual bursts have similar pulse durations.

References

- [1] Krausz F and Ivanov M 2009 Attosecond physics *Rev. Mod. Phys.* **81** 163–234
- [2] Hentschel M, Kienberger R, Spielmann C, Reider G A, Milosevic N, Brabec T, Corkum P, Heinzmann U, Drescher M and Krausz F 2001 Attosecond metrology *Nature* **414** 509–13
- [3] Krausz F and Stockman M I 2014 Attosecond metrology: from electron capture to future signal processing *Nat. Photon.* **8** 205–13
- [4] Backus S, Bartels R, Thompson S, Dollinger R, Kapteyn H C and Murnane M M 2001 High-efficiency, single-stage 7 kHz high-average-power ultrafast laser system *Opt. Lett.* **26** 465
- [5] Sansone G et al 2010 Electron localization following attosecond molecular photoionization *Nature* **465** 763–6
- [6] Stockman M I, Kling M F, Kleinberg U and Krausz F 2007 Attosecond nanoplasmonic-field microscope *Nat. Photon.* **1** 539–44
- [7] Chew S H et al 2012 Time-of-flight-photoelectron emission microscopy on plasmonic structures using attosecond extreme ultraviolet pulses *Appl. Phys. Lett.* **100** 051904
- [8] Förg B et al 2016 Attosecond nanoscale near-field sampling *Nat. Commun.* **7** 11717
- [9] Moore J E 2010 The birth of topological insulators *Nature* **464** 194–8
- [10] Gohle C, Udem T, Herrmann M, Rauschenberger J, Holzwarth R, Schuessler H A, Krausz F and Hänsch T W 2005 A frequency comb in the extreme ultraviolet *Nature* **436** 234–7
- [11] Jones R, Moll K, Thorpe M and Ye J 2005 Phase-coherent frequency combs in the vacuum ultraviolet via high-harmonic generation inside a femtosecond enhancement cavity *Phys. Rev. Lett.* **94** 193201
- [12] Carstens H et al 2014 Megawatt-scale average-power ultrashort pulses in an enhancement cavity *Opt. Lett.* **39** 2595
- [13] Carstens H et al 2016 High-harmonic generation at 250 MHz with photon energies exceeding 100 eV *Optica* **3** 366
- [14] Benko C, Allison T K, Cingöz A, Hua L, Labaye F, Yost D C and Ye J 2014 Extreme ultraviolet radiation with coherence time greater than 1 s *Nat. Photon.* **8** 530–6
- [15] Cingöz A, Yost D C, Allison T K, Ruehl A, Fermann M E, Hartl I and Ye J 2012 Direct frequency comb spectroscopy in the extreme ultraviolet *Nature* **482** 68–71
- [16] Carstens H, Holzberger S, Kaster J, Weitenberg J, Pervak V, Apolonski A, Fill E, Krausz F and Pupeza I 2013 Large-mode enhancement cavities *Opt. Express* **21** 11606
- [17] Carlson D R, Lee J, Mongelli J, Wright E M and Jones R J 2011 Intracavity ionization and pulse formation in femtosecond enhancement cavities *Opt. Lett.* **36** 2991–3
- [18] Allison T K, Cingöz A, Yost D C and Ye J 2011 Extreme nonlinear optics in a femtosecond enhancement cavity *Phys. Rev. Lett.* **107** 183903
- [19] Holzberger S et al 2015 Femtosecond enhancement cavities in the nonlinear regime *Phys. Rev. Lett.* **115** 023902
- [20] Lilienfein N, Hofer C, Holzberger S, Matzer C, Zimmermann P, Trubetskov M, Pervak V and Pupeza I 2017 Enhancement cavities for few-cycle pulses *Opt. Lett.* **42** 271
- [21] Russbueldt P et al 2015 Innoslab amplifiers *IEEE J. Sel. Top. Quantum Electron.* **21** 447–63
- [22] Pronin O, Seidel M, Lücking F, Brons J, Fedulova E, Trubetskov M, Pervak V, Apolonski A, Udem T and Krausz F 2015 High-power multi-megahertz source of waveform-stabilized few-cycle light *Nat. Commun.* **6** 6988
- [23] Hädrich S et al 2016 Energetic sub-2-cycle laser with 216 W average power *Opt. Lett.* **41** 4332
- [24] Mills A K, Hammond T J, Lam M H C and Jones D J 2012 XUV frequency combs via femtosecond enhancement cavities *J. Phys. B: At. Mol. Opt. Phys.* **45** 142001
- [25] Pupeza I, Högner M, Weitenberg J, Holzberger S, Esser D, Eidam T, Limpert J, Tünnermann A, Fill E and Yakovlev V S 2014 Cavity-enhanced high-harmonic generation with spatially tailored driving fields *Phys. Rev. Lett.* **112** 103902
- [26] Moll K D, Jones R J and Ye J 2006 Output coupling methods for cavity-based high-harmonic generation *Opt. Express* **14** 8189
- [27] Lilienfein N, Carstens H, Holzberger S, Jocher C, Eidam T, Limpert J, Tünnermann A, Apolonski A, Krausz F and Pupeza I 2015 Balancing of thermal lenses in enhancement cavities with transmissive elements *Opt. Lett.* **40** 843
- [28] Lücking F, Crozatier V, Forget N, Assion A and Krausz F 2014 Approaching the limits of carrier-envelope phase stability in a millijoule-class amplifier *Opt. Lett.* **39** 3884
- [29] Saule T, Holzberger S, DeVries O, Plötner M, Limpert J, Tünnermann A and Pupeza I 2017 Phase-stable, multi- μ J femtosecond pulses from a repetition-rate tunable Ti:Sa-oscillator-seeded Yb-fiber amplifier *Appl. Phys. B* **123** 17
- [30] Holzberger S, Lilienfein N, Trubetskov M, Carstens H, Lücking F, Pervak V, Krausz F and Pupeza I 2015 Enhancement cavities for zero-offset-frequency pulse trains *Opt. Lett.* **40** 2165
- [31] Couairon A, Brambilla E, Corti T, Majus D, Ramírez-Góngora O D J and Kolesik M 2011 Practitioner's guide to laser pulse propagation models and simulation *Eur. Phys. J. Spec. Top.* **199** 5–76
- [32] Brabec T and Krausz F 1997 Nonlinear optical pulse propagation in the single-cycle regime *Phys. Rev. Lett.* **78** 3282
- [33] Boyd R W 2008 The intensity-dependent refractive index *Nonlinear Optics* 3rd eds (Burlington: Academic) ch 4 pp 207–52
- [34] Geissler M, Tempea G, Scrinzi A, Schnürer M, Krausz F and Brabec T 1999 Light propagation in field-ionizing media: extreme nonlinear optics *Phys. Rev. Lett.* **83** 2930
- [35] Lewenstein M, Balcou P, Ivanov M Y, L'huillier A and Corkum P B 1994 Theory of high-harmonic generation by low-frequency laser fields *Phys. Rev. A* **49** 2117
- [36] Antoine P, L'huillier A, Lewenstein M, Salières P and Carré B 1996 Theory of high-order harmonic generation by an elliptically polarized laser field *Phys. Rev. A* **53** 1725
- [37] Cao W, Lu P, Lan P, Wang X and Yang G 2006 Single-attosecond pulse generation with an intense multicycle driving pulse *Phys. Rev. A* **74** 063821
- [38] Bideau-Mehu A, Guern Y, Abjean R and Johannin-Gilles A 1981 Measurement of refractive indices of neon, argon, krypton and xenon in the 253.7–140.4 nm wavelength range. Dispersion relations and estimated oscillator strengths of the resonance lines *J. Quant. Spectrosc. Radiat. Transfer* **25** 395–402

- [39] Chantler C T, Olsen K, Dragoset R A, Chang J, Kishore A R, Kotochigova S A and Zucker D S 2005 *X-Ray Form Factor, Attenuation and Scattering Tables (version 2.1)* National Institute of Standards and Technology, Gaithersburg, MD (<http://physics.nist.gov/ffast>)
- [40] Wahlstrand J K, Cheng Y-H and Milchberg H M 2012 High field optical nonlinearity and the kramers-kronig relations *Phys. Rev. Lett.* **109** 113904
- [41] Scrinzi A 2015 private communication
- [42] Scrinzi A, Geissler M and Brabec T 1999 Ionization above the coulomb barrier *Phys. Rev. Lett.* **83** 706
- [43] Scrinzi A 2000 Ionization of multielectron atoms by strong static electric fields *Phys. Rev. A* **61** 041402
- [44] Majety V P and Scrinzi A 2015 Static field ionization rates for multi-electron atoms and small molecules *J. Phys. B: At. Mol. Opt. Phys.* **48** 245603
- [45] Voelz D G 2011 Computational fourier optics a MATLAB® tutorial *Number 89 in Tutorial texts in Optical Engineering* (Bellingham, Wash: SPIE Press)
- [46] Yu L, Huang M, Chen M, Chen W, Huang W and Zhu Z 1998 Quasi-discrete hankel transform *Opt. Lett.* **23** 409–11
- [47] Högner M 2015 HHGmax <http://attoworld.de/hhgmax/>
- [48] Tosa V, Lee J S, Kim H T and Nam C H 2015 Attosecond pulses generated by the lighthouse effect in Ar gas *Phys. Rev. A* **91** 051801
- [49] Goulielmakis E et al 2008 Single-cycle nonlinear optics *Science* **320** 1614–7
- [50] Ferrari F, Calegari F, Lucchini M, Vozzi C, Stagira S, Sansone G and Nisoli M 2010 High-energy isolated attosecond pulses generated by above-saturation few-cycle fields *Nat. Photon.* **4** 875–9
- [51] Abel M J, Pfeifer T, Nagel P M, Boutu W, Bell M J, Steiner C P, Neumark D M and Leone S R 2009 Isolated attosecond pulses from ionization gating of high-harmonic emission *Chem. Phys.* **366** 9–14
- [52] Tcherbakoff O, Mével E, Descamps D, Plumridge J and Constant E 2003 Time-gated high-order harmonic generation *Phys. Rev. A* **68** 043804
- [53] Charalambidis D, Tzallas P, Benis E P, Skantzakis E, Maravelias G, Nikolopoulos L A A, Conde A P and Tsakiris G D 2008 Exploring intense attosecond pulses *New J. Phys.* **10** 025018
- [54] Koliopoulos G, Carpeggiani P A, Rompotis D, Charalambidis D and Tzallas P 2012 A compact collinear polarization gating scheme for many cycle laser pulses *Rev. Sci. Instrum.* **83** 063102
- [55] Vozzi C, Calegari F, Frassetto F, Poletto L, Sansone G, Villorosi P, Nisoli M, Silvestri S D and Stagira S 2009 Coherent continuum generation above 100 eV driven by an ir parametric source in a two-color scheme *Phys. Rev. A* **79** 033842
- [56] Feng X, Gilbertson S, Mashiko H, Wang H, Khan S D, Chini M, Wu Y, Zhao K and Chang Z 2009 Generation of isolated attosecond pulses with 20 to 28 femtosecond lasers *Phys. Rev. Lett.* **103** 183901
- [57] Heyl C M, Rudawski P, Brizuela F, Bengtsson S N, Mauritsson J and L'Huillier A 2014 Macroscopic effects in noncollinear high-order harmonic generation *Phys. Rev. Lett.* **112** 143902
- [58] Vincenti H and Quéré F 2012 Attosecond Lighthouses: how to use spatiotemporally coupled light fields to generate isolated attosecond pulses *Phys. Rev. Lett.* **108** 113904
- [59] Kim K T, Zhang C, Ruchon T, Hergott J-F, Auguste T, Villeneuve D M, Corkum P B and Quéré F 2013 Photonic streaking of attosecond pulse trains *Nat. Photon.* **7** 651–6
- [60] Hammond T J, Brown G G, Kim K T, Villeneuve D M and Corkum P B 2016 Attosecond pulses measured from the attosecond lighthouse *Nat. Photon.* **10** 171–5
- [61] Heyl C M, Bengtsson S N, Carlström S, Mauritsson J, Arnold C L and L'Huillier A 2014 Corrigendum: noncollinear optical gating *New J. Phys.* **16** 052001
- [62] Heyl C M, Bengtsson S N, Carlström S, Mauritsson J, Arnold C L and L'Huillier A 2014 *New J. Phys.* **16** 109501
- [63] Louisy M et al 2015 Gating attosecond pulses in a noncollinear geometry *Optica* **2** 563
- [64] Zhong S, He X, Jiang Y, Teng H, He P, Liu Y, Zhao K and Wei Z 2016 Noncollinear gating for high-flux isolated-attosecond-pulse generation *Phys. Rev. A* **93** 033854
- [65] Heyl C M et al 2016 Scale-invariant nonlinear optics in gases *Optica* **3** 75
- [66] Altucci C et al 2001 Beam divergence of high-order harmonics generated in the few-optical cycle regime *J. Phys. IV* **11** Pr2-351–Pr2-354
- [67] Weitenberg J, Rußbüldt P, Pupeza I, Udem T, Hoffmann H-D and Poprawe R 2015 Geometrical on-axis access to high-finesse resonators by quasi-imaging: a theoretical description *J. Opt.* **17** 025609
- [68] Seidel M, Arisholm G, Brons J, Pervak V and Pronin O 2016 All solid-state spectral broadening: an average and peak power scalable method for compression of ultrashort pulses *Opt. Express* **24** 9412
- [69] Pupeza I et al 2013 Compact high-repetition-rate source of coherent 100 eV radiation *Nat. Photon.* **7** 608–12
- [69] Nagourney W 2010 *Quantum Electronics for Atomic Physics* (Oxford: Oxford University Press)

4.2 Tailoring the Transverse Mode of a High-Finesse Optical Resonator with Stepped Mirrors

as published in

Journal of Optics (2018)

[87]

by

Maximilian Högner, Tobias Saule, Nikolai Lilienfein, Volodymyr Pervak, and
Ioachim Pupeza

Contributions I planned, set up, executed, and evaluated the experiment, with help from coworkers, and wrote most of the manuscript.

OPEN ACCESS

IOP Publishing

Journal of Optics

J. Opt. 20 (2018) 024003 (6pp)

<https://doi.org/10.1088/2040-8986/aa9ece>

Tailoring the transverse mode of a high-finesse optical resonator with stepped mirrors

M Högner^{1,2} , T Saule^{1,2}, N Lilienfein^{1,2}, V Pervak² and I Pupeza^{1,2,3} 

¹Max-Planck-Institut für Quantenoptik, Hans-Kopfermann-Straße 1, D-85748 Garching, Germany

²Ludwig-Maximilians-Universität München, Am Coulombwall 1, D-85748 Garching, Germany

E-mail: ioachim.pupeza@mpq.mpg.de

Received 30 June 2017, revised 27 October 2017

Accepted for publication 1 December 2017

Published 5 January 2018



CrossMark

Abstract

Enhancement cavities (ECs) seeded with femtosecond pulses have developed into the most powerful technique for high-order harmonic generation (HHG) at repetition rates in the tens of MHz. Here, we demonstrate the feasibility of controlling the phase front of the excited transverse eigenmode of a ring EC by using mirrors with stepped surface profiles, while maintaining the high finesse required to reach the peak intensities necessary for HHG. The two lobes of a TEM₀₁ mode of a 3.93 m long EC, seeded with a single-frequency laser, are delayed by 15.6 fs with respect to each other before a tight focus, and the delay is reversed after the focus. The tailored transverse mode exhibits an on-axis intensity maximum in the focus. Furthermore, the geometry is designed to generate a rotating wavefront in the focus when few-cycle pulses circulate in the EC. This paves the way to gating isolated attosecond pulses (IAPs) in a transverse manner (similarly to the attosecond lighthouse), heralding IAPs at repetition rates well into the multi-10 MHz range. In addition, these results promise high-efficiency harmonic output coupling from ECs in general, with an unparalleled power scalability. These prospects are expected to tremendously benefit photoelectron spectroscopy and extreme-ultraviolet frequency comb spectroscopy.

Keywords: enhancement cavity, tailored transverse mode, high harmonic generation, gating method, isolated attosecond pulses, output coupling

(Some figures may appear in colour only in the online journal)

1. Introduction

The availability of isolated attosecond pulses (IAPs), produced by high-order harmonic generation (HHG), has enabled the observation of attosecond-time-scale dynamics in atoms, molecules, solids and plasmas [1, 2]. While considerable progress has been made scaling up the photon flux at repetition rates below 1 MHz [3], some applications require increasing the repetition rate rather than the number of

photons per shot. This is the case for experiments involving the detection of charged particles, where the number of photons per shot is limited by the detection scheme, e.g. coincidence spectroscopy or time-resolved photo-electron emission spectroscopy and microscopy. One application that could particularly benefit from multi-10 MHz IAPs is time-resolved photo-electron microscopy of nano-plasmonic fields [4–6].

Coherently stacking the pulses of a high-repetition-rate modelocked femtosecond laser inside of a passive optical resonator (or enhancement cavity (EC)) provides a convenient way to reach the required peak intensities for HHG, on the order of $1 \times 10^{14} \text{ W cm}^{-2}$, at repetition rates of several tens of MHz. Recent progress in power scaling and increasing the bandwidth of ECs has allowed to produce attosecond pulse trains with photon energies exceeding 100 eV at repetition

³ Author to whom any correspondence should be addressed.

 Original content from this work may be used under the terms of the [Creative Commons Attribution 3.0 licence](https://creativecommons.org/licenses/by/3.0/). Any further distribution of this work must maintain attribution to the author(s) and the title of the work, journal citation and DOI.

J. Opt. 20 (2018) 024003

M Högner et al

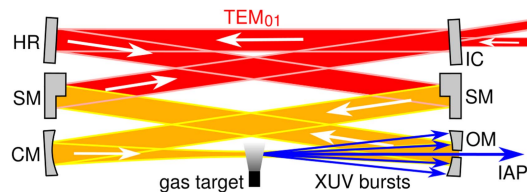


Figure 1. Working principle of transverse mode gating. IC: input coupler, HR: highly reflective mirror, SM: HR mirror with a stepped surface profile, CM: curved HR mirror, OM: curved HR mirror with a slit for output coupling, IAP: isolated attosecond pulse.

rates as high as 250 MHz [7]. Since then, the bandwidth of EC mirrors has been pushed further with the most broadband high-finesse near-infrared EC to date supporting 5-cycle pulses at a central wavelength of 1050 nm [8].

At present, dielectric multi-layer optics that allow the enhancement of near-single-cycle pulses do not seem feasible. Thus, to isolate attosecond pulses from ECs, it is necessary to implement a gating scheme. In [9], several methods have been evaluated and a new scheme termed *transverse mode gating* (TMG), similar to non-collinear optical gating [10], was identified as the preferred method in terms of robustness and expected photon flux. In TMG, a TEM_{01} mode is excited, which consists of two lobes of contrary phase, separated by an intensity minimum. One of the lobes is delayed with respect to the other by means of an EC mirror with a stepped surface profile (figure 1). After the focus, this delay is reversed by a second, identical mirror. To achieve an on-axis intensity maximum in the focus, the delay is chosen as an odd number of optical half-cycles [11]. The introduced delay leads to a wave-front rotation (WFR) in the focus and therefore to angular dispersion of the individual harmonic bursts produced in a gas target, allowing the selection of an IAP by spatial filtering. A mirror with a slit can be used for efficient output coupling while introducing negligible losses to the excited eigenmode, which has an on-axis intensity minimum on the mirror [12, 13]. Assuming a state-of-the-art EC [7, 8] and $0.7 \mu\text{J}$, phase-stable 17.5 fs seeding pulses centered at 1040 nm, parameters that are within reach with current Yb-based lasers [14, 15], thorough simulations predict that it is possible to generate IAPs with photon energies around 94 eV at a photon flux of $1 \times 10^8 \text{ s}^{-1}$ in a 2% bandwidth, at repetition rates of 10 MHz and higher [9].

Here, we present an experimental milestone towards the realization of such a source: we produce stepped mirrors and use them to introduce and compensate a delay between the two lobes of a TEM_{01} mode excited in a high-finesse resonator seeded with a single-frequency laser. The observation of an on-axis maximum in the focus is proof that the lobes are indeed shifted by a phase corresponding to the introduced delay, which is confirmed by simulations in excellent agreement to the experimental data. As the size of the mode on the mirrors and the focus size demonstrated in this experiment are in concordance with the parameters assumed for the 3+1D TMG simulations in [9], the demonstrated geometry can be expected to allow for the efficient generation of multi-MHz

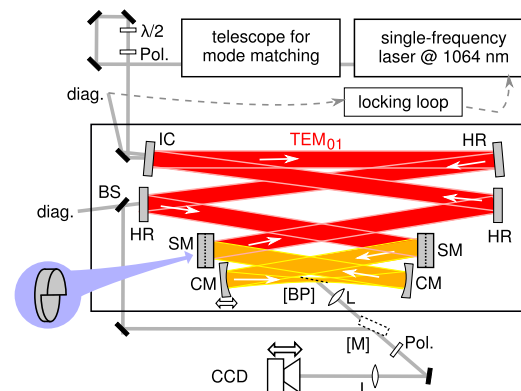


Figure 2. Experimental setup for the high-finesse enhancement cavity with stepped mirrors. $\lambda/2$: half-wave plate, Pol.: wire-grid polarizer, IC: input coupler, HR: highly reflective mirror, SM: HR mirror with a stepped surface profile, CM: curved HR mirror, BP: optional Brewster plate, L: lens, BS: beam splitter, diag.: diagnostics, M: optional mirror, CCD: camera on a translation stage.

IAPs when combined with state-of-the-art broadband mirror coatings, a high-power waveform-stable few-cycle seed and a mirror with a geometrical opening for output coupling.

2. Methods

We set up a 3.93 m long EC (figure 2), corresponding to a repetition rate of 76.3 MHz, which is similar to the repetition rate used for intracavity HHG in [16]. The geometry was chosen according to the parameters given in [9]. The EC consists of focusing mirrors with a radius of curvature of 300 mm, an input coupler with a reflectivity of 99.4% and two mirrors with a stepped surface profile. The step edge was oriented parallel to the optical plane. We operated the EC near the inner stability edge, so that the cavity arm containing the input coupler is collimated well, which is desirable for power scaling [17]. The stepped mirrors should be imaged onto each other to keep the losses of the excited mode low [9]. We placed the stepped mirrors at a distance of 10.5 mm from the curved mirrors, so that a small angle of incidence on the curved mirrors can be achieved while still being close to the imaging condition. The stepped mirrors were manufactured by sputtering $2.34 \mu\text{m}$ of SiO_2 on one half of the mirror substrate before applying the highly-reflective multi-layer coating. The height of the step determines the introduced delay, which is 15.6 fs, or 4.5 cycles of 1040 nm light. In order to prevent length fluctuations due to air movement, the EC was enclosed in a housing.

We seeded the EC with the TEM_{00} mode of a 1064 nm single-frequency laser (Coherent Mephisto S) with a maximum power of 0.5 W, which was linearly polarized in p direction. The seeding laser wavelength was locked to the EC with a Pound–Drever–Hall scheme. The seed was aligned for optimum spatial overlap with the phase-shifted TEM_{01} mode,

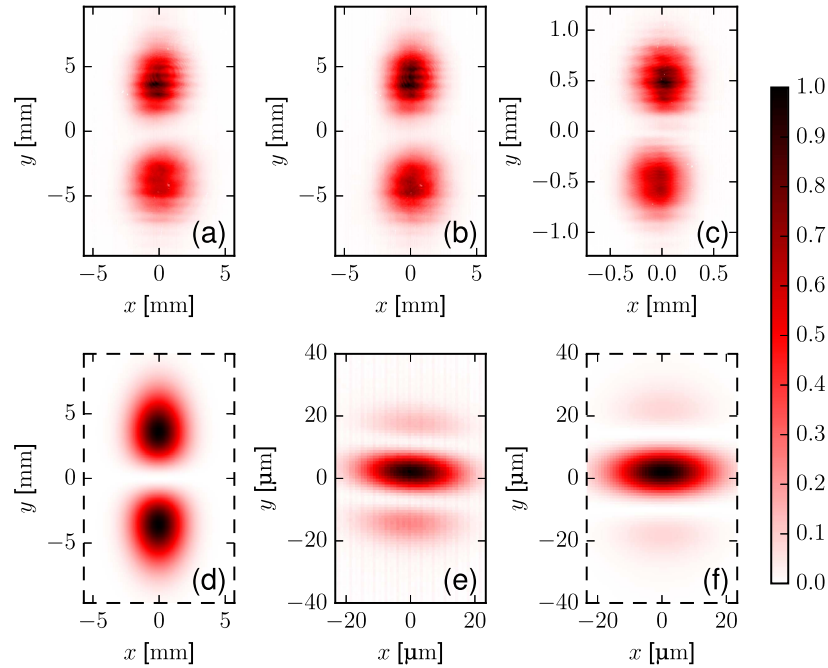


Figure 3. (a) Measured intensity profile on the plane mirror for the cavity without Brewster plate. (b) Measured profile on the plane mirror for the cavity with Brewster plate. (c) Measured profile 19.6 mm before focus, imaged via the Brewster plate. (d) Fit of a TEM_{01} to (a). (e) Measured profile at the focus, imaged via the Brewster plate. (f) Fit of a phase-shifted TEM_{01} to (e). All images are normalized to the same maximum intensity and the scaling of the y axis fits the scaling of the x axis.

which is obtained by offsetting the incoming beam to overlap with one of its lobes.

Near the focus of the EC, we placed a 100 nm thick silicon nitride Brewster plate which allowed us to image the focal region onto a camera placed on a translation stage. To suppress s polarization, which is preferentially reflected off the BP, we used a wire-grid polarizer placed between the BP and the camera. The BP was placed on a magnetic stage, so that the EC could be switched easily between operation with and without the BP.

3. Results

In the first experiment, we operated the EC without the BP and measured the profile of the eigenmode in transmission through a plane, highly reflective mirror, imaging the mirror surface. Figure 3(a) shows the excited mode, with equal scaling for both axes, and figure 3(d) shows a fit of a TEM_{01} intensity profile to the data. From the fit, we obtain a mode size of $w_x \times w_y = 2.6 \text{ mm} \times 5.1 \text{ mm}$, corresponding to a beam waist of $w_{0,x} \times w_{0,y} = 19 \text{ } \mu\text{m} \times 10 \text{ } \mu\text{m}$, i.e. Rayleigh ranges of 1105 μm in the horizontal and 296 μm in the vertical direction. Here, $w_{x/y} = \lambda / |\text{Im}(\pi/q_{x/y})|$ and $w_{0,x/y} = \sqrt{\lambda |\text{Im}(q_{x/y}/\pi)|}$ were obtained from the complex beam parameter $q_{x/y}$, and the wavelength $\lambda = \text{SI1064nm}$ assuming a wave-front radius of curvature of 150 mm as given by the focusing mirrors. From

the reflected and transmitted powers, we obtain a finesse of 652, corresponding to a round-trip loss of 0.36%. The seed power was enhanced by a factor of 97, at a spatial overlap with the seed of 37%. Theoretically, the spatial overlap can be improved to 82.7% [18] by means of cylindrical lenses and phase masks placed before the EC, which would increase the enhancement to 217. The lock was equally stable as for the operation of the cavity without stepped mirrors at the same position in the stability range. By rotating the wire-grid polarizer placed before the camera by 90° , it was possible to extinguish the signal, confirming that the eigenmode is linearly polarized in p direction.

In a second configuration, the BP was introduced, while still imaging the plane mirror. To avoid extreme suppression of p-polarization versus residual s-polarized light when imaging the focus region later, resulting in measurement artifacts, we placed the BP moderately detuned from Brewster's angle. This led to a drop in power enhancement by a factor of 5.7. However, the cavity mode did not change notably (figure 3(b)). Next, the focal region was imaged via reflection from the BP. Remaining s-polarized light was filtered out by a wire-grid polarizer placed before the camera. First, the plane 19.6 mm before the focus, i.e. well in the far field, was imaged. The intensity profile matched the one measured in transmission through the EC mirror (figure 3(c)). Next, the CCD was moved to image the focal plane. A clear on-axis

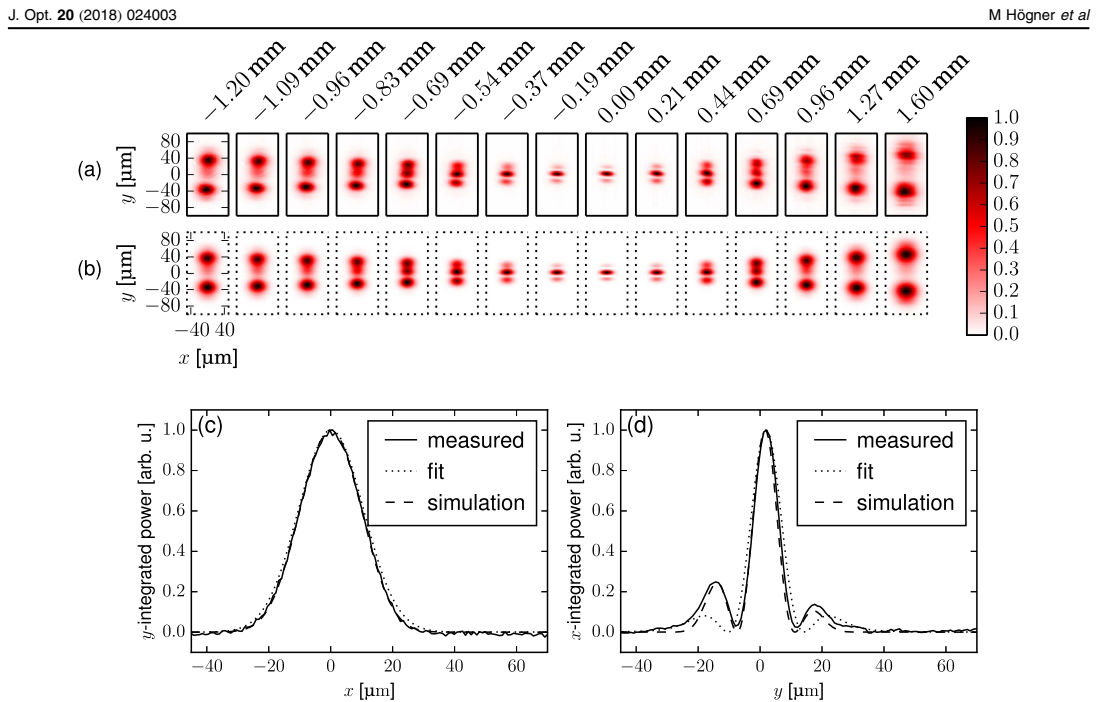


Figure 4. (a) Transverse intensity profiles of the measured resonator mode at different positions near the focus. (b) Comparison with the simulation results. (c) Intensity profile of the measured resonator mode (solid line) in the focus, integrated over the y coordinate. The dotted line shows a fitted TEM_{01} mode with one lobe phase-shifted by π and the dashed line the result of a simulation, accounting for spherical aberrations of the curved mirrors. (d) Intensity profiles, integrated over the x coordinate.

maximum was obtained, as expected for a TEM_{01} of which one lobe was phase-shifted by approximately half a wavelength (figure 3(e)). To determine the actual focus size, the focal intensity profile of an accordingly phase-shifted TEM_{01} was fitted, yielding a beam waist of $w_{0,x} \times w_{0,y} = 21 \mu\text{m} \times 13 \mu\text{m}$ (figure 3(f)).

Finally, the region near the focus was scanned by translating the camera. This allowed for the observation of the transition from a mode with an on-axis maximum to the intensity profile of a TEM_{01} (figure 4(a)).

4. Discussion

The measured mode exhibits some notable differences to a TEM_{01} of which one lobe was phase-shifted by π far from the focus: first, the mode profile in the collimated arm of the EC shows weak modulations in the vertical direction, and the upper lobe appears more intense than the lower one (figure 3(a)). Further inspection reveals that the power contained in the upper lobe is in fact equal to the power contained in the lower (51%/49%), i.e. the power of the lower lobe is just spread over a larger area. We attribute this effect to imperfections in the surface profile of the stepped mirrors. The observed modulations are most probably attributed to the fact that the first stepped mirror was not perfectly imaged onto the

second one [9], so that the modification of the mode introduced on the stepped mirror is not completely compensated for.

Another deviation is that the side lobes in the focus are asymmetric and more pronounced than expected from a perfect TEM_{01} with one lobe phase-shifted by π (figures 3(e), (f)). To understand these deviations, we numerically determine the eigenmode of a simulated resonator with the same parameters as in the experiment, using restarted Arnoldi iterations to determine the eigenvectors of a round-trip operator computed on a two-dimensional spatial grid. For this, stepped mirrors with a step height of $2.34 \mu\text{m}$, spherical focusing mirrors with a curvature of 300 mm and a resonator length of 3.93 m were assumed, and the curved mirror separation (300.045 mm) and angle of incidence (1.366°) were chosen such that a fit to the TEM_{01} intensity profile yields a mode size of $2.6 \times 5.1 \text{ mm}$, just as in the experiment. The transverse profile was computed at the same positions near the focus where the mode was imaged in the experiment. The simulated profiles (figure 4(b)) show excellent agreement with the experimental data.

When comparing the measured vertical profile in the focus plane with the simulated one, it can be seen that the asymmetry of the side lobes is reproduced (figure 4(d)). This can be attributed to the slight mismatch between the step height and the laser wavelength: the step height of $2.34 \mu\text{m}$ was chosen to introduce a delay of $2 \times 2.34 \mu\text{m} / 1040 \text{ nm} = 4.5$ cycles, and thus a phase shift of π , for 1040 nm light. This corresponds to a delay of $2 \times 2.34 \mu\text{m} /$

1064 nm = 4.4 cycles, i.e. a phase shift of 0.8π , for the actually used wavelength of 1064 nm. Accordingly, we obtained symmetric side lobes when we repeated the simulation assuming a 1040 nm seed.

The simulation results also reveal the reason why the side lobes are more pronounced than expected (figure 4(d)). Repeating the simulation with a wavelength of 1040 nm and parabolic instead of spherical mirrors, the relative lobe heights of the focal intensity profile of a TEM₀₁ mode with one lobe phase-shifted by π can be reproduced. We conclude that the side-lobes are more pronounced due to the spherical aberrations of the curved mirrors.

In the experiment and in the simulations, we observed a second resonance with a similar power enhancement. The spatial profile of the corresponding mode resembles that of a TEM₀₁ over the whole cavity length. In contrast to the mode shown in figure 4, the phase difference between the lobes is approximately π in the cavity arm delimited by the stepped mirrors and containing the focus, and 0 in the other arm. The resonant frequencies of the two modes differ by about half a free spectral range, so that each can be locked independently.

4.1. Suitability for TMG

When using broadband pulses, each frequency component of the seed will be enhanced independently by the cavity. For each component, the stepped mirrors will cause a different phase shift $\Delta\phi = \omega\Delta t$, where Δt is the delay given by the step height. Reference [9] shows that the losses for frequency components with a phase shift $\Delta\phi \neq \pi$ are even lower than the losses for phase shifts around π , the situation demonstrated here. Therefore, good enhancement can be expected even for broadband pulses, when using suitable mirror coatings.

In [9], it is calculated that IAPs around H79 with a photon flux of 10^8 s^{-1} can be obtained by TMG, assuming a 156 μm long, 4.6 bar neon gas target placed $0.9z_R$ before a 15 μm focus of a circulating Gaussian pulse with a FWHM of 17.5 fs, a pulse energy of 33 μJ , a central wavelength of 1040 nm, and a delay of 7 fs, corresponding to a step height of 2.09 μm . In the resonator geometry demonstrated here, a mode size of 2.6 mm \times 5.1 mm was measured on the cavity mirrors. Assuming that the transverse intensity profile is identical to the one of a TEM₀₁ mode, it follows that the scheme is power-scalable up to a peak power of 2.6 GW without exceeding a maximum peak intensity of $9 \times 10^9 \text{ W cm}^{-2}$ on the mirrors, which was shown to be low enough to avoid damage in commercially available dielectric mirrors [7]. For 17.5 fs pulses, this corresponds to a pulse energy of 48 μJ , which is even higher than the 33 μJ assumed in [9]. Moreover, the measured focus size of 21 $\mu\text{m} \times 13 \mu\text{m} = (16.5 \mu\text{m})^2$ is comparable to the focus size of $(15 \mu\text{m})^2$ assumed in [9]. Consequently, the demonstrated geometry would allow the necessary peak intensities in the focus and a sufficient extreme ultraviolet (XUV) generation volume for efficient TMG.

For TMG with the parameters assumed in [9], one beamlet of the generated on-axis XUV radiation can be

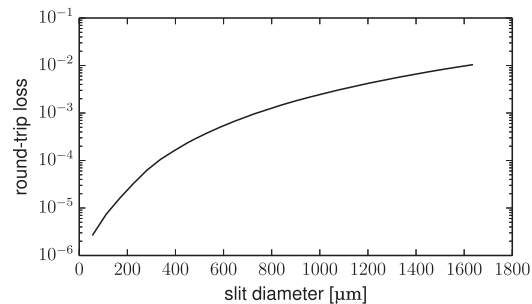


Figure 5. Round-trip losses of the simulated mode due to a slit mirror, versus slit diameter.

efficiently output-coupled through a slit opening with a diameter of $0.05w$ in one curved mirror [9]. This corresponds to a diameter of $0.05 \times 5.1 \text{ mm} = 255 \mu\text{m}$ for the mode size measured here. Figure 5(b) shows that the round-trip loss due to the slit mirror, computed from the simulated mode depicted in figure 4, can be kept on the order of 0.1% for slits as wide as 1000 μm . This would decrease the finesse from 652 to 591 for the input coupler transmission used here.

5. Conclusions

In conclusion, we produced stepped cavity mirrors with a highly reflective coating, and used these mirrors to set up a high-finesse EC which is compatible with operation at the inner stability edge, showing that such mirrors can be fabricated with sufficient profile quality as well as accuracy in the step height.

If the step height is chosen to cause a delay of half a field cycle, such a resonator does not cause significant WFR and constitutes an efficient broadband output coupling method for XUV radiation generated in an intracavity gas target [11]. In contrast to output coupling using superpositions of higher-order modes in degenerate resonators [13, 18, 19], which requires operation in the middle of the stability range, our scheme permits large modes on the EC mirrors so that mirror damage can be avoided when scaling up the power.

Here, the step is chosen high enough to cause intracavity WFR when operating with pulses, such that the demonstrated resonator geometry can be used to generate IAPs at multi-MHz repetition rates. Such an XUV source will find applications in time-resolved spectroscopy/microscopy and for coincidence measurements. It can also be of use for precision spectroscopy with ultra-broadband XUV frequency combs. Simulations in [9] predict that such a scheme can produce IAPs with a photon flux of $9 \times 10^7 \text{ s}^{-1}$ in a 2% bandwidth around 94 eV, assuming 0.7 μJ , 5-cycle pulses from the seeding laser and state-of-the-art broadband coatings for the EC mirrors. The demonstrated resonator geometry supports a comparable generating volume and peak intensities in the target, so that a similar performance can be expected.

To realize such a source, one has to combine the demonstrated geometry with a phase-stable, high-power and few-cycle pulsed seed [15], broadband cavity mirror coatings [8] and a round-trip carrier-envelope phase shift of zero [20], as well as a slit mirror for output coupling [12, 13]. The mode matching can be improved by shaping the seeding beam profile with cylindrical lenses/mirrors and phase masks, and/or by using an input coupler with a half-sided highly-reflective coating.

Acknowledgments

This research was supported by the Fraunhofer Society/Max-Planck Society cooperation 'MEGAS'. We thank Johannes Weitenberg for useful discussions.

ORCID iDs

M Högner  <https://orcid.org/0000-0002-6243-802X>
I Pupeza  <https://orcid.org/0000-0001-8422-667X>

References

- [1] Krausz F and Ivanov M 2009 Attosecond physics *Rev. Mod. Phys.* **81** 163–234
- [2] Krausz F and Stockman M I 2014 Attosecond metrology: from electron capture to future signal processing *Nat. Photon.* **8** 205–13
- [3] Krebs M, Hädrich S, Demmler S, Rothhardt J, Zaïr A, Chipperfield L, Limpert J and Tünnermann A 2013 Towards isolated attosecond pulses at megahertz repetition rates *Nat. Photon.* **7** 555–9
- [4] Stockman M I, Kling M F, Kleineberg U and Krausz F 2007 Attosecond nanoplasmonic-field microscope *Nat. Photon.* **1** 539–44
- [5] Chew S H *et al* 2012 Time-of-flight-photoelectron emission microscopy on plasmonic structures using attosecond extreme ultraviolet pulses *Appl. Phys. Lett.* **100** 051904
- [6] Förg B *et al* 2016 Attosecond nanoscale near-field sampling *Nat. Commun.* **7** 11717
- [7] Carstens H *et al* 2016 High-harmonic generation at 250 MHz with photon energies exceeding 100 eV *Optica* **3** 366
- [8] Lilienfein N, Hofer C, Holzberger S, Matzer C, Zimmermann P, Trubetskov M, Pervak V and Pupeza I 2017 Enhancement cavities for few-cycle pulses *Opt. Lett.* **42** 271
- [9] Högner M, Tosa V and Pupeza I 2017 Generation of isolated attosecond pulses with enhancement cavities—a theoretical study *New J. Phys.* **19** 033040
- [10] Heyl C M, Bengtsson S N, Carlström S, Mauritsson J, Arnold C L and L'Huillier A 2014 Corrigendum: noncollinear optical gating (2014 *New J. Phys.* 16 052001) *New J. Phys.* **16** 109501
- [11] Moll K D, Jones R J and Ye J 2006 Output coupling methods for cavity-based high-harmonic generation *Opt. Express* **14** 8189
- [12] Esser D, Weitenberg J, Bröring W, Pupeza I, Holzberger S and Hoffmann H-D 2013 Laser-manufactured mirrors for geometrical output coupling of intracavity-generated high harmonics *Opt. Express* **21** 26797–805
- [13] Pupeza I, Högner M, Weitenberg J, Holzberger S, Esser D, Eidam T, Limpert J, Tünnermann A, Fill E and Yakovlev V S 2014 Cavity-enhanced high-harmonic generation with spatially tailored driving fields *Phys. Rev. Lett.* **112** 103902
- [14] Pronin O, Seidel M, Lücking F, Brons J, Fedulova E, Trubetskov M, Pervak V, Apolonski A, Udem T and Krausz F 2015 High-power multi-megahertz source of waveform-stabilized few-cycle light *Nat. Commun.* **6** 6988
- [15] Saule T, Holzberger S, De Vries O, Plötner M, Limpert J, Tünnermann A and Pupeza I 2017 Phase-stable, multi- μ J femtosecond pulses from a repetition-rate tunable Ti:Sapphire-seeded Yb-fiber amplifier *Appl. Phys. B* **123** 17
- [16] Pupeza I *et al* 2013 Compact high-repetition-rate source of coherent 100 eV radiation *Nat. Photon.* **7** 608–12
- [17] Carstens H, Holzberger S, Kaster J, Weitenberg J, Pervak V, Apolonski A, Fill E, Krausz F and Pupeza I 2013 Large-mode enhancement cavities *Opt. Express* **21** 11606
- [18] Weitenberg J, Rußbüldt P, Pupeza I, Udem T, Hoffmann H-D and Poprawe R 2015 Geometrical on-axis access to high-finesse resonators by quasi-imaging: a theoretical description *J. Opt.* **17** 025609
- [19] Weitenberg J, Rußbüldt P, Eidam T and Pupeza I 2011 Transverse mode tailoring in a quasi-imaging high-finesse femtosecond enhancement cavity *Opt. Express* **19** 9551–61
- [20] Holzberger S, Lilienfein N, Trubetskov M, Carstens H, Lücking F, Pervak V, Krausz F and Pupeza I 2015 Enhancement cavities for zero-offset-frequency pulse trains *Opt. Lett.* **40** 2165

4.3 Cavity-Enhanced Noncollinear High-Harmonic Generation

as published in

Optics Express (2019)

[88]

by

Maximilian Högner, Tobias Saule, Stephan Heinrich, Nikolai Lilienfein, Dominik Esser, Michael Trubetskov, Volodymyr Pervak, and Ioachim Pupeza

Contributions I planned and set up the cavity and executed and evaluated the experiment, with help from coworkers, and wrote most of the manuscript.



Cavity-enhanced noncollinear high-harmonic generation

MAXIMILIAN HÖGNER,^{1,2} TOBIAS SAULE,^{1,2} STEPHAN HEINRICH,^{1,2}
NIKOLAI LILIENFEIN,^{1,2} DOMINIK ESSER,³ MICHAEL TRUBETSKOV,¹
VOLODYMYR PERVAK,² AND IOACHIM PUPEZA^{1,2,*}

¹Max-Planck-Institut für Quantenoptik, Hans-Kopfermann-Straße 1, 85748 Garching, Germany

²Ludwig-Maximilians-Universität München, Am Coulombwall 1, 85748 Garching, Germany

³Fraunhofer-Institut für Lasertechnik, Steinbachstraße 15, 52074 Aachen, Germany

*ioachim.pupeza@mpq.mpg.de

Abstract: Femtosecond enhancement cavities have enabled multi-10-MHz-repetition-rate coherent extreme ultraviolet (XUV) sources with photon energies exceeding 100 eV – albeit with rather severe limitations of the net conversion efficiency and of the duration of the XUV emission. Here, we explore the possibility of circumventing both these limitations by harnessing spatiotemporal couplings in the driving field, similar to the "attosecond lighthouse," in theory and experiment. Our results predict dramatically improved output coupling efficiencies and efficient generation of isolated XUV attosecond pulses.

© 2019 Optical Society of America under the terms of the [OSA Open Access Publishing Agreement](#)

1. Introduction

In recent years, femtosecond enhancement cavities (ECs) have matured to an enabling technology for precision metrology with coherent radiation in the vacuum and extreme ultraviolet (VUV, XUV) spectral regions. ECs are passive optical resonators that can be efficiently excited over a broad optical band, usually in the near-infrared (NIR), by the pulse train of a (post-amplified, phase-stabilized) modelocked laser. This results in a circulating pulse with an energy enhanced by a few orders of magnitude with respect to that of the seeding pulses, affording intensities high enough to drive high-order harmonic generation (HHG) in gases at repetition rates of several tens of MHz [1, 2].

Direct evidence of the temporal coherence of the emerging harmonic spectrum [3, 4] has demonstrated the viability of transferring NIR frequency combs to the VUV/XUV with ECs, thus paving the way towards precision frequency metrology of electronic transitions [5]. Very recently, geometrically coupling out the harmonic radiation through an on-axis opening in the mirror following the HHG focus [6–8] enabled MHz-HHG with photon energies high enough to liberate core electrons from metals via single-photon photoelectron spectroscopy (PES). This led to the first space-charge-free PES experiments at multi-MHz repetition rates [8, 9], in particular also with attosecond temporal resolution [8]. Significant efforts have addressed the understanding of cavity-enhanced HHG conversion efficiency limitations related to plasma nonlinearity [10–12] and plasma cumulative effects [13, 14]. Accelerating the gas to provide (nearly) single-pass conditions even at several tens of MHz has been shown to strongly mitigate the latter limitation, resulting in mW-level VUV frequency combs [13]. In addition, novel, nonlinearity-optimized ultrashort-pulse enhancement regimes [12, 15] promise a path to circumvent the blueshift-related intensity clamping [10–12]. Altogether, these recent advances indicate a vast potential of improving the intracavity conversion efficiency.

Yet, despite of the growing attention dedicated to this laser architecture uniquely combining high XUV photon energies with high repetition rates, two limitations remain without solution to this day. Firstly, geometric output coupling (OC) employing the fundamental transverse mode of the EC [6–8, 14] – the most broadband OC technique demonstrated so far – suffers from poor

efficiency [16]. Noncollinear methods or methods employing spatially tailored resonator modes have been recognized early on as promising alternatives [17–21]. Secondly, the direct generation of isolated attosecond pulses (IAP), as desirable for endowing time-resolved PES with attosecond resolution over durations of hundreds of femtoseconds [22–24], has remained out of reach due to the limited spectral coverage of today's ECs [25]. In this letter, we demonstrate a new means of control over the transverse mode of a high-finesse, broadband femtosecond EC, offering a route towards circumventing both above-mentioned limitations.

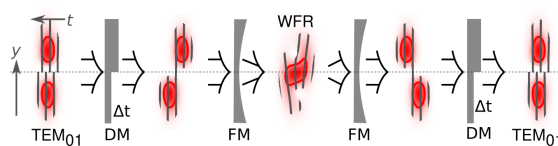


Fig. 1. Working principle of transverse mode gating: one lobe of a TEM_{01} resonator mode (wave fronts indicated by gray lines) is delayed by an odd number of half cycles using a half-sided delay mirror (DM). After a focusing mirror (FM), this leads to an on-axis maximum around the focus where the high-harmonic generation gas target is placed, with a wavefront rotation (WFR) adjustable by the step height of the DM. After the focus, the alteration of the mode is reversed, permitting low-diffraction-loss propagation in the resonator. Operating with negligible WFR affords high-efficiency geometric output coupling of the harmonic radiation emitted by all NIR half cycles. A larger WFR can be used to spatially isolate the harmonic emission of a single NIR half cycle, thus gating an isolated attosecond pulse.

2. Methods

To this end, we employ the TMG (transverse mode gating) method introduced in [26]: A TEM_{01} resonator mode is excited, which consists of two lobes of opposite phase, spatially separated by an intensity minimum (see Fig. 1). One of the lobes is delayed with respect to the other by means of an EC mirror with a stepped surface profile [27], introducing spatiotemporal coupling. Similar to noncollinear optical gating [19, 28, 29] and the attosecond lighthouse [30–33], this leads to wave-front rotation (WFR), involving contributions from spatial chirp and pulse front tilt, in a subsequent focal region. Moreover, a delay equal to an odd number of optical half cycles results in a single, on-axis maximum around the focus [17]. The delay is reversed by a second, identical mirror located such that the first mirror is imaged onto it in good approximation [26, 27]. This ascertains that the recycled field can overlap constructively with the original TEM_{01} mode, allowing the field to circulate with negligible losses inside a resonator housing this configuration. A mirror with a small on-axis opening can be used for efficient OC of the radiation generated in a gas target placed in the focal region, while introducing negligible losses to the circulating pulse thanks to the on-axis intensity minimum of the TEM_{01} mode [17, 21].

This technique is advantageous for cavity-enhanced HHG even when temporal gating is not required: By choosing a delay of just one half cycle and using multi-cycle circulating pulses, OC efficiencies $> 40\%$ can be expected irrespective of the position of the gas target, resolving a major limitation on the overall conversion efficiency of EC-based XUV sources [16]. In contrast to similar approaches based on quasi-imaging [20, 21], this technique does not require operation in the middle of the stability range of the resonator, so that limitations on the peak power of the circulating pulses are relaxed by allowing for larger spot sizes on the mirrors (see Appendix I).

When choosing higher values of the delay and using few-cycle circulating pulses, the WFR angularly disperses the individual bursts of the generated XUV radiation, allowing the selection of an IAP by spatial filtering. The delay between the two lobes is intrinsically stable due to the

monolithic step mirrors, as opposed to other proposed schemes for noncollinear HHG in ECs employing two separate cavities or crossing two pulses circulating in a single EC of twice the length [17–19].

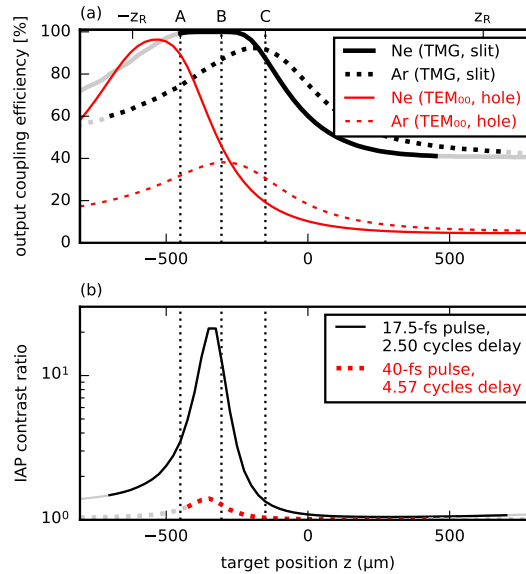


Fig. 2. Figures of merit for transverse mode gating. (a) Output coupling efficiency with the TMG mode (bold black lines) vs. hole output coupling with the fundamental mode (thin red lines), for HHG in argon (H33 at a peak intensity of $1.5 \times 10^{14} \text{ W/cm}^2$, dashed lines) and neon (H79 at a peak intensity of $3.0 \times 10^{14} \text{ W/cm}^2$, solid lines), with 40-fs pulses centered at 1025 nm and the output coupling slit/hole dimensions chosen so that the round-trip loss in both cases remains below 1%. (b) Expected on-axis inter-burst contrast ratio versus gas target position using 17.5-fs pulses and an accordingly chosen delay (solid black line) and with the demonstrated 40-fs pulses (dashed red line), in both cases computed for H79 in neon at a peak intensity of $3.0 \times 10^{14} \text{ W/cm}^2$. The gray continuations of the curves identify when pulse energies $> 80 \mu\text{J}$ are needed to reach the corresponding peak intensities. The vertical dotted lines labeled with A, B and C mark the z position for the data shown in Figs. 5(b), 4 and 5(d), respectively.

3. Results

The spatial divergence of the resulting XUV beamlets is determined by the position of the gas target relative to the focus. The divergence must be small to ensure efficient OC at the opening in the mirror and, in the case of IAP production, to avoid spatial overlap between the individual beamlets. Therefore, the gas target position is a critical parameter for both modes of operation. The smallest divergence is achieved when the wave-front curvature of the driving beam compensates for the wave-front curvature induced by the transverse intensity gradient via the intensity-dependent phase of the dipole response [16, 34]. In the following, we theoretically investigate the effect of the target position on the OC efficiency and the gating efficiency.

For the first application, i.e., applying the scheme with negligible WFR to improve the OC efficiency of the harmonic radiation, we compute the OC efficiency for different positions

of the gas target, assuming a TMG mode with 40-fs Gaussian pulses centered at 1025 nm, a step height of $0.26 \mu\text{m}$ corresponding to a delay of 0.5 cycles, focused to a spot size of $w_{0,x} \times w_{0,y} = 17.2 \times 11.8 \mu\text{m}^2$, and an OC mirror with a 7.31-mrad-angular-width slit (e.g., a 0.731-mm-broad slit in a OC mirror located 100 mm behind the focus), chosen for a maximum round-trip loss of 1%. The numerical model is described in detail in Appendix A. We compare the method to OC using a symmetric fundamental Gaussian mode focused down to the same focal spot area, using an OC mirror with a hole, with an angular diameter chosen for the same round-trip loss (2.30 mrad). Because the divergence of the XUV beamlets depends on the harmonic order, intensity and target gas [16], we consider two cases: OC of the 33th harmonic produced in argon (39.9 eV, compare [8]), with a peak intensity of $1.5 \times 10^{14} \text{ W/cm}^2$ in the target plane, and of the 79th harmonic produced in neon (95.6 eV, compare [26]), with a peak intensity of $3.0 \times 10^{14} \text{ W/cm}^2$. The results are plotted in Fig. 2(a). Using the fundamental mode results in OC efficiencies below 18% (argon) and 10% (neon) for gas targets placed near the focus. Better OC efficiency can be achieved far in front of the focus, at the cost of XUV generation efficiency [16]. Using the TMG mode allows for OC efficiencies $> 40\%$ irrespective of the target position, thereby considerably alleviating this trade-off.

To model the temporal gating performance when operating with WFR, we numerically approximated the inter-burst intensity contrast ratio of the attosecond pulse trains emitted on-axis versus gas target position (see Appendix C), assuming the same central wavelength and focal spot size as before and a peak intensity of $3.0 \times 10^{14} \text{ W/cm}^2$ in a neon gas target. For the simulations, we used the parameters from our experiment (40-fs pulses and a delay of 4.57 cycles), as well as parameters which seem technologically within reach (17.5-fs pulses [25], using a delay of 2.5 cycles). As can be seen in Fig. 2(b), generation of isolated attosecond pulses around the 79th harmonic order should be possible. For this, the target must be placed $350 \mu\text{m}$ in front of the focus.

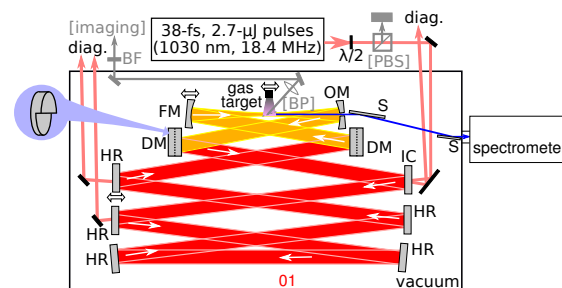


Fig. 3. Experimental setup. IC: input coupler, HR: highly reflective mirror, DM: HR delay mirror with a stepped surface profile, FM: focusing HR mirror, OM: FM with an on-axis hole for output coupling, BS: IR/XUV beam splitter, diag.: diagnostics. Optional, for imaging the spatial dispersion: BP: Brewster plate, BF: optical bandpass filter, and an attenuator consisting of a half-wave plate ($\lambda/2$) and a polarizing beam splitter (PBS)

To demonstrate the feasibility of the method, we set up a 10-mirror, 16.3-m-long EC (see Fig. 3) comprising two spherical focusing mirrors (radius of curvature $R = 300 \text{ mm}$), two delay mirrors with a stepped [27] surface profile ($2.34 \mu\text{m}$ height, corresponding to a delay of 2.57 cycles at a wavelength of 1025 nm), an input coupler with a reflectivity of 97.2% and five highly reflective plane mirrors. The EC is seeded by a laser system providing a 18.4-MHz, zero-offset-frequency train of 2.7- μJ , 38-fs pulses centered at 1030 nm, which is described in detail in [8]. The highly reflective mirror coatings were designed for a bandwidth supporting ~ 30 -fs pulses. We operated the EC near the inner stability edge to achieve large mode areas

and thereby small peak intensities on the mirrors when operating at high peak powers [35]. By selecting a proper combination of mirror coatings, we obtained a cavity with a preferred offset frequency of zero [36], which was verified by measuring the average power in the empty cavity for different values of the seeding comb offset frequency.

The radii of the focal spot were $w_{0,x} \times w_{0,y} = 17.2 \times 11.8 \mu\text{m}^2$, the same value as used for the simulations shown in Fig. 2. We measured 80- μJ pulses with a spectrum centered at 1025 nm in the empty cavity, at a finesse of 188 (round-trip loss of 0.5%). While output coupling with a quasi-imaging method [20, 21] would allow for peak powers up to 1.17 GW (assuming an EC of the same length and mirrors with the same damage threshold), our setup is, owing to the operation near the inner stability edge, scalable beyond this value, reaching 1.88 GW with a peak intensity of $7.4 \times 10^9 \text{ W/cm}^2$ on the mirrors (see Appendix I).

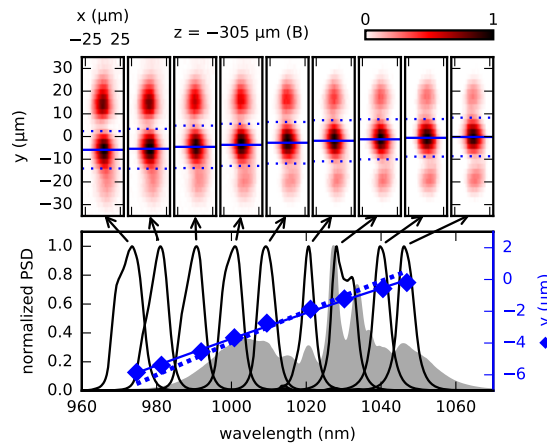


Fig. 4. Top: Transverse intensity profiles of the cavity mode 305 μm in front of the focus, imaged with the arrangement shown in Fig. 3, and filtered for different wavelengths. The blue lines mark the position (solid) and $1/e^2$ -width (dotted) of Gaussian functions fitted to the central lobe of the horizontally integrated profile. Bottom: The intracavity spectrum (gray) and, for each depicted profile, the corresponding spectrum transmitted through the bandpass filter (black, normalized). The diamonds mark the central lobe positions and corresponding central wavelengths of the filtered spectra. A linear fit (blue solid line) of the lobe position vs. frequency yields a spatial dispersion of $-44 \mu\text{m/PHz}$, compared to a theoretical value of $-53 \mu\text{m/PHz}$ (blue dotted line).

To experimentally confirm the formation of spatial chirp around the focus, we attenuated the seed power and imaged a plane slightly in front of the focus (305 μm) via a 100-nm-thick silicon nitride plate inserted under close to Brewster's angle in the cavity beam (Fig. 3, gray). We employed a tilted narrow-band transmissive optical bandpass filter placed before a beam profiling camera to record the imaged profiles for different spectral portions of the transverse mode, confirming spatial dispersion (Fig. 4). We obtain a value of $\gamma = dy/d\omega = -44 \mu\text{m/PHz}$ (blue solid line in Fig. 4, lower panel), in agreement with the prediction of the numerical model of $-53 \mu\text{m/PHz}$ (blue dotted line in Fig. 4, lower panel, see Appendix D).

From the measured spatial dispersion γ , the lobe radius $w_y = (8.8 \pm 0.4) \mu\text{m}$ and spectral width ($\Delta\omega = 58.9 \text{ THz}$ for a Fourier-limited 40-fs Gaussian pulse), we can approximate the frequency gradient $d\omega/dy = \gamma/(\gamma^2 + (w_y/\Delta\omega)^2) = -1.81 \text{ THz}/\mu\text{m}$ [37] and the spatial chirp $d\lambda/dy = -2\pi c \omega_c^{-2} d\omega/dy = 1.15 \text{ nm}/\mu\text{m}$ for a central frequency $\omega_c = 2\pi c/1025 \text{ nm}$. This

corresponds to an angular separation of $d\ell/dy/2 = 0.58$ mrad between consecutive attosecond bursts [31].

Because the target is located slightly outside the focal plane, the total angular separation includes another contribution arising from an interplay of pulse-front tilt and wave-front curvature [33]: The central lobe moves, on the time scale of one laser pulse, from a region with a wave-front pointing downwards to a region where it points upwards (compare Fig. 1). Our model predicts a total angular separation of 0.64 mrad including this effect (see Appendix D).

We demonstrate spatiotemporally coupled HHG using this setup by operating the cavity at the full seed power and supplying argon gas via a 100- μm -diameter end-fire nozzle placed 450 μm in front of the focus. In general, a strong intracavity nonlinearity can affect the excited mode, especially at high finesse. However, for the parameters demonstrated here, no mode deformations were observed (Fig. 5(a)). To determine the cutoff energy, we coupled out the generated XUV radiation through a 207- μm -diameter hole, followed by two XUV/IR beam splitters and a 300-nm-thick aluminum filter, and analyzed it with a grating spectrometer (Fig. 5(b)). We observed harmonics up to 60 eV. For the measured pulse energy of 39 μJ , our model predicts a peak intensity of 1.4×10^{14} W/cm² in the target, corresponding to a high-harmonic cutoff energy of 59 eV.

To reach higher photon energies, we placed the target closer to the focus ($-150 \mu\text{m}$) and used neon as target gas. As before, the gas plasma did not cause changes of the circulating mode (Fig. 5(c)). The XUV spectrum, measured through a 300-nm-thick zirconium filter, is shown in Fig. 5(d). The highest observed photon energies were around 120 eV, slightly below the expected cutoff of 155 eV (4.2×10^{14} W/cm²) resulting from the measured pulse energy of 57 μJ , under the assumption of a Gaussian pulse shape. During the HHG measurements, we monitored the carrier-envelope offset phase of the seed employing a spectrally resolved f -to- $2f$ interferometer [8]. Although not actively stabilized, the drift was below 300 mrad over one measurement (50 s for argon, 203 s for neon).

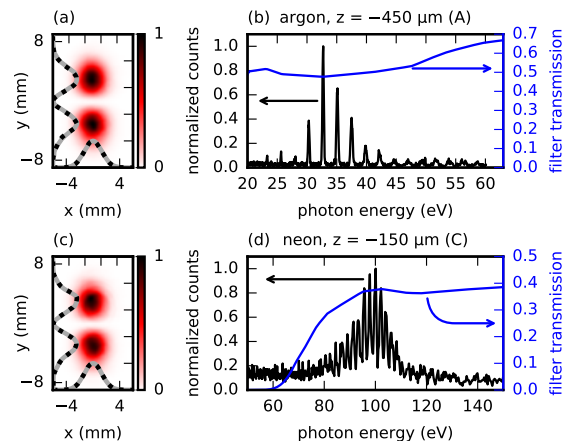


Fig. 5. (a) Transverse intensity profile of the cavity mode measured without target gas (color scale), integrated profiles in horizontal and vertical direction (gray lines), and integrated profiles with the target gas (black dotted lines). (b) Output-coupled high-harmonic spectrum (black) generated in an argon target placed 450 μm in front of the focus, after transmission through a 300-nm Al filter (blue). (c,d) Same for a neon target placed 150 μm in front of the focus, using a 300-nm Zr filter.

4. Discussion

For the demonstrated experimental parameters, the angular separation predicted by our numerical model (0.68 mrad in the case of argon, 0.61 mrad for neon) is small compared to the divergence of the beamlets (argon: 6.1 mrad, neon:4.9 mrad), which leads to significant spatial overlap between the harmonic bursts, preventing the separation of isolated attosecond pulses and, thus, the observation of a spectral continuum. We compute an IAP contrast ratio < 1.1 (compare Fig. 2(b); see also [30] and Appendix C). To achieve smaller divergence, it is necessary to operate at high photon energies and at the same time the nozzle must be placed far in front of the focus [16]. Therefore, more peak power is necessary, which can be either achieved by increasing the seed power or by using shorter pulses and a shorter delay (both within the limits given by the damage threshold of the mirror coatings). As a second measure to reduce the spatial overlap, the angular separation between the bursts can be increased. To this end, it is also beneficial to operate with shorter pulses. Our simulations (see Fig. 2(b)) have shown that 17.5-fs pulses and a delay of 2.5 cycles would be sufficient to produce IAPs around 95.6 eV with a contrast ratio of > 20 with the demonstrated geometry. For this, a pulse energy of 30 μJ is needed, leading to a peak intensity of only $0.63 \times 10^{10} \text{ W/cm}^2$ on the cavity mirrors and $3.0 \times 10^{14} \text{ W/cm}^2$ in a gas target placed 350 μm in front of the focus. Although mirror coatings supporting pulses with a Fourier limit of 17.5 fs in a four-mirror EC have already been demonstrated [25], it remains a technological challenge to achieve this value in a cavity with an optimum offset frequency of zero and more than four mirrors, mainly due to statistical errors in the coating procedure which make a large number of tries necessary.

5. Conclusion

In conclusion, we have demonstrated a femtosecond enhancement cavity with an intracavity wave-front rotation, enabled by the technique of transverse mode gating, and showed first HHG spectra of wave-form stable XUV pulse trains at photon energies beyond 100 eV generated with this method, in a focusing/repetition-rate regime avoiding cumulative plasma effects [13, 14] (see also Appendix G). Our experimental findings agree well with theoretical expectations. Numerical modeling shows that TMG can solve two main limitations of state-of-the-art fs-EC-based XUV sources: First, the tradeoff between XUV generation efficiency and OC efficiency present with conventional hole OC can be circumvented thanks to an excellent OC efficiency irrespective of the target position, promising high-flux frequency combs in the XUV region for precision spectroscopy applications and, potentially, for future nuclear clocks [38]. Together with emerging 2- μm technologies [39, 40], this method promises to boost the attainable photon energies of XUV combs to the water window and beyond. Secondly, it can be applied as an intracavity gating method to produce IAP at repetition rates in the tens of MHz. When combined with ultra-broadband cavity mirror coatings and using a suitable step height, the demonstrated geometry and pulse energy are, according to our numerical model, already sufficient for IAP approaching 100 eV with an excellent contrast ratio of > 20 .

A. Numerical model

The complex electric field E of a pulse in a TEM_{01} resonator mode can be written as

$$E(x, y, z, \omega) = \widehat{\text{TEM}}_{01}(x, y, z, \omega)E(\omega), \quad (1)$$

where x, y are the transverse coordinates, z is the longitudinal coordinate, ω is the angular frequency, $E(\omega)$ describes the temporal dependence and $\widehat{\text{TEM}}_{01}(x, y, z, \omega)$ the spatial dependence. For a Gaussian pulse, $E(\omega)$ is the Fourier transform of $E(t) = A(t) \exp(i\omega_c t)$, with the envelope $A(t) = \exp(-t^2/\tau^2)$, central frequency ω_c , and $\tau = t_{\text{FWHM}}/\sqrt{\log 4}$ with the full-width-half-

maximum intensity pulse duration t_{FWHM} . The formulas for the normalized mode $\widehat{\text{TEM}}_{01}$ are provided in [41, p. 645].

To introduce spatiotemporal coupling, we write down this field in a far-field plane ($z_{\text{ff}} = -10^5 z_R$, with the Rayleigh range $z_R = \sqrt{z_{R,x} \cdot z_{R,y}}$) and apply a delay Δt to the lower lobe:

$$\begin{aligned} E_{\text{TMG}}(x, y, z_{\text{ff}}, \omega) &= \\ &= E(x, y, z_{\text{ff}}, \omega) \exp(-i\omega\Delta t H(-y)) \end{aligned} \quad (2)$$

Here, $H(\cdot)$ is the Heaviside step function. To calculate the XUV divergence and the angular separation of the harmonic bursts, we need the driving field in the target plane. For this, we numerically computed $E_{\text{TMG}}(x, y, z_{\text{ff}}, \omega)$ on a uniformly spaced (x, y, ω) grid centered around $(0, 0, \omega_c)$ and propagated the field to the target position z_t , using a Fresnel two-step propagator [42, Appendix B]. Then, we applied a discrete Fourier transform to obtain the complex envelope $E_{\text{TMG}}(x, y, z_t, t)$ on a (x, y, t) grid.

Due to the strong nonlinearity of the high-harmonic generation (HHG) process, the main contribution to the XUV emission stems from the region around the maximum intensity $c\epsilon_0/2 |E_{\text{TMG}}(x, y, z_t, t)|^2$, located within the central lobe. In the vicinity of this maximum, we can approximate the field by a vertically tilted fundamental Gaussian beam:

$$\begin{aligned} E_{\text{TMG}}(x, y, z_t, t_{\text{max}}) &\approx \\ &\approx C \exp\left(-ik\left(\frac{x_r^2}{2q_x} + \frac{y_r^2}{2q_y}\right) - ik\beta_y y_r\right) \end{aligned} \quad (3)$$

with $x_r = x - x_{\text{max}}$, $y_r = y - y_{\text{max}}$, $k = \omega_c/c$, the complex beam parameters q_x and q_y , the vertical wave-front direction β_y and

$$(x_{\text{max}}, y_{\text{max}}, t_{\text{max}}) = \arg \max_{(x,y,t)} |E_{\text{TMG}}(x, y, z_t, t)|^2. \quad (4)$$

We determined the parameters q_x , q_y , β_y numerically with fitting procedures for the amplitude and phase along x and y line cuts through the intensity maximum, discarding data points where the intensity was below half the maximum. This resulted in effective driving beam radii $w_{x,\text{eff}} = \sqrt{2/|\Im(kq_x^{-1})|}$, $w_{y,\text{eff}} = \sqrt{2/|\Im(kq_y^{-1})|}$ and wave-front curvatures $R_{x,\text{eff}}^{-1} = \Re(q_x^{-1})$, $R_{y,\text{eff}}^{-1} = \Re(q_y^{-1})$ in the plane of the gas target. We then approximated the spot sizes w_H and wave-front curvatures R_H^{-1} of the XUV beam at z_t in y direction by assuming a power law for the driving-intensity dependence of the single-atom dipole amplitude and a linear relationship for the single-atom dipole phase [16, Appendix C]:

$$w_H = w_{\text{eff}}/\sqrt{N_H} \quad (5)$$

$$R_H^{-1} = R_{\text{eff}}^{-1} + \frac{4c\alpha_H I_t}{H\omega_c w_{\text{eff}}^2} \quad (6)$$

Here, N_H and α_H are coefficients describing the driving-intensity dependence of the single-atom dipole amplitude and phase, respectively, H is the harmonic order and I_t is the peak driving intensity in the plane of the gas target. The divergence of a beam with a near-field spot radius w_H , wave-front curvature R_H^{-1} and frequency $H\omega_c$ is (compare [16])

$$\theta = \sqrt{\frac{w_H^2}{R_H^2} + \frac{4c^2}{H^2\omega_c^2 w_H^2}}. \quad (7)$$

In the experiment, the position of the delay mirror relative to the focus was different from the value $z_{\text{ff}} = -10^3 z_R$ used here (in particular, the delay mirror was placed behind a focusing mirror). However, the exact position is irrelevant as long as the delay mirror is imaged onto a plane that is far away from the focus, which was accomplished by placing the delay mirrors at a distance of roughly $R = 300$ mm from the focusing mirrors [26, Appendix A].

To determine the output coupling efficiency for the parameters considered in the main text ($t_{\text{FWHM}} = 40$ fs, $\omega_c = c/1025$ nm, a delay Δt of 0.5 cycles and values for q_x, q_y corresponding to a focal spot size of $w_{0,x} \times w_{0,y} = 17.2 \times 11.8 \mu\text{m}^2$), we computed the effective beam radius $w_{y,\text{eff}}$ and wave-front curvature $R_{y,\text{eff}}^{-1}$ at different transverse positions z (Figs. 6(a) and (b)). Then, the near-field XUV beam radius and wave-front curvature was calculated according to (5) and (6) for the two cases of intermediate (argon, $H = 33$, $I_t = 1.5 \times 10^{14}$ W/cm²) and high (neon, $H = 79$, $I_t = 1.5 \times 10^{14}$ W/cm²) photon energy generation (Figs. 6(c) and (d)). For this, we used intensity-dependence parameters N_H, α_H taken from [16, Table B1]. The pulse energies necessary to achieve the respective peak intensities I_t in the target (Fig. 6(e)) were calculated numerically by integrating $I(x, y, z_t, t) = c\epsilon_0/2|E_{\text{TMG}}(x, y, z_t, t)|^2$ over the (x, y, t) grid after normalization to a peak intensity of I_t . Applying Eq. (7) then yields the expected divergence of the XUV radiation in y direction (Fig. 6(f)). As expected, the smallest divergence is obtained when the gas target is located in front of the focal plane [16, 34].

The XUV output coupling efficiency attainable by employing an mirror with an on-axis slit opening depends on the angular width $\delta = d/z_m$ of the slit, where d is the slit width and z_m the distance of the output coupling mirror from the focus. This angular width also determines the round-trip losses that the circulating mode experiences at the output coupling mirror. To find an acceptable value, we calculated the round-trip loss for different slit angular widths δ . To this end, we numerically computed the ratio of the energy lost by transmission through the slit and the total energy incident on the output coupling mirror (far-field beam profile given by Eq. (2)). The round-trip loss is twice the resulting value, because the same amount of energy that is transmitted through the slit is also scattered to nonresonant higher-order modes [6]:

$$L(\delta) = 2 \left(\frac{\iiint_{y < \delta z_m / 2} |E_{\text{TMG}}(x, y, z_{\text{ff}}, \omega)|^2 dx dy d\omega}{\iiint |E_{\text{TMG}}(x, y, z_{\text{ff}}, \omega)|^2 dx dy d\omega} \right) \quad (8)$$

Figure 6(g) shows the resulting losses versus slit angular width. To keep the losses below 1%, a value consistent with the typical finesse aimed for in cavity-enhanced HHG experiments, we chose picked an angular width of 7.31 mrad.

Then, we computed the output coupling efficiency ϵ , again by spatial integration. For this, we took advantage of the approximation of the harmonic beam profile as a Gaussian $|E_{\text{XUV}}(x, y)|^2 \propto \exp(-2y^2/w_{m,y}^2) \exp(-2x^2/w_{m,x}^2)$ [16], where $w_{m,x}$ and $w_{m,y} = \theta z_m$ are the XUV beam radii in x and y direction on the output coupling mirror:

$$\epsilon = \frac{\iint_{y < \delta z_m / 2} |E_{\text{XUV}}(x, y)|^2 dx dy}{\iint |E_{\text{XUV}}(x, y)|^2 dx dy} = \text{erf}(\delta/\theta/\sqrt{2}) \quad (9)$$

This resulted in output coupling efficiencies in the range 40–100% for all considered gas target positions (Fig. 6(h)).

The delay of one half cycle, necessary to obtain an on-axis intensity maximum in the focus region, introduces a slight wave-front rotation and thus angular separation between consecutive bursts. To validate that efficient output coupling of all bursts is still possible, we computed the angular separation (compare following sections) for the cases of intermediate (H33 in argon) and high (H79 in neon) photon energy production and obtained values < 0.17 mrad for all considered gas target positions, which is well below the computed divergence (compare Fig. 6(f)) and the assumed slit angular width of 7.31 mrad.

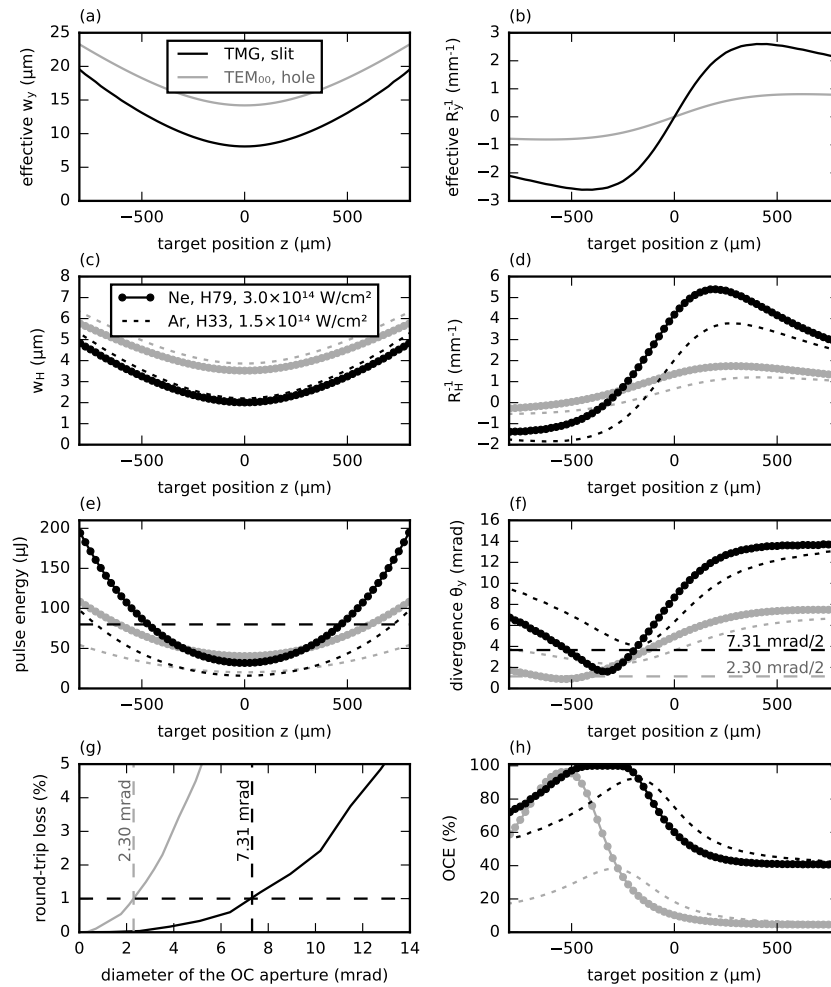


Fig. 6. a) Beam radius in y direction of a fundamental Gaussian mode fitted to the central lobe of the simulated TMG mode (delay 0.5 cycles, black) and of the fundamental Gaussian mode with the same complex beam parameter for comparison (gray). b) Wave-front curvature for both cases. c,d) Harmonic beam radius and wave-front curvature in y direction, calculated in the plane of the gas target with a simple analytical single-trajectory model for the harmonic dipole response, for generation parameters allowing for high photon energy (solid line with dot markers) and intermediate photon energy (dashed line). e) Pulse energy needed to reach $3 \times 10^{14} \text{ W/cm}^2$ (high photon energy case) and $1.5 \times 10^{14} \text{ W/cm}^2$ (intermediate photon energy case) in the gas target plane with the TMG mode (black) and the fundamental Gaussian mode (gray). f) Harmonic beam divergence in y direction, resulting from its beam radius and wave-front curvature in the gas target plane. g) Round-trip losses of the simulated TMG mode due to an on-axis output coupling slit with given angular width (black), and of the fundamental Gaussian mode due to an on-axis hole with given angular diameter (gray). h) XUV output coupling efficiencies resulting from the computed divergences, assuming output coupling apertures with a round-trip loss of 1%.

B. Comparison with output coupling using the fundamental mode

For comparison, we repeated the same procedure to determine the output coupling efficiencies attainable with the fundamental Gaussian mode and a circular opening in the output coupling mirror. For this, we used the same numerical model but replaced the TEM₀₁ mode by a symmetric TEM₀₀ mode with the same complex beam parameters and set $\Delta t = 0$. As before, we computed the round-trip losses numerically by spatial integration, but this time assuming a circular aperture:

$$L(\delta) = 2 \left(\frac{\iiint_{\sqrt{x^2+y^2} < \delta z_{ff}/2} |E|^2 dx dy d\omega}{\iiint |E|^2 dx dy d\omega} \right). \quad (10)$$

The output coupling efficiency with a hole angular diameter $\delta = 2.30$ mrad for 1% round-trip losses was computed analytically as

$$\begin{aligned} \epsilon &= \frac{\iint_{\sqrt{x^2+y^2} < \delta z_m/2} |E_{XUV}|^2 dx dy}{\iint |E_{XUV}|^2 dx dy} = \\ &= 1 - \exp\left(-2(\delta/\theta/\sqrt{2})^2\right) \end{aligned} \quad (11)$$

The dependence of the resulting quantities on the gas target position is shown in Fig. 6 in gray.

C. Gating efficiency

To estimate the angular separation between consecutive attosecond bursts, we compared the wave-front direction β_y at t_{\max} with the wave-front direction β'_y one half cycle later ($t' = t_{\max} + T/2$, with $T = 2\pi/\omega_c$), which was determined similarly to β_y by approximating the driving field in the vicinity of the intensity maximum by a fundamental Gaussian beam with vertically tilted phase fronts:

$$\begin{aligned} E_{\text{TMG}}(x, y, z_t, t') &\approx \\ &\approx C \exp\left(-ik \left(\frac{x_r'^2}{2q_x'} + \frac{y_r'^2}{2q_y'} \right) - ik\beta'_y y_r'\right) \end{aligned} \quad (12)$$

and fitting the parameters q'_x , q'_y and β'_y along x/y line cuts, with $x'_r = x - x'_{\max}$, $y'_r = y - y'_{\max}$ and

$$(x'_{\max}, y'_{\max}) = \arg \max_{(x,y)} |E_{\text{TMG}}(x, y, z_t, t')|^2. \quad (13)$$

This allowed us to approximate the angular separation $\Delta\beta = \beta'_y - \beta_y$ between the XUV beamlets of consecutive half cycles. Assuming an infinitesimally thin output coupling slit placed in the direction β_y of the strongest beamlet, the output coupled isolated attosecond pulse will have satellite pulses stemming from the XUV emission of neighboring half cycles due to spatial overlap [30, Supplementary Information, section 3.2]. The intensity of the main pulse relative to these satellite pulses, i.e., the contrast ratio Γ of the isolated attosecond pulse, is given by the divergence θ of the beamlets:

$$\Gamma = 1/|\exp(-\Delta\beta^2/\theta^2)|^2 \quad (14)$$

Figure 7 shows the dependence of the quantities θ , $\Delta\beta$ and Γ on the target position for the case of isolated attosecond pulse generation using 17.5-fs pulses in neon and for the experimentally demonstrated parameters.

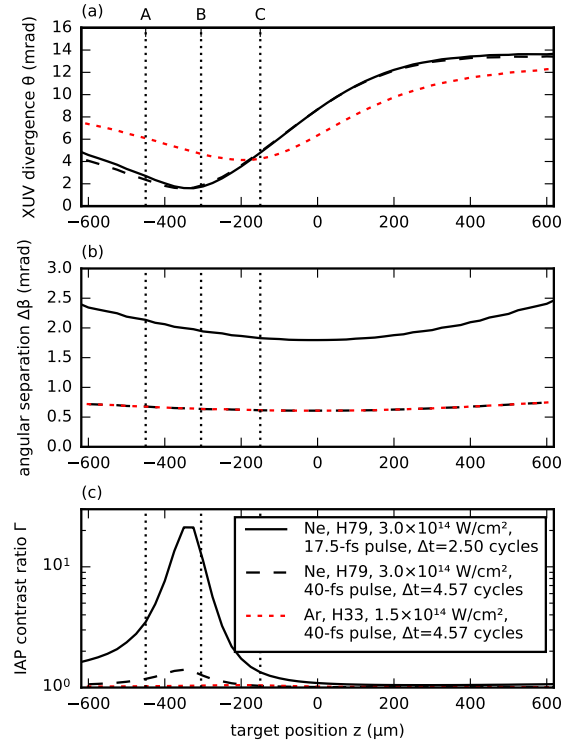


Fig. 7. a) XUV divergence in y direction for parameters enabling the gating of isolated attosecond pulses (solid line; see legend in (c)) and for the experimentally demonstrated parameters (dashed lines). b) Angular separation between consecutive attosecond bursts according to the numerical model. c) Resulting contrast ratio between strongest attosecond burst and neighboring bursts. The vertical dotted lines labeled with A, B and C mark the z position for the data shown in Figs. 5(b), 4 and 5(d), respectively.

D. Contributions to the angular separation

The total angular separation comprises contributions from the spatial chirp and, outside the focal plane, from the interplay of pulse front tilt and wave-front curvature, as illustrated in [33]. In the main text, we showed how to calculate the first contribution $\Delta\beta_c = -\pi c \omega_c^{-2} \gamma / (\gamma^2 + (w_y / \Delta\omega)^2)$ from the spatial dispersion γ , the $1/e^2$ -intensity spectral width $\Delta\omega$ and the lobe radius w_y . Here, we describe how the contribution $\Delta\beta_t$ from the pulse front tilt can be quantified.

As can be seen in Fig. 1 of the main text, the delay between the two lobes leads to a pulse front tilt around the focus region: the intensity maximum of the central lobe moves, on the time scale of one laser pulse, along the vertical direction y . Due to the wave-front curvature $R_{y,\text{eff}}^{-1}$, the wave-front direction β_t varies along this coordinate with a constant rate $d\beta_t/dy = -R_{y,\text{eff}}^{-1}$. For a given vertical velocity v of the intensity maximum, the vertical distance between the emission sites of two consecutive bursts is $vT/2$. Their angular separation is thus

$$\Delta\beta_t = vT/2 R_{y,\text{eff}}^{-1} \quad (15)$$

At each target position z_t , we calculated both contributions assuming the parameters for isolated attosecond pulse generation (compare Fig. 7(c), solid line). For this, we computed the spatial dispersion by performing a linear fit to the function $\omega \mapsto \arg \max_y |E_{\text{TMG}}(x_{\text{max}}, y, z_t, \omega)|^2$, evaluated along the (y, ω) grid. The lobe radius $w_{y,\text{eff}}$ and wave-front curvature $R_{y,\text{eff}}^{-1}$ were determined as described before, and the spectral width of a Gaussian pulse is $\Delta\omega = 2\sqrt{\log 4}/t_{\text{FWHM}}$. A linear fit to the function $t \mapsto \arg \max_y |E_{\text{TMG}}(x_{\text{max}}, y, z_t, t)|^2$, evaluated along the (y, t) grid, was used to determine the vertical velocity v of the intensity maximum. Figure 8 shows that this simple semi-analytical model for the two contributions $\Delta\beta_c$ and $\Delta\beta_t$ achieves acceptable agreement with the numerically determined total angular separation $\Delta\beta$.

The spatial dispersion was computed in the same way for the TMG mode used in the experiment (40-fs pulse, $\Delta t = 4.57T$). At the position where the transverse mode was imaged ($z = -305 \mu\text{m}$), we obtained a value of $-53 \mu\text{m}/\text{PHz}$.

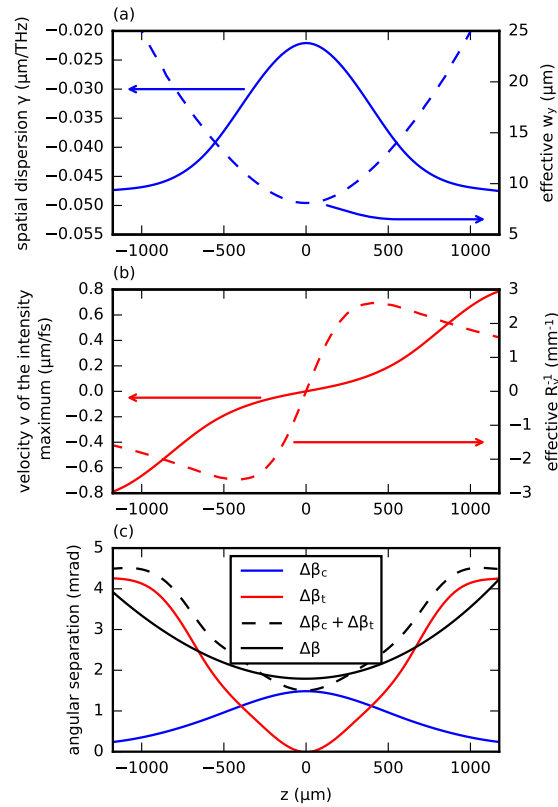


Fig. 8. a) Relevant parameters γ , w_y for the spatial chirp contribution to the angular separation, for parameters enabling the production of isolated attosecond pulses (compare Fig. 7(c), solid line). b) The same for the contribution from the pulse-front tilt. c) Semi-analytical approximations $\Delta\beta_c = -\pi c \omega_c^{-2} \gamma / (\gamma^2 + (w_y / \Delta\omega)^2)$ (spatial chirp contribution to the angular separation), $\Delta\beta_t = -vT/2 R_y^{-1}$ (pulse-front tilt contribution) and their sum, compared to the numerically computed value $\Delta\beta$.

E. Calibration of the z position in the experiments

E.1. Imaging the spatial dispersion

The focal region was imaged via a silicon nitride plate and two lenses. To determine the magnification factor and the z coordinate of the imaged plane for the data shown in Fig. 4 of the main text, we measured the distance between the two lenses (182 cm). Because it would be difficult to measure distances between the first lens (focal length $f = 50$ mm) and the focus and between the second lens ($f = 200$ mm) and the camera with sufficient precision, we recorded the caustic of the beam after the second lens by translating the camera on a stage. From this, we obtained the vertical divergence of the corresponding beam. The vertical divergence of the beam before the first lens can be calculated from the beam waist $w_{0,y} = 11.8 \mu\text{m}$, resulting from the mode size on the mirror ($w_y = 4.16$ mm) and the radius of curvature of the focusing mirrors ($R = 300$ mm). Knowing the divergence of the beam after the second and before the first lens, we selected beam radii on the two lenses consistent with these divergences by solving the corresponding system of two equations. Because the beam between both lenses is fully determined by these radii, this allows us to calculate the distances between the first lens and the focus and between the second lens and the camera, resulting in a magnification factor $U = -2.16$ and position $z = -305 \mu\text{m}$ for the plane imaged in Fig. 4 of the main text.

E.2. Position of the gas nozzle

The position z of the gas target relative to the focus was determined by translating the nozzle along the z axis while observing the plasma glow. We assumed that the position of the focus is in the middle of the two points where the plasma glow vanishes.

F. Calibration of the circulating power

The circulating power was calculated by integrating the intracavity power spectral density, which was determined indirectly by recording the power and spectrum transmitted through one of the plane, highly reflective cavity mirrors. We accounted for the spectrally dependent transmission curve of this mirror, which was measured with a spectrophotometer and calibrated using the power before and after the mirror while illuminated with a known spectrum. This approach allowed us to obtain correct values for the circulating power even in the case of strong ionization-induced spectral blueshift. For the empty cavity, we measured values up to 1.5 kW, corresponding to a pulse energy of $80 \mu\text{J}$.

G. Cumulative plasma effects

The velocity of the gas ejected by the $100\text{-}\mu\text{m}$ -diameter nozzle, pointing in the x direction, was computed with the analytical model described in [43, p. 17ff.], presuming a reservoir temperature of 300 K and a backing pressure in the order of 10 bar. This resulted in velocities > 280 m/s for argon and > 390 m/s for neon gas. At a repetition rate of 18.4 MHz, this corresponds to a translation distances of $15.2 \mu\text{m}$ (argon) and $21.2 \mu\text{m}$ (neon) between consecutive pulses. For comparison, the diameter $2w_{x,H} = 2w_{x,\text{eff}}/\sqrt{N_H}$ over which harmonics are created was $< 10.7 \mu\text{m}$ for argon and $< 9.7 \mu\text{m}$ for neon, for gas target positions $|z| < 500 \mu\text{m}$. Consequently, the demonstrated setup operated in a regime where the target gas is fully replenished between pulses so that the build-up of a cumulative plasma can be avoided.

H. Mode matching

In theory, the overlap of a Gaussian seeding mode with a spatial offset and a TEM_{01} mode can be 47.8% (value calculated with the numerical model). We measured a mode matching efficiency of only 30%, which can be attributed to several factors: First, the ellipticity of the seeding mode

did not perfectly match the ellipticity of the respective lobe of the cavity mode, second, the seeding mode was not a perfect Gaussian mode due to the compression scheme, and third, the measured overlap also includes the spectral overlap. The overlap can be improved by shaping the seeding beam using cylindrical lenses and a phase mask, so that, in theory, a value of 82.7% is possible [44]. Even better coupling efficiency can be achieved by using an input coupler with a half-sided highly-reflective coating [27], reaching values up to 98.2%. Alternatively, intracavity wave-front rotation could be obtained with a fundamental mode by placing transmissive or reflective wedges inside the resonator [45].

I. Comparison to the quasi-imaging method

Quasi-imaging-based output coupling methods require the operation of the resonator precisely in the middle of its stability range [20]. This imposes a limitation on the maximum beam radius $w_m = \sqrt{\lambda/|\pi\mathfrak{J}(q^{-1})|}$ on the focusing mirrors, determined in first approximation only by the cavity length L and the wavelength λ [20, equation 17]:

$$w_m = \sqrt{\frac{L\lambda}{\pi}} \quad (16)$$

For the experimental parameters $L = 16.3$ m, $\lambda = 1025$ nm, this results in a maximum beam radius of 2.3 mm. Using the same approach as described before, we numerically computed the electric far-field of the symmetric quasi-imaging mode $\sqrt{3/11}\widehat{\text{TEM}}_{00} - \sqrt{8/11}\widehat{\text{TEM}}_{04}$ (compare [21]) with this radius on a (x, y, ω) grid, for a 40-fs Gaussian pulse, and applied a discrete Fourier transform along the ω axis to obtain the complex envelope $E_{\text{QI}}(x, y, t)$. The ratio of the peak intensity $\max[c\epsilon_0/2 |E_{\text{QI}}(x, y, z_{\text{ff}}, t)|^2]$ and the peak power, obtained by spatial integration, was 8.55 cm^{-2} . For a damage threshold of $1 \times 10^{10} \text{ W/cm}^2$, the maximum permitted peak power is therefore $1 \times 10^{10} \text{ W/cm}^2 / (8.55 \text{ cm}^{-2}) = 1.17 \text{ GW}$. This value scales linearly with L , i.e., a shorter cavity permits less peak power when utilizing a quasi-imaging mode.

This limitation does not apply to output coupling with the TMG mode because operation in the middle of the stability range is not necessary. In our setup, the focusing mirrors were placed at a distance of 150 mm from the focus. The calculated peak intensity on the mirrors was $7.4 \times 10^9 \text{ W/cm}^2$ for a pulse energy of 80 μJ , corresponding to a peak power of 1.88 GW for 40-fs pulses.

Funding

MEGAS Fraunhofer/Max-Planck-Gesellschaft cooperation.

References

1. C. Gohle, T. Udem, M. Herrmann, J. Rauschenberger, R. Holzwarth, H. A. Schuessler, F. Krausz, and T. W. Hänsch, "A frequency comb in the extreme ultraviolet," *Nature* **436**, 234–237 (2005).
2. R. Jones, K. Moll, M. Thorpe, and J. Ye, "Phase-Coherent Frequency Combs in the Vacuum Ultraviolet via High-Harmonic Generation inside a Femtosecond Enhancement Cavity," *Phys. Rev. Lett.* **94**, 193201 (2005).
3. A. Cingöz, D. C. Yost, T. K. Allison, A. Ruehl, M. E. Fermann, I. Hartl, and J. Ye, "Direct frequency comb spectroscopy in the extreme ultraviolet," *Nature* **482**, 68–71 (2012).
4. C. Benko, T. K. Allison, A. Cingöz, L. Hua, F. Labaye, D. C. Yost, and J. Ye, "Extreme ultraviolet radiation with coherence time greater than 1 s," *Nat. Photonics* **8**, 530–536 (2014).
5. M. Herrmann, M. Haas, U. D. Jentschura, F. Kottmann, D. Leibfried, G. Saathoff, C. Gohle, A. Ozawa, V. Batteiger, S. Knünz, N. Kolachevsky, H. A. Schüssler, T. W. Hänsch, and T. Udem, "Feasibility of coherent xuv spectroscopy on the 1 S - 2 S transition in singly ionized helium," *Phys. Rev. A* **79**, 052505 (2009).
6. I. Pupeza, S. Holzberger, T. Eidam, H. Carstens, D. Esser, J. Weitenberg, P. Rußbüldt, J. Rauschenberger, J. Limpert, T. Udem, A. Tünnermann, T. W. Hänsch, A. Apolonski, F. Krausz, and E. Fill, "Compact high-repetition-rate source of coherent 100 eV radiation," *Nat. Photonics* **7**, 608–612 (2013).

7. H. Carstens, M. Högner, T. Saule, S. Holzberger, N. Lilienfein, A. Guggenmos, C. Jocher, T. Eidam, D. Esser, V. Tosa, V. Pervak, J. Limpert, A. Tünnermann, U. Kleineberg, F. Krausz, and I. Pupeza, "High-harmonic generation at 250 MHz with photon energies exceeding 100 eV," *Optica* **3**, 366 (2016).
8. T. Saule, S. Heinrich, J. Schötz, N. Lilienfein, M. Högner, O. deVries, M. Plötner, J. Weitenberg, D. Esser, J. Schulte, P. Russbuehler, J. Limpert, M. F. Kling, U. Kleineberg, and I. Pupeza, "High-flux ultrafast extreme-ultraviolet photoemission spectroscopy at 18.4 MHz pulse repetition rate," *Nat. Commun.* **10**, 458 (2019).
9. C. Corder, P. Zhao, J. Bakalis, X. Li, M. D. Kershner, A. R. Muraca, M. G. White, and T. K. Allison, "Ultrafast extreme ultraviolet photoemission without space charge," *Struct. Dyn.* **5**, 054301 (2018).
10. D. R. Carlson, J. Lee, J. Mongelli, E. M. Wright, and R. J. Jones, "Intracavity ionization and pulse formation in femtosecond enhancement cavities," *Opt. Lett.* **36**, 2991–2993 (2011).
11. T. K. Allison, A. Cingöz, D. C. Yost, and J. Ye, "Extreme Nonlinear Optics in a Femtosecond Enhancement Cavity," *Phys. Rev. Lett.* **107**, 183903 (2011).
12. S. Holzberger, N. Lilienfein, H. Carstens, T. Saule, M. Högner, F. Lücking, M. Trubetskov, V. Pervak, T. Eidam, J. Limpert, A. Tünnermann, E. Fill, F. Krausz, and I. Pupeza, "Femtosecond Enhancement Cavities in the Nonlinear Regime," *Phys. Rev. Lett.* **115**, 023902 (2015).
13. G. Porat, C. M. Heyl, S. B. Schoun, C. Benko, N. Dörre, K. L. Corwin, and J. Ye, "Phase-matched extreme-ultraviolet frequency-comb generation," *Nat. Photonics* **12**, 387–391 (2018).
14. T. Saule, M. Högner, N. Lilienfein, O. de Vries, M. Plötner, V. S. Yakovlev, N. Karpowicz, J. Limpert, and I. Pupeza, "Cumulative plasma effects in cavity-enhanced high-order harmonic generation in gases," *APL Photonics* **3**, 101301 (2018).
15. N. Lilienfein, C. Hofer, M. Högner, T. Saule, M. Trubetskov, V. Pervak, E. Fill, C. Riek, A. Leitenstorfer, J. Limpert, F. Krausz, and I. Pupeza, "Temporal solitons in free-space femtosecond enhancement cavities," *Nat. Photonics* **13**, 214–218 (2019).
16. M. Högner, T. Saule, and I. Pupeza, "Efficiency of cavity-enhanced high harmonic generation with geometric output coupling," *J. Phys. B: At. Mol. Opt. Phys.* **52**, 075401 (2019).
17. K. D. Moll, R. J. Jones, and J. Ye, "Output coupling methods for cavity-based high-harmonic generation," *Opt. Express* **14**, 8189–8197 (2006).
18. J. Wu and H. Zeng, "Cavity-enhanced noncollinear high-harmonic generation for extreme ultraviolet frequency combs," *Opt. Lett.* **32**, 3315–3317 (2007).
19. A. Ozawa, A. Vernaleken, W. Schneider, I. Gotlibovych, T. Udem, and T. W. Hänsch, "Non-collinear high harmonic generation: a promising outcoupling method for cavity-assisted XUV generation," *Opt. Express* **16**, 6233–6239 (2008).
20. J. Weitenberg, P. Rußbüldt, T. Eidam, and I. Pupeza, "Transverse mode tailoring in a quasi-imaging high-finesse femtosecond enhancement cavity," *Opt. Express* **19**, 9551–9561 (2011).
21. I. Pupeza, M. Högner, J. Weitenberg, S. Holzberger, D. Esser, T. Eidam, J. Limpert, A. Tünnermann, E. Fill, and V. Yakovlev, "Cavity-Enhanced High-Harmonic Generation with Spatially Tailored Driving Fields," *Phys. Rev. Lett.* **112**, 103902 (2014).
22. M. I. Stockman, M. F. Kling, U. Kleineberg, and F. Krausz, "Attosecond nanoplasmonic-field microscope," *Nat. Photonics* **1**, 539–544 (2007).
23. B. Förg, J. Schötz, F. Stübmann, M. Förster, M. Krüger, B. Ahn, W. A. Okell, K. Wintersperger, S. Zherebtsov, A. Guggenmos, V. Pervak, A. Kessel, S. A. Trushin, A. M. Azzeer, M. I. Stockman, D. Kim, F. Krausz, P. Hommelhoff, and M. F. Kling, "Attosecond nanoscale near-field sampling," *Nat. Commun.* **7**, 11717 (2016).
24. J. Schötz, B. Förg, M. Förster, W. A. Okell, M. I. Stockman, F. Krausz, P. Hommelhoff, and M. F. Kling, "Reconstruction of Nanoscale Near Fields by Attosecond Streaking," *IEEE J. Sel. Top. Quantum Electron.* **23**, 1–11 (2017).
25. N. Lilienfein, C. Hofer, S. Holzberger, C. Matzer, P. Zimmermann, M. Trubetskov, V. Pervak, and I. Pupeza, "Enhancement cavities for few-cycle pulses," *Opt. Lett.* **42**, 271–274 (2017).
26. M. Högner, V. Tosa, and I. Pupeza, "Generation of isolated attosecond pulses with enhancement cavities—a theoretical study," *New J. Phys.* **19**, 033040 (2017).
27. M. Högner, T. Saule, N. Lilienfein, V. Pervak, and I. Pupeza, "Tailoring the transverse mode of a high-finesse optical resonator with stepped mirrors," *J. Opt.* **20**, 024003 (2018).
28. C. M. Heyl, S. N. Bengtsson, S. Carlström, J. Mauritsson, C. L. Arnold, and A. L'Huillier, "Corrigendum: Noncollinear optical gating (2014 *New J. Phys.* **16** 052001)," *New J. Phys.* **16**, 109501 (2014).
29. M. Louisy, C. L. Arnold, M. Miranda, E. W. Larsen, S. N. Bengtsson, D. Kroon, M. Kotur, D. Guénot, L. Rading, P. Rudawski, F. Brizuela, F. Campi, B. Kim, A. Jarnac, A. Houard, J. Mauritsson, P. Johnsson, A. L'Huillier, and C. M. Heyl, "Gating attosecond pulses in a noncollinear geometry," *Optica* **2**, 563–566 (2015).
30. H. Vincenti and F. Quéré, "Attosecond Lighthouses: How To Use Spatiotemporally Coupled Light Fields To Generate Isolated Attosecond Pulses," *Phys. Rev. Lett.* **108**, 113904 (2012).
31. K. T. Kim, C. Zhang, T. Ruchon, J.-F. Hergott, T. Augustine, D. M. Villeneuve, P. B. Corkum, and F. Quéré, "Photonic streaking of attosecond pulse trains," *Nat. Photonics* **7**, 651–656 (2013).
32. T. J. Hammond, G. G. Brown, K. T. Kim, D. M. Villeneuve, and P. B. Corkum, "Attosecond pulses measured from the attosecond lighthouse," *Nat. Photonics* **10**, 171–175 (2016).
33. T. Augustine, O. Gobert, T. Ruchon, and F. Quéré, "Attosecond lighthouses in gases: A theoretical and numerical

- study," *Phys. Rev. A* **93**, 033825 (2016).
34. E. Balogh, C. Zhang, T. Ruchon, J.-F. Hergott, F. Quere, P. Corkum, C. H. Nam, and K. T. Kim, "Dynamic wavefront rotation in the attosecond lighthouse," *Optica* **4**, 48–53 (2017).
 35. H. Carstens, S. Holzberger, J. Kaster, J. Weitenberg, V. Pervak, A. Apolonski, E. Fill, F. Krausz, and I. Pupeza, "Large-mode enhancement cavities," *Opt. Express* **21**, 11606–11617 (2013).
 36. S. Holzberger, N. Lilienfein, M. Trubetskov, H. Carstens, F. Lücking, V. Pervak, F. Krausz, and I. Pupeza, "Enhancement cavities for zero-offset-frequency pulse trains," *Opt. Lett.* **40**, 2165–2168 (2015).
 37. X. Gu, S. Akturk, and R. Trebino, "Spatial chirp in ultrafast optics," *Opt. Commun.* **242**, 599–604 (2004).
 38. L. von der Wense, B. Seiferle, M. Laatiaoui, J. B. Neumayr, H.-J. Maier, H.-F. Wirth, C. Mokry, J. Runke, K. Eberhardt, C. E. Düllmann, N. G. Trautmann, and P. G. Thirolf, "Direct detection of the 229th nuclear clock transition," *Nature* **533**, 47–51 (2016).
 39. C. Gaida, M. Gebhardt, T. Heuermann, F. Stutzki, C. Jauregui, and J. Limpert, "Ultrafast thulium fiber laser system emitting more than 1 kW of average power," *Opt. Lett.* **43**, 5853–5856 (2018).
 40. J. Zhang, K. Fai Mak, N. Nagl, M. Seidel, D. Bauer, D. Sutter, V. Pervak, F. Krausz, and O. Pronin, "Multi-mW, few-cycle mid-infrared continuum spanning from 500 to 2250 cm⁻¹," *Light. Sci. Appl.* **7**, 17180 (2018).
 41. A. E. Siegman, *Lasers* (University Science Books, 1986).
 42. D. G. Voelz, *Computational fourier optics – a MATLAB® tutorial* (SPIE Press, Bellingham, Wash, 2011).
 43. G. Scoles, *Atomic and Molecular Beam Methods* (Oxford University Press, 1988).
 44. J. Weitenberg, P. Rußbüldt, I. Pupeza, T. Udem, H.-D. Hoffmann, and R. Poprawe, "Geometrical on-axis access to high-finesse resonators by quasi-imaging: a theoretical description," *J. Opt.* **17**, 025609 (2015).
 45. I. Pupeza, E. E. Fill, and F. Krausz, "Low-loss VIS/IR-XUV beam splitter for high-power applications," *Opt. Express* **19**, 12108–12118 (2011).

Chapter 5

Outlook

5.1 Toward Cavity-Enhanced Generation of Isolated Attosecond Pulses

The transverse mode gating technique, whose development is outlined in Chapter 4, has enabled the demonstration of an EC with an intracavity wave-front rotation and of the first XUV spectra measured from a resonator eigenmode tailored in this way (see Section 4.3). As shown with the numerical model, the individual attosecond beamlets in this first experiment overlapped, preventing the separation of IAPs by spatial filtering. To obtain IAP, the angular separation between the beamlets must be increased either by using a larger delay or shorter driving pulses. In Sections 4.1 and 4.3, it was illustrated that 17.5-fs-long pulses and a delay of 5 half cycles would be sufficient for IAP generation without changes to the demonstrated geometry and seed pulse energy.

Such short pulse durations have in fact already been shown in ECs [57], but remain a challenge due to statistical variations in the refractive indices and thicknesses of the individual layers in the production of highly reflective multilayer mirror coatings¹. As a result, the spectral phase deviates from the design. This circumstance can be alleviated to some extent by combining the mirrors from several coating runs with different deviations that cancel out in sum, thus enabling an acceptably flat round-trip phase curve. An additional constraint is that the comb offset frequency preferred by the EC, which is given by the mirror coatings, must be zero for a waveform-stable XUV source [83].

The seed pulse has to be compressed accordingly without introducing noise that impairs the frequency comb properties, which can be deemed possible even at high pulse energies with present-day all-solid-state multi-stage schemes [109, 110]. The manufacturing and applicability of EC output coupling mirrors with a slit-shaped aperture was already shown in [73, 111]. In the demonstrated geometry, phase matching pressures around 2 bar are expected for a peak intensity of $3 \times 10^{14} \text{ W/cm}^2$ in neon. While the technology to achieve the necessary pressures in the target exists, it may be advisable to use several turbomolecular pumps or a gas catcher to

¹Several coating runs were attempted in preparation for the experiment described in Section 4.3, but failed to provide the necessary bandwidth.

maintain low XUV reabsorption in the background gas [112, 113]. Looser focusing also helps to reduce the phase matching pressure, but necessitates higher pulse energies to reach the same peak intensities in the target and increases cumulative plasma effects.

To further examine which combinations of intracavity pulse duration and delay are viable for the generation of IAPs, the model described in Section 4.3 was applied to compute the intensity contrast ratio between the most intense attosecond burst and its neighboring bursts, obtained for pulse durations of 17.5 fs, 25 fs and 30 fs, and delays of 5, 7 and 9 half cycles, respectively, for the same geometry and a pulse energy normalized for a peak intensity of 3×10^{14} W/cm² (Fig. 5.1). These simulations show that even with 30-fs-pulses, contrast ratios > 3 are possible. Pulses with a FWHM of 25 fs are predicted to enable IAP with a contrast ratio > 10 . In all cases, the necessary pulse energy and the peak intensity on the cavity mirrors was computed and found to remain below 80 μ J (demonstrated value) and 1×10^{10} W/cm² (estimated damage threshold).

In conclusion, a clear route toward the efficient production of IAPs at multi-10-MHz repetition rates was presented. Such a source holds prospects for enabling space-charge free multidimensional photoelectron emission studies with attosecond temporal resolution, e.g., the time-resolved microscopy of plasmonic fields in nanostructures, known as attoPEEM [18–20, 114, 115].

5.2 Future Directions for Free-Space Cavity Solitons

The soliton experiment described in Section 2.2.3 and [89] was the first experimental demonstration of spectrally tailoring EC mirrors for cavity-housed nonlinearities. This approach was formerly also suggested for the plasma nonlinearity in ECs with a gas target and was theoretically identified as a way to mitigate the main limitation for the scalability of the XUV power from EC-based sources – plasma-induced intensity clamping [77]. In this context, several directions for future research arise.

First, it was observed that low-frequency intensity noise of the seed is considerably reduced in the circulating pulse, which intriguingly complements the high-frequency-noise-filtering properties inherent to ECs. However, additional noise at frequencies between 30 and 500 kHz was observed. It can be investigated, e.g., by using the developed numerical model, whether the low-frequency noise is converted to higher-frequency noise by an overshooting behavior of the intensity-self-stabilizing mechanism and if there are ways to prevent such an overshooting. Moreover, it would be interesting to study whether and to what extent phase noise introduced by the seed or by a jitter in the EC length is transferred to intensity and phase noise of the pulse inside the EC.

A second question is how the circulating power in this architecture can be scaled up, which could enable applications in cavity-enhanced HHG or as a pulse compression scheme which can, in analogy to compression in multi-pass cells, provide excellent beam quality owing to the partitioning of the total effective nonlinearity into a large number of smaller portions, separated by free-space propagation [116].

It is still unclear why comparably stable solitons at higher circulating power were not observed. One possible hindering mechanism, that could, in principle, be verified with a 3D version of the numerical model presented here, are spatial effects, i.e., Kerr lensing in the nonlinear medium.

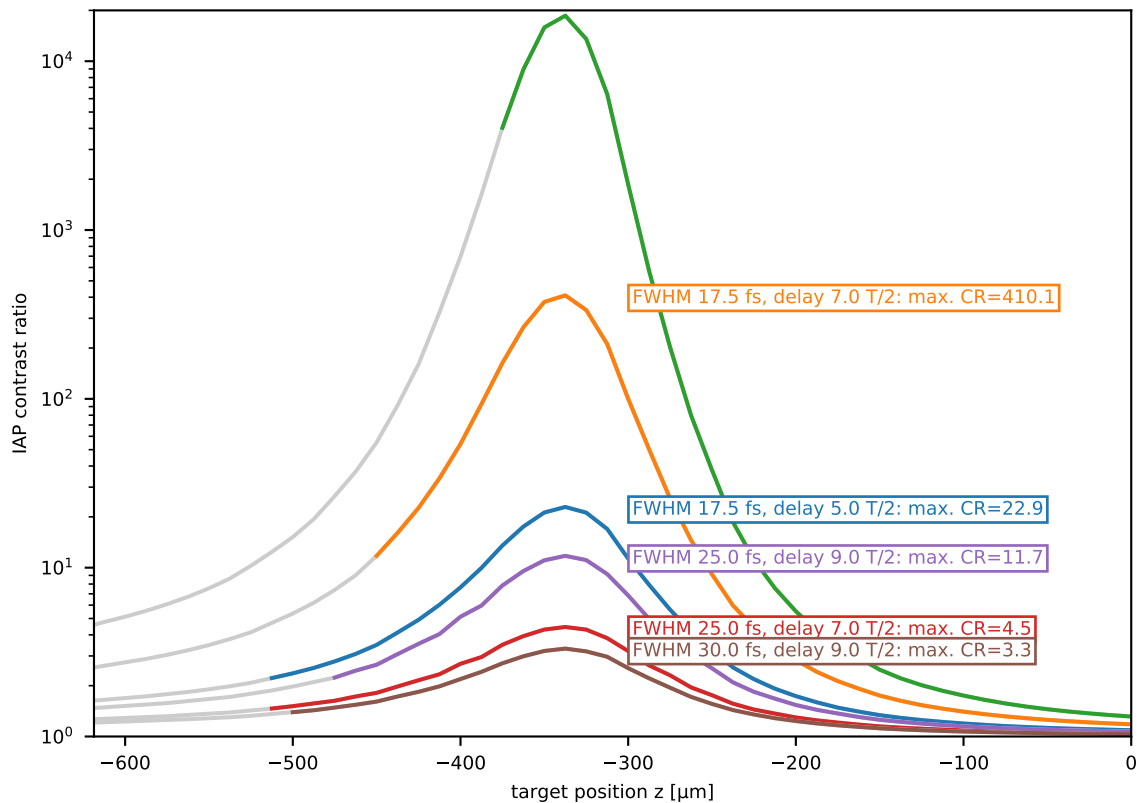


Figure 5.1: Contrast ratios achievable with transverse mode gating, using the focusing conditions and pulse energy demonstrated in Section 4.3. Each line corresponds to a choice of the full-width-half-maximum (FWHM) intracavity pulse duration and delay introduced by the stepped mirrors ($T/2$ is the half cycle duration). The contrast ratio (CR) of the generated isolated attosecond pulses (IAP) is computed for each position z of the gas target relative to the focal plane. The gray continuations of the lines identify where the pulse energy necessary to reach a peak intensity of $3 \times 10^{14} \text{ W/cm}^2$ in the gas target exceeds the experimentally demonstrated value of $80 \mu\text{J}$, or the peak intensity on the mirror exceeds the assumed damage threshold ($1 \times 10^{10} \text{ W/cm}^2$). Combinations of pulse duration and delay that resulted in contrast ratios below three were omitted for clearness.

If a significant fraction of the seeding power can be coupled out efficiently from the power circulating inside the cavity, the platform can also hold prospects as a pulse compression scheme with inherent intensity stability and excellent beam quality. Simulations could be used to investigate how the soliton behaves in the case of the high round-trip losses associated with high output coupling ratios.

Temporal optical solitons arise from the combination of a second-order linear spectral phase and the self-phase modulation due to the Kerr effect. In the presence of an additional higher-order spectral phase, steady-state solutions can still exist as a form of generalized solitons [117]. It is worthwhile to analyze whether this can be exploited for reduced sensitivity to higher-order phase deviations. This could allow additional flexibility in the production of highly reflective EC mirrors, possibly enabling significantly broader circulating spectra than those achievable in a linear EC.

For cavity-enhanced HHG, the plasma-induced refractive index modulation entails an effective spectral phase shift that contributes, beside the blueshift, to intensity clamping. Provided that a solution for power scaling can be found, it may be feasible to drive HHG in gases with free-space cavity solitons, mitigating clamping. Because such generalized steady-state solutions can also exist when the plasma nonlinearity takes over the role of the Kerr nonlinearity, it may even be possible to reduce clamping effects without the use of the Kerr effect – the very approach suggested in [77]. The numerical models presented in this thesis allow to investigate the possibilities of this approach, and a mathematical framework similar to the time-domain Lugiato-Lefever equation [118, 119] and its generalizations would be desirable. Other interesting questions are whether such steady states exhibit a similar inherent intensity stability and how to tune into the steady state from the cold state.

If it turns out, as described above, that nonlinear ECs in the soliton regime support a broader bandwidth than linear ECs, this makes them a very promising platform for cavity-enhanced absorption spectroscopy of optically thin media, e.g., in the molecular fingerprint region. For this, a thorough understanding of the interplay between linear absorptive features and the nonlinear soliton dynamics must be developed [120].

Very recently, cavity-enhanced HHG in solids has been reported [121]. Such all-solid-state sources of VUV radiation may be an ideal fit for first investigations of cavity-soliton-driven HHG – all the more, because the target usually exhibits a strong Kerr nonlinearity anyway and because power scaling of the soliton EC is not necessary: The soliton pulse energy of 5 μJ demonstrated in [89] was already more than one order of magnitude higher than the one used for solid-state HHG in [121].

5.3 Multi-Color Enhancement Cavities

The mode tailoring approach described in Chapter 4, where one lobe of a TEM_{01} resonator mode is delayed by a half cycle by means of a mirror with a stepped surface profile, enables highly efficient geometric output coupling thanks to an intensity minimum along a slit-shaped aperture in an output coupling mirror. What is more, the intensity profile of this mode allows a narrow lossy region oriented along the x axis to extend in width with increasing distance from the optical axis, without introducing severe losses (Fig. 5.2a). When the separation between the two lobes of the mode is increased, the angular diameter of such a bow-tie-shaped region can be increased correspondingly. This can be done by increasing the ellipticity of the

mode (Fig. 5.2b), e.g., by using focusing mirrors with different radii of curvature in vertical and horizontal direction or by proper choice of the incidence angles, and also by exploiting the astigmatism introduced by spherical focusing mirrors [87].

More generally, accordingly tailored surface profiles of the focusing mirrors can allow for increasing the angular diameter of the unilluminated area, up to the point that a 90°-wide bow-tie-shaped lossy region is tolerated. Then, a second mode where the lobes are oriented in the orthogonal direction can be superposed over the first mode. On the mirrors, these two modes will illuminate separate quadrants (Fig. 5.3b), such that different coatings can be used (Fig. 5.3c). This allows to enhance two broadband pulses centered at different wavelengths at the same time, which otherwise would not be possible due to bandwidth limitations of the highly reflective multilayer mirror coatings. Laser manufacturing is a promising approach to produce the necessary free-form focusing mirrors [122, 123]. Stepped mirrors with step heights adapted to the two different wavelengths can be used to obtain on-axis maxima in the focus (Figs. 5.3a and f), e.g., for improved intensity and beam quality when driving frequency conversion processes. For efficient input coupling, for each of both wavelengths one can overlap a Gaussian seeding beam with one of the lobes of the EC eigenmode and use an input coupler that is highly reflective at the position of the other lobe (Figs. 5.3a and e).

Such a scheme would have several interesting applications: First, it could be used to double the bandwidth for cavity-enhanced absorption spectroscopy in optically thin media. This can be done without step mirrors because it is usually not important that the two spectral regions overlap spatially. Moreover, it can be applied with step mirrors to obtain a broad spectrum and thus a considerably shorter pulse in the focus region than possible with a single-color EC. For HHG applications, this will further mitigate intensity clamping restrictions and allow for higher XUV power [53]. The flexibility of using two different central wavelengths can also be exploited for gating isolated attosecond pulses, to reach photon energies in the soft x-ray range and to significantly improve the phase matching [124–126]. Apart from HHG, this method is also promising for driving other frequency conversion processes, e.g., terahertz generation from strong-field-induced gas plasmas, where the second harmonic is used to introduce an AC bias [127, 128].

Even without using different coatings for the mirror segments, such a monolithic two-in-one enhancement cavity scheme could be applied for simultaneously enhancing two separate frequency combs with slightly different repetition rates, which are then spatially overlapped in the focus. For this, slightly different cavity lengths can be achieved by coating additional material on two opposing quadrants of the stepped mirrors. This could enable cavity-enhanced dual-comb coherent anti-Stokes Raman spectroscopy of vibrational transitions in molecules [129].

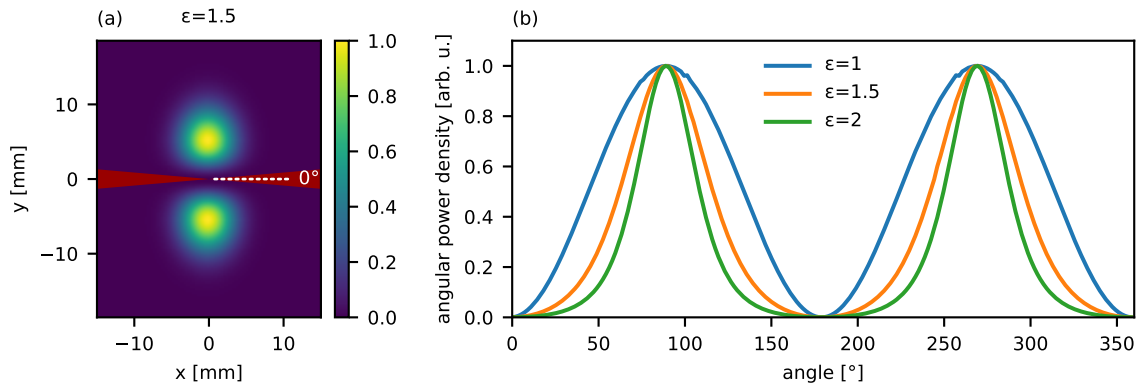


Figure 5.2: Angular distribution of the power in a TEM_{01} mode. (a) Normalized intensity profile of a TEM_{01} mode with an ellipticity of $\epsilon = 1.5$, with a narrow bow-tie-shaped lossy area (red) that is avoided by the mode. (b) Angular power density, as seen from the origin $x = y = 0$, for different ellipticities ϵ , versus angle relative to the x axis.

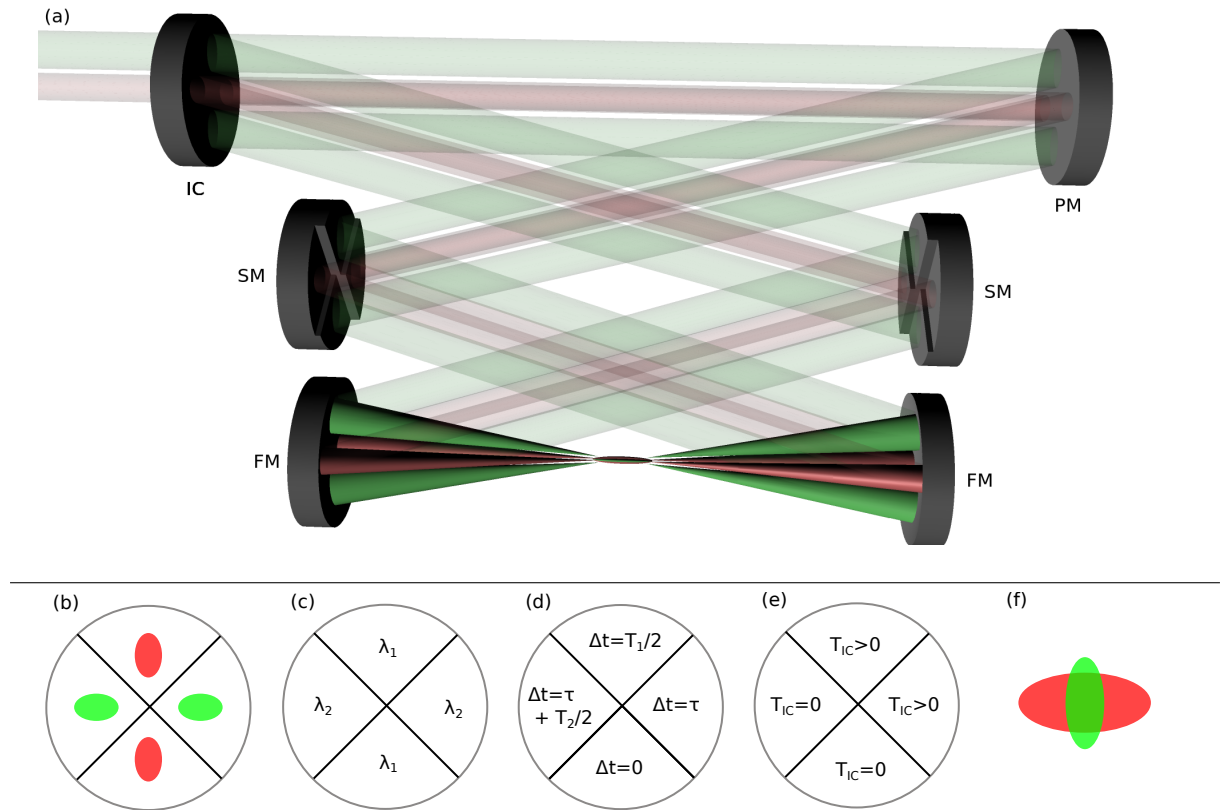


Figure 5.3: Working principle of a multi-color enhancement cavity. (a) Setup. IC: input coupling mirror, PM: plane mirror, SM: mirror with a stepped surface profile, FM: focusing mirror. (b) Transverse mode profiles on the resonator mirrors (red: first wavelength, green: second wavelength). (c) Segmented mirror coatings: two opposed quadrants are highly reflective in a bandwidth centered at the first wavelength, λ_1 , the other two around the second wavelength, λ_2 . (d) Delay Δt for each quadrant of the stepped mirrors, with half cycles $T_1/2 = \lambda_1/c/2$ and $T_2/2 = \lambda_2/c/2$, and a correction τ to obtain the same effective cavity length for both wavelengths. (e) Input coupler with two highly reflective quadrants to improve the overlap with the seed mode. T_{IC} : input coupling transmission. (f) Transverse mode profiles in the focus, where the two wavelengths overlap spatially.

Appendix **A**

Comparison of HHG Sources

Table A.1: Photon rates Γ from single-pass (SP) and cavity (EC)-enhanced HHG sources reported in literature. f_{rep} , λ , t_{FWHM} and P are the repetition rate, central wavelength, full-width-half-maximum pulse duration and average power of the laser system, respectively, and E_{ph} is the central photon energy of each measured harmonic order.

Reference	Type	f_{rep}	λ [nm]	t_{FWHM} [fs]	P [W]	E_{ph} [eV]	Γ [s^{-1}]
Co99 [130]	SP	1.0 kHz	800	40	1.50	23.0	8.1×10^{12}
Ta04A [131]	SP	10.0 Hz	800	30	0.50	48.1	1.8×10^{10}
						51.0	2.1×10^{10}
						54.2	2.1×10^{10}
						57.2	2.0×10^{10}
						60.7	1.8×10^{10}
						63.3	1.9×10^{10}
						66.5	2.0×10^{10}
						69.8	2.0×10^{10}
						72.7	1.9×10^{10}
						75.9	2.0×10^{10}
						79.1	1.8×10^{10}
						82.2	1.8×10^{10}
						85.2	1.7×10^{10}
						88.5	1.6×10^{10}
91.5	1.7×10^{10}						
94.6	1.8×10^{10}						
97.7	1.4×10^{10}						
Ta04I [132]	SP	10.0 Hz	800	30	0.16	17.0	2.3×10^{13}
						20.1	1.5×10^{13}
						23.2	2.6×10^{12}
						26.3	1.5×10^{12}

Reference	Type	f_{rep}	λ [nm]	t_{FWHM} [fs]	P [W]	E_{ph} [eV]	Γ [s^{-1}]
						29.4	1.7×10^{12}
Ta04I [132]	SP	10.0 Hz	800	30	2.00	35.6	8.8×10^{10}
						38.7	2.4×10^{11}
						41.8	3.7×10^{11}
						44.9	1.4×10^{11}
						48.0	2.6×10^{10}
Ta04I [132]	SP	10.0 Hz	800	30	0.50	91.4	1.7×10^{10}
Go05 [44]	EC	112.0 MHz	800	30	0.85	13.9	3.0×10^4
						17.0	3.0×10^4
Jo05 [43]	EC	100.0 MHz	800	60	0.80	4.6	5.4×10^{12}
Oz08 [61]	EC	10.8 MHz	810	57	1.00	10.7	2.6×10^{12}
						13.8	2.4×10^{11}
						16.8	5.2×10^{11}
						19.9	2.6×10^{11}
						23.0	2.2×10^{10}
						26.0	6.2×10^8
						29.1	1.2×10^8
Yo08 [60]	EC	136.0 MHz	1070	100	10.00	15.1	1.0×10^{11}
						17.4	7.2×10^9
						19.7	1.7×10^{10}
						22.0	1.1×10^{10}
Al11 [65]	EC	154.0 MHz	1070	120	80.00	15.1	8.3×10^{12}
Ha11 [62]	EC	66.0 MHz	790	70	0.70	17.0	3.7×10^{11}
Le11 [63]	EC	50.0 MHz	800	80	6.00	11.0	1.9×10^{12}
						14.1	1.5×10^{12}
						17.2	1.3×10^{12}
						20.3	7.0×10^{11}
						23.4	1.2×10^{11}
Be12 [64]	EC	128.0 MHz	518	155	5.00	7.2	4.3×10^{13}
						12.0	2.6×10^{10}
						16.8	1.9×10^8
						21.5	1.4×10^7
Ci12 [48]	EC	154.0 MHz	1080	120	30.00	10.3	1.1×10^{13}
						12.6	1.1×10^{13}
						14.9	6.7×10^{12}
						17.2	7.6×10^{12}
						19.5	6.1×10^{12}
						21.8	6.0×10^{12}

Reference	Type	f_{rep}	λ [nm]	t_{FWHM} [fs]	P [W]	E_{ph} [eV]	Γ [s^{-1}]
						24.1	2.8×10^{12}
						26.4	3.3×10^{11}
Oz13 [49]	EC	79.0 MHz	1030	200	11.00	8.4	4.5×10^{10}
Pu13 [53]	EC	78.0 MHz	1040	57	60.00	31.8 108.3	1.0×10^{12} 4.6×10^5
Di14 [133]	SP	1.0 kHz	1300	30	2.00	200.0	1.0×10^9
Ha14 [79]	SP	600.0 kHz	1030	30	80.00	25.2 27.6 30.0 32.4 34.8 37.2	2.3×10^{13} 2.9×10^{13} 3.0×10^{13} 2.0×10^{13} 5.9×10^{12} 8.4×10^{11}
Ha14 [79]	SP	600.0 kHz	1030	30	80.00	27.6 30.0 32.4 34.8 37.2 39.6	7.2×10^{12} 8.3×10^{12} 8.1×10^{12} 7.2×10^{12} 6.0×10^{12} 5.0×10^{12}
Lo14 [134]	SP	20.0 kHz	1030	170	3.14	15.6 18.1 20.5 22.9 25.3 27.7 30.1 32.5 34.9 37.3 39.7 42.1 44.5 46.9	3.8×10^{10} 4.3×10^{10} 2.1×10^{11} 2.7×10^{11} 3.8×10^{11} 2.1×10^{11} 2.0×10^{11} 1.6×10^{11} 1.2×10^{11} 1.2×10^{11} 8.4×10^{10} 3.3×10^{10} 8.8×10^9 2.9×10^9
Lo14 [134]	SP	100.0 kHz	1030	170	5.40	18.1 20.5 22.9 25.3 27.7 30.1 32.5 34.9	3.7×10^9 3.1×10^{10} 4.0×10^{10} 4.1×10^{10} 4.1×10^{10} 4.4×10^{10} 4.1×10^{10} 3.6×10^{10}

Reference	Type	f_{rep}	λ [nm]	t_{FWHM} [fs]	P [W]	E_{ph} [eV]	Γ [s^{-1}]
						37.3	1.4×10^{10}
						39.7	8.5×10^8
Pu14 [73]	EC	78.0 MHz	1040	100	45.00	15.5	3.2×10^{12}
						17.9	3.8×10^{12}
						20.3	3.4×10^{12}
						22.7	1.9×10^{12}
Ro14N [135]	SP	150.0 kHz	820	8	0.97	25.7	1.9×10^{12}
						40.8	2.1×10^{11}
Ro14O [136]	SP	150.0 kHz	1030	8	35.00	120.0	3.1×10^9
						180.0	1.0×10^8
Ci15 [137]	SP	700.0 kHz	1030	300	9.80	16.0	4.6×10^7
						25.0	8.0×10^8
						32.0	1.2×10^5
Ha15 [50]	SP	10.7 MHz	1030	31	75.00	20.7	8.2×10^{12}
						23.0	9.4×10^{12}
						25.3	9.6×10^{12}
						27.6	1.1×10^{13}
						30.2	5.3×10^{12}
Mi15 [81]	EC	60.0 MHz	1050	120	20.00	17.7	1.1×10^{12}
Oz15 [138]	EC	10.0 MHz	1040	200	23.00	8.3	3.7×10^{14}
						17.9	3.5×10^{12}
						20.3	3.1×10^{12}
						22.7	2.8×10^{12}
Ca16 [55]	EC	250.0 MHz	1030	30	170.00	41.3	3.8×10^{11}
						94.0	8.6×10^7
Kl16 [139]	SP	120.0 kHz	515	85	11.00	21.7	2.4×10^{14}
						26.6	1.7×10^{13}
Ro16 [140]	SP	100.0 kHz	1030	35	60.00	56.6	5.0×10^{10}
						59.0	6.4×10^{10}
						61.4	7.9×10^{10}
						63.8	7.9×10^{10}
						66.2	7.8×10^{10}
						68.6	6.8×10^{10}
						71.0	4.0×10^{10}
Zh17 [141]	SP	1.0 MHz	347	100	5.00	10.7	7.3×10^{14}
Co18 [82]	EC	88.0 MHz	1030	155	40.00	10.7	2.0×10^{10}
						10.8	1.4×10^{10}
						13.2	3.0×10^{10}

Reference	Type	f_{rep}	λ [nm]	t_{FWHM} [fs]	P [W]	E_{ph} [eV]	Γ [s^{-1}]
						13.2	1.4×10^{10}
						15.6	5.0×10^{10}
						15.7	4.2×10^{10}
						18.0	3.7×10^{10}
						18.0	1.3×10^{11}
						18.0	1.1×10^{11}
						20.4	2.4×10^{11}
						20.4	1.3×10^{11}
						20.4	6.3×10^{10}
						22.8	1.0×10^{11}
						22.8	4.7×10^{11}
						22.9	2.0×10^{11}
						25.2	1.7×10^{11}
						25.2	2.8×10^{11}
						25.3	2.1×10^{11}
						27.6	1.9×10^{11}
						27.6	1.5×10^{10}
						27.7	3.5×10^{11}
						30.0	1.8×10^{11}
						30.1	2.4×10^{11}
						32.4	2.0×10^{11}
						32.4	6.9×10^{10}
						34.8	1.6×10^{11}
						37.2	9.3×10^{10}
						39.6	3.8×10^{10}
						42.0	1.8×10^{10}
Po18 [112]	EC	77.0 MHz	1070	120	80.00	12.7	6.5×10^{13}
						19.7	3.0×10^{13}
Sa19 [56]	EC	18.0 MHz	1030	40	77.00	27.7	1.8×10^{11}
						30.1	5.2×10^{11}
						32.5	1.1×10^{12}
						34.9	2.1×10^{12}
						37.3	2.4×10^{12}
						39.7	1.7×10^{12}
						42.1	1.1×10^{12}
						44.5	8.0×10^{11}
						46.9	5.6×10^{11}
						49.4	2.9×10^{11}
						51.8	1.1×10^{11}

References

- [1] J. P. Gordon, H. J. Zeiger, and C. H. Townes, “*Molecular microwave oscillator and new hyperfine structure in the microwave spectrum of NH₃*”, *Physical Review* **95**, 282–284 (1954) [10.1103/physrev.95.282](https://doi.org/10.1103/physrev.95.282).
- [2] J. P. Gordon, H. J. Zeiger, and C. H. Townes, “*The maser—new type of microwave amplifier, frequency standard, and spectrometer*”, *Physical Review* **99**, 1264–1274 (1955) [10.1103/physrev.99.1264](https://doi.org/10.1103/physrev.99.1264).
- [3] T. H. Maiman, “*Stimulated optical radiation in ruby*”, *Nature* **187**, 493–494 (1960) [10.1038/187493a0](https://doi.org/10.1038/187493a0).
- [4] H. Haus, “*Mode-locking of lasers*”, *IEEE Journal of Selected Topics in Quantum Electronics* **6**, 1173–1185 (2000) [10.1109/2944.902165](https://doi.org/10.1109/2944.902165).
- [5] U. Morgner, F. X. Kärtner, S. H. Cho, Y. Chen, H. A. Haus, J. G. Fujimoto, E. P. Ippen, V. Scheuer, G. Angelow, and T. Tschudi, “*Sub-two-cycle pulses from a Kerr-lens mode-locked ti:sapphire laser*”, *Optics Letters* **24**, 411 (1999) [10.1364/ol.24.000411](https://doi.org/10.1364/ol.24.000411).
- [6] D. H. Sutter, G. Steinmeyer, L. Gallmann, N. Matuschek, F. Morier-Genoud, U. Keller, V. Scheuer, G. Angelow, and T. Tschudi, “*Semiconductor saturable-absorber mirror-assisted Kerr-lens mode-locked ti:sapphire laser producing pulses in the two-cycle regime*”, *Optics Letters* **24**, 631 (1999) [10.1364/ol.24.000631](https://doi.org/10.1364/ol.24.000631).
- [7] J.-C. Diels and W. Rudolph, *Ultrashort laser pulse phenomena* (Elsevier, Burlington, MA, 2006), [10.1016/b978-0-12-215493-5.x5000-9](https://doi.org/10.1016/b978-0-12-215493-5.x5000-9).
- [8] J. Reichert, M. Niering, R. Holzwarth, M. Weitz, T. Udem, and T. W. Hänsch, “*Phase coherent vacuum-ultraviolet to radio frequency comparison with a mode-locked laser*”, *Physical Review Letters* **84**, 3232–3235 (2000) [10.1103/physrevlett.84.3232](https://doi.org/10.1103/physrevlett.84.3232).
- [9] C. G. Parthey, A. Matveev, J. Alnis, B. Bernhardt, A. Beyer, R. Holzwarth, A. Maistrou, R. Pohl, K. Predehl, T. Udem, T. Wilken, N. Kolachevsky, M. Abgrall, D. Rovera, C. Salomon, P. Laurent, and T. W. Hänsch, “*Improved measurement of the hydrogen 1S–2S transition frequency*”, *Physical Review Letters* **107**, 203001 (2011) [10.1103/physrevlett.107.203001](https://doi.org/10.1103/physrevlett.107.203001).
- [10] T. Udem, A. Huber, B. Gross, J. Reichert, M. Prevedelli, M. Weitz, and T. W. Hänsch, “*Phase-coherent measurement of the hydrogen 1S–2S transition frequency with an optical frequency interval divider chain*”, *Physical Review Letters* **79**, 2646–2649 (1997) [10.1103/physrevlett.79.2646](https://doi.org/10.1103/physrevlett.79.2646).
- [11] T. Udem, R. Holzwarth, and T. W. Hänsch, “*Optical frequency metrology*”, *Nature* **416**, 233–237 (2002) [10.1038/416233a](https://doi.org/10.1038/416233a).
- [12] J. Rothhardt, G. K. Tadesse, W. Eschen, and J. Limpert, “*Table-top nanoscale coherent imaging with XUV light*”, *Journal of Optics* **20**, 113001 (2018) [10.1088/2040-8986/aae2d8](https://doi.org/10.1088/2040-8986/aae2d8).
- [13] I. S. Osborne, “*PHYSICS: Attosecond streak camera*”, *Science* **303**, 437b–437 (2004) [10.1126/science.303.5657.437b](https://doi.org/10.1126/science.303.5657.437b).

- [14] M. Hentschel, R. Kienberger, C. Spielmann, G. A. Reider, N. Milosevic, T. Brabec, P. Corkum, U. Heinzmann, M. Drescher, and F. Krausz, “Attosecond metrology”, *Nature* **414**, 509–513 (2001) [10.1038/35107000](https://doi.org/10.1038/35107000).
- [15] M. Ossiander, F. Siegrist, V. Shirvanyan, R. Pazourek, A. Sommer, T. Latka, A. Guggenmos, S. Nagele, J. Feist, J. Burgdörfer, R. Kienberger, and M. Schultze, “Attosecond correlation dynamics”, *Nature Physics* **13**, 280–285 (2016) [10.1038/nphys3941](https://doi.org/10.1038/nphys3941).
- [16] H. Muller, “Reconstruction of attosecond harmonic beating by interference of two-photon transitions”, *Applied Physics B* **74**, s17–s21 (2002) [10.1007/s00340-002-0894-8](https://doi.org/10.1007/s00340-002-0894-8).
- [17] T. Haarlammert and H. Zacharias, “Application of high harmonic radiation in surface science”, *Current Opinion in Solid State and Materials Science* **13**, 13–27 (2009) [10.1016/j.cossms.2008.12.003](https://doi.org/10.1016/j.cossms.2008.12.003).
- [18] M. I. Stockman, M. F. Kling, U. Kleineberg, and F. Krausz, “Attosecond nanoplasmonic-field microscope”, *Nature Photonics* **1**, 539–544 (2007) [10.1038/nphoton.2007.169](https://doi.org/10.1038/nphoton.2007.169).
- [19] S. H. Chew, F. Süßmann, C. Späth, A. Wirth, J. Schmidt, S. Zherebtsov, A. Guggenmos, A. Oelsner, N. Weber, J. Kapaldo, A. Gliserin, M. I. Stockman, M. F. Kling, and U. Kleineberg, “Time-of-flight-photoelectron emission microscopy on plasmonic structures using attosecond extreme ultraviolet pulses”, *Applied Physics Letters* **100**, 051904 (2012) [10.1063/1.3670324](https://doi.org/10.1063/1.3670324).
- [20] S. H. Chew, K. Pearce, C. Späth, A. Guggenmos, J. Schmidt, F. Süßmann, M. F. Kling, U. Kleineberg, E. Mårzell, C. L. Arnold, E. Lorek, P. Rudawski, C. Guo, M. Miranda, F. Ardana, J. Mauritsson, A. L’Huillier, and A. Mikkelsen, “Imaging localized surface plasmons by femtosecond to attosecond time-resolved photoelectron emission microscopy – ‘ATTO-PEEM’”, in *Attosecond nanophysics* (Wiley-VCH Verlag GmbH & Co. KGaA, Jan. 2015), pp. 325–364, [10.1002/9783527665624.ch10](https://doi.org/10.1002/9783527665624.ch10).
- [21] G. Sansone, F. Kelkensberg, J. F. Pérez-Torres, F. Morales, M. F. Kling, W. Siu, O. Ghafur, P. Johnsson, M. Swoboda, E. Benedetti, F. Ferrari, F. Lépine, J. L. Sanz-Vicario, S. Zherebtsov, I. Znakovskaya, A. L’Huillier, M. Y. Ivanov, M. Nisoli, F. Martín, and M. J. J. Vrakking, “Electron localization following attosecond molecular photoionization”, *Nature* **465**, 763–766 (2010) [10.1038/nature09084](https://doi.org/10.1038/nature09084).
- [22] B. Bergues, M. Kübel, N. G. Johnson, B. Fischer, N. Camus, K. J. Betsch, O. Herrwerth, A. Senftleben, A. M. Sayler, T. Rathje, T. Pfeifer, I. Ben-Itzhak, R. R. Jones, G. G. Paulus, F. Krausz, R. Moshhammer, J. Ullrich, and M. F. Kling, “Attosecond tracing of correlated electron-emission in non-sequential double ionization”, *Nature Communications* **3**, 813 (2012) [10.1038/ncomms1807](https://doi.org/10.1038/ncomms1807).
- [23] X. Zhou, P. Ranitovic, C. W. Hogle, J. H. D. Eland, H. C. Kapteyn, and M. M. Murnane, “Probing and controlling non-born–Oppenheimer dynamics in highly excited molecular ions”, *Nature Physics* **8**, 232–237 (2012) [10.1038/nphys2211](https://doi.org/10.1038/nphys2211).
- [24] A. Pirati, R. Peeters, D. Smith, S. Lok, M. van Noordenburg, R. van Es, E. Verhoeven, H. Meijer, A. Minnaert, J.-W. van der Horst, H. Meiling, J. Mallmann, C. Wagner, J. Stoeldraijer, G. Fisser, J. Finders, C. Zoldesi, U. Stamm, H. Boom, D. Brandt, D. Brown, I. Fomenkov, and M. Purvis, “EUV lithography performance for manufacturing: Status and outlook”, in *Extreme ultraviolet (EUV) lithography VII*, edited by E. M. Panning and K. A. Goldberg (Mar. 2016), [10.1117/12.2220423](https://doi.org/10.1117/12.2220423).

- [25] F. Krausz and M. Ivanov, “Attosecond physics”, *Reviews of Modern Physics* **81**, 163–234 (2009) [10.1103/revmodphys.81.163](https://doi.org/10.1103/revmodphys.81.163).
- [26] F. Krausz and M. I. Stockman, “Attosecond metrology: From electron capture to future signal processing”, *Nature Photonics* **8**, 205–213 (2014) [10.1038/nphoton.2014.28](https://doi.org/10.1038/nphoton.2014.28).
- [27] E. Goulielmakis, M. Schultze, M. Hofstetter, V. S. Yakovlev, J. Gagnon, M. Uiberacker, A. L. Aquila, E. M. Gullikson, D. T. Attwood, R. Kienberger, F. Krausz, and U. Kleineberg, “Single-cycle nonlinear optics”, *Science* **320**, 1614–1617 (2008) [10.1126/science.1157846](https://doi.org/10.1126/science.1157846).
- [28] O. Tcherbakoff, E. Mével, D. Descamps, J. Plumridge, and E. Constant, “Time-gated high-order harmonic generation”, *Physical Review A* **68**, 043804 (2003) [10.1103/physreva.68.043804](https://doi.org/10.1103/physreva.68.043804).
- [29] M. Louisy, C. L. Arnold, M. Miranda, E. W. Larsen, S. N. Bengtsson, D. Kroon, M. Kotur, D. Guénot, L. Rading, P. Rudawski, F. Brizuela, F. Campi, B. Kim, A. Jarnac, A. Houard, J. Mauritsson, P. Johnsson, A. L’Huillier, and C. M. Heyl, “Gating attosecond pulses in a noncollinear geometry”, *Optica* **2**, 563 (2015) [10.1364/optica.2.000563](https://doi.org/10.1364/optica.2.000563).
- [30] H. Vincenti and F. Quéré, “Attosecond lighthouses: How to use spatiotemporally coupled light fields to generate isolated attosecond pulses”, *Physical Review Letters* **108**, 113904 (2012) [10.1103/physrevlett.108.113904](https://doi.org/10.1103/physrevlett.108.113904).
- [31] T. J. Hammond, G. G. Brown, K. T. Kim, D. M. Villeneuve, and P. B. Corkum, “Attosecond pulses measured from the attosecond lighthouse”, *Nature Photonics* **10**, 171–175 (2016) [10.1038/nphoton.2015.271](https://doi.org/10.1038/nphoton.2015.271).
- [32] E. Goulielmakis, Z.-H. Loh, A. Wirth, R. Santra, N. Rohringer, V. S. Yakovlev, S. Zherebtsov, T. Pfeifer, A. M. Azzeer, M. F. Kling, S. R. Leone, and F. Krausz, “Real-time observation of valence electron motion”, *Nature* **466**, 739–743 (2010) [10.1038/nature09212](https://doi.org/10.1038/nature09212).
- [33] A. Wirth, M. T. Hassan, I. Grguras, J. Gagnon, A. Moulet, T. T. Luu, S. Pabst, R. Santra, Z. A. Alahmed, A. M. Azzeer, V. S. Yakovlev, V. Pervak, F. Krausz, and E. Goulielmakis, “Synthesized light transients”, *Science* **334**, 195–200 (2011) [10.1126/science.1210268](https://doi.org/10.1126/science.1210268).
- [34] A. L. Cavalieri, N. Müller, T. Uphues, V. S. Yakovlev, A. Baltuška, B. Horvath, B. Schmidt, L. Blümel, R. Holzwarth, S. Hendel, M. Drescher, U. Kleineberg, P. M. Echenique, R. Kienberger, F. Krausz, and U. Heinzmann, “Attosecond spectroscopy in condensed matter”, *Nature* **449**, 1029–1032 (2007) [10.1038/nature06229](https://doi.org/10.1038/nature06229).
- [35] Z. Tao, C. Chen, T. Szilvási, M. Keller, M. Mavrikakis, H. Kapteyn, and M. Murnane, “Direct time-domain observation of attosecond final-state lifetimes in photoemission from solids”, *Science* **353**, 62–67 (2016) [10.1126/science.aaf6793](https://doi.org/10.1126/science.aaf6793).
- [36] M. Isinger, R. J. Squibb, D. Busto, S. Zhong, A. Harth, D. Kroon, S. Nandi, C. L. Arnold, M. Miranda, J. M. Dahlström, E. Lindroth, R. Feifel, M. Gisselbrecht, and A. L’Huillier, “Photoionization in the time and frequency domain”, *Science* **358**, 893–896 (2017) [10.1126/science.aao7043](https://doi.org/10.1126/science.aao7043).
- [37] L. Cattaneo, J. Vos, M. Lucchini, L. Gallmann, C. Cirelli, and U. Keller, “Comparison of attosecond streaking and RABBITT”, *Optics Express* **24**, 29060 (2016) [10.1364/oe.24.029060](https://doi.org/10.1364/oe.24.029060).

- [38] M. Schultze, M. Fiess, N. Karpowicz, J. Gagnon, M. Korbman, M. Hofstetter, S. Neppl, A. L. Cavalieri, Y. Komninos, T. Mercouris, C. A. Nicolaides, R. Pazourek, S. Nagele, J. Feist, J. Burgdorfer, A. M. Azzeer, R. Ernstorfer, R. Kienberger, U. Kleineberg, E. Goulielmakis, F. Krausz, and V. S. Yakovlev, “*Delay in photoemission*”, *Science* **328**, 1658–1662 (2010) [10.1126/science.1189401](https://doi.org/10.1126/science.1189401).
- [39] R. Locher, L. Castiglioni, M. Lucchini, M. Greif, L. Gallmann, J. Osterwalder, M. Hengsberger, and U. Keller, “*Energy-dependent photoemission delays from noble metal surfaces by attosecond interferometry*”, *Optica* **2**, 405 (2015) [10.1364/optica.2.000405](https://doi.org/10.1364/optica.2.000405).
- [40] M. Lucchini, L. Castiglioni, L. Kasmi, P. Kliuiev, A. Ludwig, M. Greif, J. Osterwalder, M. Hengsberger, L. Gallmann, and U. Keller, “*Light-matter interaction at surfaces in the spatiotemporal limit of macroscopic models*”, *Physical Review Letters* **115**, 137401 (2015) [10.1103/physrevlett.115.137401](https://doi.org/10.1103/physrevlett.115.137401).
- [41] C. Chen, Z. Tao, A. Carr, P. Matyba, T. Szilvási, S. Emmerich, M. Piecuch, M. Keller, D. Zusin, S. Eich, M. Rollinger, W. You, S. Mathias, U. Thumm, M. Mavrikakis, M. Aeschlimann, P. M. Oppeneer, H. Kapteyn, and M. Murnane, “*Distinguishing attosecond electron–electron scattering and screening in transition metals*”, *Proceedings of the National Academy of Sciences* **114**, E5300–E5307 (2017) [10.1073/pnas.1706466114](https://doi.org/10.1073/pnas.1706466114).
- [42] S. Hellmann, K. Rossnagel, M. Marczyński-Bühlow, and L. Kipp, “*Vacuum space-charge effects in solid-state photoemission*”, *Physical Review B* **79**, 035402 (2009) [10.1103/physrevb.79.035402](https://doi.org/10.1103/physrevb.79.035402).
- [43] R. J. Jones, K. D. Moll, M. J. Thorpe, and J. Ye, “*Phase-coherent frequency combs in the vacuum ultraviolet via high-harmonic generation inside a femtosecond enhancement cavity*”, *Physical Review Letters* **94**, 193201 (2005) [10.1103/physrevlett.94.193201](https://doi.org/10.1103/physrevlett.94.193201).
- [44] C. Gohle, T. Udem, M. Herrmann, J. Rauschenberger, R. Holzwarth, H. A. Schuessler, F. Krausz, and T. W. Hänsch, “*A frequency comb in the extreme ultraviolet*”, *Nature* **436**, 234–237 (2005) [10.1038/nature03851](https://doi.org/10.1038/nature03851).
- [45] C. Benko, T. K. Allison, A. Cingöz, L. Hua, F. Labaye, D. C. Yost, and J. Ye, “*Extreme ultraviolet radiation with coherence time greater than 1 s*”, *Nature Photonics* **8**, 530–536 (2014) [10.1038/nphoton.2014.132](https://doi.org/10.1038/nphoton.2014.132).
- [46] F. Merkt and T. P. Softley, “*Final-state interactions in the zero-kinetic-energy-photoelectron spectrum of h_2* ”, *The Journal of Chemical Physics* **96**, 4149–4156 (1992) [10.1063/1.461870](https://doi.org/10.1063/1.461870).
- [47] M. Fischer, N. Kolachevsky, M. Zimmermann, R. Holzwarth, T. Udem, T. W. Hänsch, M. Abgrall, J. Grünert, I. Maksimovic, S. Bize, H. Marion, F. P. D. Santos, P. Lemonde, G. Santarelli, P. Laurent, A. Clairon, C. Salomon, M. Haas, U. D. Jentschura, and C. H. Keitel, “*New limits on the drift of fundamental constants from laboratory measurements*”, *Physical Review Letters* **92**, 230802 (2004) [10.1103/physrevlett.92.230802](https://doi.org/10.1103/physrevlett.92.230802).
- [48] A. Cingöz, D. C. Yost, T. K. Allison, A. Ruehl, M. E. Fermann, I. Hartl, and J. Ye, “*Direct frequency comb spectroscopy in the extreme ultraviolet*”, *Nature* **482**, 68–71 (2012) [10.1038/nature10711](https://doi.org/10.1038/nature10711).
- [49] A. Ozawa and Y. Kobayashi, “*Vuv frequency-comb spectroscopy of atomic xenon*”, *Physical Review A* **87**, 022507 (2013) [10.1103/physreva.87.022507](https://doi.org/10.1103/physreva.87.022507).

- [50] S. Hädrich, M. Krebs, A. Hoffmann, A. Klenke, J. Rothhardt, J. Limpert, and A. Tünnermann, “Exploring new avenues in high repetition rate table-top coherent extreme ultraviolet sources”, *Light: Science & Applications* **4**, e320–e320 (2015) [10.1038/lsa.2015.93](https://doi.org/10.1038/lsa.2015.93).
- [51] D. C. Yost, A. Cingöz, T. K. Allison, A. Ruehl, M. E. Fermann, I. Hartl, and J. Ye, “Power optimization of XUV frequency combs for spectroscopy applications [Invited]”, *Optics Express* **19**, 23483 (2011) [10.1364/oe.19.023483](https://doi.org/10.1364/oe.19.023483).
- [52] A. K. Mills, T. J. Hammond, M. H. C. Lam, and D. J. Jones, “XUV frequency combs via femtosecond enhancement cavities”, *Journal of Physics B: Atomic, Molecular and Optical Physics* **45**, 142001 (2012) [10.1088/0953-4075/45/14/142001](https://doi.org/10.1088/0953-4075/45/14/142001).
- [53] I. Pupeza, S. Holzberger, T. Eidam, H. Carstens, D. Esser, J. Weitenberg, P. Rußbüldt, J. Rauschenberger, J. Limpert, T. Udem, A. Tünnermann, T. W. Hänsch, A. Apolonski, F. Krausz, and E. Fill, “Compact high-repetition-rate source of coherent 100 eV radiation”, *Nature Photonics* **7**, 608–612 (2013) [10.1038/nphoton.2013.156](https://doi.org/10.1038/nphoton.2013.156).
- [54] H. Carstens, N. Lilienfein, S. Holzberger, C. Jocher, T. Eidam, J. Limpert, A. Tünnermann, J. Weitenberg, D. C. Yost, A. Alghamdi, Z. Alahmed, A. Azzeer, A. Apolonski, E. Fill, F. Krausz, and I. Pupeza, “Megawatt-scale average-power ultrashort pulses in an enhancement cavity”, *Optics Letters* **39**, 2595 (2014) [10.1364/ol.39.002595](https://doi.org/10.1364/ol.39.002595).
- [55] H. Carstens, M. Högner, T. Saule, S. Holzberger, N. Lilienfein, A. Guggenmos, C. Jocher, T. Eidam, D. Esser, V. Tosa, V. Pervak, J. Limpert, A. Tünnermann, U. Kleineberg, F. Krausz, and I. Pupeza, “High-harmonic generation at 250 MHz with photon energies exceeding 100 eV”, *Optica* **3**, 366 (2016) [10.1364/optica.3.000366](https://doi.org/10.1364/optica.3.000366).
- [56] T. Saule, S. Heinrich, J. Schötz, N. Lilienfein, M. Högner, O. deVries, M. Plötner, J. Weitenberg, D. Esser, J. Schulte, P. Russbuedt, J. Limpert, M. F. Kling, U. Kleineberg, and I. Pupeza, “High-flux ultrafast extreme-ultraviolet photoemission spectroscopy at 18.4 MHz pulse repetition rate”, *Nature Communications* **10**, 458 (2019) [10.1038/s41467-019-08367-y](https://doi.org/10.1038/s41467-019-08367-y).
- [57] N. Lilienfein, C. Hofer, S. Holzberger, C. Matzer, P. Zimmermann, M. Trubetskov, V. Pervak, and I. Pupeza, “Enhancement cavities for few-cycle pulses”, *Optics Letters* **42**, 271 (2017) [10.1364/ol.42.000271](https://doi.org/10.1364/ol.42.000271).
- [58] I. Pupeza, T. Eidam, J. Rauschenberger, B. Bernhardt, A. Ozawa, E. Fill, A. Apolonski, T. Udem, J. Limpert, Z. A. Alahmed, A. M. Azzeer, A. Tünnermann, T. W. Hänsch, and F. Krausz, “Power scaling of a high-repetition-rate enhancement cavity”, *Optics Letters* **35**, 2052 (2010) [10.1364/ol.35.002052](https://doi.org/10.1364/ol.35.002052).
- [59] H. Carstens, S. Holzberger, J. Kaster, J. Weitenberg, V. Pervak, A. Apolonski, E. Fill, F. Krausz, and I. Pupeza, “Large-mode enhancement cavities”, *Optics Express* **21**, 11606 (2013) [10.1364/oe.21.011606](https://doi.org/10.1364/oe.21.011606).
- [60] D. C. Yost, T. R. Schibli, and J. Ye, “Efficient output coupling of intracavity high-harmonic generation”, *Optics Letters* **33**, 1099 (2008) [10.1364/ol.33.001099](https://doi.org/10.1364/ol.33.001099).
- [61] A. Ozawa, J. Rauschenberger, C. Gohle, M. Herrmann, D. R. Walker, V. Pervak, A. Fernandez, R. Graf, A. Apolonski, R. Holzwarth, F. Krausz, T. W. Hänsch, and T. Udem, “High harmonic frequency combs for high resolution spectroscopy”, *Physical Review Letters* **100**, 253901 (2008) [10.1103/physrevlett.100.253901](https://doi.org/10.1103/physrevlett.100.253901).

- [62] T. J. Hammond, A. K. Mills, and D. J. Jones, “Near-threshold harmonics from a femtosecond enhancement cavity-based EUV source: Effects of multiple quantum pathways on spatial profile and yield”, *Optics Express* **19**, 24871 (2011) [10.1364/oe.19.024871](https://doi.org/10.1364/oe.19.024871).
- [63] J. Lee, D. R. Carlson, and R. J. Jones, “Optimizing intracavity high harmonic generation for XUV fs frequency combs”, *Optics Express* **19**, 23315 (2011) [10.1364/oe.19.023315](https://doi.org/10.1364/oe.19.023315).
- [64] B. Bernhardt, A. Ozawa, A. Vernaleken, I. Pupeza, J. Kaster, Y. Kobayashi, R. Holzwarth, E. Fill, F. Krausz, T. W. Hänsch, and T. Udem, “Vacuum ultraviolet frequency combs generated by a femtosecond enhancement cavity in the visible”, *Optics Letters* **37**, 503 (2012) [10.1364/ol.37.000503](https://doi.org/10.1364/ol.37.000503).
- [65] T. K. Allison, A. Cingöz, D. C. Yost, and J. Ye, “Extreme nonlinear optics in a femtosecond enhancement cavity”, *Physical Review Letters* **107**, 183903 (2011) [10.1103/physrevlett.107.183903](https://doi.org/10.1103/physrevlett.107.183903).
- [66] D. R. Carlson, J. Lee, J. Mongelli, E. M. Wright, and R. J. Jones, “Intracavity ionization and pulse formation in femtosecond enhancement cavities”, *Optics Letters* **36**, 2991 (2011) [10.1364/ol.36.002991](https://doi.org/10.1364/ol.36.002991).
- [67] K. D. Moll, R. J. Jones, and J. Ye, “Output coupling methods for cavity-based high-harmonic generation”, *Optics Express* **14**, 8189 (2006) [10.1364/oe.14.008189](https://doi.org/10.1364/oe.14.008189).
- [68] J. Wu and H. Zeng, “Cavity-enhanced noncollinear high-harmonic generation for extreme ultraviolet frequency combs”, *Optics Letters* **32**, 3315 (2007) [10.1364/ol.32.003315](https://doi.org/10.1364/ol.32.003315).
- [69] A. Ozawa, A. Vernaleken, W. Schneider, I. Gotlibovych, T. Udem, and T. W. Hänsch, “Non-collinear high harmonic generation: a promising outcoupling method for cavity-assisted XUV generation”, *Optics Express* **16**, 6233 (2008) [10.1364/oe.16.006233](https://doi.org/10.1364/oe.16.006233).
- [70] I. Pupeza, E. E. Fill, and F. Krausz, “Low-loss VIS/IR-XUV beam splitter for high-power applications”, *Optics Express* **19**, 12108 (2011) [10.1364/oe.19.012108](https://doi.org/10.1364/oe.19.012108).
- [71] J. Weitenberg, P. Rußbüldt, T. Eidam, and I. Pupeza, “Transverse mode tailoring in a quasi-imaging high-finesse femtosecond enhancement cavity”, *Optics Express* **19**, 9551 (2011) [10.1364/oe.19.009551](https://doi.org/10.1364/oe.19.009551).
- [72] W. P. Putnam, D. N. Schimpf, G. Abram, and F. X. Kärtner, “Bessel-Gauss beam enhancement cavities for high-intensity applications”, *Optics Express* **20**, 24429 (2012) [10.1364/oe.20.024429](https://doi.org/10.1364/oe.20.024429).
- [73] I. Pupeza, M. Högner, J. Weitenberg, S. Holzberger, D. Esser, T. Eidam, J. Limpert, A. Tünnermann, E. Fill, and V. S. Yakovlev, “Cavity-enhanced high-harmonic generation with spatially tailored driving fields”, *Physical Review Letters* **112**, 103902 (2014) [10.1103/physrevlett.112.103902](https://doi.org/10.1103/physrevlett.112.103902).
- [74] K. Wakui, K. Hayasaka, and T. Ido, “Generation of vacuum ultraviolet radiation by intracavity high-harmonic generation toward state detection of single trapped ions”, *Applied Physics B* **117**, 957–967 (2014) [10.1007/s00340-014-5914-y](https://doi.org/10.1007/s00340-014-5914-y).
- [75] C. M. Heyl, H. Coudert-Alteirac, M. Miranda, M. Louisy, K. Kovacs, V. Tosa, E. Balogh, K. Varjú, A. L’Huillier, A. Couairon, and C. L. Arnold, “Scale-invariant nonlinear optics in gases”, *Optica* **3**, 75 (2016) [10.1364/optica.3.000075](https://doi.org/10.1364/optica.3.000075).

- [76] A. D. Shiner, C. Trallero-Herrero, N. Kajumba, H.-C. Bandulet, D. Comtois, F. Légaré, M. Giguère, J.-C. Kieffer, P. B. Corkum, and D. M. Villeneuve, “*Wavelength scaling of high harmonic generation efficiency*”, *Physical Review Letters* **103**, 073902 (2009) [10.1103/physrevlett.103.073902](https://doi.org/10.1103/physrevlett.103.073902).
- [77] S. Holzberger, N. Lilienfein, H. Carstens, T. Saule, M. Högner, F. Lücking, M. Trubetskov, V. Pervak, T. Eidam, J. Limpert, A. Tünnermann, E. Fill, F. Krausz, and I. Pupeza, “*Femtosecond enhancement cavities in the nonlinear regime*”, *Physical Review Letters* **115**, 023902 (2015) [10.1103/physrevlett.115.023902](https://doi.org/10.1103/physrevlett.115.023902).
- [78] T. Saule, M. Högner, N. Lilienfein, O. de Vries, M. Plötner, V. S. Yakovlev, N. Karpowicz, J. Limpert, and I. Pupeza, “*Cumulative plasma effects in cavity-enhanced high-order harmonic generation in gases*”, *APL Photonics* **3**, 101301 (2018) [10.1063/1.5037196](https://doi.org/10.1063/1.5037196).
- [79] S. Hädrich, A. Klenke, J. Rothhardt, M. Krebs, A. Hoffmann, O. Pronin, V. Pervak, J. Limpert, and A. Tünnermann, “*High photon flux table-top coherent extreme-ultraviolet source*”, *Nature Photonics* **8**, 779–783 (2014) [10.1038/nphoton.2014.214](https://doi.org/10.1038/nphoton.2014.214).
- [80] M. Högner, T. Saule, and I. Pupeza, “*Efficiency of cavity-enhanced high harmonic generation with geometric output coupling*”, *Journal of Physics B: Atomic, Molecular and Optical Physics* **52**, 075401 (2019) [10.1088/1361-6455/ab06db](https://doi.org/10.1088/1361-6455/ab06db).
- [81] A. K. Mills, S. Zhdanovich, A. Sheyerman, G. Levy, A. Damascelli, and D. J. Jones, “An XUV source using a femtosecond enhancement cavity for photoemission spectroscopy”, in *Advances in x-ray free-electron lasers instrumentation iii*, edited by S. G. Biedron (May 2015), [10.1117/12.2184547](https://doi.org/10.1117/12.2184547).
- [82] C. Corder, P. Zhao, J. Bakalis, X. Li, M. D. Kershish, A. R. Muraca, M. G. White, and T. K. Allison, “*Ultrafast extreme ultraviolet photoemission without space charge*”, *Structural Dynamics* **5**, 054301 (2018) [10.1063/1.5045578](https://doi.org/10.1063/1.5045578).
- [83] S. Holzberger, N. Lilienfein, M. Trubetskov, H. Carstens, F. Lücking, V. Pervak, F. Krausz, and I. Pupeza, “*Enhancement cavities for zero-offset-frequency pulse trains*”, *Optics Letters* **40**, 2165 (2015) [10.1364/ol.40.002165](https://doi.org/10.1364/ol.40.002165).
- [84] C. M. Heyl, S. N. Bengtsson, S. Carlström, J. Mauritsson, C. L. Arnold, and A. L’Huillier, “*Noncollinear optical gating*”, *New Journal of Physics* **16**, 052001 (2014) [10.1088/1367-2630/16/5/052001](https://doi.org/10.1088/1367-2630/16/5/052001).
- [85] C. M. Heyl, S. N. Bengtsson, S. Carlström, J. Mauritsson, C. L. Arnold, and A. L’Huillier, “*Corrigendum: Noncollinear optical gating (2014 New J. Phys. 16 052001)*”, *New Journal of Physics* **16**, 109501 (2014) [10.1088/1367-2630/16/10/109501](https://doi.org/10.1088/1367-2630/16/10/109501).
- [86] M. Högner, V. Tosa, and I. Pupeza, “*Generation of isolated attosecond pulses with enhancement cavities—a theoretical study*”, *New Journal of Physics* **19**, 033040 (2017) [10.1088/1367-2630/aa6315](https://doi.org/10.1088/1367-2630/aa6315).
- [87] M. Högner, T. Saule, N. Lilienfein, V. Pervak, and I. Pupeza, “*Tailoring the transverse mode of a high-finesse optical resonator with stepped mirrors*”, *Journal of Optics* **20**, 024003 (2018) [10.1088/2040-8986/aa9ece](https://doi.org/10.1088/2040-8986/aa9ece).
- [88] M. Högner, T. Saule, S. Heinrich, N. Lilienfein, D. Esser, M. Trubetskov, V. Pervak, and I. Pupeza, “*Cavity-enhanced noncollinear high-harmonic generation*”, *Optics Express* **27**, 19675 (2019) [10.1364/oe.27.019675](https://doi.org/10.1364/oe.27.019675).

- [89] N. Lilienfein, C. Hofer, M. Högner, T. Saule, M. Trubetskov, V. Pervak, E. Fill, C. Riek, A. Leitenstorfer, J. Limpert, F. Krausz, and I. Pupeza, “*Temporal solitons in free-space femtosecond enhancement cavities*”, *Nature Photonics* **13**, 214–218 (2019) [10.1038/s41566-018-0341-y](https://doi.org/10.1038/s41566-018-0341-y).
- [90] P. B. Corkum, “*Plasma perspective on strong field multiphoton ionization*”, *Physical Review Letters* **71**, 1994–1997 (1993) [10.1103/physrevlett.71.1994](https://doi.org/10.1103/physrevlett.71.1994).
- [91] M. Lewenstein, P. Balcou, M. Y. Ivanov, A. L’Huillier, and P. B. Corkum, “*Theory of high-harmonic generation by low-frequency laser fields*”, *Physical Review A* **49**, 2117–2132 (1994) [10.1103/physreva.49.2117](https://doi.org/10.1103/physreva.49.2117).
- [92] M. Högner, V. Yakovlev, and I. Pupeza, *HHGmax*, <https://gitlab.com/mhoegner/HHGmax>.
- [93] M. Högner, “*Optical High-Order Harmonic Generation in Gas Targets with Spatially Tailored Driving Fields*”, Master’s thesis (Ludwig-Maximilians-Universität München, 2013).
- [94] P. Antoine, A. L’Huillier, M. Lewenstein, P. Salières, and B. Carré, “*Theory of high-order harmonic generation by an elliptically polarized laser field*”, *Physical Review A* **53**, 1725–1745 (1996) [10.1103/physreva.53.1725](https://doi.org/10.1103/physreva.53.1725).
- [95] M. Y. Ivanov, T. Brabec, and N. Burnett, “*Coulomb corrections and polarization effects in high-intensity high-harmonic emission*”, *Physical Review A* **54**, 742–745 (1996) [10.1103/physreva.54.742](https://doi.org/10.1103/physreva.54.742).
- [96] M. Geissler, G. Tempea, A. Scrinzi, M. Schnürer, F. Krausz, and T. Brabec, “*Light propagation in field-ionizing media: Extreme nonlinear optics*”, *Physical Review Letters* **83**, 2930–2933 (1999) [10.1103/physrevlett.83.2930](https://doi.org/10.1103/physrevlett.83.2930).
- [97] A. Couairon, E. Brambilla, T. Corti, D. Majus, O. de J. Ramírez-Góngora, and M. Kolesik, “*Practitioner’s guide to laser pulse propagation models and simulation, Numerical implementation and practical usage of modern pulse propagation models*”, *The European Physical Journal Special Topics* **199**, 5–76 (2011) [10.1140/epjst/e2011-01503-3](https://doi.org/10.1140/epjst/e2011-01503-3).
- [98] A.-T. Le, T. Morishita, and C. D. Lin, “*Extraction of the species-dependent dipole amplitude and phase from high-order harmonic spectra in rare-gas atoms*”, *Physical Review A* **78**, 023814 (2008) [10.1103/physreva.78.023814](https://doi.org/10.1103/physreva.78.023814).
- [99] V. Tosa, J. S. Lee, H. T. Kim, and C. H. Nam, “*Attosecond pulses generated by the lighthouse effect in Ar gas*”, *Physical Review A* **91**, 051801 (2015) [10.1103/physreva.91.051801](https://doi.org/10.1103/physreva.91.051801).
- [100] B. M. Penetrante, W. M. Wood, C. W. Siders, J. N. Bardsley, and M. C. Downer, “*Ionization-induced frequency shifts in intense femtosecond laser pulses*”, *Journal of the Optical Society of America B* **9**, 2032 (1992) [10.1364/josab.9.002032](https://doi.org/10.1364/josab.9.002032).
- [101] W. Nagourney, *Quantum electronics for atomic physics and telecommunication, Second edition* (Oxford University Press, May 2014), [10.1093/acprof:oso/9780199665488.001.0001](https://doi.org/10.1093/acprof:oso/9780199665488.001.0001).
- [102] F. Leo, S. Coen, P. Kockaert, S.-P. Gorza, P. Emplit, and M. Haelterman, “*Temporal cavity solitons in one-dimensional Kerr media as bits in an all-optical buffer*”, *Nature Photonics* **4**, 471–476 (2010) [10.1038/nphoton.2010.120](https://doi.org/10.1038/nphoton.2010.120).

- [103] T. Herr, V. Brasch, J. D. Jost, C. Y. Wang, N. M. Kondratiev, M. L. Gorodetsky, and T. J. Kippenberg, “*Temporal solitons in optical microresonators*”, *Nature Photonics* **8**, 145–152 (2013) [10.1038/nphoton.2013.343](https://doi.org/10.1038/nphoton.2013.343).
- [104] K. Saha, Y. Okawachi, B. Shim, J. S. Levy, R. Salem, A. R. Johnson, M. A. Foster, M. R. E. Lamont, M. Lipson, and A. L. Gaeta, “*Modelocking and femtosecond pulse generation in chip-based frequency combs*”, *Optics Express* **21**, 1335 (2013) [10.1364/oe.21.001335](https://doi.org/10.1364/oe.21.001335).
- [105] W. Liang, D. Eliyahu, V. S. Ilchenko, A. A. Savchenkov, A. B. Matsko, D. Seidel, and L. Maleki, “*High spectral purity Kerr frequency comb radio frequency photonic oscillator*”, *Nature Communications* **6**, 7957 (2015) [10.1038/ncomms8957](https://doi.org/10.1038/ncomms8957).
- [106] X. Yi, Q.-F. Yang, K. Y. Yang, M.-G. Suh, and K. Vahala, “*Soliton frequency comb at microwave rates in a high-q silica microresonator*”, *Optica* **2**, 1078 (2015) [10.1364/optica.2.001078](https://doi.org/10.1364/optica.2.001078).
- [107] V. Brasch, M. Geiselmann, T. Herr, G. Lihachev, M. H. P. Pfeiffer, M. L. Gorodetsky, and T. J. Kippenberg, “*Photonic chip-based optical frequency comb using soliton Cherenkov radiation*”, *Science* **351**, 357–360 (2015) [10.1126/science.aad4811](https://doi.org/10.1126/science.aad4811).
- [108] E. Obrzud, S. Lecomte, and T. Herr, “*Temporal solitons in microresonators driven by optical pulses*”, *Nature Photonics* **11**, 600–607 (2017) [10.1038/nphoton.2017.140](https://doi.org/10.1038/nphoton.2017.140).
- [109] M. Seidel, G. Arisholm, J. Brons, V. Pervak, and O. Pronin, “*All solid-state spectral broadening: An average and peak power scalable method for compression of ultrashort pulses*”, *Optics Express* **24**, 9412 (2016) [10.1364/oe.24.009412](https://doi.org/10.1364/oe.24.009412).
- [110] K. Fritsch, M. Poetzlberger, V. Pervak, J. Brons, and O. Pronin, “*All-solid-state multipass spectral broadening to sub-20 fs*”, *Optics Letters* **43**, 4643 (2018) [10.1364/ol.43.004643](https://doi.org/10.1364/ol.43.004643).
- [111] D. Esser, J. Weitenberg, W. Bröring, I. Pupeza, S. Holzberger, and H.-D. Hoffmann, “*Laser-manufactured mirrors for geometrical output coupling of intracavity-generated high harmonics*”, *Optics Express* **21**, 26797 (2013) [10.1364/oe.21.026797](https://doi.org/10.1364/oe.21.026797).
- [112] G. Porat, C. M. Heyl, S. B. Schoun, C. Benko, N. Dörre, K. L. Corwin, and J. Ye, “*Phase-matched extreme-ultraviolet frequency-comb generation*”, *Nature Photonics* **12**, 387–391 (2018) [10.1038/s41566-018-0199-z](https://doi.org/10.1038/s41566-018-0199-z).
- [113] C. M. Heyl, S. B. Schoun, G. Porat, H. Green, and J. Ye, “*A nozzle for high-density supersonic gas jets at elevated temperatures*”, *Review of Scientific Instruments* **89**, 113114 (2018) [10.1063/1.5051586](https://doi.org/10.1063/1.5051586).
- [114] E. Mårzell, C. L. Arnold, E. Lorek, D. Guenot, T. Fordell, M. Miranda, J. Mauritsson, H. Xu, A. L’Huillier, and A. Mikkelsen, “*Secondary electron imaging of nanostructures using extreme ultra-violet attosecond pulse trains and infra-red femtosecond pulses, Secondary electron imaging of nanostructures*”, *Annalen der Physik* **525**, 162–170 (2013) [10.1002/andp.201200269](https://doi.org/10.1002/andp.201200269).
- [115] B. Förg, J. Schötz, F. Süßmann, M. Förster, M. Krüger, B. Ahn, W. A. Okell, K. Winter-sperger, S. Zherebtsov, A. Guggenmos, V. Pervak, A. Kessel, S. A. Trushin, A. M. Azzeer, M. I. Stockman, D. Kim, F. Krausz, P. Hommelhoff, and M. F. Kling, “*Attosecond nanoscale near-field sampling*”, *Nature Communications* **7**, 11717 (2016) [10.1038/ncomms11717](https://doi.org/10.1038/ncomms11717).

- [116] J. Schulte, T. Sartorius, J. Weitenberg, A. Vernaleken, and P. Russbueldt, “*Nonlinear pulse compression in a multi-pass cell*”, *Optics Letters* **41**, 4511 (2016) [10.1364/ol.41.004511](https://doi.org/10.1364/ol.41.004511).
- [117] S. Coen, H. G. Randle, T. Sylvestre, and M. Erkintalo, “*Modeling of octave-spanning Kerr frequency combs using a generalized mean-field Lugiato–Lefever model*”, *Optics Letters* **38**, 37 (2012) [10.1364/ol.38.000037](https://doi.org/10.1364/ol.38.000037).
- [118] L. A. Lugiato and R. Lefever, “*Spatial dissipative structures in passive optical systems*”, *Physical Review Letters* **58**, 2209–2211 (1987) [10.1103/physrevlett.58.2209](https://doi.org/10.1103/physrevlett.58.2209).
- [119] M. Haelterman, S. Trillo, and S. Wabnitz, “*Dissipative modulation instability in a nonlinear dispersive ring cavity*”, *Optics Communications* **91**, 401–407 (1992) [10.1016/0030-4018\(92\)90367-z](https://doi.org/10.1016/0030-4018(92)90367-z).
- [120] C. Hofer, “*Ultrabroadband enhancement cavities for nonlinear optics*”, Master’s thesis (Ludwig-Maximilians-Universität München, 2016).
- [121] J. Seres, E. Seres, C. Serrat, E. C. Young, J. S. Speck, and T. Schumm, “*All-solid-state VUV frequency comb at 160 nm using high-harmonic generation in nonlinear femtosecond enhancement cavity*”, *Optics Express* **27**, 6618 (2019) [10.1364/oe.27.006618](https://doi.org/10.1364/oe.27.006618).
- [122] C. Weingarten, A. Schmickler, E. Willenborg, K. Wissenbach, and R. Poprawe, “*Laser polishing and laser shape correction of optical glass*”, *Journal of Laser Applications* **29**, 011702 (2017) [10.2351/1.4974905](https://doi.org/10.2351/1.4974905).
- [123] C. Weingarten, E. Uluz, A. Schmickler, K. Braun, E. Willenborg, A. Temmler, and S. Heidrich, “*Glass processing with pulsed CO₂ laser radiation*”, *Applied Optics* **56**, 777 (2017) [10.1364/ao.56.000777](https://doi.org/10.1364/ao.56.000777).
- [124] I. J. Kim, C. M. Kim, H. T. Kim, G. H. Lee, Y. S. Lee, J. Y. Park, D. J. Cho, and C. H. Nam, “*Highly efficient high-harmonic generation in an orthogonally polarized two-color laser field*”, *Physical Review Letters* **94**, 243901 (2005) [10.1103/physrevlett.94.243901](https://doi.org/10.1103/physrevlett.94.243901).
- [125] E. J. Takahashi, P. Lan, O. D. Mücke, Y. Nabekawa, and K. Midorikawa, “*Infrared two-color multicycle laser field synthesis for generating an intense attosecond pulse*”, *Physical Review Letters* **104**, 233901 (2010) [10.1103/physrevlett.104.233901](https://doi.org/10.1103/physrevlett.104.233901).
- [126] B. Schütte, P. Weber, K. Kovács, E. Balogh, B. Major, V. Tosa, S. Han, M. J. J. Vrakking, K. Varjú, and A. Rouzée, “*Bright attosecond soft x-ray pulse trains by transient phase-matching in two-color high-order harmonic generation*”, *Optics Express* **23**, 33947 (2015) [10.1364/oe.23.033947](https://doi.org/10.1364/oe.23.033947).
- [127] H. Roskos, M. Thomson, M. Kreß, and T. Löffler, “*Broadband THz emission from gas plasmas induced by femtosecond optical pulses: From fundamentals to applications*”, *Laser & Photonics Review* **1**, 349–368 (2007) [10.1002/lpor.200710025](https://doi.org/10.1002/lpor.200710025).
- [128] N. V. Vvedenskii, A. I. Korytin, V. A. Kostin, A. A. Murzanev, A. A. Silaev, and A. N. Stepanov, “*Two-color laser-plasma generation of terahertz radiation using a frequency-tunable half harmonic of a femtosecond pulse*”, *Physical Review Letters* **112**, 055004 (2014) [10.1103/physrevlett.112.055004](https://doi.org/10.1103/physrevlett.112.055004).
- [129] T. Ideguchi, S. Holzner, B. Bernhardt, G. Guelachvili, N. Picqué, and T. W. Hänsch, “*Coherent raman spectro-imaging with laser frequency combs*”, *Nature* **502**, 355–358 (2013) [10.1038/nature12607](https://doi.org/10.1038/nature12607).

- [130] E. Constant, D. Garzella, P. Breger, E. Mével, C. Dorrer, C. Le Blanc, F. Salin, and P. Agostini, “*Optimizing high harmonic generation in absorbing gases: Model and experiment*”, *Physical Review Letters* **82**, 1668–1671 (1999) [10.1103/physrevlett.82.1668](https://doi.org/10.1103/physrevlett.82.1668).
- [131] E. J. Takahashi, Y. Nabekawa, and K. Midorikawa, “*Low-divergence coherent soft x-ray source at 13 nm by high-order harmonics*”, *Applied Physics Letters* **84**, 4–6 (2004) [10.1063/1.1637949](https://doi.org/10.1063/1.1637949).
- [132] E. Takahashi, Y. Nabekawa, H. Mashiko, H. Hasegawa, A. Suda, and K. Midorikawa, “*Generation of strong optical field in soft x-ray region by using high-order harmonics*”, *IEEE Journal of Selected Topics in Quantum Electronics* **10**, 1315–1328 (2004) [10.1109/jstqe.2004.838077](https://doi.org/10.1109/jstqe.2004.838077).
- [133] C. Ding, W. Xiong, T. Fan, D. D. Hickstein, T. Popmintchev, X. Zhang, M. Walls, M. M. Murnane, and H. C. Kapteyn, “*High flux coherent super-continuum soft x-ray source driven by a single-stage, 10mJ, Ti:sapphire amplifier-pumped OPA*”, *Optics Express* **22**, 6194 (2014) [10.1364/oe.22.006194](https://doi.org/10.1364/oe.22.006194).
- [134] E. Lorek, E. W. Larsen, C. M. Heyl, S. Carlström, D. Paleček, D. Zigmantas, and J. Mauritsson, “*High-order harmonic generation using a high-repetition-rate turnkey laser*”, *Review of Scientific Instruments* **85**, 123106 (2014) [10.1063/1.4902819](https://doi.org/10.1063/1.4902819).
- [135] J. Rothhardt, M. Krebs, S. Hädrich, S. Demmler, J. Limpert, and A. Tünnermann, “*Absorption-limited and phase-matched high harmonic generation in the tight focusing regime*”, *New Journal of Physics* **16**, 033022 (2014) [10.1088/1367-2630/16/3/033022](https://doi.org/10.1088/1367-2630/16/3/033022).
- [136] J. Rothhardt, S. Hädrich, A. Klenke, S. Demmler, A. Hoffmann, T. Gotschall, T. Eidam, M. Krebs, J. Limpert, and A. Tünnermann, “*53 W average power few-cycle fiber laser system generating soft x rays up to the water window*”, *Optics Letters* **39**, 5224 (2014) [10.1364/ol.39.005224](https://doi.org/10.1364/ol.39.005224).
- [137] C.-T. Chiang, M. Huth, A. Trützschler, M. Kiel, F. O. Schumann, J. Kirschner, and W. Widdra, “*Boosting laboratory photoelectron spectroscopy by megahertz high-order harmonics*”, *New Journal of Physics* **17**, 013035 (2015) [10.1088/1367-2630/17/1/013035](https://doi.org/10.1088/1367-2630/17/1/013035).
- [138] A. Ozawa, Z. Zhao, M. Kuwata-Gonokami, and Y. Kobayashi, “*High average power coherent vuv generation at 10 MHz repetition frequency by intracavity high harmonic generation*”, *Optics Express* **23**, 15107 (2015) [10.1364/oe.23.015107](https://doi.org/10.1364/oe.23.015107).
- [139] R. Klas, S. Demmler, M. Tschernajew, S. Hädrich, Y. Shamir, A. Tünnermann, J. Rothhardt, and J. Limpert, “*Table-top milliwatt-class extreme ultraviolet high harmonic light source*”, *Optica* **3**, 1167 (2016) [10.1364/optica.3.001167](https://doi.org/10.1364/optica.3.001167).
- [140] J. Rothhardt, S. Hädrich, Y. Shamir, M. Tschernajew, R. Klas, A. Hoffmann, G. K. Tadesse, A. Klenke, T. Gotschall, T. Eidam, J. Limpert, A. Tünnermann, R. Boll, C. Bomme, H. Dachraoui, B. Erk, M. Di Fraia, D. A. Horke, T. Kierspel, T. Mullins, A. Przystawik, E. Saveliev, J. Wiese, T. Laarmann, J. Küpper, and D. Rolles, “*High-repetition-rate and high-photon-flux 70 eV high-harmonic source for coincidence ion imaging of gas-phase molecules*”, *Optics Express* **24**, 18133 (2016) [10.1364/oe.24.018133](https://doi.org/10.1364/oe.24.018133).
- [141] Z. Zhao and Y. Kobayashi, “*Realization of a mW-level 10.7-eV ($\lambda = 115.6$ nm) laser by cascaded third harmonic generation of a Yb: fiber CPA laser at 1-MHz*”, *Optics Express* **25**, 13517 (2017) [10.1364/oe.25.013517](https://doi.org/10.1364/oe.25.013517).

List of Figures

1.1	Frequency comb in the frequency and time domain	4
1.2	Schematic of an enhancement cavity housing a (nonlinear) medium	4
1.3	Comparison of HHG sources	6
2.1	Three-step model for high-harmonic generation	11
2.2	Validation of the implemented single-atom model	14
2.3	Validation of the implemented propagation model	15
2.4	3D validation of the 1D model for intensity clamping	17
2.5	Observed mode deformations owing to cumulative plasma	20
2.6	Simulated mode spectra with cumulative plasma	21
2.7	Simulated free-space cavity soliton	23
5.1	Achievable IAP contrast ratio for different pulse durations	103
5.2	Angular distribution of the power in a TEM_{01} mode	106
5.3	Working principle of a multi-color enhancement cavity	106

List of Tables

A.1 Photon rates from HHG sources reported in literature	109
--	-----

Acknowledgments

Finally, I would like to thank all people which were directly or indirectly involved in the preparation of this thesis. First of all, I owe gratitude to Ferenc Krausz for supervising this doctoral thesis and establishing the great surrounding conditions in our research group. Ioachim Pupeza, my direct advisor, deserves wholehearted thanks for his idealistic way of leading a group, which always made me feel to be in good hands, and his never-ending and contagious enthusiasm. I have learned a lot thanks to his strong support and, at the same time, the great conferred independence. His good long-term vision and planning were a decisive factor for the successful termination of this thesis.

I sincerely thank Valer Tosa for his hospitality, his invaluable help in verifying the numerical model, and his magic creativity-enhancing Romanian mineral water! Michael's and Vova's commitment for ultra-broadband, highly-reflective multilayer coatings and Dominik's hard work for high-quality slit mirror substrates is highly appreciated. Vlad, Nick and Marcelo were a great help in theoretical as well as numerical questions.

Thanks to all the people with whom I was able to gain experimental experience in the course of my thesis and from whom I could learn experimental and theoretical skills: Henning, Simon, Tobi, Stephan, Niko, and of course Ioachim. I would especially like to thank Tobi and Stephan, with whom I spent most of my time in the lab and who introduced me to a couple of musical treasures and "treasures"! Thanks also for lab-related loans and rescue attempts, e.g. from the Kling group. I want to thank Niko for the good and productive collaboration on the soliton simulations, which was a great experience!

Many thanks to everyone who blue-pencilled publications, especially Johannes Weitenberg for his always helpful, detailed and well-founded comments. Special thanks to the victims who proofread the dissertation: Tobi, Niko, Stephan, Christina, Johannes, Ioachim, Flo and Andi.

I would also like to thank the people who organized and attended enjoyable events for the group and Marinus for the fun trip through China. In general, also the people who brought life into work, especially office colleagues and the lunch clique.

Sincere thanks to the professors who have agreed to be part of the examination board, especially to the secondary reviewer, Thomas Udem.

Last but not least, to my friends, parents and siblings who have alleviated and endured my unsoundness of mind, which has sometimes resulted from work stress and long hours of debugging simulation code – particularly Flo for adopting me and cooking for me in the exhausting final phase of the preparation of the thesis and Letty for her wonderful company.